MHD Wave Dynamics and Seismological Applications along Umbral Fan Loops

A thesis submitted in partial fulfilment of
the requirements for the degree of

Doctor of Philosophy

by

Ananya Rawat
Roll No: 20330002

Under the guidance of
Dr. Girjesh R Gupta

Udaipur Solar Observatory
Physical Research Laboratory, Ahmedabad, India

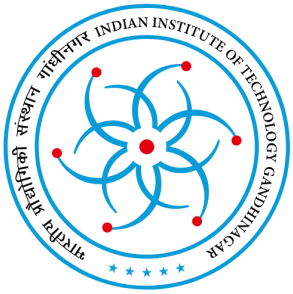

Department of Physics
Indian Institute of Technology Gandhinagar, India
2025

To my
beloved mother

Declaration

I hereby declare that this PhD thesis, titled **"MHD Wave Dynamics and Seismological Applications along Umbral Fan Loops"** is carried out by me to fulfil the requirement of PhD degree at *Udaipur Solar Observatory* of Physical Research Laboratory (PRL) under the supervision of Dr. Girjesh R Gupta. All information and facts provided in this thesis are correct to the best of my knowledge. I also declare that wherever I have borrowed any ideas or results of someone else, I have properly cited to the original sources. No part of this thesis has formed the basis for award of any other degree in any university or institution.

Date:

Place:

Ananya Rawat
IITGN Roll No: 20330002
Udaipur Solar Observatory
Physical Research Laboratory
Ahmedabad, India

Certificate

It is certified that the work contained in this thesis titled **"MHD Wave Dynamics and Seismological Applications along Umbral Fan Loops"**, submitted by Ananya Rawat (Roll No. 20330002) to the Indian Institute of Technology Gandhinagar, is a record of bonafide research work carried out by her under my supervision. This work has not been submitted elsewhere, either in part or full, for the award of any degree.

Date:

Place:

Dr. Girjesh R Gupta
Udaipur Solar Observatory
Physical Research Laboratory
Ahmedabad, India

Acknowledgement

There are moments in life when words feel inadequate. As I approach the culmination of my PhD journey, I find myself overwhelmed with emotion—gratitude, nostalgia, and a sense of indebtedness to those who have shaped this path.

First and foremost, I extend my deepest gratitude to my supervisor, **Dr. Girjesh R Gupta**, for his invaluable guidance, support, and encouragement throughout this journey. His expertise, patience, and insight have been instrumental in shaping both this research and my growth as a scholar. More than just a mentor, he has been a friend—his unique blend of strictness and friendliness made my PhD journey not only manageable but enjoyable. I am grateful for his encouragement to interact and collaborate with experts, and also for encouraging me to explore my own ideas. It has been a great privilege and honour to work under his mentorship. I am the luckiest person since I am his first student. I would also like to thank the Director of PRL, **Prof. Anil Bharadwaj**, for guiding me during the supervisor selection process.

I am also deeply thankful to **Prof. Sandeep Sahijpal** of Panjab University, my Master's professor, who first sparked my interest in astrophysics and helped me realize that physics can be truly beautiful when approached with passion.

I am sincerely grateful to my doctoral studies committee— **Prof. Nandita Srivastava**, **Prof. Brajesh Kumar**, and **Prof. Santosh Vadawale**—for their time, thoughtful feedback, and constructive suggestions. Our discussions during the half-yearly meetings were always intellectually stimulating and helped shape the direction of my work. A special note of thanks to **Nandita Ma'am**, whose keen observations during my initial presentations significantly enhanced my presentation skills.

My thanks also go to the academic committee at PRL for designing a rigorous and comprehensive coursework that laid a strong foundation for my PhD research. I thank all my course instructors. The solar physics module, in particular, deepened my understanding of the field and provided a broader perspective. The annual academic reviews offered invaluable encouragement, insightful critiques, and challenging questions that pushed me to grow. I am equally thankful to the **USO faculty members** for their constructive inputs during my area seminars. I also thank **Computer Networking and Information Technology Division (CNIT) team**, especially **Mr. Vaibhav Rathore** for all

the IT and setup-related issues.

My deepest gratitude goes out to my collaborators – **Prof. Tom Van Doorsselaere**, **Dr. S. Krishna Prasad**, **Prof. Robertus Erdélyi**, and **Prof. Helen Mason,** for the fruitful discussions and insightful thoughts through our meetings and emails. I am grateful to have the pleasure of working with them during my research.

I am also grateful to **Prof. Shashikiran Ganesh** and **Ms. Prachi Prajapati** for giving me the opportunity to do a project under their guidance on NICS data, which is a near-infrared 1.2-m telescope at Mount Abu, which resulted in a research paper. I would also like to thank **Prof. Aveek Sarkar** for helpful discussions and constant encouragement throughout my PhD journey.

I acknowledge **SDO**, **IRIS**, and the **Hinode** Team for making such an excellent telescope. AIA and HMI data are courtesy of SDO (NASA). IRIS is a NASA small explorer mission developed and operated by LMSAL with mission operations executed at NASA Ames Research Center and major contributions to downlink communications funded by the Norwegian Space Center (NSC, Norway) through an ESA PRODEX contract. Hinode is a Japanese mission developed and launched by ISAS/JAXA, collaborating with NAOJ as a domestic partner, NASA, and STFC (UK) as international partners. Scientific operation of the Hinode mission is conducted by the Hinode science team organized at ISAS/JAXA. This team mainly consists of scientists from institutes in partner countries. Support for the post-launch operation is provided by JAXA and NAOJ (Japan), STFC (UK), NASA (USA), ESA, and NSC (Norway). I also thank **CHIANTI atomic database** that is used in this thesis to perform spectral analysis and plasma diagnostics. CHIANTI is a collaborative project involving George Mason University, the University of Michigan (USA), the University of Cambridge (UK), and NASA Goddard Space Flight Center (USA).

I thank all my research paper referees for their helpful comments and suggestions that improved the quality of presentation of my work. The research work is carried out at the **Physical Research Laboratory (PRL)** is funded by the **Department of Space**, **Government of India**. I thank PRL for my PhD research fellowship.

I owe a special debt of gratitude to my friends and colleagues—your camaraderie, thoughtful conversations, and unwavering support turned this academic journey into a personally enriching experience. A special thanks to all my batch-mates, some are already doctors, and some will soon become doctors, for helping me out whenever I have

academic or admin-related problems or questions, or thesis compilation issues. I would also like to thank all those who took a printout of all my approvals and submitted them to the head of academic services. Thank you very much **Arup Chakrobarty**, **Malika Singhal**, **Wafikul Khan**, **Trinesh Sana**, **Debasish Pachhar**, and **Gurucharan Mohanta**. I would also like to thank **Abhishek Rana, Kamlesh Bora, Prabir Mitra, Satyam Aggarwal, Kushagra Upadhyay**, and **Binal Patel** for helping me adjust at USO. I would also like to acknowledge all the **juniors and Dr. Anshu Kumari** who came to USO after me; they literally lighten the USO campus, making it a more lively and fun place.

Last but not least, all my extroverted friends, **Himani Arora**, **Khyati Redhu**, **Mariya Ahsaan**, and people from **flat no. 81** thank you for adopting an introvert like me, for encouraging me to seek balance, and for being a continuous source of laughter and motivation. I would also like to thank all my **cousins** for their constant cheer and support.

Above all, I am profoundly grateful to my family. To my parents, **Mrs. Rekha Rawat** and **Mr. D.S. Rawat**, and to my brother, **Mr. Ujjwal Rawat**—thank you for your unwavering belief in me, your endless support, and for your patience, love, and encouragement through every high and low.

There are many in the list who directly and indirectly helped and motivated me during this journey. I thank all of them from the core of my heart.

I thank you all.

Abstract

Sunspots exhibit a wealth of magnetohydrodynamic (MHD) waves observed in the form of oscillations and wave phenomena like umbral flashes, umbral oscillations, running penumbral waves, and coronal waves. Despite the abundance of reports on the propagation and damping characteristics of waves in different layers of the solar atmosphere, observational reports on their generation, source regions, propagation from photosphere to corona, and damping parameters remain scarce. These waves can be further utilized to determine plasma and waveguide properties as important seismological applications. Comprehensive spectroscopic and imaging observations at high resolution shall provide new insights into the plasma parameters and Alfvén wave energy flux across the whole umbral atmosphere.

Coronal fan loops rooted in sunspot umbra constantly show 3-min period propagating slow magnetoacoustic waves (SMAWs) in the corona. However, the origin of these waves in the lower atmosphere is still unclear. We traced these loops in the lower atmosphere, where they are not visible using a recently devised novel data analysis technique developed using 3-min slow magnetoacoustic waves. Tracing of these loops also provided the first observational evidence of cross-sectional area expansion of loops with height from the photosphere to the corona, which is in accordance with flux tube expansion theory. We further traced the origin of these waves using amplitude and frequency modulations of 3-min waves along these loops from the corona to the photosphere via the transition region and chromosphere. We found similar modulation periods in the range 20-35 min. We concluded that the 3-min slow magnetoacoustic waves propagating along coronal fan loops are driven by 3-min oscillations observed at the photospheric footpoint of these fan loops.

While propagating, these waves show a signature of damping as well. We investigated the role of area divergence and frequencies on the damping of SMAWs from the photosphere to the corona and along the corona. We estimated the energy flux of propagating SMAWs from the photosphere to the corona along the fan loops and obtained their damping lengths in different period bands to study any period-dependent damping. Changes in the damping lengths of different-period waves were found. We further investigated the role of the area expansion of these loops on the damping of these SMAWs. A significant change in the damping lengths of waves was found before

and after incorporating the area divergence effect. Henceforth, we present the actual damping of SMAWs from the photosphere to the corona after incorporating the geometric effect of area expansion of the loops. Upon reaching the corona, these 3-min waves are observed to damp quickly; therefore, the area divergence does not play any significant role in the damping of 3-min waves in the corona. In the corona, these 3-min period waves can be further divided into various period sub-bands where they show a clean dispersive nature. The phase speed of these waves decreases with period in the selected period bands and thus highlights a clear dispersive nature of these slow waves propagating along coronal fan loops.

The recently devised technique to trace fan loops in the lower solar atmosphere, along with their cross-sectional area, was then utilized to determine the magnetic field strength along the loops using the flux conservation condition. We find the RMS magnetic field strengths in the range 1596-2269 G at the photospheric footpoints of the fan loops, which decreased rapidly to 158-236 G at the coronal footpoints. We further estimated the variation of plasma-β and Alfvén wave speed along the loop from photosphere to corona and in corona. The plasma-β at the photospheric and coronal footpoints are in the range 0.2-0.5 and 0.0001-0.001, respectively. We found plasma-$\beta < 1$ along the whole loop, whereas the plasma-$\beta \approx 1$ layer is found to be at sub-photospheric heights.

We further utilized spectroscopic and imaging data from the EIS and AIA, respectively, for plasma diagnostics. We compared the temperature and electron number density obtained along the loop length using various spectroscopic and imaging data analysis techniques. We further utilized the spectroscopic data from EIS to determine the velocity amplitude of Alfvén waves from non-thermal broadening of spectral lines. Combining these parameters with the already calculated magnetic field strength, we determined the Alfvén wave energy flux to be $\approx$ 1-2$\times10^7$ erg cm^{-2} s^{-1}, which is sufficient to heat the active region corona.

In summary, we conclude that the 3-min slow magnetoacoustic waves propagating along coronal fan loops are driven by 3-min oscillations observed at the photospheric footpoint of these fan loops. Our findings reveal that the area expansion of loops with height plays an important role in the damping of waves from the photosphere to the corona. However, its role in wave damping in the corona is negligible. In the corona, we observed the dispersive nature of the wave, which can explain the frequency-dependent

damping. Our results demonstrate the seismological potential of 3-min slow waves omnipresent in the umbral solar atmosphere to probe and map isolated loops and determine magnetic field and plasma-β variation along these loops. We further confirmed that the Alfvén waves carry sufficient energy flux to heat the active region corona. Finally, our results provide clear evidence of magnetic coupling of the whole solar umbral atmosphere through the propagation of 3-min slow waves along the fan loops at different atmospheric heights.

Keywords: Sunspots – Solar atmosphere — Corona – UV radiation – Magnetohydrodynamic waves – Solar coronal loops – Spectroscopic diagnostics.

List of publications

Published Articles:

- "Exploring the source region of 3-min slow magnetoacoustic waves observed in coronal fan loops rooted in sunspot umbra", **Ananya Rawat**, and Girjesh Gupta, 2023, MNRAS, 525, 4815, DOI: 10.1093/mnras/stad2426
- "Effect of area divergence and frequency on damping of slow magnetoacoustic waves propagating along umbral fan loops", **Ananya Rawat**, and Girjesh Gupta, 2024, MNRAS, 533, 1166, DOI: 10.1093/mnras/stae1889
- "Understanding the magnetic field and plasma-β along umbral fan loops traced using 3 minute slow waves", **Ananya Rawat**, Girjesh Gupta, Tom Van Doorsselaere, S. Krishna Prasad, and Robertus Erdélyi, 2025, ApJL, 988, L26, DOI: 10.3847/2041-8213/ade9be

In-preparation Articles:

- "Exploring the dispersive nature of slow magnetoacoustic waves propagating along coronal fan loops and their effect on the frequency-dependent damping", **Ananya Rawat**, and Girjesh Gupta, 2025, MNRAS
- "Spectroscopic diagnostics of coronal fan loops using AIA and EIS", **Ananya Rawat**, and Girjesh Gupta, 2025, Sol. Phys.

Refereed Conference Proceedings:

- "Exploring magnetic coupling of solar atmosphere through frequency modulations of 3-min slow magnetoacoustic waves", **Ananya Rawat**, and Girjesh Gupta, 2024, BSRSL, 93, 948, DOI: 10.25518/0037-9565.11933

Contributed Articles (not part of thesis):

- "Near infrared background with the 1.2 m telescope at Mount Abu", Prachi Prajapati, Anwesh Mishra, **Ananya Rawat**, Shashikiran Ganesh, Vishal Joshi, Navpreet Kaur, Neeraj Kumar, Sachindra Naik, and Sunil Chandra, 2023, JAA, 44, 54, DOI: 10.1007/s12036-023-09933-z

- "Investigating propagation of small-scale flare heat flux in the lower and upper atmosphere of solar active region", Girjesh Gupta, **Ananya Rawat**, Helen Mason, and Robertus Erdélyi, 2025, MNRAS, under revision

- "Critical Science Plan of the Solar Ultraviolet Imaging Telescope (SUIT) onboard Aditya-L1 mission", Durgesh Tripathi,.....**Ananya Rawat**,..... et al. 2025, Sol. Phys., In preparation

Contents

List of Figures

List of Tables

Chapter 1

Introduction

Various Sanskrit mantras highlight humans early realization of the significance of our nearest star, the Sun. The optimal distance of the Sun provides the essential energy that nurtures life on Earth. Since the prehistoric era, cultures across the globe have worshiped the Sun, recognizing its power. In 1543, Polish astronomer Nicolaus Copernicus discovered the heliocentric model (all the celestial bodies orbit around the Sun) over the popular belief of the geocentric model (all the celestial bodies orbit around the Earth), revolutionizing our understanding of the solar system. The Earth revolves around the Sun in an ecliptic plane having a tilt of 23.5°. This axial tilt is responsible for the changing seasons. Sun traverses the sky by rising in the east and setting in the west, but its path shifts daily due to Earth's eastward rotation (e.g., Narayanan, 2013).

The Sun's journey began as a vast cloud of gas and dust, known as the solar nebula, which underwent gravitational collapse. This collapse ignited nuclear fusion in its core, generating an immense amount of energy. The outward pressure from this fusion balances the inward gravitational pull, maintaining the stable size of the Sun. The thermonuclear fusion reaction in the core of the Sun generates heat and light. The Sun is now a middle-aged star located in the outer spiral arm of the Milky Way galaxy (e.g., Giovanelli, 1984). It is a massive, incandescent sphere of gas spanning 1.4 million kilometers in diameter [1].

Galileo Galilei (1564–1642) was the first to identify sunspots and their changing shapes on the surface of the Sun using his newly invented telescope. The discovery of sunspots paved the way for the observation of other solar features. A detailed review on the historical records of sunspots is provided in Arlt and Vaquero (2020). This made

[1] https://science.nasa.gov/sun/facts/

the Sun a dynamic star, giving rise to modern solar physics (e.g., Foukal, 2004).

Our current understanding about the Sun comes from observing the radiation it emits. Various instruments on Earth and in space are capturing these radiations. In the early 1800s, German physicist Joseph Fraunhofer (1787-1826) identified dark spectral lines in the solar spectrum, known as Fraunhofer lines. However, he failed to explain his findings. Later, Gustav Kirchhoff (1824-1887) and Robert Bunsen (1811-1899) explained that each gas produces a unique spectral signature, enabling scientists to classify stars based on their spectral type. The Sun, for example, is an ordinary star, a G2V main-sequence yellow star. Here, G2 stands for the second hottest star of the yellow G band (this band of atomic and molecular spectral lines was designated as G by Joseph Fraunhofer) with surface temperature $\approx$ 5,800 K, and the V represents a main sequence star[2].

However, many mysteries regarding the Sun remain unsolved, such as the million-degree temperature of its corona, the violent energy releases during solar flares, and the mechanisms behind the generation of the solar magnetic field and solar cycle interruptions. The proximity of the Sun provides an unprecedented opportunity to study stellar and plasma physics in great detail.

The nuclear fusion process inside the core of the Sun fuses four hydrogen nuclei into one helium nucleus, releasing a tremendous amount of energy. This energy is then transported through radiation up to 0.67 $R_\odot$ and by convection from that point to the photosphere, from where the solar atmosphere starts. The structure of the Sun is shown in Figure 1.1. The light from the Sun is studied by scientists to determine the Sun's temperature, chemical composition, and Doppler velocities, further deepening our understanding of this vital celestial body.

A detailed discussion of the Sun is given in the books; Foukal (2004); Bhatnagar and Livingston (2005); Judge (2020); Edmonds and Bond (2022).

1.1 Solar Atmosphere

The solar atmosphere is the outer region of the Sun, starting from the photosphere, where energy generated at the Sun's core begins to escape into space without any collision. This is because the solar atmosphere is less dense compared to the solar interior,

[2]https://www.britannica.com/place/Sun

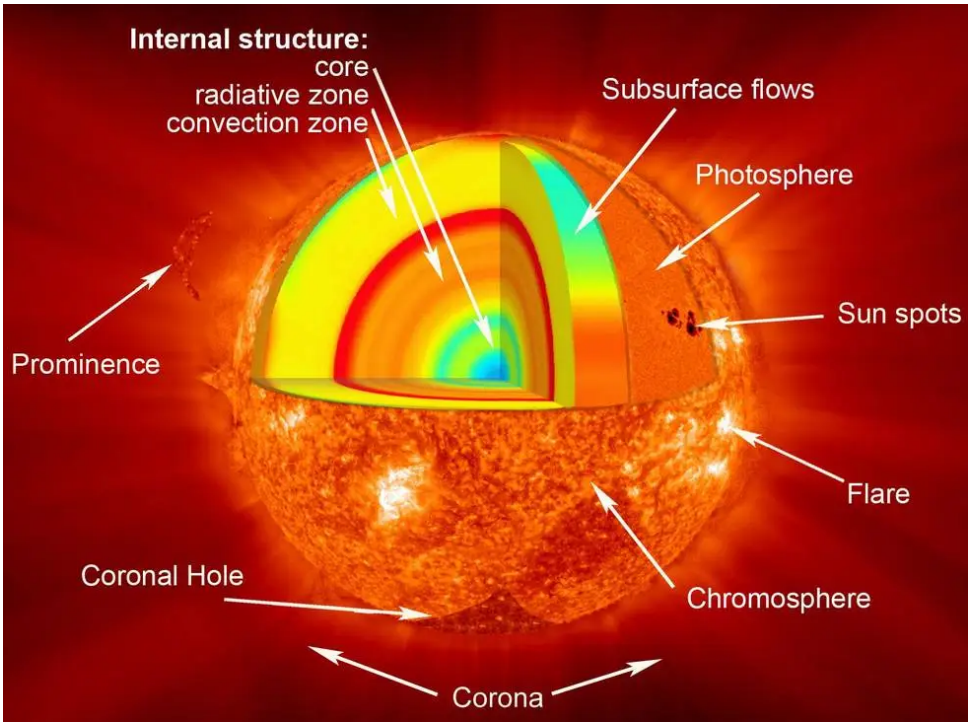

Figure 1.1: Structure of the solar interior and atmosphere, along with some features present at different atmospheric layers. Image courtesy: NASA/Goddard.

making the photons less susceptible to absorption and scattering. The temperature structure of the solar atmosphere is very unique and quite interesting to study. From the second law of thermodynamics, we expect the temperature to fall with distance as we move away from the Sun's core (Phillips et al., 2008). Therefore, we expect a decrease in the temperature along the solar atmosphere as we move away from the heat source. However, surprisingly, the temperature starts to rise after a certain height, eventually reaching a million degrees Kelvin. This is one of the unresolved mysteries of the Sun, known as the coronal heating problem. This temperature variation gives rise to an atmosphere that emits radiation in the whole electromagnetic spectrum, with each layer emitting in certain wavelength bands. Variations of mean density and temperature at various atmospheric heights are shown in Figure 1.2.

1.1.1 Photosphere and temperature minimum region

The solar atmosphere is nearly transparent to photons emitted by the photosphere. Therefore, the photosphere is regarded as the surface of the Sun, which is about 500 km thick, with a temperature around 6000 K, and emits mainly in the visible spectral range centered around 5000 Å. Optical depth (τ) is the measure of transparency of a

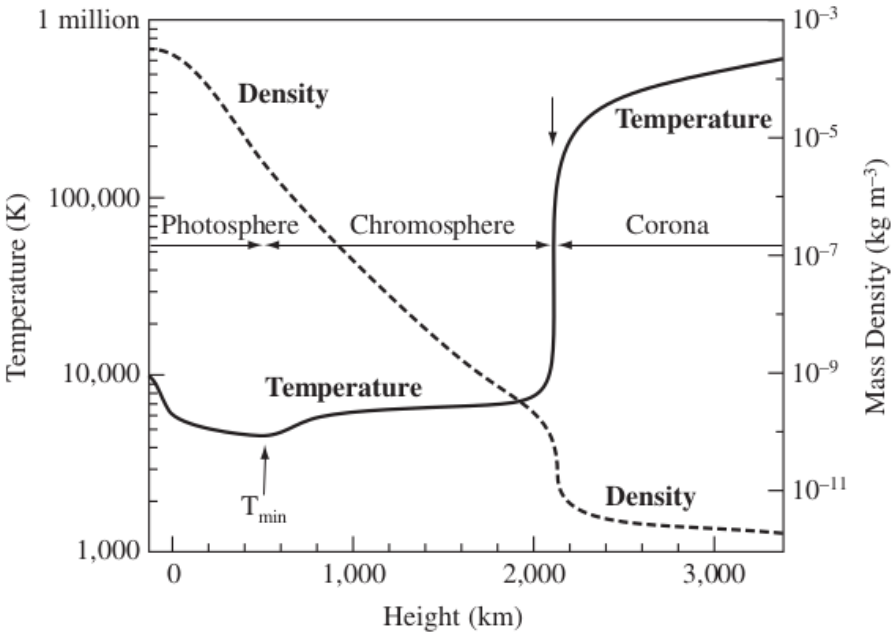

Figure 1.2: Schematic image showing variation of mean density and temperature in the plane parallel solar atmosphere known as the VAL (Vernazza-Avrett-Loeset) model. However, in reality, the solar atmosphere varies with time and id highly inhomogeneous and dynamic. Image courtesy: Priest (2014).

medium, and this region has $\tau_{5000} = 1$ for radiation of wavelength 5000 Å. The characteristic feature of the photosphere is the granulation patterns, which are the signature of the convection occurring below. This convective motion generates acoustic waves that peak around 5-min also known as solar p-modes. This time-scale is similar to the lifetime of these granules. The outer boundary of the photosphere where the temperature decreases to 4400 K, is called the temperature minimum region. After the temperature minimum region, the temperature starts to increase in the chromosphere.

The strong magnetic field of the Sun makes its surface very inhomogeneous. The presence of varying magnetic fields gives rise to different types of structures, namely, plage, quiet-sun regions, sunspots, etc. In this thesis, we focus our study on the sunspot umbra (see details in Section 1.3).

1.1.2 Chromosphere and Transition region

Above the temperature minimum lies the more transparent chromosphere. It is an optically thin region seen in the near-ultraviolet, visible, and near-infrared continua. The chromosphere is visible in the red colour of the Balmer series due to the H-α transition

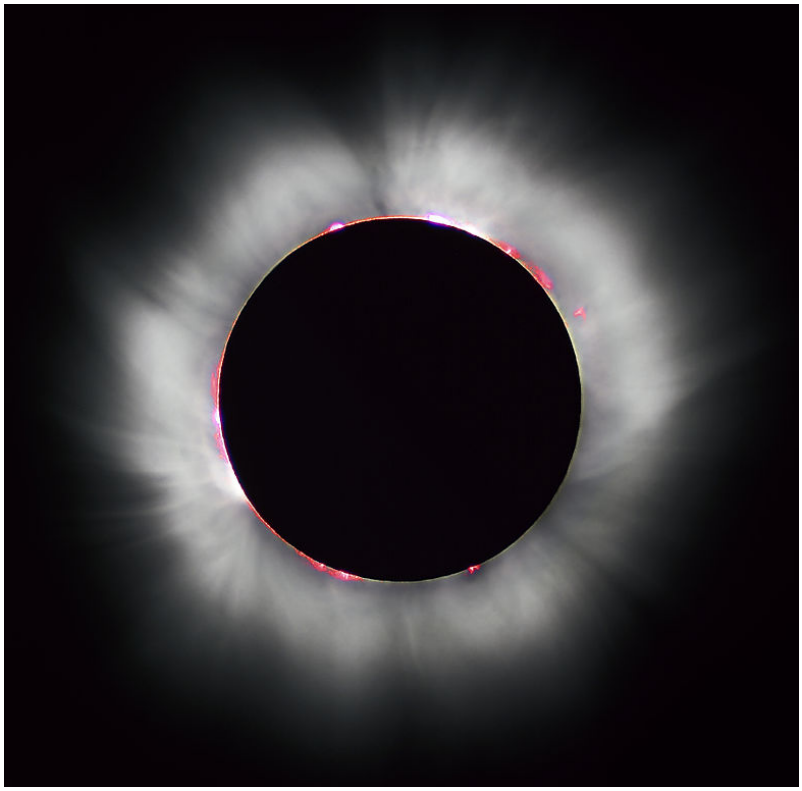

Figure 1.3: This is a beautiful image of the Sun taken during the 1999 solar eclipse by photographer Luc Viatour, showing the solar atmosphere. The red colour depicts the chromosphere in Hα, and faint white structures depict the corona. Image courtesy: NASA.

for a brief period of a few seconds at the start and end of a total solar eclipse, as shown in Figure 1.3 and Figure 1.4. The average temperature and density show a gradual increase and steep decrease, respectively, through the chromosphere. The chromosphere hosts different fine-scale magnetic features like umbral flashes, spicules, fibrils, mottles, prominences, etc. At a height of about 2,000 km (see Figure 1.2), temperature increases from 15,000 K to 1 MK through a narrow transition region of only a few 100 km thick. In this thesis, we also focus on umbral flashes (see details in Section 1.4.3.1).

1.1.3 Corona

The corona is the outer and least dense part of the solar atmosphere. It is visible in optical wavelength during a total solar eclipse in the form of a faint crown, see Figure 1.3. The spectrum of the corona during the eclipse revealed unexpected emission (red and green) lines shown in Figure 1.4, which was previously assumed to be emitted from a new element present in the corona named coronium. Later, with advancements in

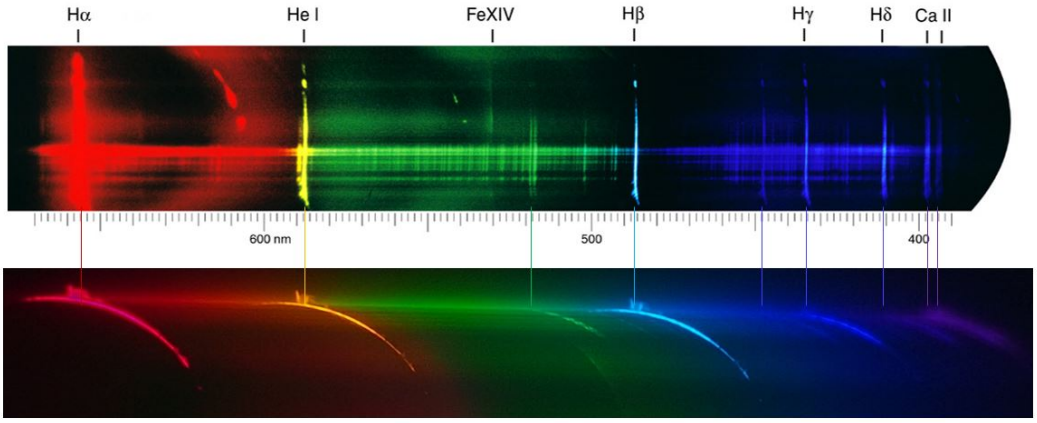

Figure 1.4: Flash spectra obtained at the starting and ending moments of the total solar eclipse showing the full visible spectra. Image courtesy: Montana State University.

atomic and molecular physics, it was discovered that these lines were emitted from a highly ionized state of iron such as Fe^{+9} and Fe^{+13} (Grotrian, 1939; Edlén, 1943). This made us realize that the tenuous corona is at a very high temperature ($>$ 1 MK), ionizing almost all the gases present in the corona and highlighting the coronal heating mystery (e.g., Parnell and De Moortel, 2012) (see details in Section 1.2). Fully ionized gas (plasma) emits mainly in the EUV and X-ray bands, in which the disc of the solar corona is observed. Characteristic features of the corona are coronal loops and coronal holes. These loops are the fundamental structures shaping the solar corona, which are anchored at the surface of the Sun (i.e., photosphere) (e.g., Reale, 2014). In this thesis, we mainly focus on the coronal loops emanating from the sunspot umbra (see details in Section 1.3).

1.2 Atmospheric heating problem

One of the long-standing problems in solar physics is the solar atmospheric heating problem. This mystery arises from the observation that the Sun's atmosphere is far hotter than its surface. The Surface of the Sun (photosphere) has a temperature of ≈6000 K, while the outermost layer of the Sun (corona) has a temperature of >1 MK, commonly known as the coronal heating problem. This contradicts the expected behaviour of heat flow according to the second law of thermodynamics. Therefore, there has to be some form of energy from within the Sun that propagates into the solar atmosphere and dissipates to release heat energy into the solar atmosphere. Understanding the

Table 1.1: Various coronal and chromospheric flux losses (erg cm^{-2} s^{-1}) from the quiet Sun and active region of the Sun. Table is adapted from Withbroe and Noyes (1977).

Parameter	Quiet Sun	Active region
Coronal energy losses		
Conduction flux F_c	2×10^5	10^5 to 10^7
Radiative flux F_r	10^5	5×10^6
Solar wind flux F_w	$\leq5\times10^4$	$<10^5$
Total coronal loss $F_c+F_r+F_w$	3×10^5	10^7
Chromospheric radiative losses		
Low chromosphere	2×10^6	$\geq10^7$
Middle chromosphere	2×10^6	10^7
Upper chromosphere	3×10^5	2×10^6
Total chromospheric loss	4×10^6	2×10^7

mechanisms responsible for this unexpected heating remains a fundamental challenge in solar physics. It is widely believed that the magnetic field of the Sun plays a vital role in the heating of the solar atmosphere. As the magnetic field extends from the solar interior to very far into the heliosphere, the whole of the solar atmosphere forms a magnetically coupled system due to the continuous supply of mass and energy between the different layers of the atmosphere in both directions (e.g., Parnell and De Moortel, 2012). Therefore, tackling the coronal heating problem alone is not possible, as the corona is not energetically isolated, and including the lower atmosphere is important. Solving the heating problem by considering the whole solar atmosphere as one system is complicated due to the different plasma properties and observational signatures of different atmospheric layers of the solar atmosphere. However, the inclusion of the lower atmosphere is important to fully understand the coronal/atmospheric heating problem as the lower atmosphere is an important energy conduit (e.g., van Ballegooijen et al., 2014; Jess et al., 2015; Van Doorsselaere et al., 2020).

In corona and chromosphere, the loss rate in the active region is 10^7 erg cm^{-2} s^{-1} and 2×10^7 erg cm^{-2} s^{-1}, respectively, see Table 2.2. The high density of chromosphere compared to the corona results in a higher heat requirement, approximately two times greater than that of the corona (Withbroe and Noyes, 1977). Therefore, we need a continuous source of heat energy to maintain these energy losses. High-spatial resolution instruments have revealed the existence of granular motions on the surface of the Sun. The convective motion beneath the surface of the Sun is the reason for this motion. The timescale and length scale of granules vary with size. The typical lifetime of these granules is around 2-10 min. These granular motions continuously shake the footpoints

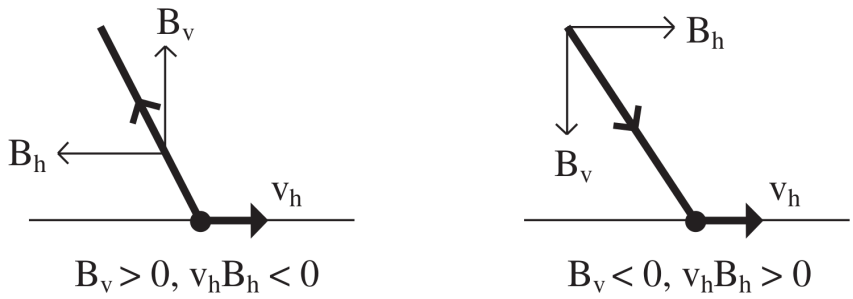

Figure 1.5: The movement of vertical (v) and horizontal (h) components of magnetic field line (**B**) when its footpoint, denoted by a large dot, is moved by a horizontal velocity (v_h). Here, (a) when B_v >0 then $v_h B_h$ < 0, (b) when B_v <0 then $v_h B_h$ > 0. Image courtesy: Priest (2014).

of the magnetic loops, giving rise to two possible heating mechanisms. The dominant mechanism for this atmospheric heating depends on the granular motion timescale (τ_f) and the Alfvén wave travel time (τ_A) of the loop. The fast driving motion produces waves known as wave or AC heating mechanism (Alfvén, 1947). The slow driving motion causes braiding, producing magnetic re-connection known as transient or DC heating mechanism (Parker, 1988).

The energy flux transported into or out of the solar atmosphere by this convective motion is calculated by the Poynting flux (**S**) per unit area through the surface of the Sun,

$$\mathbf{S} = \frac{1}{\mu_o}(\mathbf{E} \times \mathbf{B}) \cdot \hat{v} = -\frac{1}{\mu_o}(B_h \cdot v_h)B_v + \frac{1}{\mu_o}(B_h \cdot B_h)v_v. \tag{1.1}$$

Here, horizontal and vertical components are denoted by the subscripts h and v, respectively. E is the electric field, B is the magnetic field, and μ_o is the magnetic permeability.

The first term represents the movement of the magnetic field lines by horizontal convective motions, and the second term represents the movement of the magnetic field lines in the vertical direction, resulting in the emergence or submergence of magnetic fluxes. Here, we are interested in the first term, which represents the inflow and outflow of the flux depending on the tilt of the magnetic field as shown in Figure 1.5. If we assume the typical mean magnetic field strength, horizontal motion, and field inclination to be 500 G, 1 km s^{-1}, and 20°, respectively, the Poynting flux per unit area is $\approx 1.2 \times 10^9$ erg $cm^{-2}s^{-1}$. This shows that the footpoint motion provides more than enough energy to heat the solar atmosphere (e.g., Parnell and De Moortel, 2012; Priest, 2014).

Recent literature on the coronal heating problem can be found in Klimchuk (2006); Parnell and De Moortel (2012); De Moortel and Browning (2015); Sakurai (2017); Viall

et al. (2021); De Pontieu et al. (2022), etc.

AC heating mechanism:

When $\tau_A > \tau_f$, the footpoint motion induces waves in the loop. The footpoint motion will generate perturbations in magnetic pressure, gas pressure, and magnetic tension, which act as a restoring force to generate different types of waves. The basic principle on which the wave heating mechanism works is: (i) Theoretically, we know that granular motions on the photosphere can act as a driver and excite these waves in the magnetic loops, but the direct observations of wave generation are difficult with the current generation of telescopes. We need high spatial resolution to resolve the footpoints of the magnetic loops on the photosphere, which is not feasible till now. (ii) Wave energy generated on the photosphere needs to be transported to the corona via the chromosphere and transition region. While propagating from the photosphere to the corona, they suffer from reflection and transmission due to the steep temperature and density gradients in the transition region. Only a small fraction of these waves reach up to the corona. So, waves must carry a sufficient amount of energy with them, as most of the energy gets reflected back. (iii) While propagating in the atmosphere, these waves suffer from damping. Damping of these waves is observed from the decay of wave amplitude. The waves must dissipate efficiently to contribute to the coronal heating.

As the magnetic field prevails all over the solar surface, the acoustic theory was extended to magnetic waves. In a magnetic medium, three wave modes may propagate: the fast mode, the slow mode, and the Alfvén mode. These waves are discussed in detail in Section 1.4. In this thesis, we focus on the wave heating mechanism.

Recent reviews on wave heating mechanism can be found in Arregui (2015); Jess et al. (2015); Van Doorsselaere et al. (2020); Srivastava et al. (2021); Morton et al. (2023); Nakariakov et al. (2024), etc.

DC heating mechanism:

When $\tau_A < \tau_f$, the footpoint motions due to convection get enough time to stress/braid the magnetic field lines. The braided field lines lead to the formation of a gradient in the magnetic fields and, hence, the formation of small current sheets that would continuously dissipate and reform, providing direct heating via ohmic dissipation. Such heating events are called nano-flares, where the energy released is of the order of 10^{24} erg (10^9

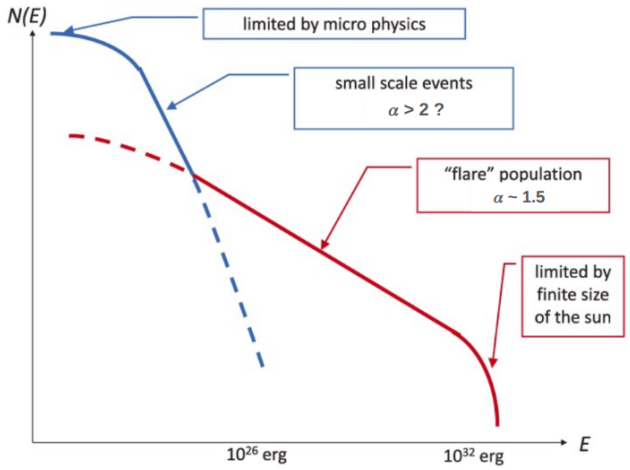

Figure 1.6: Frequency spectra of large (red) and small (blue) flares. The red spectra contributes to $\approx$ 20% of the energy input to the corona. The blue spectra, along with contributions from wave heating, constitute more than 80% of the energy input to the corona. Image adapted from Sakurai (2017).

times smaller than normal solar flares). Flux emergence and cancellation at the photosphere can also drive reconnections. These processes heat and form new loops and are also associated with bulk acceleration of plasma, particle acceleration, and transport of mass into chromosphere/corona (e.g., von Rekowski and Hood, 2008; Martínez-Sykora et al., 2009; Parnell and De Moortel, 2012). In the solar atmosphere, a wide range of events based on their sizes and energies have been observed. The large-scale events release total energy around 10^{30} to 10^{33} ergs, which can account for only 20% of the overall coronal energy requirement (Sakurai, 2017). However, the small-scale events that are ubiquitous over the solar surface may fulfill the energy requirements for coronal heating. Parker (1988) proposed that the solar corona can be heated by numerous small-scale events termed as "nanoflares" with energies around 10^{24} ergs.

These events follow a power-law distribution of event rates with varying power-law index (α)

$$\frac{dN}{dE} \propto E^{-\alpha} \tag{1.2}$$

where N is the number of flares with energy E (Lin et al., 1984).

The power-law distribution of flare event rates with varying indices is shown in Figure 1.6. If the $\alpha < 2$, large flares dominate the total flare energy contents, whereas if $\alpha > 2$, small flares will dominate the total flare energy contents (Hudson, 1991). Therefore, it is important to determine the power-law index through observations in order to confirm the nanoflare hypothesis (e.g., Vadawale et al., 2021).

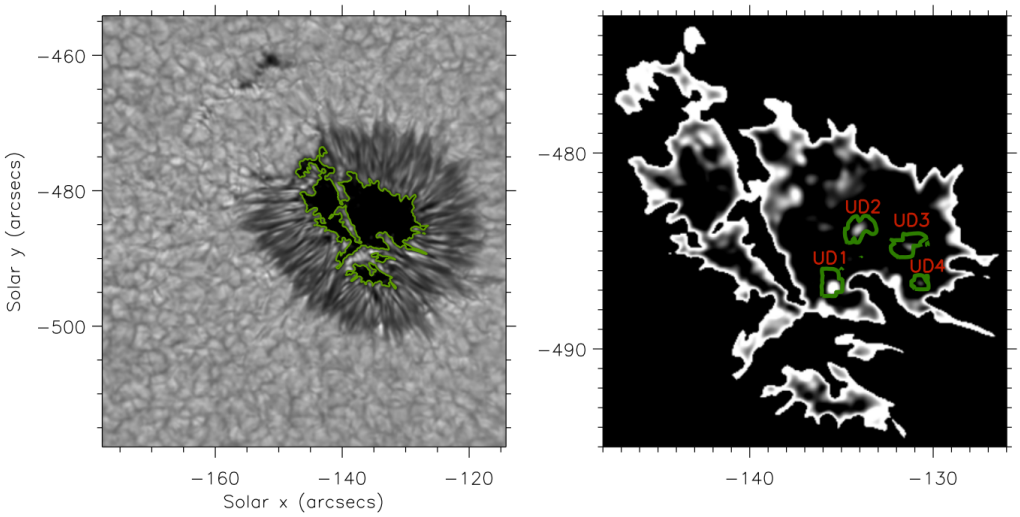

Figure 1.7: Left: Image of the sunspot, where the solid green contour represents the umbral boundary of the sunspot. Right: A close-up of time-averaged isolated sunspot umbra showing locations of the umbral dots. These dots have a periodicity of approximately 3-min. Image courtesy: Jess et al. (2012b).

Literature on transient heating mechanism can be found in Peter et al. (2005); Klimchuk (2015); Cargill et al. (2015); Young et al. (2018); Huang et al. (2019); Upendran and Tripathi (2021); Chitta et al. (2022); Mason et al. (2023), etc.

1.3 Sunspots and loops

Sunspots are dark patches on the bright surface of the Sun (Hasan and Rutten, 2010). The typical diameter of the sunspot ranges from 20 to 40 Mm with a typical magnetic strength of about 2000-4000 G. This exceptionally large concentration of magnetic flux inhibits convection and makes them cooler than their surroundings. Inhibition of convection decreases the gas pressure, which reduces the opacity of this region. $\tau_{5000} = 1$, which defines the geometric height of the quiet Sun, is depressed due to inhibition of convection. This depression is called Wilson depression (Wilson and Maskelyne, 1774), which is ≈500 km deep. The sunspot can be divided into two parts: a central dark part, called the umbra, having almost vertical magnetic field, surrounded by a less dark and highly filamentary part, called the penumbra, having a weaker, more horizontal magnetic field. In this thesis, we focus on the sunspot umbra.

The umbral radius is about 40% of the overall spot diameter, and its brightness is about 30% less compared to the surrounding quiet-Sun photosphere. The temperature of the umbra and penumbra is ≈ 4400 K and 5500 K, respectively, at the photosphere,

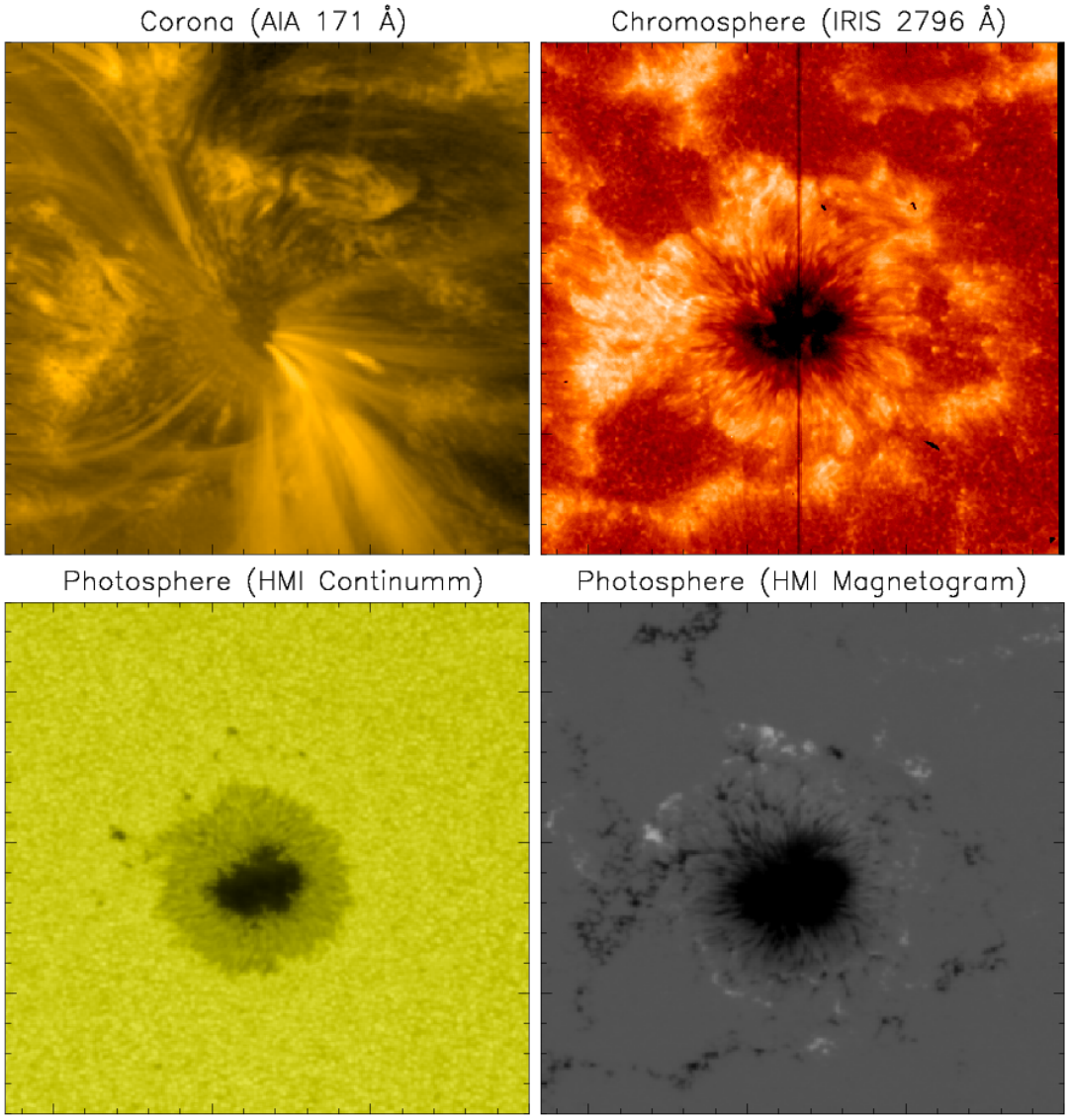

Figure 1.8: Image of a unipolar sunspot at different atmospheric heights observed at different passbands as labelled. Image adapted from Rawat et al. (2025).

which is around 1500 K and 500 K less than its surroundings. The penumbral brightness is about 75% compared to the quiet-Sun photosphere. Large sunspots live longer compared to smaller ones. The umbra is also quite inhomogeneous, having dark and bright features. Umbra also shows bright dot-like features called umbral dots which have diameters between 100 and 450 km, lifetimes 10 min to 2 hr, and a typical brightness of 10 to 20% of the penumbral brightness as shown in Figure 1.7 (e.g., Wilson, 1969; Watanabe et al., 2009; Yadav and Mathew, 2018). They are hotter than the surrounding umbra. Umbra also shows thin bright features called light bridges that cross over an umbra and have reduced and more horizontal magnetic field (Giordano et al., 2008; Louis et al., 2008).

As we move up in the solar atmosphere, the appearance and dynamics of the sunspot are different at different atmospheric heights, Figure 1.8. At the photosphere, we can clearly distinguish between the umbra and penumbra boundaries. In the chromosphere, the distinction between umbra and penumbra is faint, and different features like umbral flashes, running penumbral waves, and bright sunspot jets are observed. In the corona, the sunspot is invisible, and coronal loops are visible, which are anchored at the photosphere. These loops are prominent features in the corona and are considered the basic building blocks of the solar corona (e.g., Reale, 2014). These loops host various wave modes and display a diverse range of wave dynamics and eruptive events. Due to this vast diversity in the observational features, the observational structural connectivity of the sunspot atmosphere is a very challenging task. The various sunspot features host various oscillations and waves.

In this thesis, we focus on unipolar isolated sunspots, which are also known as α-sunspots. The loops emanating from these sunspot umbra are open loops, which are very long with minimum inclination, and the length of the loop (l) determines the Alfvén travel time ($\tau_A = l/v_A$), which decides the heating mechanism. Therefore, the τ_A is larger than τ_f, making them ideal to study the wave heating mechanism. Additionally, the minimum inclination of these loops further reduces the probability of small transients, which can hamper the propagation of these waves. Here, we are utilizing sunspots located near the disc centre to minimize the inclination effect. Therefore, the selected sunspot umbra and umbral fan loops are ideal to study waves and oscillations in the solar atmosphere.

An elaborate description of sunspots and their magnetic structures are provided in

Borrero and Ichimoto (2011); Löhner-Böttcher (2016); Arlt and Vaquero (2020).

1.4 MHD Waves theory and observations

Waves are considered as the primary mechanism that can transfer energy from one place to another. Different kinds of waves, like electromagnetic waves (e.g., radio waves) and hydrodynamic waves (e.g., sound waves), are transverse and longitudinal in nature, respectively. The presence of these hydrodynamic waves in the magnetized medium produces magnetohydrodynamic (MHD) waves. The active regions are regions of strong magnetic fields; therefore, MHD waves can be a key contributor to the transport of energy and heating of the solar atmosphere. In this section, the basic fundamentals of MHD and MHD wave theory are introduced.

1.4.1 Basic magnetohydrodynamics

MHD is the combination of fluid dynamics (Navier-Stokes equations) and electromagnetic theory (Maxwell equations). As the temperature of the solar atmosphere increases, the atoms start to ionize and form positive ions and negative electrons, which can move around freely. This ionized gas is called plasma, which is also called the 'fourth state of matter'. Plasma, being an electrically conducting fluid, is treated as a continuous fluid provided that the spatial scales are larger than the typical mean free path of particle collisions. The dynamics of the plasma are closely connected to the magnetic field and vice versa. The strong magnetic environment of sunspots facilitates the excitation of MHD waves due to the interaction of plasma and magnetic fields.

Maxwells Equations:

$$\nabla \cdot \mathbf{E} = \frac{\rho_e}{\epsilon_o}, \tag{1.3}$$

$$\nabla \cdot \mathbf{B} = 0, \tag{1.4}$$

$$\nabla \times \mathbf{B} = \mu_o \mathbf{j} + \frac{1}{c^2}\frac{\partial \mathbf{E}}{\partial t}, \tag{1.5}$$

$$\nabla \times \mathbf{E} = -\frac{\partial \mathbf{B}}{\partial t}. \tag{1.6}$$

Here, $\mathbf{B}$, μ_o, $\mathbf{j}$, c, $\mathbf{E}$, ρ_e, and ϵ_o are the magnetic field vector, magnetic permeability, current density vector, speed of light, electric field vector, electric charge density, and permeability of free space, respectively.

Navier-Stokes equation:

In fluid mechanics, the Navier-Stokes equation describes the flow of incompressible fluids ($\nabla \cdot \mathbf{v} = 0$).

$$\rho \frac{d\mathbf{v}}{dt} = -\nabla P + \rho \mathbf{g} + \kappa \nabla^2 \mathbf{v}. \tag{1.7}$$

Here, $\mathbf{v}$, ρ, P, g and κ are flow velocity, mass density, pressure, acceleration due to gravity and coefficient of viscosity, respectively. Also, here Lagrangian derivative $\frac{d\mathbf{v}}{dt} = \frac{\partial \mathbf{v}}{\partial t} + \mathbf{v} \cdot \nabla \mathbf{v}$.

We assume that plasma follows the Maxwell-Boltzmann distribution function with the most probable speed (v), which is considered as the plasma speed. The plasma speed is directly proportional to the square root of the temperature (T) of the plasma. Since $v << c$ in the solar atmosphere, we use a non-relativistic approach and neglect displacement current in Ampere's law (see Equation 1.5), which leads to $\nabla \times \mathbf{B} = \mu_o \mathbf{j}$. In the plasma, charge neutrality implies that an electric field can be solely generated by a changing magnetic field. Therefore, excesses of charge are not allowed to accumulate, and Gauss law (Equation 1.3) becomes $\nabla \cdot \mathbf{E} = 0$. Currents in the plasma are determined by the generalized Ohm's law in the lab frame of reference,

$$\mathbf{j} = \sigma(\mathbf{E} + \mathbf{v} \times \mathbf{B}), \tag{1.8}$$

where σ is the electrical conductivity. The two sets of Maxwell and Navier-Stokes fluid equations are coupled by Ohm's law. Substituting E from Equation 1.8 and j from Equation 1.5 in Equation 1.6

$$\frac{\partial \mathbf{B}}{\partial t} = \nabla \times \mathbf{v} \times \mathbf{B} - \nabla \times \frac{\nabla \times \mathbf{B}}{\sigma \mu_o}. \tag{1.9}$$

Using Equation 1.4, we simplify Equation 1.9 which gives us the 'induction equation',

$$\frac{\partial \mathbf{B}}{\partial t} = \nabla \times \mathbf{v} \times \mathbf{B} - \eta \nabla^2 \mathbf{B}, \tag{1.10}$$

where, magnetic diffusivity (η) is defined by $\eta = \frac{1}{\sigma \mu_o}$.

The induction equation shows the relationship between plasma motion and magnetic field. Here, the first term represents advection, which describes how magnetic field dynamics change due to plasma flows, and the second term represents diffusion, which describes the diffusion/dissipation of the magnetic field due to the magnetic field gradients. The ratio of the diffusive and advection terms yields the magnetic Reynolds number (R_m),

$$R_m = \frac{\nabla \times \mathbf{v} \times \mathbf{B}}{\eta \nabla^2 \mathbf{B}} = \frac{v \Delta l}{\eta} \tag{1.11}$$

where Δl is a characteristic length scale.

Magnetic Reynolds number dictates plasma dynamics. The value of R_m ranges from 10^6–10^{12} on a large spatial scale such as solar and astrophysical plasma (Priest, 2014). Therefore, we neglect the magnetic diffusion term in Equation 1.10. Since $R_m >> 1$, we consider an ideal MHD plasma in which the Alfvén flux-freezing theorem holds. This theorem implies that magnetic flux is conserved, and magnetic field lines are tied to plasma motion. For the non-ideal (diffusive term) to dominate, we need a small spatial scale of a few meters; however, at this scale, the MHD assumption breaks, and we enter in the kinetic scale.

Ideal MHD equations

$$\frac{\partial \rho}{\partial t} + \nabla \cdot (\rho \mathbf{v}) = 0, \tag{1.12}$$

$$\rho \frac{d\mathbf{v}}{dt} = -\nabla p + \frac{1}{\mu_o} (\nabla \times \mathbf{B}) \times \mathbf{B}, \tag{1.13}$$

$$\frac{d}{dt} \left(\frac{p}{\rho^\gamma} \right) = 0, \tag{1.14}$$

$$\frac{\partial \mathbf{B}}{\partial t} = \nabla \times (\mathbf{v} \times \mathbf{B}). \tag{1.15}$$

Here $\mathbf{v}$, ρ, p and γ represents the plasma velocity, density, pressure and adiabatic index.

The second term on the right-hand side of Equation 1.13 represents the Lorentz force.

$$F_L = \frac{(\nabla \times \mathbf{B}) \times \mathbf{B}}{\mu_o} = -\nabla \frac{B^2}{2\mu_o} + \frac{(\mathbf{B} \cdot \nabla) B}{\mu_o}, \tag{1.16}$$

Here, the first term represents magnetic pressure, and the second term represents magnetic tension. Magnetic pressure causes the apparent expansion of loops as they move up in the atmosphere. Magnetic tension acts as a restoring force to bring the loops back

into their original place after it is disturbed by an external force.

Loops visible in coronal intensity images are manifestations of magnetic loops. For a stable magnetic loop, the total pressure (thermal and magnetic) inside and outside should be balanced. For magnetic loops, the pressure balance equation is

$$p_{int}(h) + \frac{B_{int}^2(h)}{8\pi} = p_{ext}(h) + \frac{B_{ext}^2(h)}{8\pi} \tag{1.17}$$

where B_{int}, p_{int}, B_{ext}, and p_{ext} are the magnetic field and thermal pressure inside and outside the loop along loop length h, respectively. The thermal pressure decreases exponentially with height due to hydrostatic equilibrium. Therefore, the magnetic loop expands with height while keeping the total magnetic flux $\phi(h) = B(h)A(h)$ constant.

Another important quantity of MHD is the plasma-β, which is the ratio of the thermal plasma pressure (p_{th}) to the magnetic pressure (p_m),

$$\beta = \frac{p_{th}}{p_m} = \frac{8\pi N k_b T}{B^2} = \frac{2v_s^2}{\gamma v_A^2}. \tag{1.18}$$

Where k_b is the Boltzmann constant, B is the magnetic field strength (G), $N = N_e + N_h$ is the total number density (cm^{-3}), and T is the temperature (K). Furthermore, semi-empirical models of solar atmosphere developed by Vernazza et al. (1981); Maltby et al. (1986); Fontenla et al. (1999) can provide N_e, N_h, and T variations with height. When plasma-$\beta > 1$, magnetic field dynamics are dominated by plasma motions, and when plasma-$\beta < 1$, magnetic fields determine the plasma motions.

Assumptions made in the ideal MHD equations:

- Plasma is assumed to be a single fluid for simplicity.
- Relativistic effects are ignored. Since the plasma speed is less than the speed of light.
- Number of charged particles inside the Debye sphere of radius λ_d should be large ($4\pi n\lambda_d^3/3 > 1$). Debye length (λ_d) is the length over which plasma is approximated to be neutral.
- The plasma is considered continuous over the length scales larger than the ion gyroradius.
- The plasma is assumed to be in thermodynamic equilibrium, where particles in

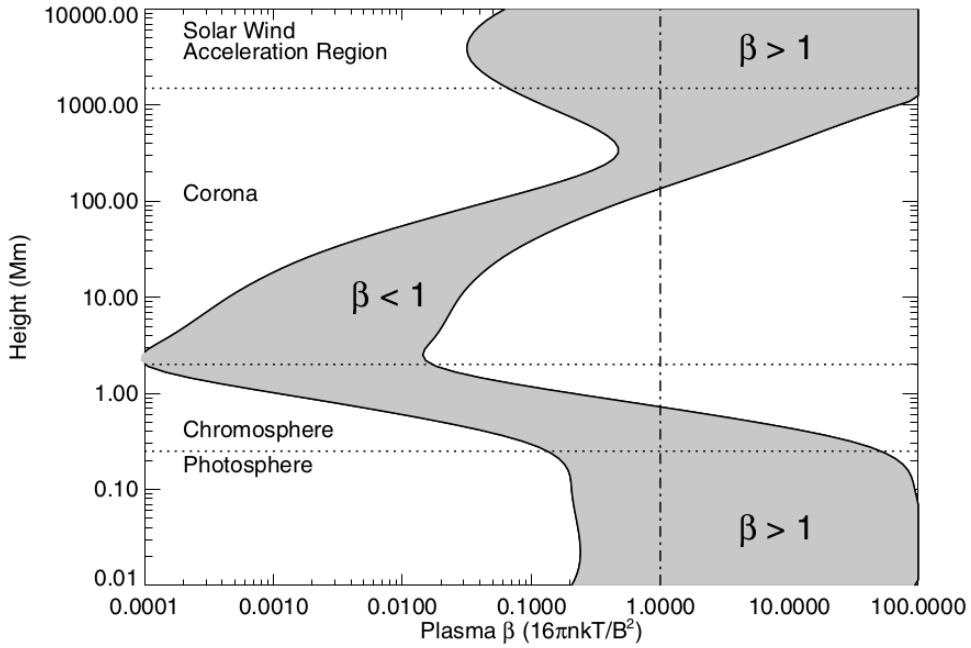

Figure 1.9: Plasma-β variation with height in the solar atmosphere for the active region between two assumed field strengths of 100 G (plage) and 2500 G (umbra) (Gary, 2001). Image courtesy: Aschwanden (2004).

the fluid elements follow the Maxwell-Boltzmann distribution. This assumption is valid when length and time scales are much larger than the collision time scale and mean free path, respectively.

- All the MHD equations are written in the inertial frame of reference.

The different forces in Equation 1.13, like gas pressure, magnetic tension, and magnetic pressure, act as a restoring force that generates oscillations which propagate along the magnetic field lines. To analyse the behaviour of these waves, we linearized the ideal MHD equations by adding small perturbations in a uniform and stationary plasma.

$$\mathbf{B} = \mathbf{B}_o + \mathbf{B}_1, \quad \rho = \rho_o + \rho_1, \quad \mathbf{v} = \mathbf{v}_o + \mathbf{v}_1, \quad p = p_o + p_1 \tag{1.19}$$

Here, the subscripts o and 1 denote the physical variables that are in equilibrium and perturbed states, respectively. Under equilibrium conditions, we assume $\mathbf{v}_o$ to be 0. Here, we are neglecting squares and products of small quantities, denoted by subscript 1. This gives the linearized set of ideal MHD equations,

$$\frac{\partial \rho_1}{\partial t} + (\mathbf{v}_1 \cdot \nabla)\rho_o + \rho_o(\nabla \cdot \mathbf{v}_1) = 0, \tag{1.20}$$

$$\rho_o \frac{\partial \mathbf{v}_1}{\partial t} = -\nabla p_1 + \frac{1}{\mu_o}(\nabla \times \mathbf{B}_1) \times \mathbf{B}_o, \tag{1.21}$$

$$\frac{\partial p_1}{\partial t} + (\mathbf{v}_1 \cdot \nabla) p_o - v_s^2 (\frac{\partial \rho_1}{\partial t} + (\mathbf{v}_1 \cdot \nabla)\rho_o) = 0, \tag{1.22}$$

$$\frac{\partial \mathbf{B}_1}{\partial t} = \nabla \times (\mathbf{v}_1 \times \mathbf{B}_o) \tag{1.23}$$

$$\nabla \cdot \mathbf{B} = 0, \tag{1.24}$$

where the sound speed, $v_s = \sqrt{\frac{\gamma p_o}{\rho_o}}$ and Alfvén speed, $v_A = \sqrt{\frac{B_o^2}{\mu_o \rho_o}}$.

Small perturbations with subscript 1 are proportional to $e^{(ikz - i\omega t)}$, where ω is the angular frequency of waves and k is the wave vector. Solving the above equation gives us a dispersion relation

$$(\omega^2 - k^2 cos^2\theta v_A^2)(\omega^4 - \omega^2 k^2 (v_A^2 + v_s^2) + k^4 v_A^2 v_s^2 cos^2\theta) = 0, \tag{1.25}$$

where θ is the angle between the magnetic field and the wave vector. This dispersion relation has three distinct roots, which give three different MHD waves having different properties.

$$\frac{\omega}{k} = v_A cos\theta, \tag{1.26}$$

$$\frac{\omega}{k} = \sqrt{\frac{(v_A^2 + v_s^2) \pm \sqrt{(v_A^2 + v_s^2) - 4 v_A^2 v_s^2 cos^2\theta}}{2}}. \tag{1.27}$$

Here, Equation 1.26 and Equation 1.27 represent Alfvén and magnetosonic phase speed, where $\omega = k v_+$ (fast magnetoacoustic wave) and $\omega = k v_-$ (slow magnetoacoustic wave).

- **Alfvén waves:** These are transverse waves, where the motion of a plasma parcel is in a direction perpendicular to the magnetic field. These incompressible waves do not modify the density of the plasma and propagate along the magnetic field. The restoring force in these waves is magnetic tension, which restores any deformation in the field lines. These waves are named after Hannes Alfvén, who received the Nobel Prize in 1970 for predicting these waves.

- **Fast magnetoacoustic waves:** These are one of the compressible waves showing density perturbations. These are longitudinal waves with perturbations in the quasi-isotropic direction relative to the magnetic field. The restoring forces that act are magnetic tension, gas pressure, and magnetic pressure. Here, the gas and

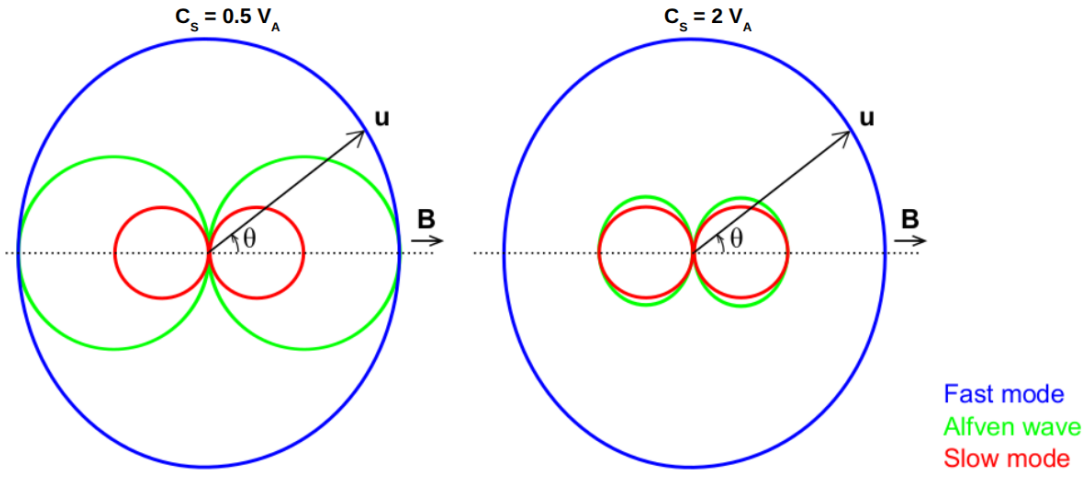

Figure 1.10: Phase diagram for MHD waves shown by different colours in a homogeneous unbounded system under different plasma-β conditions. The phase speed (ω/k) is shown by the vector **u** as a function of the angle θ. Image adapted from Spruit (2013).

magnetic pressure are in phase. Therefore, the propagation speed of these waves is more than Alfvén and sound speed and is represented by the + sign in Equation 1.27.

- **Slow magnetoacoustic waves:** These are also compressible waves, restoring forces acting are magnetic tension, gas pressure, and magnetic pressure. Here, the fluctuations in plasma pressure and magnetic pressure act out of phase. Therefore, the speed of these waves is less than the acoustic and Alfvén speed and is represented by the - sign in Equation 1.27. The propagation of these waves is anisotropic relative to the direction of the magnetic field.

The phase diagram for the MHD waves in a uniform and unbounded magnetized plasma is shown in Figure 1.10.

All the above MHD derivations and descriptions are adapted from various textbooks (Infeld, 1998; Goossens, 2003; Aschwanden, 2004; Spruit, 2013; Priest, 2014).

1.4.2 Waves in magnetic loops

The above description of MHD waves was in a homogeneous, unbounded system with a constant magnetic field. These waves exhibit complex behaviour in the solar atmosphere owing to the plasma structuring by strong magnetic fields, density stratification, varying temperatures, etc. In the umbral atmosphere plasma-β < 1, hence the properties of the acoustic waves are strongly affected by the magnetic field. Therefore, the sunspot

umbra is an ideal structure for studying MHD waves. In this section, we will discuss the nature and observational characteristics of these waves in magnetically bounded structured loops. Magnetic loops are bundles of concentrated magnetic field lines. The magnetic flux $F = \int \mathbf{B} \cdot d\mathbf{S}$, where $\mathbf{B}$ is the magnetic field strength in the closed surface $\mathbf{S}$. Perturbations in these magnetic loops can excite several types of MHD waves.

Sausage waves: These are compressible waves and are detected in density oscillations. The periodic perturbations in the magnetic loops by stretching or squeezing it in the direction normal to the magnetic field are called the sausage mode due to their appearance, see the left panel of Figure 1.11. When the cross-sectional area of the loop decreases, the magnetic field strength increases, and vice versa. The loop cross-section is perturbed without displacing the loop. This induces a change in the density and, hence, the intensity inside the tube is perturbed. These waves propagate in the direction of the magnetic field. Depending on the direction of velocity perturbations and the relation between gas and magnetic pressure, these waves can be further divided into slow and fast sausage waves. If the velocity perturbation is perpendicular to the magnetic field direction and the density perturbation is in phase with the magnetic perturbation, we call it fast sausage waves (e.g., Morton et al., 2012). However, if the velocity perturbation is parallel to the magnetic field direction and the density perturbation is out of phase with the magnetic perturbation, we call it the slow sausage waves (e.g., Grant et al., 2022).

Kink waves: These are transverse periodic perturbations in the magnetic loops as shown in the right panel of Figure 1.11. The axis of the magnetic loop is spatially displaced from its equilibrium position and sways perpendicular to the magnetic field direction, resembling a moving snake. The loop cross-section is not perturbed; therefore, the density inside the tube is not affected. These waves propagate in the direction of the magnetic field. In long-wavelength limits, these are also called compressional Alfvén waves or fast magnetoacoustic waves (e.g., Van Doorsselaere et al., 2008a; Morton et al., 2012).

Torsional Alfvén waves: These are incompressible waves, and the only restoring force is the magnetic tension. These are also transverse waves excited when a constant torque is applied to the magnetic loop, which produces a twist in the magnetic loop, see Figure 1.12. This twist changes the direction of the magnetic field lines; however, the magnitude of magnetic field strength remains the same (the field lines remain equidis-

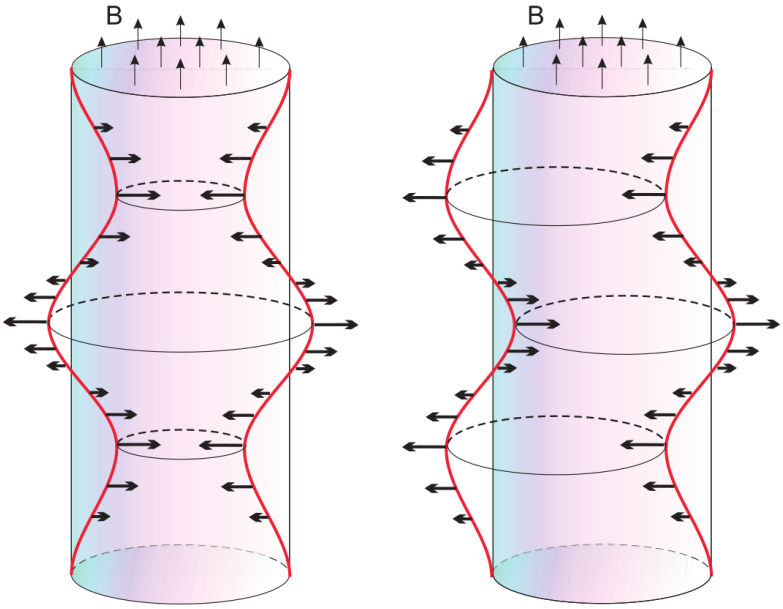

Figure 1.11: Schematic image of MHD waves in a cylindrical magnetic loop. Left: Fast MHD sausage wave characterized by a periodic contraction and expansion of the cross-section area of the tube symmetric about the central axis. Right: Kink wave, the central axis of the tube is displaced. Image courtesy: Morton et al. (2012).

tant from each other). Therefore, these waves are not detected by Zeeman or Hanle effects. Additionally, due to their incompressible nature, these waves cannot be detected in the form of intensity fluctuations since the density is not perturbed. Therefore, the direct signature of torsional Alfvén waves is difficult to observe in the solar atmosphere as they do not perturb the shape, location, and density of the magnetic loop. Indirect signatures of these waves are observed by spectroscopic data in the Doppler velocity perturbations. Here, the velocity perturbations are perpendicular to the direction of the magnetic field (e.g., Jess et al., 2009).

1.4.3 Waves and oscillations in sunspot umbral atmosphere

Waves are present throughout the whole solar atmosphere, covering a broad range of frequencies and powers. These waves are studied mainly for their role in coronal heating and atmospheric seismology (De Moortel and Nakariakov, 2012). In the various photospheric features, strong acoustic waves (p-mode) with a period of 5-min are tabulated in Table 1.2. These p-modes are generated due to convective motions and are seen in the form of a granulation pattern on the solar photosphere. However, the generation mechanism of MHD waves in the sunspot umbra is still unclear. The two proposed mechanisms generating these waves are first, when acoustic p-modes enter the sunspot,

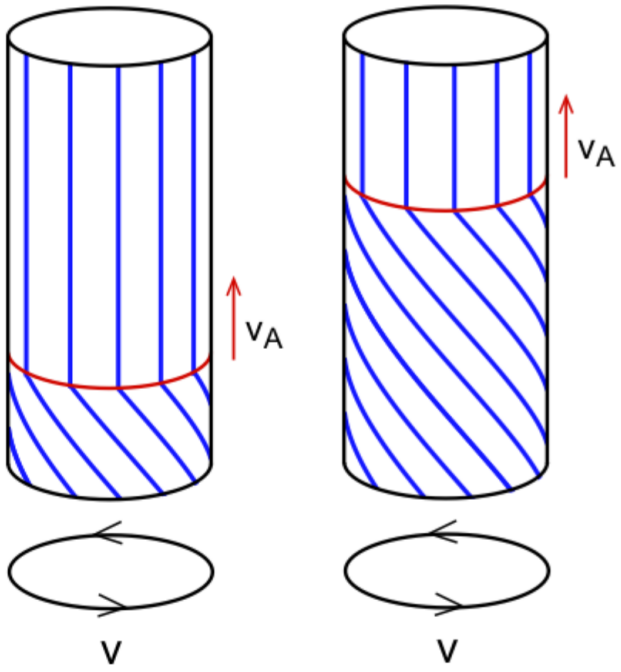

Figure 1.12: Torsional Alfvén wave propagating along a cylindrical magnetic loop. Image courtesy: Spruit (2013).

Table 1.2: **B** is the vector magnetic field strength in Gauss, γ is the inclination of the structure in degree (○), M is the magnetic flux (B_{LOS}) in Mx cm^{-2}, LW is the line width in mÅ, v is the velocity in m s^{-1}, I_c is the intensity counts. 5-min and 3-min periods represent 4-8 min and 2.7-3.3 min period bands, respectively. Here, the bold text represents noise. The table is adapted from Norton et al. (2021).

Period	feature	B	δB	γ	$\delta\gamma$	M	δM	LW	δLW	δv	δI_c
5-min	umbra	2030	31	23	0.9	1517	12	128	1.4	58	0.8%
	PIL	1213	38	96	0.8	-53	11	152	1.8	86	1.0%
	plage	602	38	126	2.9	-388	13	122	1.4	126	1.0%
	quiet	**153**	**32**	**90**	**2.6**	**0.2**	**4.6**	108	2.4	222	1.5%
3-min	umbra	2245	–	75	–	1460 –	12	126	1.5	35	0.3%

they interact with the intense magnetic field, and the energy of this p-mode is absorbed, and a significant fraction is converted to slow magnetoacoustic waves formed within the sunspot (Cally et al., 1994; Bogdan, 2000; Norton et al., 2021). The second one is magneto-convection, in which convective cells in the umbra are small and inhibited due to the strong vertical magnetic field (Chae et al., 2017; Stein, 2012; Schmassmann et al., 2021). In the umbra, umbral dots are considered as the potential sites of magnetoconvection (Riethmüller et al., 2013). Apart from photospheric origin, MHD waves can also be triggered by flares (Kosovichev and Sekii, 2007; Nakariakov et al., 1999).

Transverse kink oscillations in coronal loops produced by flares have been studied by Nakariakov et al. (1999); Aschwanden et al. (1999a). The period of global kink oscillations is around 4-min (Nakariakov and Ofman, 2001). Alfvén waves are also present in sunspots (Nye and Hollweg, 1980). Different period propagating waves are studied in various magnetic structures (e.g., De Pontieu et al., 2007; Tomczyk et al., 2007; Jess et al., 2009; Chae et al., 2022).

In this thesis, we mainly focus on slow and Alfvén waves propagating along magnetic loops rooted in the sunspot umbra, which are described below.

1.4.3.1 Slow wave oscillations

Traditionally, the slow wave phenomenon observed in the different layers of the sunspot umbra is classified into i) 5-min p-mode at the photosphere, ii) 3-min umbral flashes in the chromosphere, and iii) 3-min propagating waves in the corona, along with other higher periods (see details in Khomenko and Collados, 2015).

Photospheric oscillations

Velocity and intensity oscillations in the umbral photosphere have been very well studied. The FFT power spectrum of the umbra is similar to that of the quiet Sun, except for its reduced power (Parchevsky and Kosovichev, 2006). At the photosphere, the amplitude of intensity oscillations is usually small compared to velocity oscillations. Periodic oscillations of Doppler velocity and intensity extracted from spectral lines provide evidence of the presence of compressional waves. The FFT power spectrum of these oscillations shows maximum power around a 5-min period with traces of a 3-min period (Bellot Rubio et al., 2000; Norton et al., 2021). Velocity amplitude of 5-min and 3-min period bands at the photosphere are $\approx$ 100 and 30 m s^{-1}, respectively (Lites et al., 1998).

Chromospheric and transition region oscillations

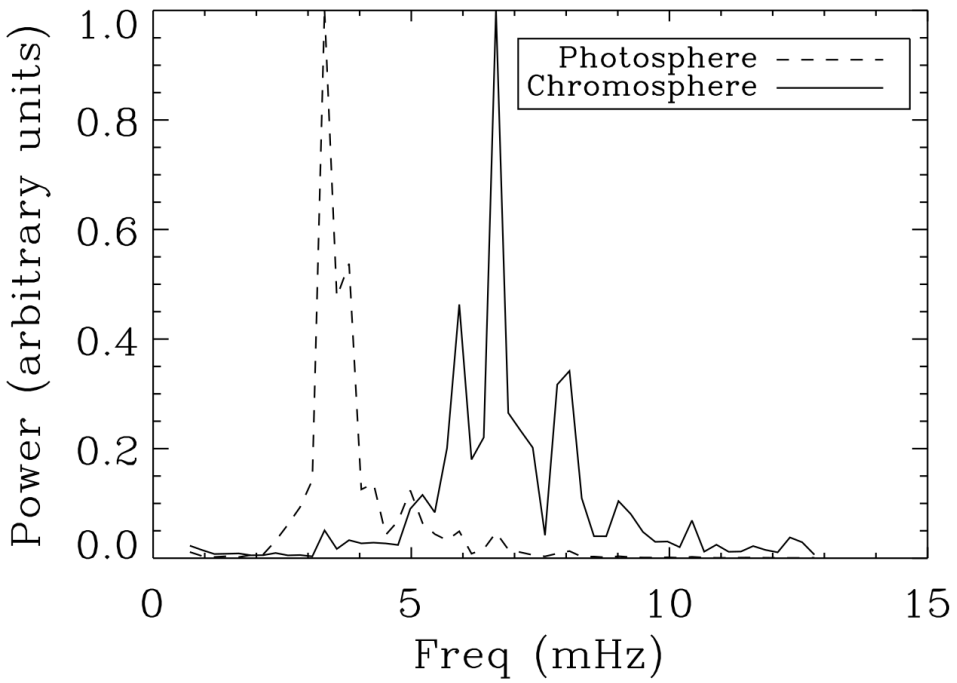

Figure 1.13: Average FFT power spectrum integrated over sunspot umbra. Solid and dashed lines represent the power spectrum obtained from the chromospheric and photospheric velocity oscillations, which peak around 6 mHz (2.7-min) and 3.3 mHz (5-min), respectively. Image courtesy: Centeno et al. (2006).

Figure 1.14: A schematic image shows a finite-amplitude wave profile that steepens into a shock wave. Image courtesy: Priest (2014)

Periodic intensity oscillations of 3-min are more prominent in the chromosphere than in the photosphere. The shift in the vertical period from 5-min in the photosphere to 3-min in the chromosphere can be due to the acoustic filtering of these waves (Centeno et al., 2006; Felipe et al., 2010) as shown in Figure 1.13. Waves with periods above the cut-off value become evanescent and cannot reach the upper layers of the solar atmosphere (Yuan et al., 2014). The equation for cut-off frequency is given by (e.g., Bel and Leroy, 1977; Yuan et al., 2014) which depends on the gravity (g), adiabatic index (γ) and acoustic speed (c_s),

$$\nu_o = \frac{\gamma g}{4\pi c_s}. \tag{1.28}$$

In the low plasma-β regime, the magnetic field inclination angle ϕ reduces the cutoff frequency by $\nu_{mag} = \nu_o cos\phi$. The phase difference between 3-min photospheric velocity oscillations and chromospheric intensity oscillations shows a linear trend, which signifies vertical wave propagation of 3-min waves (Lites, 1984; Kentischer and Mattig, 1995). Due to exponential decay in plasma density with height, the velocity amplitude of the wave increases. Bogdan and Judge (2006) provided a relation between the frequency-dependent power of oscillation and the density at two atmospheric heights

$$\frac{P_{ch}(f)}{P_{ph}(f)} = (\frac{\rho_{ph}}{\rho_{ch}})^{1-\sqrt{1-(f/5.2mHz)^2}}, \tag{1.29}$$

where P is the power of oscillation with frequency ($f \leq 5.2$ mHz).

This increase in the amplitude of a wave is called a shock or umbral flash (Beckers and Tallant, 1969) where the wave reaches a non-linear regime and dissipative processes, such as viscosity or thermal conduction, come into the picture (see Figure 1.14). These shock wave fronts are seen as sawtooth patterns (asymmetric light curves) in observations, see Figure 1.14. They occur with a period of 2-3 min with average velocity amplitude around 1 km s^{-1} and are interpreted as signatures of upward propagating magnetoacoustic shock waves (Centeno et al., 2006). The shock wave front is ≈1500 K hotter than the surroundings (de la Cruz Rodríguez et al., 2013).

3-min oscillations are observed in the transition region (Gurman et al., 1982; O'Shea et al., 2002; Banerjee et al., 2002). The non-linear behavior of oscillations present at the chromosphere and transition region was first observed by Tian et al. (2014) using IRIS spectroscopic data.

Coronal oscillations

Chromospheric and transition region umbra are filled with oscillations; however, in the corona, they are confined to a smaller area identified as coronal loops. Propagating MHD waves along the coronal loops having different periods and propagation speeds have been studied by De Moortel et al. (2000); Nakariakov et al. (2000).

The first interpretation of propagating slow waves along coronal loops was given by Nakariakov et al. (2000) using TRACE EUV observations. Coronal loops rooted in the sunspot umbra show outward propagating disturbances with subsonic phase speed and period around 3 min (e.g., De Moortel et al., 2002a). These propagating disturbances exhibit wave-like characteristics, and are manifestations of propagating slow magnetoacoustic waves (e.g., Gupta et al., 2012; Kiddie et al., 2012). The temperature dependence of the propagation speed of these waves in the sunspot loops confirms that these are waves. The propagation speed is less than the local sound speed, further confirming that these are slow magnetoacoustic waves (Kiddie et al., 2012).

1.4.3.2 Alfvén waves oscillations

Alfvén waves are also produced due to footpoint motion of the magnetic loop, i.e., all the MHD waves have the same photospheric driver (Hollweg, 1978; van Ballegooijen et al., 2014). Due to the incompressible nature of these waves, the signature of Alfvén waves can be found only in Doppler velocities. Additionally, simultaneous spatial and temporal spectroscopic data at each atmospheric height over the same structure is not possible with the current generation of telescopes. However, there exist a few examples of Alfvén wave detection in different magnetic structures and at different atmospheric heights separately. Therefore, till now, there are not many reports on the detection of Alfvén wave propagation and damping in the lower solar atmosphere (e.g., Khomenko and Collados, 2015; Morton et al., 2023). Below, we discuss the various Alfvén wave detections in various magnetic structures present at different atmospheric heights.

Jess et al. (2009) utilized spectroscopic data and determined the oscillation in the full-width half-maximum (FWHM) of the spectral line originating above the magnetic bright point at the photosphere and found the period around 2-12 min. They found the signature of Alfvén waves produced by a torsional twist of 22° and propagating up from the photosphere to the chromosphere, see Figure 1.15. To further verify their results, they showed the absence of co-spatial intensity oscillations and transversal displacements, which ruled out the presence of magneto-acoustic waves.

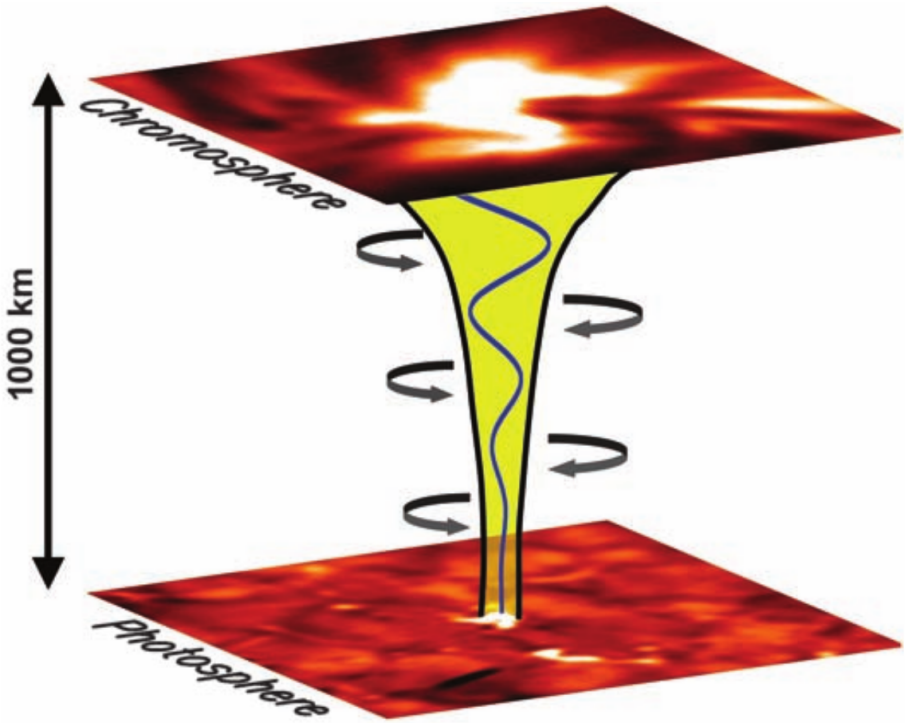

Figure 1.15: Schematic image of torsional Alfvén wave propagating along an expanding magnetic loop sandwiched between photospheric and chromospheric intensity images. The figure is not to scale. Image courtesy: Jess et al. (2009)

The propagation of 3-min and 10-min Alfvén waves around the sunspot umbra in the chromosphere is studied by Chae et al. (2022). They suggested that these two groups have different origins, where 3-min waves are excited by the slow-to-Alfvén mode conversion in the chromosphere, and the 10-min Alfvén waves are excited by photospheric motion of thin magnetic loops.

The ubiquitous presence of outward propagating 5-min period Alfvén wave in coronal loops was first reported by Tomczyk et al. (2007). Morton et al. (2015) confirmed that the photospheric 5-min acoustic oscillations (p-modes) escape into the corona. Alfvén waves are also studied in the coronal loops using the non-thermal broadening of coronal spectral lines (e.g., Brooks and Warren, 2016; Gupta et al., 2019).

1.5 Damping of waves in sunspot umbral atmosphere

The dispersion relations in Section 1.4 can help us in understanding the dependence of wave frequency and phase speed on physical plasma parameters, e.g., density and temperature. However, the main drawback of this approach is that it neglects the dissipative term from the induction equation (see Equation 1.15) and the heating term from the en-

ergy equation (see Equation 1.14), which affects the real propagation and damping of the waves.

The transfer and conversion of mechanical energy flux produced by the convective motion into heat in the upper atmosphere (e.g., Cranmer et al., 2007; van Ballegooijen et al., 2011) is still not completely understood. Convective motions on the photosphere have sufficient energy to replenish the atmospheric losses, and waves propagating upward may carry these energy fluxes with them into the upper solar atmosphere (Poynting flux, Section 1.2). Nature of waves, i.e., either longitudinal or transverse, frequency, magnetic topology, wave amplitude, propagation speed, and other parameters such as plasma density, field strength, etc., may decide upon the amount of energy fluxes carried by them.

There are several ideal effects that change the amplitude of the wave but do not contribute to the actual damping of waves, such as gravitational stratification and area divergence of the loop.

Gravitational stratification: Wave propagation along the vertical magnetic loops in a stratified medium where the density is decreasing exponentially

$$\rho = \rho_o exp(-h/\lambda_T), \tag{1.30}$$

where h is the atmospheric height and λ_T is the gravitational scale height. In order to conserve the vertically propagating wave energy flux (F),

$$F = \rho \delta v^2 v_s, \tag{1.31}$$

where ρ is mass density, δv is velocity amplitude and v_s is speed of sound, the amplitude of the wave increases, see Figure 1.14.

$$\rho \propto \frac{1}{\delta v^2} \Longrightarrow \delta v \propto exp(h/2\lambda_T) \tag{1.32}$$

Therefore, gravitational stratification causes a non-linear increase in the amplitude of the waves as they propagate upward along the loop. These non-linear effects can compress and heat the plasma in the presence of non-ideal damping mechanisms explained below (Verwichte et al., 2008).

Area divergence: To balance the total horizontal pressure, the cross-sectional area

of the magnetic loop increases with height in the solar atmosphere. This leads to the apparent damping of slow magnetoacoustic waves due to area divergence. A pictorial representation of area divergence is shown in Figure 1.16 where area divergence causes the wave amplitude to decay as $A(s)^{-1/2}$, where $A(s)$ is the cross-sectional area of coronal loop with height (De Moortel and Hood, 2004). Area divergence does not contribute to any heating as the wave energy redistributes itself to conserve total wave energy within the magnetic loop. This is purely a geometric effect. These expanding fields also enhance the transmission of waves to the corona by decreasing the reflection from the chromosphere and transition region (Soler et al., 2017).

These ideal effects play a very important role in the propagation and apparent damping of slow propagating waves (De Moortel and Hood, 2004; Marsh et al., 2011). However, they do not contribute to the real damping of the waves. Therefore, it is important to take into account the effect of area divergence and gravitational stratification for an accurate estimation of the real wave damping.

Non-ideal adiabatic effects such as thermal conduction, compressive viscosity, optically thin radiation, etc., are the dominant damping mechanisms for slow magnetoacoustic waves. However, these damping mechanisms depend on the physical conditions of the loops, e.g., density (n_o), temperature (T_o), coronal loop length (L) (see details in Wang et al., 2021).

Thermal conduction: This is a dominant damping mechanism for coronal loops with $n_o \approx 10^9 - 10^{10} cm^{-3}$, $T_o \approx 5 - 10 MK$, and $L \geq 100$ Mm.

Compressive viscosity: This is a dominant damping mechanism for coronal loops with $n_o < 10^9 cm^{-3}$, $T_o > 10 MK$, and $L < 100$ Mm.

Optically thin radiation: This is a dominating mechanism for coronal loops with $n_o > 10^{10} cm^{-3}$, $T_o < 5 MK$, and $L < 100$ Mm.

Alfvén waves are considered a potential candidate to heat the solar atmosphere. Due to their incompressible nature, they can carry energy over longer distances without damping (e.g., Goossens et al., 2011). However, due to this incompressible nature, it is difficult to understand the mechanism involved in the damping of these waves. Therefore, there are various mechanisms proposed for Alfvén wave damping, such as phase mixing, mode conversion, resonant absorption, or turbulence (see recent review by Van Doorsselaere et al., 2020) and references therein. The Alfvén waves can also dissipate their energy via turbulence while interacting with counter-propagating Alfvén waves

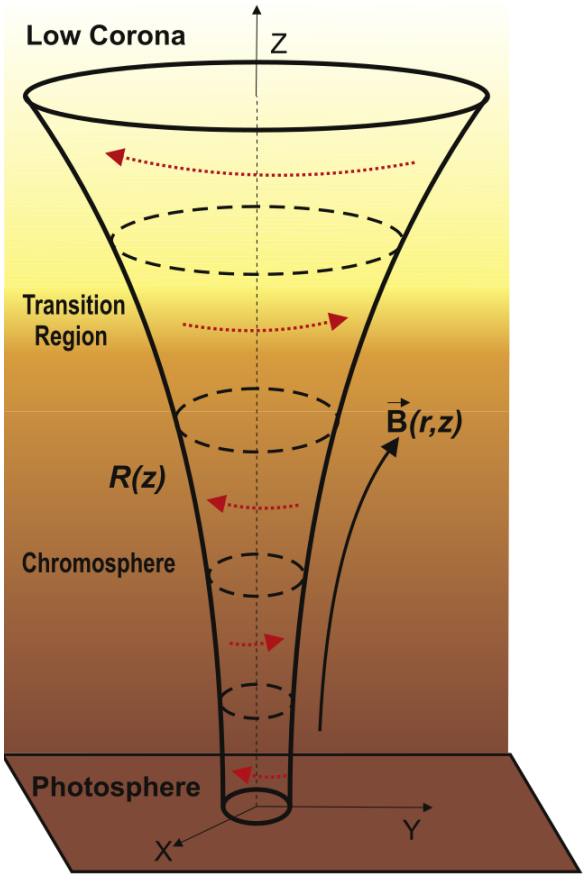

Figure 1.16: Schematic image of an expanding magnetic loop embedded in the stratified atmosphere. The red dotted arrows represent the torsional Alfvén waves. Image courtesy: Soler et al. (2017)

(van Ballegooijen et al., 2011). Dissipation of wave energy can cause the heating of the corona.

These dissipative models are:

Resonant absorption: In this model, strong absorption is expected to take place in the narrow layer where local Alfvén resonance frequency ν_{res} becomes equal to the oscillation frequency of the driver at the photosphere. This leads to damping by Ohmic or viscous dissipation (e.g., Ionson, 1978; Goossens et al., 2006).

Phase mixing: In a coronal loop, due to the cross-sectional density profile $n_e(r)$, a large gradient in Alfvén velocity, v_A exists. Due to this, wave oscillations of neighbouring field lines within a coronal loop suffer from friction (from kinematic and shear viscosity) due to slight differences in phase speeds. This friction leads to the heating of local plasma. This dissipation process is called phase mixing (e.g., Heyvaerts and Priest, 1983).

Turbulence: The propagation and reflection of Alfvén waves along magnetic loops produce non-linear interaction of waves, which causes turbulence at different atmospheric heights inside the magnetic loops. A turbulent cascade of energy produces small scales, leading to localized heating. At these small scales, dissipation mechanisms like viscosity, etc., convert wave energy into heat energy (e.g., van Ballegooijen et al., 2011; Verdini et al., 2012).

Mode conversion: In this process, one wave type transfers its energy to another wave type when it encounters a change in plasma parameters. For Alfvén wave dissipation, we consider that the Alfvén waves generated by the photospheric motion transfer their energy to other compressible modes like slow or fast waves when they encounter a plasma-β=1 region, where $v_A = v_s$ (e.g., Centeno et al., 2006; Khomenko and Cally, 2012). These compressible waves now damp via conduction, radiation, etc., as described above.

A detailed review on Alfvén waves is provided in Goossens (1994); Mathioudakis et al. (2013); Morton et al. (2023).

These models propose that these incompressible waves transfer their energy to compressible waves or compressible wave-damping mechanisms, which can easily damp in the solar atmosphere. Energy flux carried by Alfvén waves is adequate to heat the quiet Sun regions in the corona; however, it has also been noted that the Alfvén wave energy cannot heat active region corona (e.g., Tomczyk et al., 2007; McIntosh et al., 2011).

Moreover, there still exists several open questions related to studies of waves and oscillations in the sunspots, which need to be addressed and clarified (for more details, see, Liu and Ofman, 2014; Khomenko and Collados, 2015; Löhner-Böttcher, 2016; Nakariakov and Kolotkov, 2020; Banerjee et al., 2021).

1.6 Thesis outline

Waves have been studied for decades in the solar atmosphere. With the advancement in multi-wavelength imaging and spectroscopic data, these omnipresent waves, having different modes, can be studied in greater detail. Despite all the advancements, we still don't have a complete understanding of the physics behind the generation, propagation, and damping of these waves and their role in the coupling of the solar atmosphere.

In this thesis, the main objective is to provide a detailed study on the propagation

and damping of MHD waves guided along magnetic loops in the following steps:

- **Propagation:** Propagation properties of these waves are well studied independently in the solar photosphere, chromosphere, and corona. However, any connection/coupling between them at different heights in the solar atmosphere is poorly understood (Sych, 2016).

- **Damping:** Area divergence of magnetic loops in the solar atmosphere plays an important role in apparent wave damping (e.g., De Moortel and Hood, 2003). However, their role is not yet explored and quantified (e.g., Kanoh et al., 2016).

- **Seismological applications:** Using the observed waves and plasma properties, we will determine various plasma parameters along the loops, which are otherwise difficult to measure Anfinogentov et al. (2022); Nakariakov et al. (2024).

- **Spectroscopic diagnostics:** We will employ several spectroscopic diagnostic techniques to determine various plasma parameters along coronal loops using imaging and spectroscopic data (e.g., Brooks and Warren, 2016; Gupta et al., 2019). These parameters will enable us to explore the damping of waves along loops.

To achieve these objectives, we utilize multi-wavelength imaging and spectroscopic observations to understand the dynamics of propagating waves in fan loop structures rooted in the sunspot umbra. Below, we summarize the structure of this thesis.

The thesis consists of seven chapters, and the specific content of each chapter is summarized below.

Chapter 2: Data, methodology and techniques

This chapter provides a brief overview of the space-based imaging and spectroscopic instruments and observational data utilized in this thesis. Details of data, telescopes, wavelengths, resolution, and data preparation techniques are provided here. Various spectroscopic and time series diagnostic tools and techniques employed in this thesis to derive various parameters are also explained.

Chapter 3: Exploring the source region of 3-min slow waves

This chapter is associated with a detailed study on the source region of 3-min slow magnetoacoustic waves propagating along steady fan loops emanating from the sunspot

umbra. Results provide clear evidence of magnetic coupling of the solar atmosphere through the propagation of 3-min waves along the fan loops at different atmospheric heights.

Chapter 4: Effect of area divergence and frequency on damping of slow waves

In this chapter, we investigate the role of area divergence and frequencies on the damping of slow magnetoacoustic waves propagating from the photosphere to the corona and in the corona along several fan loops rooted in the sunspot umbra. Finding reveals that the area expansion of loops with height plays an important role in the damping of these waves from the photosphere to the corona, while in the corona, the effect is negligible. The damping length decreases with frequency, which further highlights the frequency-dependent damping.

Chapter 5: Magnetic field and plasma-β along fan loops

This chapter utilizes the loop tracing and area divergence along the whole fan loops from the photosphere to the corona and along the corona to determine various plasma parameters. Our results demonstrate the seismological potential of 3-min slow waves omnipresent in the umbral sunspot atmosphere.

Chapter 6: Spectroscopic diagnostics using AIA and EIS

In this chapter, we utilize the spectroscopic data from EIS onboard Hinode. We determined the non-thermal velocity amplitude of Alfvén waves, temperature, and electron number density along the loop length using various spectral line diagnostic techniques. Combining these parameters with the already calculated magnetic field strength, we determined the Alfvén wave energy flux, which is sufficient to heat the active region corona. We also compared plasma parameters obtained along coronal loops from different imaging and spectroscopic diagnostic techniques.

Chapter 7: Conclusions and Future Prospects

This chapter summarizes the key results of the thesis and highlights several potential directions for future research.

Chapter 2

Data, methodology and techniques

The Earth's atmosphere distorts the incoming radiation from the Sun and also blocks part of the electromagnetic spectrum. This distortion can be improved using adaptive optics. The telescopes placed outside the Earth's atmosphere (space-based telescopes) are unaffected by these effects. Additionally, space-based telescopes mainly operate in the low wavelength regime (e.g., UV, EUV, and X-ray) in which we study the on-disk part of the solar atmosphere. Using the imaging data of the Sun from space, we can explore the solar atmospheric dynamics, and spectroscopic data can provide various plasma parameters in the solar atmosphere from the line profiles.

2.1 Data and data reduction

To study and understand the wave dynamics in the whole solar atmosphere, we are utilizing data from space-based observatories, Solar Dynamics Observatory (SDO; Pesnell et al., 2012), Interface Region Imaging Spectrograph (IRIS; De Pontieu et al., 2014), and Hinode (Kosugi et al., 2007), which are described in this chapter. The raw data needs specific corrections before analysis, for which we have used some standard routines for data correction, which is called data reduction. Different instruments have different correction requirements. The data reduction procedures for all the instruments utilized in this thesis are described in this section.

2.1.1 Solar Dynamics Observatory (SDO)

SDO is a space-based solar mission launched on February 11, 2010. The spacecraft is in a circular geosynchronous orbit with an inclination of 28°. It is launched under NASA's

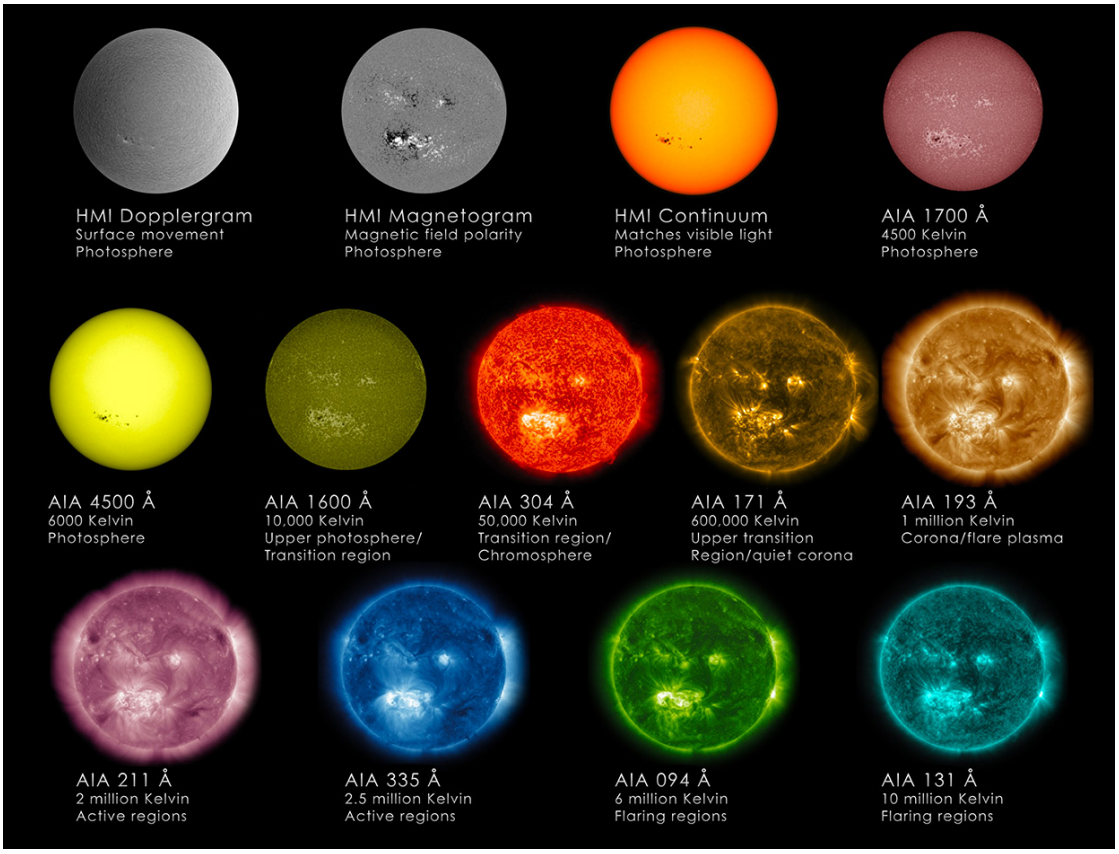

Figure 2.1: Images of the Sun in ten different wavelengths obtained from the AIA and HMI instruments onboard SDO. Image courtesy: The Sun Today.

Living With a Star (LWS) program. The main goal of SDO is to continuously monitor the solar interior and different layers of its atmosphere with high spatial and temporal resolution simultaneously in multiple wavelengths. Solar Dynamic Observatory (SDO; Pesnell et al., 2012) consists of three advanced solar telescopes: Atmospheric Imaging Assembly (AIA), Extreme Ultraviolet Variability Experiment (EVE), and Helioseismic and Magnetic Imager (HMI). In this section, we describe AIA and HMI in detail since the data obtained from these instruments form the major portion of this thesis. Sample images of the Sun taken in all the AIA and HMI passbands are shown in Figure 2.1.

2.1.1.1 Atmospheric Imaging Assembly (AIA)

AIA provides multi-wavelength simultaneous high-resolution (0.6"/pixel) full-disk images of the Sun up to 0.5 $R_{\odot}$ above the solar limb in ten passbands (Lemen et al., 2012). It has six coronal passbands, two transition region, one temperature minimum, and one photospheric continuum passband operating at different wavelengths as described in Table 2.1. Images in seven EUV coronal and transition region passbands are obtained at

Table 2.1: All AIA passbands with their primary ions, along with the solar layers that are probed with their characteristic emission temperatures (Lemen et al., 2012).

Passband	Primary ion(s)	Region of atmosphere	Char. log(T)
4500 Å	continuum	photosphere	3.7
1700 Å	continuum	temperature minimum, photosphere	3.7
1600 Å	C IV+cont.	transition region, upper photosphere	5.0
304 Å	He II	chromosphere, transition region	4.7
171 Å	Fe IX	quiet corona, upper transition region	5.8
193 Å	Fe XII, XXIV	corona and hot flare plasma	6.2,7.3
211 Å	Fe XIV	active-region corona	6.3
335 Å	Fe XVI	active-region corona	6.4
94 Å	Fe XVIII	flaring corona	6.8
131 Å	Fe VIII, XXI	transition region, flaring corona	5.6,7.0

12 s cadence, whereas those in two UV passbands are obtained at 24 s cadence. Photospheric continuum images are taken every hour.

Spacecraft continuously transmits level 0 data to the ground station in New Mexico and is archived at the Joint SDO Operations Center (JSOC[1]). Various steps involved in the further processing of the data are

- **Level 0 data to Level 1 data:** From Level 0 data, CCD read out noise, dark current, bad pixels and spikes are removed, and then flat field corrections are performed to obtain Level 1 data and then distributed in fits format (Pence et al., 2010). SDO Level 1 data can be directly accessed from JSOC or using the Virtual Solar Observatory (VSO) package[2].

- **Level 1 data to Level 1.5 data:** Level 1 data is then rescaled to a common plate scale, co-aligned to a specified pointing. The intensities at each pixel are normalized using the exposure time. These operations are performed using the solar software (SSW, Freeland and Handy, 1998) routine aia_prep.pro[3].

SSW routine aia_get_response.pro[4] provides the temperature response function of all the EUV passbands in the AIA instrument. These responses are calculated using the CHIANTI[5] atomic database (Dere et al., 1997; Dufresne et al., 2024). The response function of AIA EUV passbands with respect to temperature is shown in Figure 2.2.

[1]http://jsoc.stanford.edu/
[2]https://sdac.virtualsolar.org/cgi/search
[3]https://hesperia.gsfc.nasa.gov/ssw/sdo/aia/idl/calibration/aia_prep.pro
[4]https://hesperia.gsfc.nasa.gov/ssw/sdo/aia/idl/response/aia_ get_response.pro
[5]http://chiantidatabase.org/

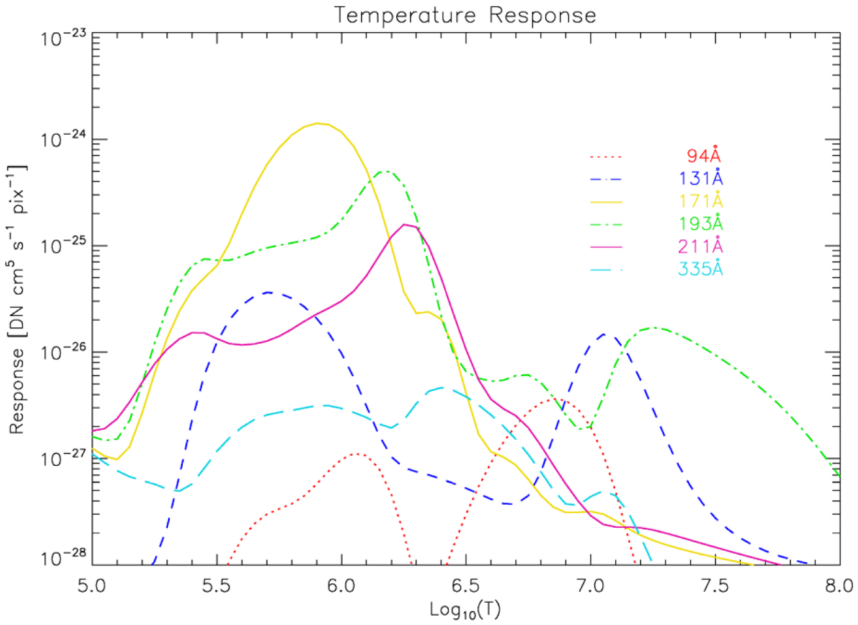

Figure 2.2: AIA temperature response functions for the six EUV passbands dominated by various coronal emission lines calculated using the CHIANTI model for the solar emissivity and the effective-area functions. Image courtesy: Boerner et al. (2012).

Each passband is sensitive to multiple temperatures, sometimes showing double peaks, which confirms the multi-thermal nature of these passbands. Therefore, the temperature information from these passbands needs to be interpreted cautiously.

2.1.1.2 Helioseismic and Magnetic Imager (HMI)

The Helioseismic and Magnetic Imager (HMI) onboard Solar Dynamics Observatory (SDO) is designed to provide an unprecedented view of the solar photosphere (Scherrer et al., 2012; Schou et al., 2012). HMI utilizes Fe I 6173 Å absorption line to provide Doppler shifts, continuum intensities, and line-of-sight (LOS) magnetic field at the photosphere (Norton et al., 2006). All the HMI data products are full-disk images of the Sun at high-resolution (0.5"/pixel) with a cadence of 45 s. It also provides a full-disk vector magnetogram with a cadence of 12 min by measuring the Stokes parameters.

HMI level 1 data is also available at the Joint SDO Operations Center (JSOC). Level 1 data is converted to Level 1.5 data using the SSW routine hmi_prep.pro[6].

[6]https://darts.isas.jaxa.jp/pub/ssw/sdo/aia/idl/calibration/hmi_prep.pro

Table 2.2: Details of IRIS slit-jaw-images (SJIs) passbands of two (Glass and Broad) for ground testing and four for observing the Sun (De Pontieu et al., 2014).

Bandpass	Name	Center [Å]	Width [Å]	FOV ["×"]	Pix. ["]	EA [cm^2]	Temp. [log T]
Glass	5000	5000	broad	175^2	0.1679	–	–
Broad	1600 W	1370	90	175^2	0.1656	–	–
C II	1330	1340	55	175^2	0.1656	0.5	3.7-7.0
Mg II h/k	2796	2796	4	175^2	0.1679	0.005	3.7-4.2
Si IV	1400	1400	55	175^2	0.1656	0.6	3.7-5.2
Mg II wing	2832	2830	4	175^2	0.1679	0.004	3.7-3.8

Table 2.3: IRIS spectrograph passbands with their wavelength bands, dispersion, field-of-view (FOV), spatial resolution, and effective area (EA) as provided in De Pontieu et al. (2014).

Band	Wavelength [Å]	Disp. [mÅ pix^{-1}]	FOV ["]	Pixel ["]	EA [cm^2]	Temp. [log T]
FUV1	1331.7-1358.4	12.98	175	0.1663	1.6	3.7-7.0
FUV2	1389.0-1407.0	12.72	175	0.1663	2.2	3.7-5.2
NUV	2782.7-2835.1	25.46	175	0.1664	0.2	3.7-4.2

2.1.2 Interface Region Imaging Spectrograph (IRIS)

IRIS is a NASA spacecraft that was launched in July 2013 to study the interface region (chromosphere and transition region). The spacecraft is in a polar, Sun-synchronous orbit and provides continuous observations for 8 months per year. The spacecraft consists of two instruments: a Slit-Jaw Imager (SJI) and a SpectroGraph (SG), which provide simultaneous images and spectra of the Sun in the far ultraviolet (FUV) and near ultraviolet (NUV) wavelengths (see Table 2.2 and Table 2.3). The IRIS Spectrograph observes spectral lines formed in the chromosphere (C II 1334/1335 Å, Mg II h 2803 Å and Mg II k 2796 Å) and transition region (Si IV 1394 and 1403 Å), see sample IRIS spectra in Figure 2.3. IRIS provides images in four passbands covering wavelengths 1330 Å (FUV1), 1400 Å (FUV2), 2796 Å (NUV), and 2832 Å continuum.

IRIS[7] provides simultaneous high-resolution images with 0.33–0.4" spatial resolution, up to 2 s temporal resolution, and 26 mÅ and 53 mÅ spectral resolution for FUV and NUV, respectively (De Pontieu et al., 2014). The IRIS spectrograph slit is 0.33" wide and 175" long. It records spectra in three modes, first by moving the slit across the solar disk and taking dense and sparse rasters, another by keeping the slit at one fixed position and taking spectra of a solar structure with repeated exposures, providing sit-and-stare observation.

Various steps involved in the processing of IRIS data are

[7]https://www.nasa.gov/mission_pages/iris/index.html

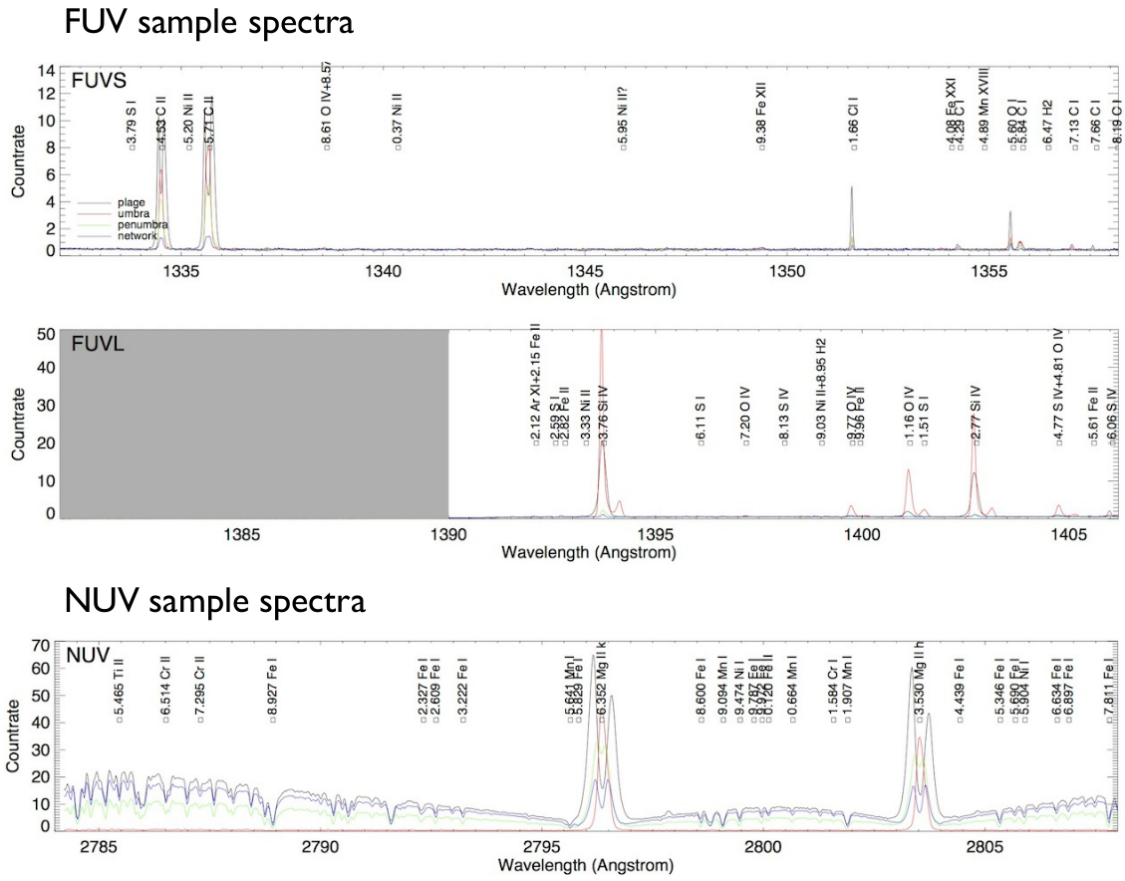

Figure 2.3: IRIS sample spectra of far ultraviolet short (FUVS), long (FUVL) and near ultraviolet (NUV) wavelengths. Image courtesy: IRIS tutorial.

- IRIS team distributes Level 2 data to the users from the European Hinode/IRIS Science Data Center[8] and the IRIS website[9]. Level 2 data are corrected for dark current, flat-field, geometric, and wavelength calibration, FUV background subtraction, etc. Level 2 data are available in 3-D cube format; for spectrograph in [wavelength λ, spatial y, spatial x], and SJI passbands in [spatial x, spatial y, time t].

- Orbital variation correction: Spectroscopic level 2 data is then corrected for the orbital variation (thermal and the spacecraft velocity component) using SSW routine *iris_orbitvar_corr_l2s.pro*[10].

- Dark region and cosmic ray removal: Due to dust accumulation on the CCD, dark regions can be seen in the SJI FUV images, which are removed using the SSW

[8]http://sdc.uio.no
[9]http://iris.lmsal.com/search
[10]https://darts.isas.jaxa.jp/pub/ssw/iris/idl/sao/util/tian/iris_orbitvar_corr_l2s.pro

routine *iris_dustbuster.pro*, and the cosmic rays are also removed using the SSW routine *despike.pro*.

The SSW routine iris_getwindata.pro[11] provides information regarding intensity array, error array, exposure time, plate-scale, etc., in a structured format for each spectral window. Details on instrument calibration of IRIS is provided in Wülser et al. (2018).

2.1.3 Hinode

Hinode is a space-based solar mission launched on September 23, 2006, at 6:36 am in Japan Standard Time (JST). The spacecraft is in a polar, Sun-synchronous orbit at an altitude of 600 km with an inclination of -987.9°. Hinode consists of three advanced solar telescopes: X-ray telescope (XRT), EUV imaging spectrometer (EIS), and solar optical telescope (SOT), see details in Kosugi et al. (2007). The instruments continuously study the Sun for nine months, accompanied by a three-month eclipse period. EIS could be used to study the coronal heating mechanism and dynamics in the active region. In this section, we describe EIS in detail since the data obtained from it forms a chapter of this thesis.

2.1.3.1 EUV Imaging Spectrometer (EIS)

The EUV Imaging Spectrometer (EIS; Culhane et al., 2007) was designed to study high-resolution spectra of the solar transition region and corona with temperatures ranging from 50,000 K to 20 MK. It has two wavelength bands, 170–211 Å and 246–292 Å referred to here as the short and long wavelength bands (SW and LW, respectively). These spectra are rich in the various ionization states of iron, magnesium, silicon, etc. The sample EIS active region spectra are provided in Figure 2.4. EIS data can be utilized to perform spectroscopic diagnostics to measure various plasma parameters such as electron number density, temperatures, non-thermal broadening, etc. (see details in Section 2.2.2).

EIS has a slit/slot exchanger that contains two narrow slits (1" and 2" width) and two wide slots (40" and 266" width), producing almost monochromatic images. The motion of the slit in the solar East-West direction provides raster scanning mode. In Figure 2.5, we show EIS raster image of fan loop system obtained from different spectral lines sensitive to different temperatures as labelled.

[11] https://darts.isas.jaxa.jp/pub/ssw/iris/idl/nrl/iris getwindata.pro

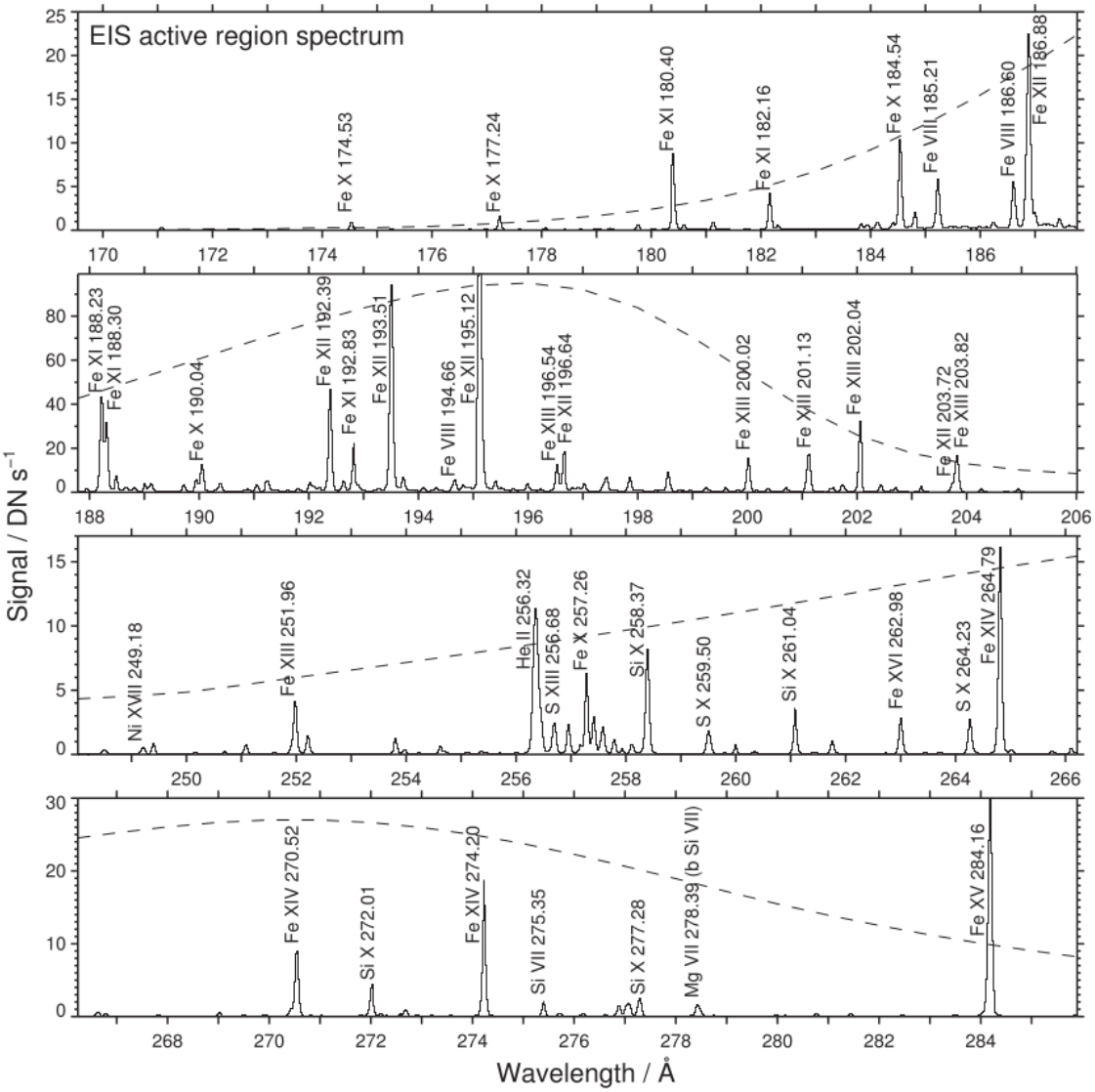

Figure 2.4: EIS sample spectra of active region. Image courtesy: Young et al. (2007).

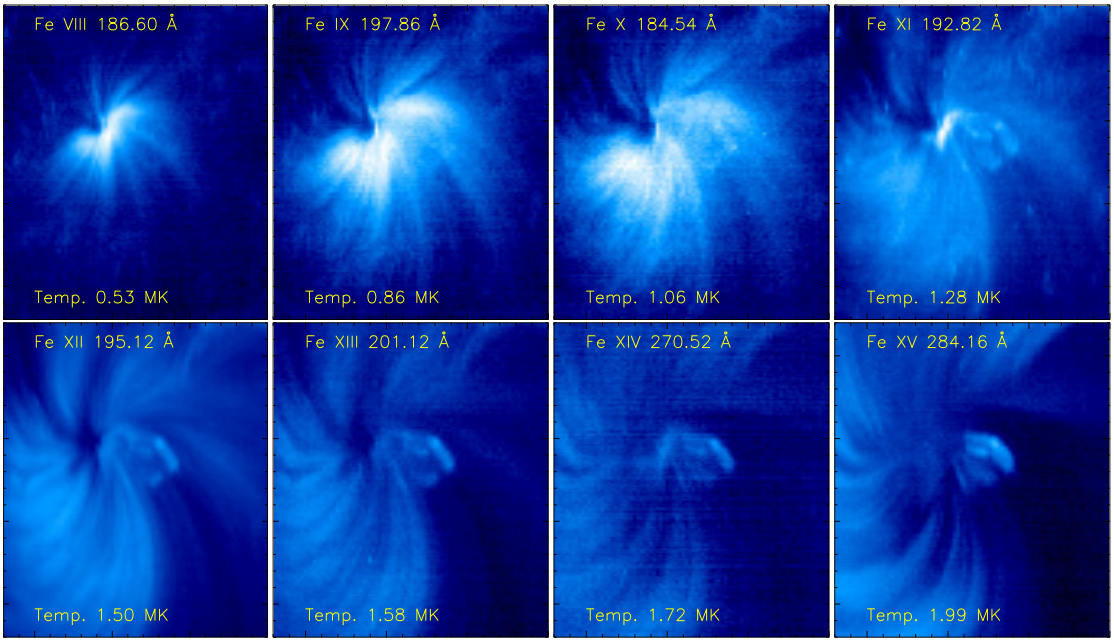

Figure 2.5: EIS raster image of fan loop system obtained from different spectral lines sensitive to different temperatures as labelled. Image adapted from Rawat and Gupta (2025).

The level 0 data from EIS can be accessed from ESA's Hinode Science Data Centre [12]. The various steps involved in processing EIS data are

- Level 0 data to Level 1 data: From Level 0 data, saturated data, dark current, and cosmic rays, hot, warm, and dusty pixels are removed. We can perform these corrections on the data using the SSW routine *eis_prep.pro*[13].

- Fitting Gaussian functions to level 1 data: EIS emission lines are fitted using single and/or multiple Gaussian components. The intensities in data number (DN) can be converted into calibrated units, absolute intensities (ergs cm^{-2} s^{-1} sr^{-1}) using the radiometric calibrations. The satellite's orbital motion around the Earth results in a periodic shift of the wavelength scale due to periodic fluctuation in temperature (instrument receives variable illumination from Earth; Kamio et al., 2010). SSW routine *eis_auto_fit.pro* takes into account all these offsets and fits a single or multiple Gaussians to each pixel in the image.

- Slit tilt: There is a total spatial offset of 18.5 pixels in the Y-direction between the CCD detectors of the SW and LW channels. SSW routine *eis_slit_tilt_array.pro*[14]

[12]http://sdc.uio.no/sdc/
[13]http://www.heliodocs.com/php/xdocprint.php?file=SSW/hinode/eis/idl/calibration/eis_prep.pro
[14]http://www.heliodocs.com/php/xdoc print.php?file=$SSW/hinode/eis/idl/atest/pyoung/eis_slit_tilt_array.pro

corrects this tilt with respect to the CCD axis.

One can further derive line intensity, line width, and velocity maps from the fitted data using the routine *eis_get_fit_data.pro*[15].

2.2 Atomic processes in the solar atmosphere

Different ions present in the solar atmosphere exist in a wide range of excited states. Various atomic processes contribute to the excitation of ions present in different layers of the solar atmosphere. The different atomic processes that contribute to the continuum and line emission of the solar corona are pictorially represented in Figure 2.6. Figure 2.6 shows the interactions between photons, electrons, atoms, and ions, depicting absorption, emission, excitation, de-excitation, ionization, and recombination processes; more details can be found in Aschwanden (2004); Phillips et al. (2008); Del Zanna and Mason (2018). For coronal plasma, the collision between ions and free electrons (bound-free) is the key process, which is found in photoionization, di-electronic recombination, and collisional ionization.

2.2.1 Spectral line formation

The transition of ion (X^{+m}) from an excited level f to ground level g emits a photon of energy (hc/λ), and the total emissivity (erg cm^{-2} s^{-1}) of the spontaneous radiation can be written as

$$\epsilon_{gf} = \frac{hc}{\lambda} A_{gf} N(X_f^{+m}). \tag{2.1}$$

Where A_{gf} is the radiative transition probability (Einstein transition probability), h is the Planck's constant (6.63×10^{-34} m^2 kg s^{-1}), c is the speed of light (3×10^8 m s^{-1}), $N(X_f^{+m})$ is the number density of ion X in the excited level f and ionization stage $+m$.

The flux F (erg cm $^{-2}$ s^{-1}) for an optically thin line of wavelength λ_{fg} can be written as,

$$F(\lambda_{fg}) = \frac{1}{4\pi d^2} \int_{\Delta V} \frac{hc}{\lambda_{fg}} A_{fg} N(X_f^{+m}) \, dV, \tag{2.2}$$

where d is the distance between the Sun and the Earth. The number density of the

[15]https://hesperia.gsfc.nasa.gov/ssw/hinode/eis/idl/analysis/line_fitting/auto_fit/eis_get_fitdata.pro

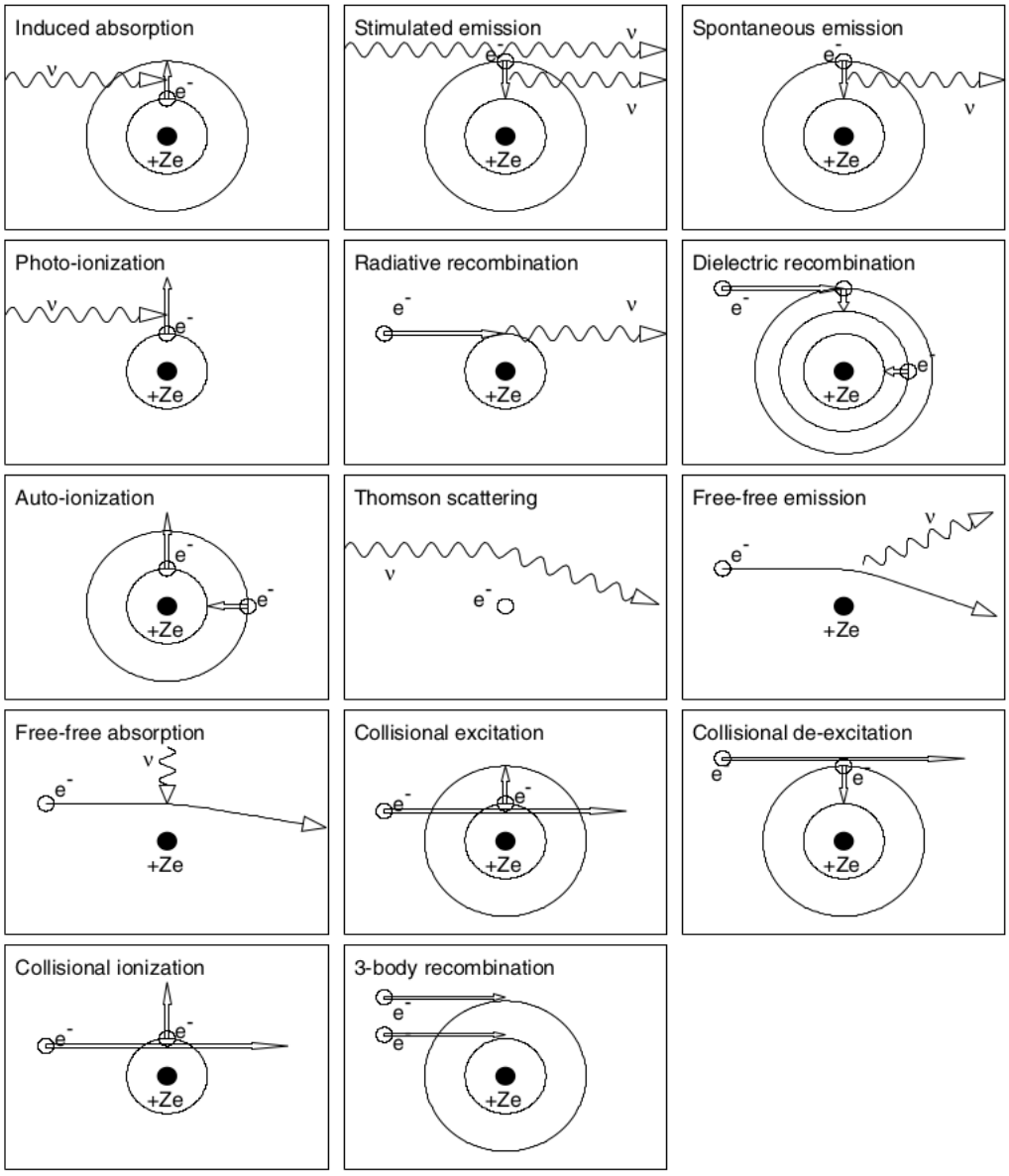

Figure 2.6: Pictorial representation of various atomic processes happening in the Sun. Here, the atoms and ions are depicted with filled dots, electrons and their orbits are depicted with open dots and circles. The electronic transitions are depicted with arrows, and photons are depicted with a wiggly arrow. Image courtesy: Aschwanden (2004).

excited level can be written as:

$$N(X_f^{+m}) = \frac{N(X_f^{+m})}{N(X^{+m})} \frac{N(X^{+m}}{N(X)} \frac{N(X)}{N_H} \frac{N_H}{N_e} N_e, \tag{2.3}$$

where

- $\frac{N(X_f^{+m})}{N(X^{+m})}$ is the relative level population of the excited level f with respect to the total number density of the ion,
- $\frac{N(X^{+m})}{N(X)}$ the relative abundance of ion X^{+m} with respect to the total number density of the element X,
- $\frac{N(X)}{N_H}$ = Ab(X) is the element abundance relative to hydrogen,
- $\frac{N_H}{N_e}$ is the relative abundance of hydrogen with respect to the free electron number density (≈0.83 in the solar atmosphere at temperature $> 10^5$ K).

The plasma is fully ionized at coronal temperatures. In general, it is assumed that the quantities $\frac{N(X_f^{+m})}{N(X^{+m})}$ and $\frac{N(X^{+m})}{N(X)}$ are calculated separately using Boltzmann equation and Saha ionization equation, respectively. The level populations within an ion and the ionization balance are independent. This may not be the case in all circumstances in the solar atmosphere.

The value $C(N_e,T,\lambda_{fg})$ is called the contribution function and has unit erg cm^3 s^{-1} sr^{-1}. This contains all the atomic parameters for each spectral line and can be written as

$$C(N_e, T, \lambda_{fg}) = Ab(X) \frac{hc}{4\pi\lambda_{gf}} \frac{A_{jg}}{N_e} \frac{N_j(X^{+m})}{N(X^{+m})} \frac{N(X^{+m})}{N(X)} \tag{2.4}$$

The flux $F(\lambda_{fg})$ can be further written as,

$$F(\lambda_{fg}) = \frac{1}{4\pi d^2} \int_{\Delta V} C(N_e, T, \lambda_{fg})\, N_e^2\, dV \tag{2.5}$$

The total emission measure EM$_V$ (cm^{-3}) over the total emitting volume V is defined as

$$EM_V = \int_V N_e^2\, dV \tag{2.6}$$

In the solar atmosphere, all the atomic parameters are calculated using the CHIANTI database (Dere et al., 1997; Dufresne et al., 2024). It provides atomic data for optically thin spectral lines at UV, X-ray, and infrared wavelengths. The atomic data have been

benchmarked using solar observations and laboratory calculations. The CHIANTI software package is included in the SSW library and can be used for the calculation of plasma parameters using spectroscopic diagnostics. CHIANTI package has been utilized in this thesis to measure line intensities, FWHM, density, and temperature using optically thin spectral line diagnostics.

2.2.2 Plasma diagnostics

Spectroscopic instruments provide observations of spectral lines and their intensity values. For an optically thin emission line of a wavelength λ_{fg} the intensity I(λ_{fg}) emitted along the line-of-sight (LOS) h in units of erg cm^{-2} s^{-1} sr^{-1} can be written as

$$I(\lambda_{fg}) = \frac{hc}{4\pi\lambda_{fg}} \int_h A_{fg}\ N(X_j^{+g})\ dh \tag{2.7}$$

or

$$I(\lambda_{fg}) = \int_h C(N_e, T, \lambda_{fg})\ N_e\ N_H\ dh \tag{2.8}$$

2.2.2.1 Differential Emission Measure (DEM)

Column differential emission measure DEM(T) (cm^{-5} k^{-1}) is the amount of plasma along the LOS that emits the observed radiation in the temperature between T and $T + dT$ and can be expressed as

$$DEM(T) = N_e\ N_H\ \frac{dh}{dT} \tag{2.9}$$

$$\int_T DEM(T)\ dT = \int_h N_e\ N_h\ dh \tag{2.10}$$

Using the above equation and assuming the abundance of element Ab(X) as constant along the LOS, the intensity I(λ_{fg}) of an emission line can be written in the form,

$$I(\lambda_{fg}) = \int_T C(N_e, T, \lambda_{fg})\ DEM(T)\ dT \tag{2.11}$$

The total column emission measure (EM$_{col}$) can be calculated by integrating the DEM over the temperature range that was used in the DEM analysis.

$$EM_{col} = \int_h N_e\ N_H\ dh = \int_T DEM(T)\ dT \tag{2.12}$$

In fully ionized corona, we assume $N_e \approx N_H$

$$N_e = \sqrt{\frac{EM_{col}}{h}} \tag{2.13}$$

The effective temperature T_{eff} of a spectral line is an important quantity that provides the temperature where the spectral line is actually formed in the plasma being studied. The T_{eff} may be different from the temperature where the C(T) has its maximum value.

$$logT_{eff} = \frac{\int C(T, N_e)\ DEM(T)\ logT\ dT}{\int C(T, N_e)\ DEM(T)\ dT} \tag{2.14}$$

If a DEM is obtained by using EUV and X-ray imaging observations, then it is useful to measure the DEM weighted average temperature T (e.g., Del Zanna and Mason, 2018),

$$T = \frac{\int DEM(T)\ logT\ dT}{\int DEM(T)\ dT} \tag{2.15}$$

2.2.2.2 Spectral line analysis

High-resolution spectroscopic data can resolve the spectral line profiles, which provide information about the physical conditions in the line-forming region. The intensity of an optically thin emission line is given in Equation 2.7. In the upper solar atmosphere, due to the thermal motion of atoms, the wavelength of the photons emitted show Doppler shifts, which results in the broadening of the spectral line profile. Each atom has its own velocity. Assuming the Maxwellian distribution of atomic velocities, the probability P(v) that the velocity of an atom lies between v and $v + dv$ is,

$$dP(v) = \sqrt{(\frac{m}{2\pi k_b T})}\ exp(\frac{mv^2}{2k_b T})\ dv \tag{2.16}$$

where m is the mass of the atom, k_b is the Boltzmann constant, and T is the ion temperature. The change in wavelength $\Delta\lambda$ (Doppler shift) caused by the velocity component u along the line-of-sight is given by,

$$\frac{\Delta\lambda}{\lambda} = \frac{u\ cos\theta}{c} \tag{2.17}$$

where θ is the angle between u and the line-of-sight. Substituting Equation 2.17 in Equation 2.16, we determine the line profile as a function of wavelength λ

$$\psi(\lambda) = \psi_o \; exp(\frac{-m \; c^2 \; \Delta\lambda^2}{2 \; k_b \; T \; \lambda^2}) \tag{2.18}$$

Electron number density Diagnostics

The emission line intensity I(λ_{fi}) contains electron number density due to its dependence on the number density of ions in the excited level and the density dependence of the collision states. Electron number densities can be measured by using the intensity ratio of two spectral lines emitted by the same ion. For a multi-thermal plasma, the intensity ratio of two lines is given by Equation 2.11.

$$\frac{I(\lambda_{ij})}{I(\lambda_{kl})} = \frac{\int_T C(N_e, T, \lambda_{ij}) DEM(T) dT}{\int_T C(N_e, T, \lambda_{kl}) DEM(T) dT} \tag{2.19}$$

Since we are using the same ion, the ion and elemental abundances are the same for both the lines, and therefore the integrals only depend on the populations of upper transition levels j and l of the lines and the respective Einstein coefficients. The population of the lower level from which the upper level is populated decides the density sensitivity of the population ratio.

Temperature diagnostics

Combining Equation 2.8 and Equation 2.12 provides the emission measure distribution as a function of temperature:

$$EM_{col} = \frac{I(\lambda)}{C(N_e, T)} \tag{2.20}$$

If the EM loci curves for a number of spectral lines intersect at a common temperature, it indicates that the plasma along the LOS is isothermal. In case the EM curves do not intersect at a single temperature, it indicates the presence of multi-thermal plasma along the LOS. This method is known as the EM loci method, which assumes that the N_e and the elemental abundances do not vary along the LOS.

More details on above techniques can be found in Aschwanden (2004); Phillips et al. (2008); Del Zanna and Mason (2018). The above techniques are utilized to extract electron number density and temperature in Chapter 5 and Chapter 6.

2.3 Data Analysis

For analysing the time-series data to study oscillations, we have utilized various signal processing techniques described below.

2.3.1 Time-series analysis

A time series represents the light curve of MHD oscillations. The original time series contains noise and non-periodic background processes. To detect pure oscillatory signals in the time series, we need to remove high-frequency noise and low-frequency background from the original time series before performing the actual analysis. Such pre-processing is called trend removal. Here, we introduce a new smoothed time series and then subtract it from the original time series to obtain a de-trended time series. This may cause false periodicity, so we have to choose our smoothing range carefully. This method can efficiently suppress higher and lower frequency fluctuations depending on the smoothing range of the original time series, which will be visible in the Fourier power spectrum of the smoothed signal. Recent updates on the novel analysis techniques can be found in Anfinogentov et al. (2022); Jess et al. (2023).

2.3.2 Fourier Analysis

Fourier analysis is an important time series processing tool that is used to decompose a time series into its frequency components. The result of the analysis represents the signal in the frequency domain. The main advantage of Fourier analysis is that very little information is lost from the signal during the transformation (Cooley et al., 1969). It maintains information on amplitude, harmonics, and phase and uses all parts of the waveform to translate the signal into the frequency domain (Anfinogentov et al., 2022).

Here, we are using Fast Fourier transform (FFT), which is an efficient algorithm for computing the discrete Fourier transform (DFT), see details in Press et al. (1986). Dividing the DFTs into smaller DFTs allows for more efficient computation. The DFT of x_n is:

$$\hat{x_k} = \frac{1}{N}\Sigma_{N=0}^{N-1}\, x_n e^{-2\pi i k n/N} \tag{2.21}$$

where k is the frequency index and N is the number of points in the time series.
FFT is faster than DFT as it reduces the number of operations from O(N^2) for DFT to O(Nlog$N$) for FFT.

2.3.3 Wavelet Analysis

The Fourier transform provides information on the dominant frequencies, and wavelet analysis provides the localisation of the various frequency components over time. Wavelet analysis is a powerful technique to study the temporal variation of the frequency as it allows a local decomposition of time scales in the time series and, therefore, is ideal for analysing non-stationary time series. Most of the wave motions observed in the solar atmosphere are not stationary but tend to be waves with only a few periods and of a finite lifetime; hence, wavelet analysis is ideal to study solar time series. The choice of the wavelet is decided by the signal characteristics and the nature of the application. We can understand the properties of the analysis and synthesis wavelet that is optimized for our application. Wavelet can incorporate a finite wave of a certain period.

Here we are using the Morlet wavelet for our analysis. It is composed of a complex exponential (carrier) multiplied by a Gaussian window (envelope). The wave function of the Morlet wavelet is:

$$\psi_o(\eta) = \pi^{-1/4} e^{i\omega_o \eta} e^{-\eta^2/2}, \tag{2.22}$$

where ω_o and η is the non-dimensional frequency and time parameter and provide the best trade-off between spatial and frequency resolution.

By the convolution theorem, it is the inverse Fourier transform of the product:

$$W_n(s) = \Sigma_{k=0}^{N-1} \hat{x}_k \hat{\psi}^*(s\omega_k) e^{i\omega_k n \delta t}, \tag{2.23}$$

where, s is the wavelet scale, and n is the translation parameter used to slide in time, ω is the angular frequency, δt is the time step, k is the frequency index, $\hat{x_k}$ is DFT of discrete sequence x_n. More details on the wavelet tool can be found in Torrence and Compo (1998); De Moortel et al. (2004); Anfinogentov et al. (2022).

2.3.4 Correlation analysis

Cross-correlation analysis is used to analyse the similarity between time series. It is a measure of similarity between two different time series as a function of the time delay between them. The directions and strength of the correlation is given by the correlation coefficient (r),

$$r = \frac{\Sigma_{i=1}^{N}(x_i - \bar{x})(y_i - \bar{y})}{\sqrt{\Sigma_{i=1}^{N}(x_i - \bar{x})^2}\sqrt{\Sigma_{i=1}^{N}(y_i - \bar{y})^2}}, \tag{2.24}$$

where, N is the length of the time series x and y and their respective means are $\bar{x}$ and $\bar{y}$. If the two time series are perfectly correlated, anti-correlated, and completely uncorrelated, the value of r is 1, -1, and 0, respectively, see details in Bevington (1969). If we plot both r as functions of time, we can determine the time lag between the two light curves, i.e., the time at which the correlation coefficient is maximum (correlated) or minimum (anti-correlated).

Chapter 3

Source region of waves observed in coronal fan loops

Magnetohydrodynamic (MHD) waves observed in the solar atmosphere are studied mainly for their role in coronal heating and atmospheric seismology (De Moortel and Nakariakov, 2012). At different atmospheric heights, sunspots show different features that host various oscillations and waves. There are numerous observational reports of waves and oscillations above the sunspot umbra in the photosphere, umbral flashes and running waves in the chromosphere, and propagating waves in the corona. Details of slow waves and oscillations present in the solar umbral atmosphere are provided in Section 1.4.3.1. However, several open questions still exist related to studies of waves and oscillations in the sunspots, which need to be addressed and clarified as suggested in Khomenko and Collados (2015) and Löhner-Böttcher (2016).

Coronal loops rooted in the sunspot umbra show outward propagating disturbances with subsonic phase speed and period around 3-min (e.g., De Moortel et al., 2002a; Sharma et al., 2020). Similar propagating disturbances with a period of around 15 min are also observed along plume-like structures in the polar coronal holes (e.g. DeForest and Gurman, 1998; Gupta et al., 2010). These propagating disturbances are found to have wave-like properties and are often interpreted in terms of propagating slow magnetoacoustic waves (e.g., Kiddie et al., 2012; Gupta et al., 2012). 3-min slow magnetoacoustic waves propagating along coronal fan loops show amplitude modulations in the period range of 20-30 min (Sharma et al., 2020). Such amplitude modulations are the result of the interaction of various beat-like phenomena formed due to the number of

closely spaced frequencies within the 3-min period band (e.g., Marsh and Walsh, 2006; Krishna Prasad et al., 2015; Sharma et al., 2020). Formation of such closely spaced multiple frequencies within the 3-min period band are explained either as eigenvalues of umbral oscillations or through the resonant filtering mechanism by Zhukov (2005). Although multiple frequencies exist within the 3-min period band, reports of modulation period are limited to only isolated periods within 20-30 min range (e.g., Krishna Prasad et al., 2015; Sharma et al., 2020). Moreover, these waves are also found to show modulations in dominant frequency within the 3-min period band with time while propagating (e.g., Sych et al., 2012).

Although propagating coronal slow waves are ubiquitous in the different structures, observational evidence of their source region is still rare (e.g. Jess et al., 2012a; Krishna Prasad et al., 2015). Jess et al. (2012a) found 3-min magnetoacoustic waves in the coronal fan loops, which were rooted in the umbral dots at the photosphere. In these umbral dots, the power of 3-min oscillations was enhanced compared to the surrounding regions. Krishna Prasad et al. (2015) utilised the amplitude modulation of 3-min Fourier-filtered light curves obtained near the footpoint of the fan loop at different atmospheric layers above the sunspot umbra and associated the presence of 3-min slow magnetoacoustic waves in corona with the 5-min photospheric p-mode. Similarly, Zhao et al. (2016) tracked 5-min p-mode waves from the photosphere to the corona in active regions using a time-distance helioseismology analysis technique. Sharma et al. (2017) reported the influence of umbral flashes on different sunspot waves in the upper atmosphere based on their synchronized change in the amplitude of 3-min oscillations. On the other hand, Kobanov et al. (2013) found no connection between 3-min oscillations and coronal fan structures in AIA 171 Å passband. Henceforth, there are mixed opinions on the origin of these 3-min waves in the umbra based on a few reports. Moreover, contrary views exist on 3-min and 5-min oscillations observed at the photosphere. Lites (1986) concluded that 5-min oscillations do not drive 3-min oscillations in the umbra because 3-min chromospheric oscillations are not correlated with the 5-min photospheric oscillations. Krishna Prasad et al. (2015) suggested that 5-min oscillations are responsible for the 3-min waves present in the coronal loops, whereas Chae et al. (2017) suggested that these are not coupled in the umbra due to their different origins. Therefore, to obtain a more general understanding of how these 5-min photospheric p-mode oscillations compare with 3-min waves, a detailed investigation is needed.

For direct and unambiguous detection of waves, it is mandatory to have excellent signals at different atmospheric layers, which is not always the case. In this chapter, we present a multi-wavelength analysis of the propagation of slow magnetoacoustic waves from the photosphere to the corona by studying fan loop structures anchored within a sunspot umbra. Fan loop structures provide an excellent site to study the propagation of 3-min slow magnetoacoustic waves in the solar atmosphere. We investigate whether the 3-min waves present in the corona owe their origin to the photosphere or not. For this, we utilize amplitude and less explored frequency modulation properties of 3-min waves. Henceforth, this study will also probe the magnetic connectivity of the whole solar atmosphere. The content of this chapter is published in the Rawat and Gupta (2023, 2024b).

3.1 Observations

To investigate the origin and characteristics of waves, we are using multi-wavelength observations of cool fan loops observed within the active region. For this purpose, we have identified an appropriate data set observed by the Atmospheric Imaging Assembly (AIA; Lemen et al., 2012), Helioseismic and Magnetic Imager (HMI; Scherrer et al., 2012) both onboard Solar Dynamics Observatory (SDO; Pesnell et al., 2012), and Interface Region Imaging Spectrograph (IRIS; De Pontieu et al., 2014). To study waves at the photosphere, we utilize continuum intensity and Dopplergram images obtained from the HMI. AIA EUV images provide good coverage over the transition region and the corona. To obtain good coverage over the chromosphere, we are utilizing UV images obtained from the AIA and IRIS. The sunspot studied here belongs to the active region NOAA AR 12553 (7°S, 8°W), which was observed on June 16, 2016. We obtained 4 hours of data starting from 07:19:11 UT, as shown in Figure 3.1.

AIA/SDO provides full-disk solar images in the seven EUV passbands that manifest the upper atmosphere and three UV-visible passbands that manifest the lower atmosphere. HMI/SDO provides full disk images of the photospheric Sun in continuum intensity, Dopplergram, and magnetogram, which are derived using the Fe I 6173 Å spectral line. These instruments have been recording continuous images of the Sun since their launch. All the images were calibrated, co−aligned, and re-scaled to a common 0.6"/pixel resolution, and 12 s temporal resolution using the robust SDO library

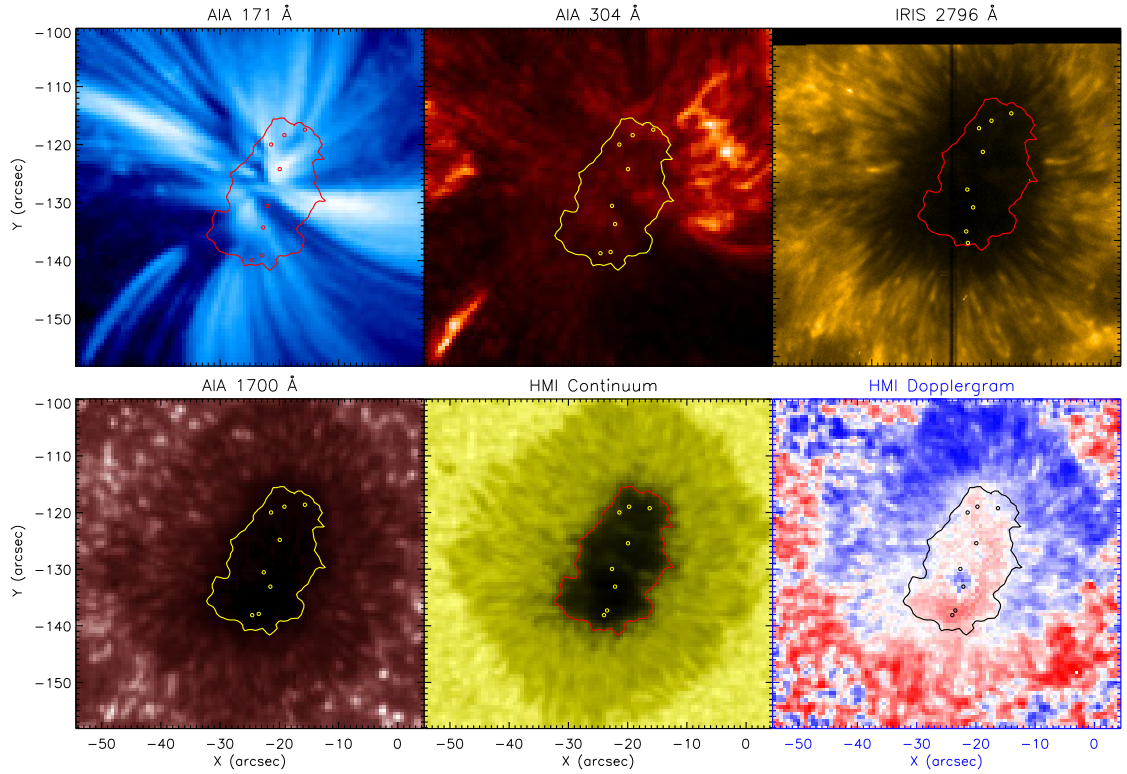

Figure 3.1: Images of sunspot and fan loops as obtained from different AIA, IRIS, and HMI passbands as labelled. Small circles (o) over different panels represent the location of all the identified loops at that atmospheric height (details in Figure 3.2 and Figure 3.3), which are used for detailed analysis. Contours over different panels indicate the umbra-penumbra boundary as obtained from the HMI continuum image.

of Rob Rutten[1]. This tool incorporates standard *aia_prep.pro* and *hmi_prep.pro* routines available in the standard solar software (SSW, Freeland and Handy, 1998), and they also align images from multiple passbands and correct them for any time-dependent shifts.

Active region was also observed by IRIS in 2-step raster mode for more than 4 hours starting from 07:19:13 UT. IRIS provided Slit-Jaw-Images (SJI) in 2796 Å and 1400 Å passbands. IRIS-SJI 2796 Å passband manifests a chromospheric temperature of 10,000 K due to coverage of the Mg II line. However, due to the poor signal in IRIS 1400 Å images, we are not utilizing them in our analysis. Images obtained from the IRIS-SJI 2796 Å passband have an exposure time of 2 s with an effective cadence of 6.88 s, 0.166"/pixel resolution, and a field-of-view of 60"× 65" centered around the sunspot umbra. In the later part of the observation, several data gaps were found. Therefore, we selected only the first 4 hours of continuous data, without any data gaps, to perform our analysis.

[1]https://robrutten.nl/rridl/00-README/sdo-manual.html

Imaging data allows us to co-align data from different instruments, thus allowing us to simultaneously use data from different instruments operating at different wavelengths. We co-aligned IRIS and SDO observations using IRIS-SJI 2796 Å and AIA 1700 Å images using the cross-correlation method. All IRIS, AIA, and HMI images are derotated with respect to time at 07:19:17 UT using the SSW routines. The identified dataset provides a unique opportunity to study the spatial and temporal evolution of waves in the plane-of-sky along the whole solar atmosphere.

Since the observed sunspot is slightly off the disk centre (heliocentric co-ordinates $X \approx -25'', Y \approx -125''$), the angle between vertical and line-of-sight is $\approx 7.7^{\circ}$, which leads to $\mu = cos\theta \approx 0.99$. So, any projection effect on Dopplergram velocity oscillations and other parameters will be almost negligible. In the umbral region, the plasma-$\beta = 1$ layer is below the photosphere ($\tau_{5000} = 1$), and at this layer, fast waves get converted into slow waves (Przybylski et al., 2015), and thus enables us to detect slow waves from the HMI continuum data. We studied the sunspot in AIA 193 Å, AIA 171 Å, AIA 304 Å, IRIS 2796 Å, AIA 1700 Å, and HMI continuum and Dopplergram images manifesting coronal temperature of 1.6 MK, 0.7 MK, transition region temperature of 50,000 K, chromospheric temperature of 10,000 K, temperature minimum region of 5000 K, and photospheric temperature of 6000 K, respectively, covering the different layers of solar atmosphere. Figure 3.1 shows the images of a sunspot observed from different passbands as labelled. It is clear from the images that the analysed sunspot looks quite different at different atmospheric layers, which highlights the complexities involved in its dynamics.

3.2 Data Analysis and Results

Figure 3.2 shows the analysed fan loop structures in AIA 171 Å passband. The overplotted contour represents the umbral boundary of the sunspot obtained from the HMI continuum image at a count of 9000 DN. Asterisks (*) represent the coronal footpoint of fan loops in the AIA 171 Å passband. This location will be further used as a reference while identifying the location of these loops in the lower solar atmosphere, where these loops are not visible. We have identified eight fan loops emanating from the sunspot umbra for our study purposes and labelled them accordingly. Associated coronal loops are also drawn for visualisation purposes only. Properties of slow magnetoacoustic waves prop-

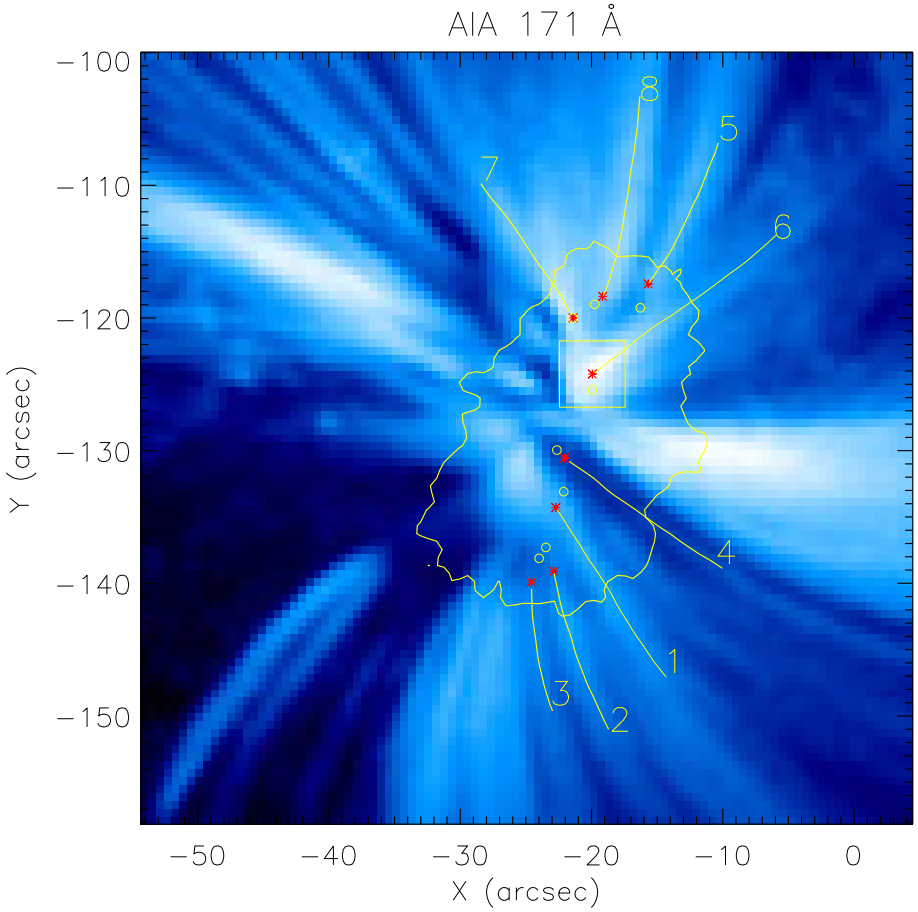

Figure 3.2: Fan loop system observed in AIA 171 Å passband. Identified loop footpoints in the corona and photosphere are marked with asterisks (*) and circles (o), respectively, which are used for detailed analysis. Traced coronal loops are also drawn for visualization purposes only. Contour indicates the umbra-penumbra boundary as obtained from the HMI continuum image. The box enclosing the coronal footpoint of loop 6 indicates the region chosen for image correlation analysis to identify locations of the loop in the lower atmosphere.

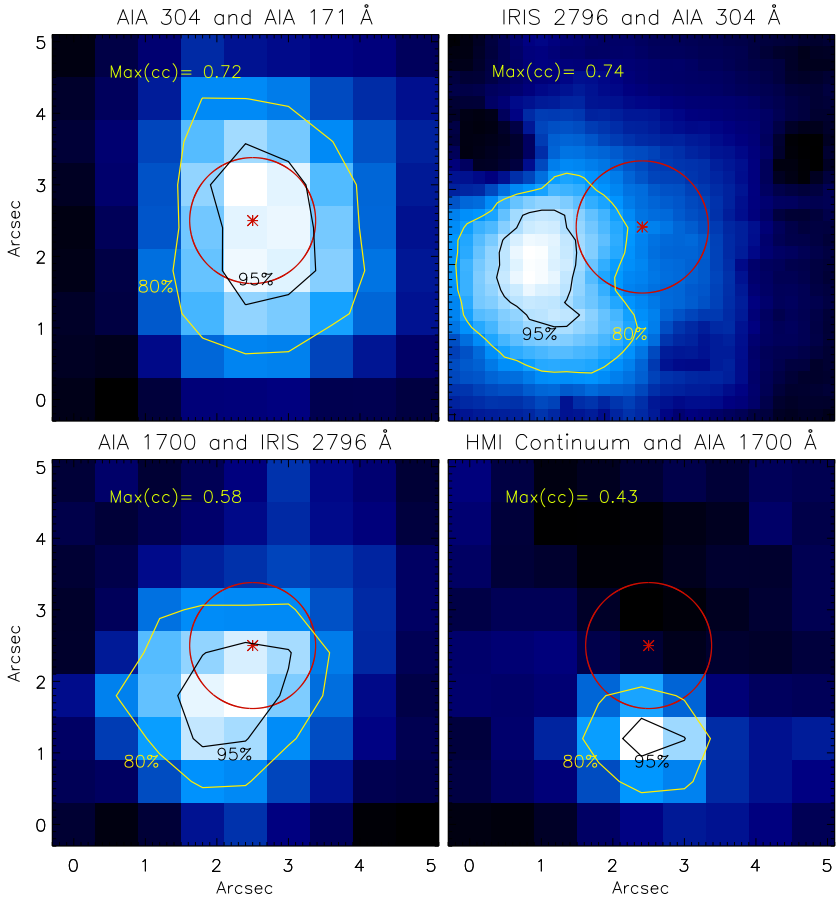

Figure 3.3: Correlation images obtained between various atmospheric heights as labelled. In each panel, the asterisk sign (*) in the centre refers to the coronal footpoint of loop 6. The red circle in all the panels represents the cross-section of the loop obtained from AIA 171 Å image (see details in Section A.1). Overplotted black and yellow colour contours are obtained at ≈ 95% and 80% of maximum correlation values, respectively.

agating along some of these coronal fan loops are described and discussed in Sharma et al. (2020). In this work, we identified loop locations at different atmospheric heights for all the loops. However, here we present results from loop 6 as a representative example. Results from all the other loops are summarized in Section 3.2.4.

3.2.1 Identification of loop locations in the lower atmosphere

To determine the cross-sectional area of the coronal fan loop in AIA 171 Å, we obtained intensity across the coronal footpoint marked by an asterisk sign (*) in Figure 3.2 and its neighbouring pixels. We then fitted the intensity profile with a Gaussian function. We then extracted the full width half maxima (FWHM) of this Gaussian and considered it

as the diameter of the loop at the coronal footpoint $\approx 1.76'' \pm 0.18$ (1.27 ± 0.13 Mm) as described in the Section A.1.

Similarly, for lower heights where the loop is not visible, we perform correlation analysis on the complete 240 min time series to determine the loop location and also its cross-sectional area. Here, we choose a box of size $5'' \times 5''$ by keeping the location of loop 6 in the AIA 171 Å image in the centre as indicated by an asterisk sign (*) in Figure 3.3. To perform the cross-correlation, we utilized 16-min background-subtracted and 1-min smoothed light curves so as to remove any low-frequency background and high-frequency noise from the light curves. This makes correlations depend only on 3-min oscillations and their related variations. We have interpolated the AIA 304 and 1700 Å light curves at the cadence of 6.88 s to match the cadence of IRIS SJI 2796 Å using the IDL routine *interpol* for the purpose of correlation. For the correlation between AIA 1700 Å and HMI continuum light curves, we are utilizing 3-min filtered light curves for both passbands to avoid any influence of 5-min oscillations observed in the HMI continuum. We noted the maximum correlation coefficient at each pixel, and created a cross-correlation image as shown in Figure 3.3. Therefore, the image provides maximum correlation coefficient values at each pixel. It should also be noted that the image appears similar if we utilize 3-min filtered light curves for all the passbands. We obtain a black colour contour over this correlation image at 95% of the maximum correlation value within the image, whereas the red circle represents the cross-section of the loop in the corona as obtained from the AIA 171 Å image. Choice of contour level at 95% of maximum correlation value is obtained by comparing correlation images in the corona with FWHM of loop cross-section as described in the Section A.2.

The central pixel of the black contour in the correlation images of Figure 3.3 depicts the location of the loop at that atmospheric height. This location has been further utilized to identify loop locations at the lower heights from the cross-correlation of light curves as described above. In this way, we are able to trace the same source of 3-min oscillations from the corona to the photosphere. Since these 3-min waves can propagate from the photosphere to the corona only through the waveguide, black contours here represent either a single loop or a collection of loops emanating from the same photospheric oscillating region, and chosen contours depict the loop cross-section at that height. The size of the loop or oscillating region mainly depends on the choice of contour level. Therefore, we also obtained contour levels at 80% of the maximum correlation

value. These contours cover the correlation patches observed in correlation images very nicely, and result in quite broader oscillating regions. However, more importantly, for any choice of contour levels, we find that the size of the coherent oscillating region decreases as we move into the lower atmosphere. This is expected as per the theory of flux tube expansion with height (e.g., Aschwanden, 2004).

Nevertheless, we obtained area of 95% and 80% contour levels in AIA 304 Å, IRIS 2796 Å, AIA 1700 Å, and HMI continuum passbands by visually fitting the contours with either a circle or an ellipse, depending on their shape. Obtained areas are $\approx 2.03 \pm 1.16$ (1.07 ± 0.61), 1.24 ± 0.23 (0.65 ± 0.12), 1.16 ± 0.74 (0.61 ± 0.45), and 0.18 ± 0.32 (0.09 ± 0.16) arcsec^2 (Mm^2), respectively for 95% contour level whereas that for 80% contour levels are $\approx 7.46 \pm 2.09$ (3.92 ± 1.1), 6.78 ± 0.61 (3.56 ± 0.32), 5.45 ± 1.74 (2.86 ± 0.91), and 2.06 ± 1.07 (1.08 ± 0.56) arcsec^2 (Mm^2) respectively. Error bars are calculated by assuming errors on the fitted diameter of a circle (or the length of major and minor axes of the ellipse) to be equal to the resolution limit of AIA (0.6"/pixel) and IRIS (0.166"/pixel). Here, we clearly see the decrease in size of the oscillating region as we move down in the lower atmosphere, as expected from the size of the flux tube with height in the solar atmosphere. In the correlation images of AIA 304 Å, IRIS 2796 Å, AIA 1700 Å, and HMI continuum, we also notice a shift of (0",0"), (1.5",0.5"), (0",0.6") and (0",1.2"), respectively in the central position of black contour with respect to the coronal footpoint located in AIA 171 Å passband. This shift can either be due to the inclination of the loop or due to the alignment errors between AIA, IRIS, and HMI. Moreover, we also notice that the identified loop footpoint at the photosphere is directed towards the umbral centre rather than in any random direction with respect to the coronal footpoint of the loop. This shows that the loop is continuing towards the umbral centre as visualized in Figure 3.2.

After determining the loop locations at different atmospheric heights, we obtained light curves at those locations from the AIA, IRIS, and HMI passbands. We also performed, similar analysis using smaller time series, where we noticed an offset of ± 1 pixel for the maximum correlated pixel in Figure 3.3. Therefore, we obtained light curves from 3×3 pixel^2 binning for all the AIA and HMI passbands. This binning also incorporates alignment uncertainties of about 2 pixels in different AIA passbands (Young et al., 2013), and any lateral shift of loops from the photosphere to corona (Krishna Prasad et al., 2015). Similarly, for IRIS, we are taking 5×5 pixel^2 binning. This

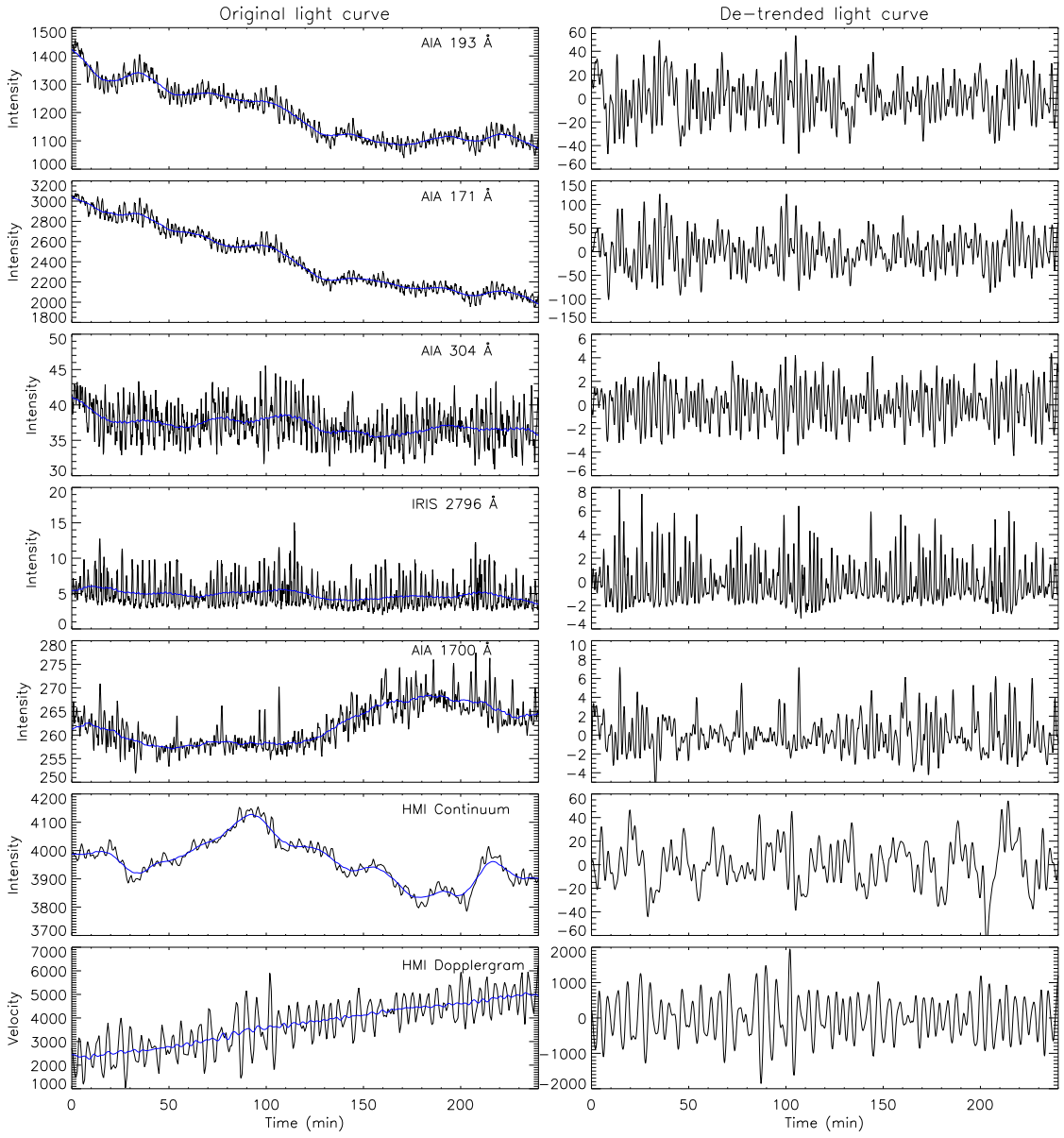

Figure 3.4: The left and right panels show original and background subtracted, smoothed light curves for loop location 6 in AIA 193 Å, AIA 171 Å, AIA 304 Å, IRIS 2796 Å, AIA 1700 Å, HMI continuum, and HMI Dopplergram as labelled. The overplotted blue lines in the left panels show the background trend at each layer of the solar atmosphere of loop location 6.

pixel binning also improves the strength of the signals. In the left panels of Figure 3.4, we plot original light curves obtained at loop locations at various atmospheric heights as labelled. Overplotted blue lines represent the background trends, which were obtained by taking the 16-min running average. In the right panels, we plot 1-min smoothed background-subtracted light curves. Detrended light curves provide clean intensity oscillations without any low-frequency background at all atmospheric layers recorded.

3.2.2 Fourier analysis and filtration

In the left panels of Figure 3.5, we show the Fast Fourier Transform (FFT) power spectrum obtained from the original light curves of loop locations at various atmospheric heights as labelled. The FFT power spectrum is obtained using the standard IDL routine $fft\_powerspectrum$. Plots show a wide distribution of power peaks in the period range of approximately 2-3.74 min at all the atmospheric heights, and also in the range of 4.2-6 min only at the photosphere. The two dominant period ranges are called 3-min and 5-min period bands, and are shaded with light and dark blue colours, respectively, in the left panels of Figure 3.5. There are several nearby power peaks present in both the period bands. Vertical dashed lines represent the dominant peak in the 3-min and 5-min period bands, which are present at all the atmospheric heights and at the photosphere, respectively. We have ignored 3.74-4.2 min period window, which may have arised because of an artefact due to pixel crossing time due to differential rotation of the sunspot (Norton et al., 2021). Details of this artefact is described in Section A.3.

3-min period waves are generally observed in all the layers of the upper sunspot atmosphere (Khomenko and Collados, 2015). Sometimes they are also detected at the photospheric heights, though weaker than the 5-min period (Bellot Rubio et al., 2000). Since we have found significant power in the 3-min period band at every atmospheric height, we will utilize it for further detailed analysis. We apply a bandpass filter over the period range of 2-3.74 min (light blue colour shaded region in Figure 3.5) on the original signals. The filtered signals are shown in the right panel of Figure 3.5. Filtration provides a clean intensity oscillation in the 2-3.74 min period range. Due to several nearby power peaks in this period band, we see oscillations in the form of unclean wave packets. Such wave packets are also reported at several locations along the coronal fan loops by Sharma et al. (2020).

In Figure 3.6, we plot cross-correlation coefficients as a function of time lag obtained

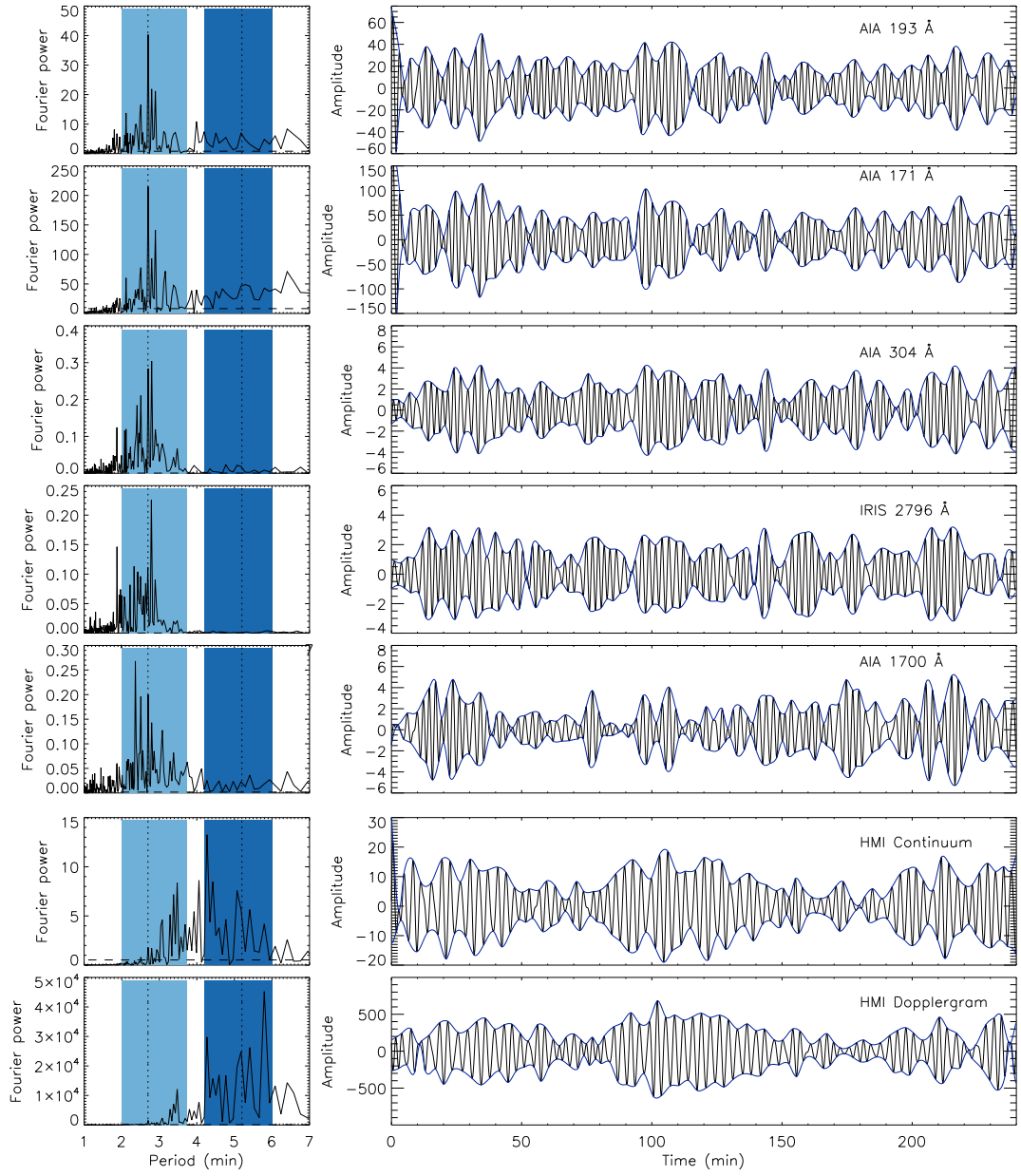

Figure 3.5: Left panels: FFT power spectrum of original light curves obtained at each location of Loop 6 in the solar atmosphere as shown in the left panels of Figure 3.4. Shaded regions in light blue colour denote the 3-min period band used to produce the filtered light curves shown in the right panels. Shaded regions in dark blue colour denote the 5-min period band. Horizontal dashed lines represent 95% significance level. Vertical dashed lines represent the dominant peak in the 3-min and 5-min period bands present at all the atmospheric heights and at the photosphere, respectively. Right panels: 3-min filtered light curves with over-plotted blue lines show amplitude modulation envelopes traced using maxima and minima of respective filtered light curves.

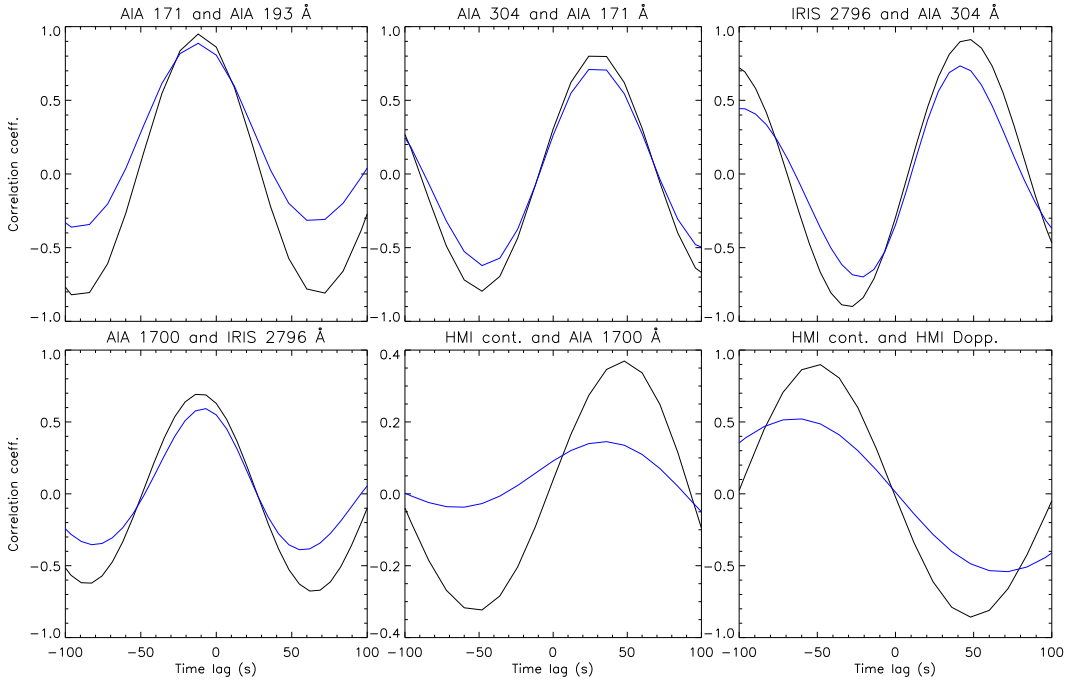

Figure 3.6: Variation of cross-correlation coefficients with respect to time lag obtained between light curves at Loop 6 in different passbands as labelled. Black and blue lines show cross-correlation analysis performed on the Fourier-filtered and background-subtracted light curves, respectively.

between pairs of detrended (right panel of Figure 3.4) and 3-min Fourier-filtered light curves (right panel of Figure 3.5) as labelled with blue and black lines, respectively. Time lags obtained from both the light curves are consistent with each other, except between AIA 1700 Å and HMI continuum pair, where the correlation is very poor due to the presence of 5-min oscillations in the background-subtracted light curve of HMI continuum. Using time lags obtained from filtered light curves and formation heights of various passbands, we determined the propagation speed of these 3-min waves at various heights. These estimated speeds provide lower limits on propagation speeds as

Table 3.1: Correlation values obtained from both background-subtracted (BS) and Fourier-filtered (FF) light curves for Loop 6 between different pairs of atmospheric heights. Wave propagation speeds at different heights are also provided.

Passbands (Å)	Distance (km)	Correlation with BS		Correlation with FF		Adiabatic acoustic speed (km s^{-1})	Obs. speed (km s^{-1})
		Correl. coeff.	Time lag (s)	Correl. coeff.	Time lag (s)		
193-171	–	0.89	-12.0 ± 12.0	0.95	-12.0 ± 12.0	–	–
171-304	102 ± 78.5	0.71	24.0 ± 12.0	0.80	24.0 ± 12.0	81.9±13.5	4.2 ± 3.9
304-2796	158 ± 69	0.73	39.3 ± 6.9	0.91	46.2 ± 6.9	23.8 ±3.6	3.4 ± 1.6
2796-1700	695 ± 46	0.59	-8.9 ± 6.9	0.69	-15.8 ± 6.9	12.2 ±1.8	44 ± 19.4
1700-cont.	167 ± 10	0.14	36.0 ± 12.0	0.37	48.0 ± 12.0	10.5 ±1.5	3.5 ± 0.9
Dopp.-cont.	62 ± 5	0.52	-60.0 ± 12.0	0.90	-48.0 ± 12.0	10.5 ±1.5	1.3 ± 0.3

line-of-sight projection effects are also involved. We have assumed formation heights for these passbands from the umbral atmospheric model of de Oliveira e Silva et al. (2022), which they claimed to be in agreement with Fontenla et al. (1999, 2009) and others. Formation heights for photosphere HMI continuum is at 38 $\pm$1.9 km, HMI Dopplergram 6173.34 Å at 100 ± 5 km, temperature minimum AIA 1700 Å at 205.0 ± 10.25 km, chromosphere IRIS 2796 Å at 900.0 ± 45.0 km, transition region AIA 304 Å at 1058.0 ± 52.9 km, corona AIA 171 Å 1160.0 ± 58.0 km, and AIA 193 Å at 1190.0 ± 59.5 km, see details in Figure A.4 in Section A.4. Estimated wave speeds at various atmospheric heights are provided in Table 3.1. Moreover, within the error bars, propagation speeds obtained in the lower atmosphere from different atmospheric models such as Maltby et al. (1986) and Avrett et al. (2015) are almost similar. Estimated speeds are less than the adiabatic acoustic speed $c_s = \sqrt{\gamma 2 k_b T / \mu m_p}$, where $\gamma = 5/3$ is adiabatic index, k_b is Boltzmann constant, T is temperature, $\mu = 1.27$ is mean molecular weight, m_p mass of proton (e.g., Aschwanden, 2004) at that particular height. This confirms that these are propagating slow magnetoacoustic waves except at chromospheric height, where the speed becomes supersonic. Moreover, it should also be noted that effects of partial ionization in the lower atmosphere can make γ as low as $\gtrsim 1$ (section 4.1, Aschwanden, 2004). However, in this case also the observed propagation speeds will remain mainly subsonic. For the error estimate, we have assumed error in time as the cadence of each passband, which is 12 s and 6.88 s for SDO and IRIS, respectively. Since de Oliveira e Silva et al. (2022) did not provide any method to calculate errors in the formation heights, we have assumed an overall made-up error of 5% in all the formation heights, as we noted $\approx 5\%$ to be the maximum error in height quoted by them.

3.2.3 Wavelet analysis

The above Fourier analysis provided information in the period domain only. Therefore, wavelet analysis is incorporated to obtain the variation of power of these 3-min oscillations with time. Here, we are using the Morlet wavelet for our analysis and utilizing the wavelet tool developed in IDL by Torrence and Compo (1998).

In Figure 3.7, we show the wavelet power spectrum of the filtered light curve of the coronal footpoint of Loop 6 as obtained from AIA 171 Å passband (see right panel of Figure 3.5). The left panel shows the wavelet power spectrum with time on the x-axis and period on the y-axis, showing variation of oscillatory power. Different colour

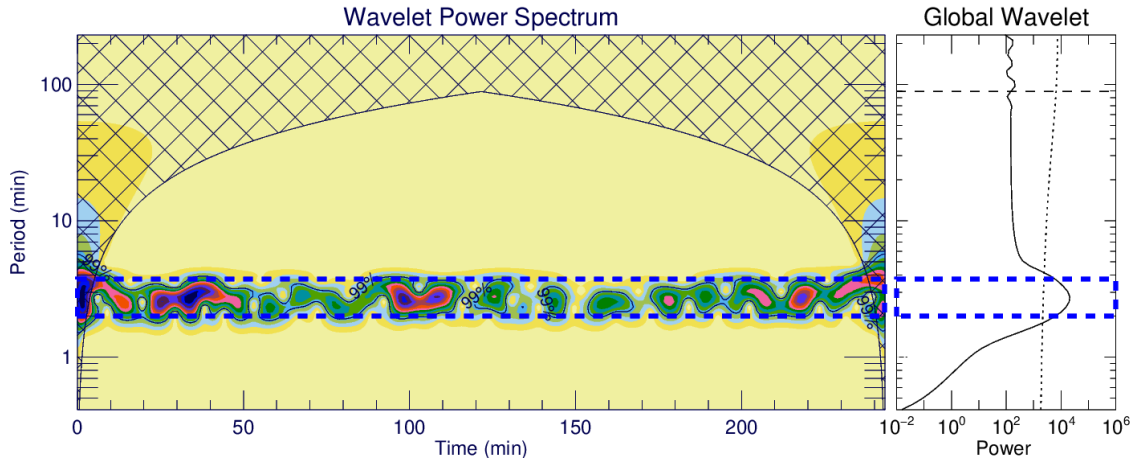

Figure 3.7: The left panel shows the colour-inverted wavelet power spectrum of the filtered light curve of Loop 6 coronal footpoint obtained from AIA 171 Å passband with 99% confidence-level contours. The region marked with crossed lines denotes the cone of influence. The right panel shows the global wavelet power spectrum obtained by averaging the wavelet power spectrum over time. The thin dashed lines specify the maximum period detectable from wavelet analysis because of the cone-of-influence, and the dotted line specifies the 99% confidence level curve. The overplotted blue colour rectangular boxes denote the period window extracted for detailed analysis. The time axis starts at 7:19 UT.

contours show varying power densities, with blue being the highest. Here, the region marked with crossed lines is called the Cone-of-Influence (COI), which refers to the region where the transform suffers from the edge effect. Oscillation periods in this region are unreliable. In the right panel of Figure 3.7, we show the global wavelet power spectrum, which is obtained by taking the average over the time domain of the wavelet transform. The thin dashed line shows the maximum period detectable from the wavelet analysis due to the COI.

The overplotted blue rectangular box shows a 2-3.74 min period window in the wavelet and global wavelet power spectrum. This period window will be utilized to extract more detailed properties of 3-min waves. We are extracting amplitude modulations of 3-min waves from this rectangular box and describe them in the following subsections.

3.2.4 Modulations

In the left panel of Figure 3.5, we can see many closely spaced frequencies in the 3-min period band, which results in amplitude modulation of the signal as shown in the right panel of Figure 3.5. In Figure 3.7, we can see that the oscillatory power is not constant

but changes with time. Using these properties of 3-min waves, we explore the source region of these waves in the lower atmosphere, and thus the magnetic connectivity of the solar atmosphere.

3.2.4.1 Amplitude modulation

To determine the modulation of the amplitude of these 3-min waves, we extracted the wavelet power in the 2-3.74 min window as shown by the blue box in the left panel of Figure 3.7. We then averaged the extracted window over the period and thus obtained amplitude variations (square root of wavelet power) with time for all the light curves at different atmospheric heights. We also devised another method in which we identified the local maxima and minima of the filtered light curves using the IDL routine *extrema* to trace the amplitude modulation envelopes. Obtained amplitude modulations with time from wavelet and extrema (-maxima) methods are plotted in the left panels of Figure 3.8 with black and blue colour lines, respectively, for all the atmospheric heights as labelled. We cross-correlated all the amplitude modulations obtained at different atmospheric heights with the nearest atmospheric layers. Amplitude modulation correlations obtained from wavelet, and extrema- maxima and minima are plotted in black, green, and blue colour lines, respectively, in Figure 3.9. Time lags obtained from the wavelet and extrema (-maxima and -minima) methods match well with the time lags obtained in Figure 3.6 within the error bar. However, with an exception for HMI-continuum and AIA 1700 Å pair, where the time lag of amplitude modulation matches well with the time lag of the second peak of the 3-min correlation curve at 228 s, which has a higher correlation value compared to the first peak at 48 s. Moreover, the correlation value decreases if we correlate the amplitude modulation curves from neighbouring pixels, and thus supports the robustness of our loop tracing. Correlated 3-min amplitude modulations at different atmospheric heights clearly indicate that these waves originate in the lower atmosphere, and different atmospheric heights are coupled together. Thus, it provides clear evidence of magnetic connectivity of the whole solar atmosphere.

Further, to check the periods of amplitude modulation, we obtained the FFT power spectrum of amplitude modulations and plotted them in the right panels of Figure 3.8. Here we can clearly see that dominant amplitude modulation periods are approximately in the range of 9–14 min, 20–24 min, and 30–40 min and are present at all the layers of the solar atmosphere as shown by shaded regions in the right panels of Figure 3.8. These

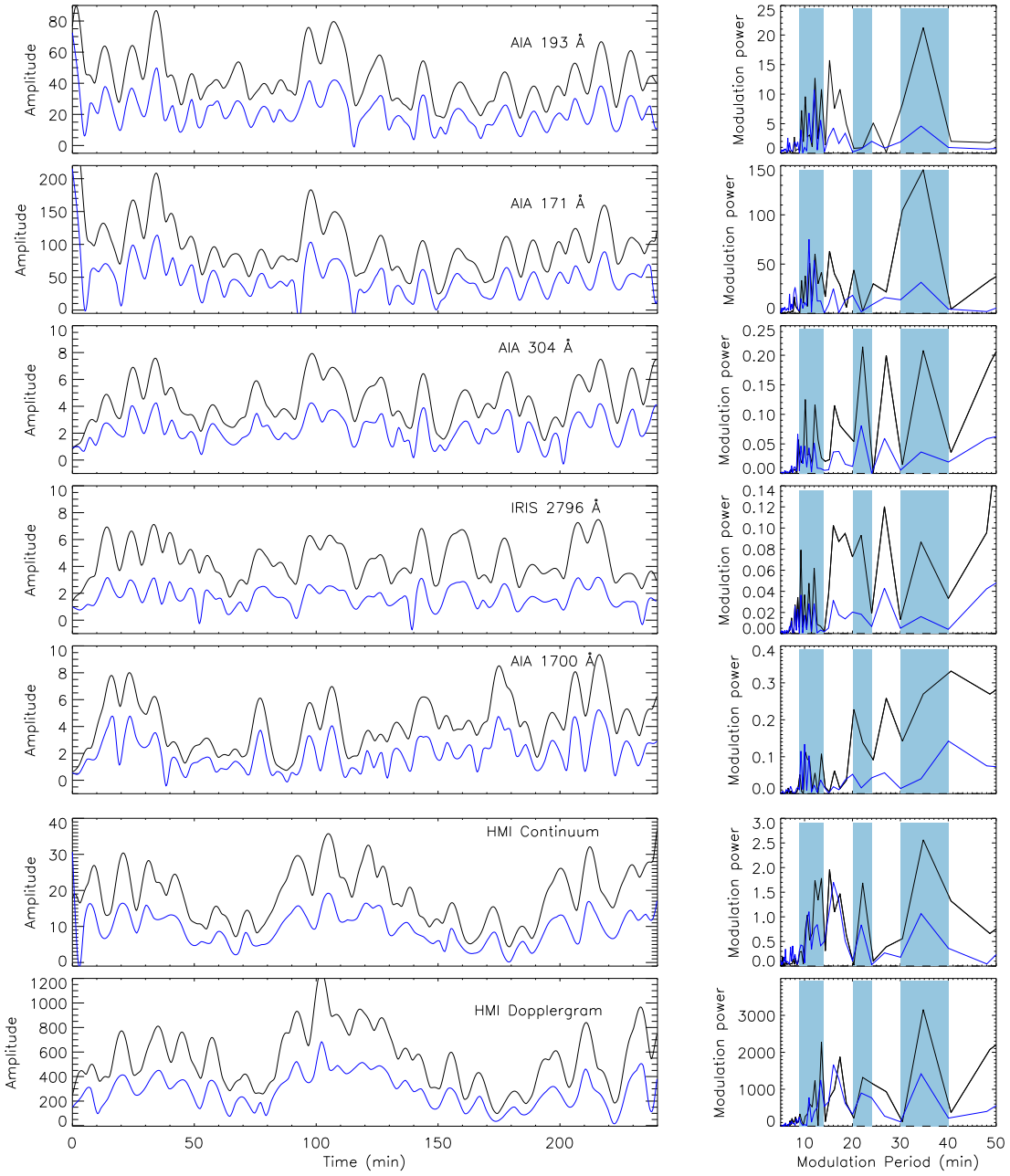

Figure 3.8: Left panels show the amplitude modulations of 3-min oscillations. Black and blue colour lines show amplitude modulations extracted from the wavelet spectrum and extrema (maxima) of all 3-min filtered light curves shown in Figure 3.5, respectively. The right panels show the FFT power spectrum of the corresponding amplitude modulations. Shaded regions in sky blue colour highlight dominant modulation periods observed at different atmospheric heights.

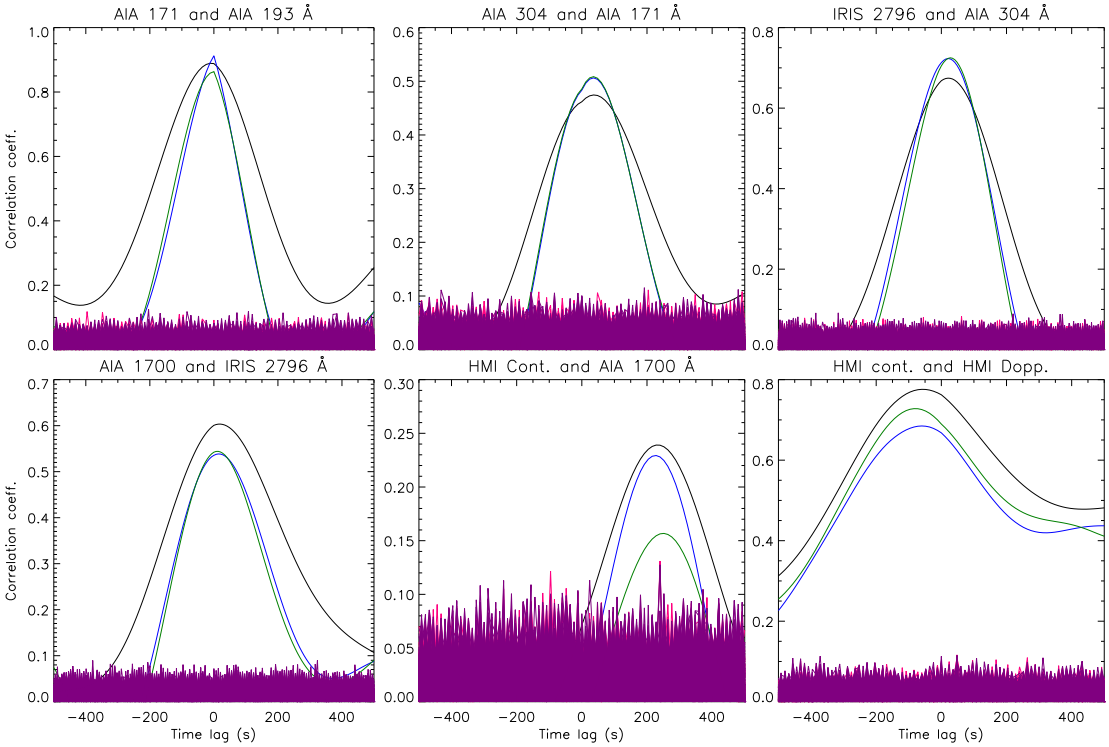

Figure 3.9: The black, green, and blue coloured lines show correlation coefficients with respect to time lag between amplitude modulation curves obtained from wavelet, maxima, and minima, respectively, at different atmospheric heights as labelled and shown in the left panel of Figure 3.8. Pink and purple colour lines are obtained by carrying out correlation analysis on randomized amplitude modulation curves from wavelet and maxima curves, respectively (see details in Section A.5).

modulations are formed due to the various combinations of closely spaced power peaks present within the 3-min period band. Some of the dominant periods present within this band are 2.51 min (6.64 mHz), 2.7 min (6.17 mHz), 2.8 min (5.95 mHz), 3.08 min (5.41 mHz), etc. Combinations of these periods, like 2.51 and 2.7 min, 2.7 and 3.08 min, 2.8 and 3.08 min, 2.7 and 2.51 min, etc., can result in beat periods of 35.67 min, 21.88 min, 30.80 min, 10.59 min, etc., respectively. These derived beat periods are within the range of observed modulation periods, as noted above, at all the layers of the solar atmosphere. The presence of similar modulation periods at all the heights signifies that modulations of 3-min waves are essentially coupled to each other at different atmospheric layers, as also found from the correlation analysis. Thus, the result provides clear evidence of upward propagating waves from the photosphere to the corona along the observed fan loop at different atmospheric heights.

3.2.4.2 Frequency modulations

To determine the frequency modulation of 3-min waves, we first obtained the wavelet power spectrum of background-subtracted light curves for all the passbands. We then smoothed the wavelet spectrum by applying a running average of 7-point on time and 3-point on period axes. From this smoothened wavelet spectrum, we extracted the 2-3.8 min period window. With this subset, we further extract the period at which power is maximum at each time frame. Following the same procedure, we obtained a period or frequency variation of 3-min oscillation with time at all the atmospheric heights. Obtained period variations with time (i.e., frequency modulations) are plotted in the left panels of Figure 3.10 for all the passbands as labelled. We also obtained the FFT power spectrum of frequency modulations and plotted it in the right panels of Figure 3.10. Here, we can see that dominant 3-min frequency modulation periods are approximately in the range 14-20 min and 24-35 min, which are present at all the layers of the solar atmosphere. These modulation periods are shown as shaded regions in the right panel of Figure 3.10. This similarity in modulation periods signifies that 3-min oscillations are essentially coupled together at different atmospheric layers. Thus, provides clear evidence of upward propagating waves from the photosphere to the corona along the observed fan loop locations. We also noticed that power peaks within the 24-35 min shaded region are shifting towards the left for coronal heights. However, these shifts are within the error range and demand high-frequency resolution data to deduce any such shifts in modulation periods. We also cross-correlated the frequency modulation curves obtained at different atmospheric heights with the nearest atmospheric layers. These correlation curves are plotted in Figure 3.11. Correlations between different height pairs follow a similar pattern as obtained from amplitude modulations, but correlation values are smaller. Especially, for pairs of AIA 1700 Å and HMI continuum, and HMI continuum and Dopplergram, correlations are poor and within the error range, whereas for the IRIS 2796 and AIA 1700 Å pair, correlation is weak but crosses the error range. Therefore, correlation analysis between frequency modulation curves provides evidence of magnetic connectivity of the solar atmosphere from the temperature minimum region (AIA 1700 Å) to the corona (AIA 171 and 193 Å). However, all the frequency modulation curves show similar modulation periods. Together, these findings provide clear evidence of magnetic connectivity of the whole solar atmosphere. Further to check the reliability of correlation coefficient values, we performed randomization boot-strap analysis (see

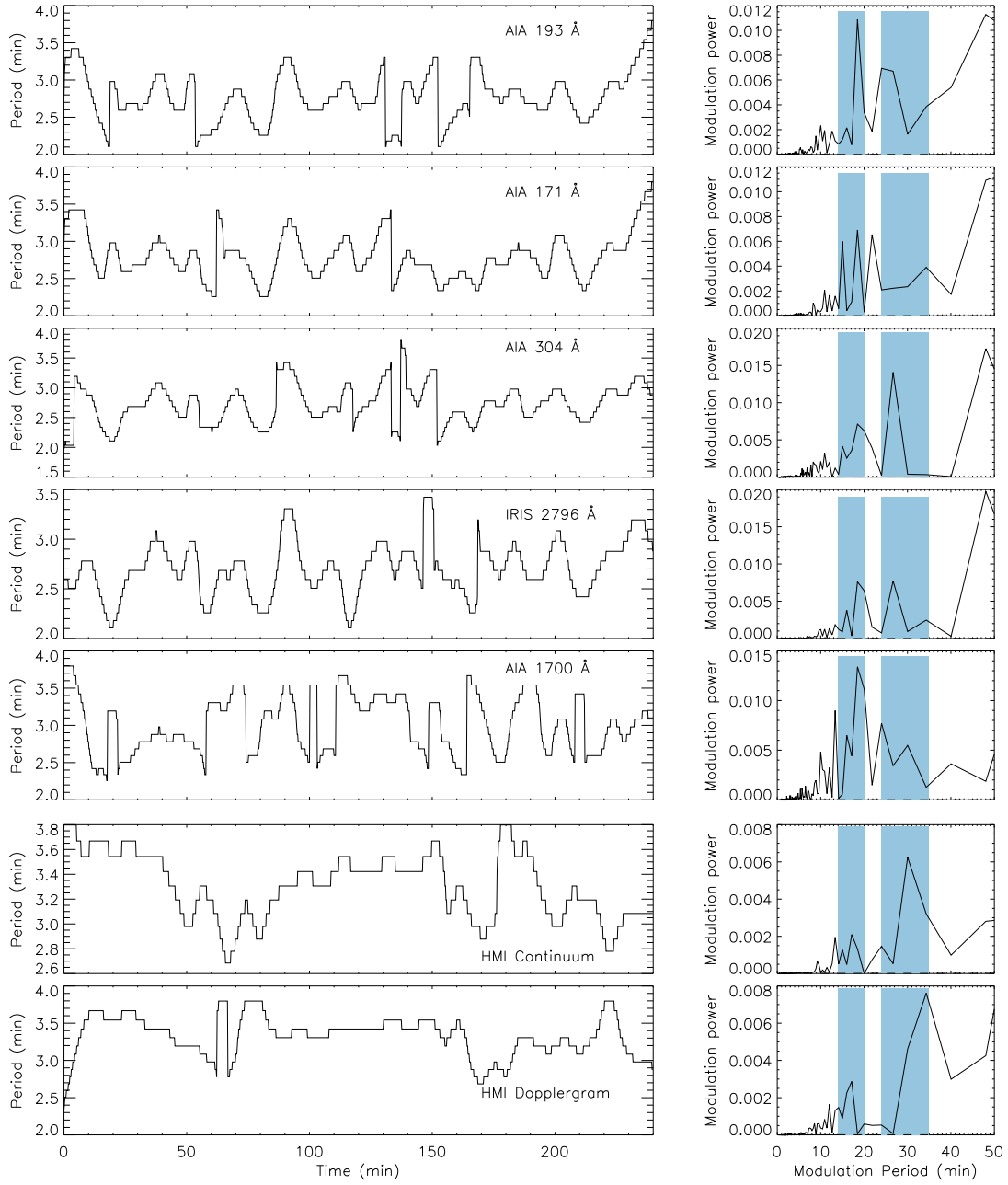

Figure 3.10: Left panels show frequency modulations of 3-min oscillations extracted from the wavelet spectrum for different passbands as labelled. The right panels show the FFT power spectrum of the corresponding frequency modulation curves. Shaded regions in sky blue colour highlight dominant modulation periods observed at different atmospheric heights.

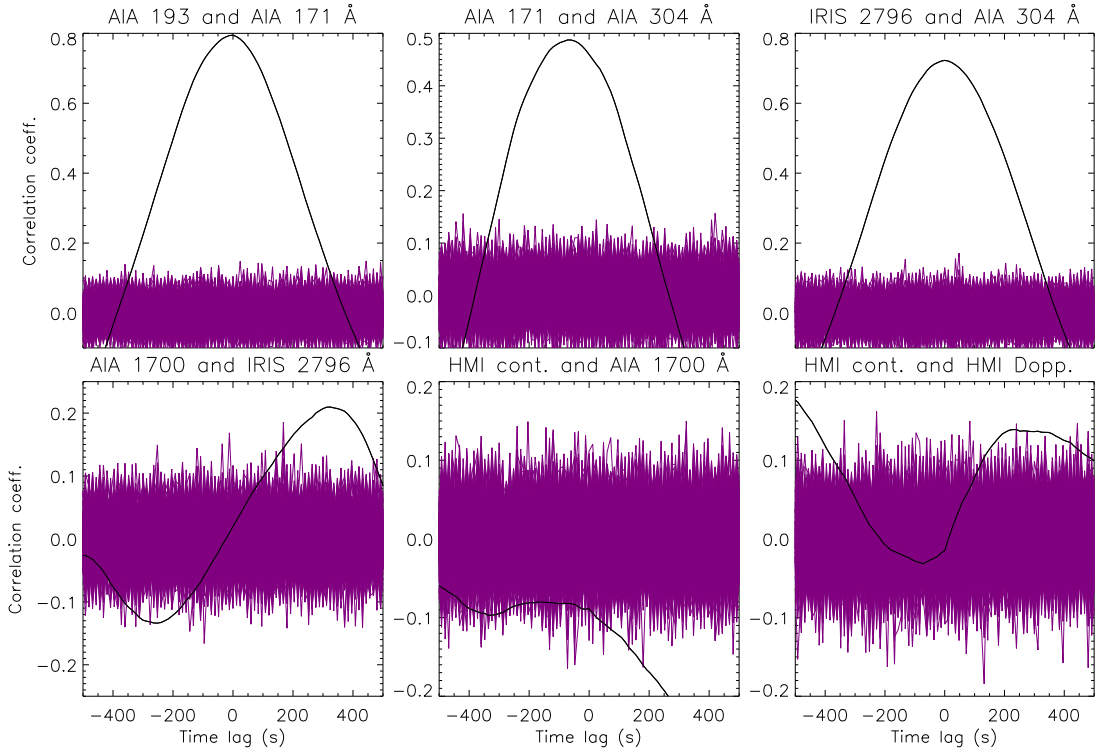

Figure 3.11: Correlation coefficients at different time lags obtained between frequency modulation curves for different atmospheric heights as shown in the left panel of Figure 3.10. Purple colour lines are obtained by carrying out correlation analysis on randomized frequency modulation curves.

details in Section A.5). In Figure 3.11, we clearly see that correlation values are either above or below the error range provided by the bootstrap analysis. We also noticed that the correlation between modulation curves decreases as we move into the lower atmosphere, but values are still outside the error range. This implies that modulations from upper heights are correlated with modulations from lower heights. Henceforth, we can clearly interpret that 3-min oscillations and thus frequency modulations originate at the photosphere, and move upward as waves.

3.2.4.3 Relation between modulations of 3- and 5-min oscillations at the photosphere

As evident from the FFT power spectrum obtained from the HMI continuum and Dopplergram curves in Figure 3.5, both 3-min and 5-min oscillations are present at the photosphere. Therefore, we also obtain amplitude and frequency modulations of 5-min oscillations at the photosphere to explore any relation between the two oscillations. In Figure 3.12, we plot amplitude modulation of 5-min oscillation as labelled, and their respective FFT power spectrum. From the plots, we can clearly see that dominant am-

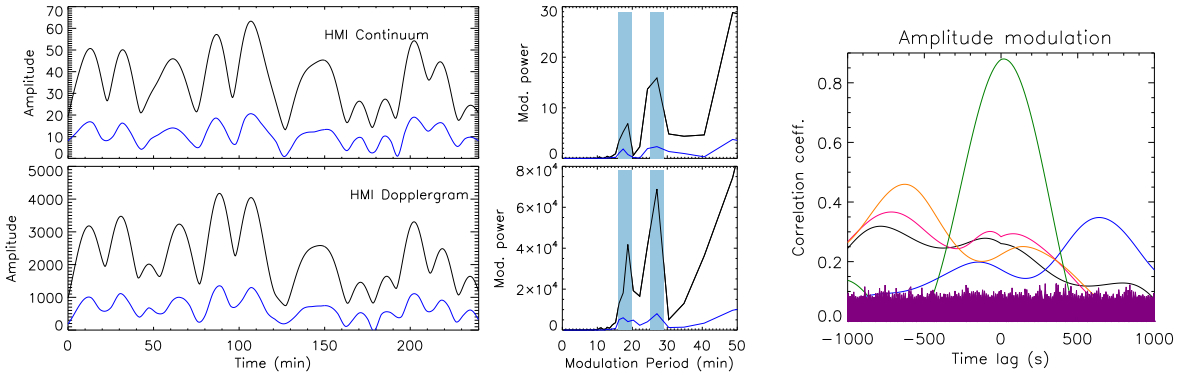

Figure 3.12: Left: The amplitude modulation of 5-min oscillations on the photosphere (HMI continuum and Dopplergram) as labelled. Black and blue colour lines show modulations extracted from the wavelet spectrum and extrema of 5-min filtered light curves, respectively. Middle: The FFT power spectrum of the corresponding modulations. Shaded regions in sky blue colour highlight dominant modulation periods observed in different HMI passbands. Right: Correlations between amplitude modulation curves of 3-min and 5-min oscillations obtained from maxima with respect to time lag. Orange, black, pink, blue, and green colour lines show correlations obtained between Fourier filtered curves of 3-min and 5-min period windows obtained from HMI Dopplergram, 3-min and 5-min period windows obtained from HMI continuum, 3-min window of continuum and 5-min window of Dopplergram, 5-min window of continuum and 3-min window of Dopplergram, and 5-min window of continuum and 5-min window of Dopplergram, respectively. Purple colour lines are obtained by carrying out correlation analysis on respective randomized modulation curves (see details in Section A.5).

plitude modulation periods are in the range of 16–20 and 25–29 min, as shown by shaded regions in the right panels. On comparing it with modulations of 3-min oscillations in Figure 3.8, we notice that one of the dominant short-period ($\approx$ 12 min) modulations for 3-min oscillations present at all heights is not present in the modulations of 5-min oscillations. However, other longer periods, such as 20 min band and above, are present in both modulations. This indicates that 5-min oscillations are unable to capture small time-scale modulations as found in the modulations of 3-min oscillations. We also noticed that 27 min period detected in the amplitude modulation of 5-min oscillations at the photosphere is not present in the amplitude modulation of 3-min oscillations at the photosphere. However, it can be observed at the chromosphere (AIA 1700 Å and IRIS 2796 Å) and transition region (AIA 304 Å). This may indicate that amplitude modulations observed in 5-min oscillations are also propagating upward through 3-min oscillations. Therefore, we further carried out a correlation analysis to verify any coupling between these modulations.

In Figure 3.12, we plot the correlation coefficient with respect to time lag obtained

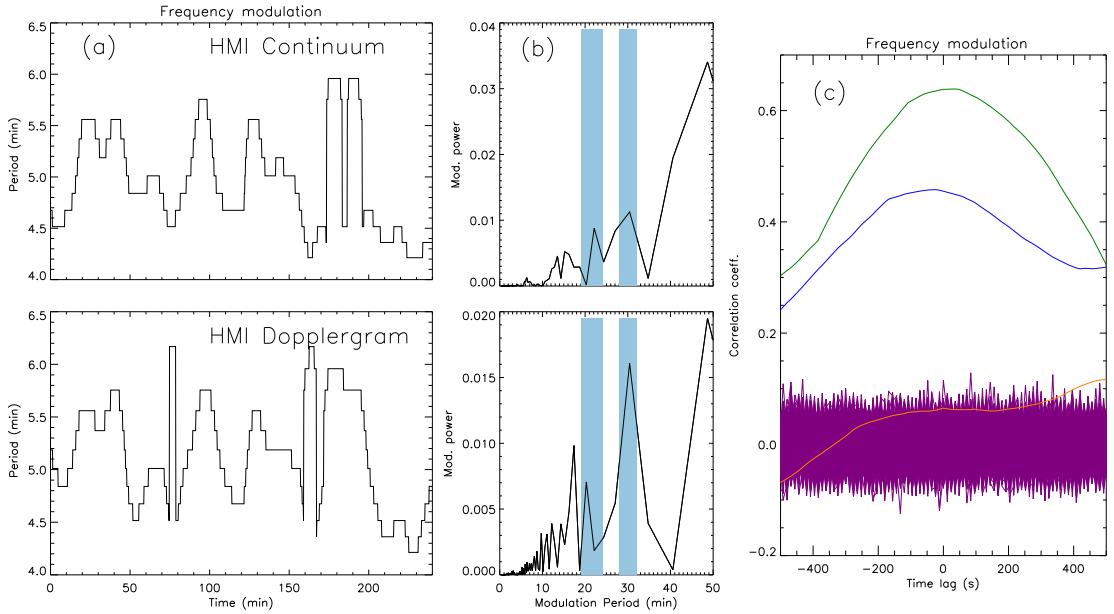

Figure 3.13: (a) Frequency modulations of 5-min oscillations at the photosphere obtained from HMI continuum and Dopplergram as labelled. (b) The FFT power spectrum of the corresponding modulations. Shaded regions in sky blue colour highlight dominant modulation periods observed in different HMI passbands. (c) Correlations with respect to time lags obtained between frequency modulations of 3-min and 5-min oscillations. Green, blue, and orange colour lines show correlations obtained between frequency modulation curves of 5-min oscillations from HMI continuum and Dopplergram, modulations of 3-min and 5-min oscillations from HMI continuum, and modulations of 3-min and 5-min oscillations from HMI Dopplergram, respectively. Purple colour lines are obtained by carrying out correlation analysis on respective randomized modulation curves.

between amplitude modulations of 3-min and 5-min oscillations observed from HMI continuum and Dopplergram as labelled. The maximum correlation coefficient between the amplitude modulation of 5-min and 3-min oscillations from the HMI Dopplergram is about 0.46, with a time lag of -624 s. Similarly, the corresponding amplitude modulation correlation obtained from the HMI continuum is about 0.35 with a time lag of -780 s. Although these correlation values are reasonable, the large time lags obtained between 3-min and 5-min oscillations are unclear and demand a dedicated investigation.

We also obtained frequency modulation of 5-min oscillations at the photosphere to examine any relation between the two oscillations. To determine this, we performed a similar wavelet analysis by selecting the period window between 4.1–6.2 min. In Figure 3.13, we plot frequency modulations of 5-min oscillations as labelled (panel a), and their respective FFT power spectrum (panel b). From the plots, we clearly see power

peaks between 19-24 min, and 28-32 min periods, which are shown as shaded regions from both HMI continuum and Dopplergram as labelled. We also notice a weak frequency modulation period of around 16-17 min in both the passbands. Correlation between frequency modulations from both the HMI passbands for 5-min oscillations is about 0.64 with a time lag of ≈24 s, as shown with the green line in Figure 3.13. On comparing frequency modulation periods of both 3-min and 5-min oscillations from Figure 3.10 and Figure 3.13, we find that longer frequency modulation periods above 25 min and weaker modulation periods around 16-17 min are present in both the oscillations. Therefore, we further carry out correlation analysis to verify any coupling between these frequency modulations, and thus any coupling between 3-min and 5-min oscillations.

In Figure 3.13, we plot correlation coefficients with respect to time lags obtained between frequency modulations of 3-min and 5-min oscillations observed from HMI continuum and Dopplergram as labelled. Maximum correlation coefficients between modulations of 3-min and 5-min oscillations from HMI continuum data is about 0.46 with a time lag of ≈ -24 s, whereas corresponding correlations obtained from HMI Dopplergram data is very small and within the error range. Here again, the error range is obtained from randomization bootstrap analysis as before. Therefore, these correlation values indicate a poor or weak connection between 3-min and 5-min oscillations at the photosphere. Henceforth, any connection between them at the photosphere is still unclear, as also noticed by amplitude modulation, and thus demands a dedicated study to explore their connection in detail.

In Figure 3.9, we can clearly see that correlation values are above the error range provided by the randomization test (see details in Section A.5). This implies that the amplitude modulation time series of upper height is clearly correlated to the time series of lower height. Hence, we can say that 3-min amplitude modulation originated at the photosphere and is moving upward as waves move upward. Furthermore, we also carried out analysis as described in Krishna Prasad et al. (2015) by taking the same pixel-to-pixel correspondence of the loop locations at different heights. Although our findings remain similar, correlation values obtained between the light curves and amplitude modulation curves at different heights were less than our maximum correlation values. This is expected as we are maximizing our correlation by shifting the loop location to the maximum correlated pixel location in the neighbourhood at different heights.

We performed a similar analysis on the other seven fan loops identified in Figure 3.2. Here, also, loop footpoints at the photosphere are directed towards the umbral center, and their oscillating regions are smaller with respect to their coronal counterpart as found for Loop 6. Estimated wave propagation speeds and correlation coefficients at various atmospheric heights for all the loops are provided in Table 3.2, Table 3.3, Table 3.4 and Table 3.5. Estimated speeds are less than the acoustic speeds at that particular height, which confirms that these are propagating slow magnetoacoustic waves except at chromospheric height, as also found for Loop 6 (see Table 3.1). Within the error bar, propagation speed increases with height, which essentially reflects the increase in acoustic speed due to the increase in temperature with height. We assumed the error in the time lag to be the cadence of the passband pairs. Therefore, small time lags result in large uncertainties in the time lags and, consequently, in speeds, which are approximately 50% or more in several passband pairs. Therefore, these propagation speeds should be taken with caution due to the large error bars and the strong inclination effects along the loops, as visible in Figure 3.1 and Figure 3.2. Summary of amplitude and frequency modulation periods of 3-min and 5-min oscillations at various atmospheric heights for all the loops are provided in Table 3.6, Table 3.7, Table 3.8, and Table 3.9. Obtained modulation periods are in the range of 10-40 min, similar to those in Loop 6. Some of the common amplitude modulation periods found in all the fan loops are in the range of 12-14, 20-22, 27-30, and 35-40 min. Frequency modulation periods are also in the range of 14-20, and 24-35 min throughout the photosphere to the corona along fan loops. All the fan loops show at least one common modulation period, which is observed at all the atmospheric heights. We also found a similar pattern in the correlation of modulations between various atmospheric heights as for Loop 6. Correlations become poor at heights where atmospheric parameters change drastically, as also found for Loop 6. The obtained results suggest more or less similar statistics near the footpoints of these loops at various atmospheric heights. Such similarity in behaviour of fan loops emanating from the same sunspot umbra is expected, as also noted by de Moortel (2009). Obtained results confirm that 3-min waves observed in coronal fan loops originate at the photosphere and are propagating upward as they have at least one common modulation period at each atmospheric height (e.g., Krishna Prasad et al., 2015). We also find several common modulation periods between amplitude and frequency modulations at all atmospheric heights, which implies that these modulations are also

Table 3.2: Correlation coefficient values and corresponding time lags obtained from Fourier-filtered light curve pairs for all the loops. Wave propagation speeds at different heights are also provided.

Passbands (Å)	Loop 1			Loop 2		
	Corr. coeff.	Time lag (s)	Speed (km s^{-1})	Corr. coeff.	Time lag (s)	Speed (km s^{-1})
193-171	0.53	-12.0±12.0	–	0.96	0.0 ±12.0	–
171-304	0.60	0.0 ±12.0	–	0.93	12.0 ±12.0	8.5 ±10.7
304-2796	0.82	32.4 ±6.9	4.9 ±2.9	0.86	59.9 ±6.9	2.6 ±1.2
2796-1700	0.65	-15.8 ±6.9	44.0 ±19.4	0.70	-15.8 ±6.9	44.0 ±19.4
1700-cont.	0.34	48.0 ±12.0	3.5±0.9	0.41	24.0 ±12.0	6.96 ±3.51
Dopp.-cont.	0.37	-48.0 ±12.0	1.29 ±0.33	0.61	-72.0 ±12.0	0.86 ±0.16

Table 3.3: Same as Table 3.2.

Passbands (Å)	Loop 3			Loop 4		
	Corr. coeff.	Time lag (s)	Speed (km s^{-1})	Corr. coeff.	Time lag (s)	Speed (km s^{-1})
193-171	0.94	0.0 ±12.0	–	0.87	0.0 ±12.0	–
171-304	0.95	12.0 ±12.0	8.5 ±10.7	0.70	24.0 ±12.0	4.2 ±3.9
304-2796	0.82	53.0 ±6.9	3.0 ±1.37	0.70	32.4 ±6.9	4.9 ±2.9
2796-1700	0.69	-8.9 ±6.9	78.0 ±60.7	0.77	-8.9 ±6.9	78.0 ±60.7
1700-cont.	0.43	12.0 ±12.0	13.92 ±13.92	0.24	24.0 ±12.0	6.96±3.51
Dopp.-cont.	0.47	2352 ±12	–	0.75	-48.0 ±12.0	1.29 ±0.33

connected to each other. Results presented here provide clear evidence of magnetic connectivity of the whole solar atmosphere.

3.3 Discussion and Summary

In this work, we traced coronal fan loops from the corona to the photosphere in the sunspot umbra. Jess et al. (2012a) found that coronal fan loops are anchored at the photosphere where umbral dots are located. Şahin et al. (2019) also noticed that bright loops rooted in the sunspot are a result of light bridge and umbral dots activities. However, in our observation, due to the limited spatial resolution of the photospheric dataset (HMI continuum), we could not verify whether identified photospheric footpoints of fan loops

Table 3.4: Same as Table 3.2.

Passbands (Å)	Loop 5			Loop 6		
	Corr. coeff.	Time lag (s)	Speed (km s^{-1})	Corr. coeff.	Time lag (s)	Speed (km s^{-1})
193-171	0.95	-12.0 ±12.0	–	0.95	-12.0 ±12.0	–
171-304	0.87	12.0 ±12.0	8.5 ±10.7	0.80	24.0 ±12.0	4.2 ±3.9
304-2796	0.82	46.2 ±6.9	3.4±1.6	0.91	46.2 ±6.9	3.4 ±1.6
2796-1700	0.78	-15.8 ±6.9	44.0±19.4	0.69	-15.8 ±6.9	44.0 ±19.4
1700-cont.	0.47	60.0 ±12.0	2.8±0.5	0.37	48.0 ±12.0	3.5±0.9
Dopp.-cont.	0.74	-48.0 ±12.0	1.3 ±0.3	0.90	-48.0 ±12.0	1.3 ±0.3

Table 3.5: Same as Table 3.2.

Passbands (Å)	Loop 7			Loop 8		
	Corr. coeff.	Time lag (s)	Speed (km s^{-1})	Corr. coeff.	Time lag (s)	Speed (km s^{-1})
193-171	0.97	0.0 ±12.0	–	0.94	0.0 ±12.0	–
171-304	0.86	12.0 ±12.0	8.5 ±10.7	0.92	12.0 ±12.0	8.5 ±10.7
304-2796	0.90	53.0 ±6.9	3.0 ±1.4	0.90	46.2 ±6.9	3.4±1.4
2796-1700	0.81	-15.8 ±6.9	44.0 ±19.4	0.87	-15.8 ±6.9	44.0±19.4
1700-cont.	0.49	60.0 ± 12.0	2.8±0.5	0.46	48.0 ±12.0	3.5±0.9
Dopp.-cont.	0.80	−48.0 ± 12.0	1.3±0.3	0.80	-48.0 ±12.0	1.3 ±0.3

Table 3.6: Amplitude modulation periods (min) of 3-min oscillations observed in various fan loop locations at different atmospheric heights as marked in Figure 3.1 and Figure 3.2.

Passbands (Å)	Loop 1	Loop 2	Loop 3	Loop 4	Loop 5	Loop 6	Loop 7	Loop 8
AIA 193	23,30	12,15,27,35	15,30	13,16,24	14,19,27,40	12,15,35	13,18,40	14,20,27,35
AIA 171	12,22,40	12,15,27,35	16,30	13,16,24	14,19,27	12,21,35	13,18,40	15,20,27,35
AIA 304	14,20,40	16,21,31	16,30	13,16,24,34	14,18,30,40	12,22,27,34	14,27,40	16,20,27,35
IRIS 2796	12,19,30,40	16,20,34	12,16,31	13,20,34	10,22,27	12,22,27,34	14,20,34	16,20,35
AIA 1700	13,16,20,24	16,22,35	16,22,35	14,17,35	10,22,40	13,20,27,40	14,20,37	16,20,35
HMI continuum	12,21,25,35	15,27,35	15,27,35	17,22,30	22,40	13,22,35	13,27	12,20,35
HMI Dopplergram	14,21,40	15,22,27,40	16,27,40	17,22,30	20,40	13,22,35	13,30	11,20,35

Table 3.7: Amplitude modulation periods (min) of 5-min oscillations observed in various fan loop locations at the photosphere as marked in Figure 3.1 and Figure 3.2.

Passbands (Å)	Loop 1	Loop 2	Loop 3	Loop 4	Loop 5	Loop 6	Loop 7	Loop 8
HMI continuum	23,41	22,35	17,35	20,30	23,40	18,27	27,50	27,48
HMI Dopplergram	17,23,41	22,41	17,22,40	20,35	23,48	17,27	27,50	27,48

Table 3.8: Frequency modulation periods (min) of 3-min oscillation observed in various fan loop footpoints marked in Figure 3.2 at different atmospheric heights.

Passbands (Å)	Loop 1	Loop 2	Loop 3	Loop 4	Loop 5	Loop 6	Loop 7	Loop 8
AIA 193	11,17,27	16,21,34	17,22,27	12,16,22	19,22	9,18,35	13,24,35	15,24,35
AIA 171	10,19,24	18,22,35	16,22,27	17,25,30	19,22	11,18,35	15,22,35	15,22,35
AIA 304	11,22,35	18,22,30	14,22,27	16,22	13,22	11,18,27	15,20,35	15,20,35
IRIS 2796	16,22,36	16,19,23	16,25,32	16,22,35	13,20	11,19,28	16,21,35	16,21,35
AIA 1700	15,23,34	16,22,30	17,22,27	13,20,35	11,19	10,18,27	15,20,27	15,20,27
HMI Doppler	13,18,34	15,22,27	15,18,24	16,30	11,22	12,21,27	20,35	20,35
HMI continumm	13,20,35	20,24,34	13,22,35	24,34	9,20	12,19,27	16,19,35	16,19,35

Table 3.9: Frequency modulation periods (min) of 5-min oscillations observed in various fan loop locations at the photosphere as marked in Figure 3.1.

Passbands (Å)	Loop 1	Loop 2	Loop 3	Loop 4	Loop 5	Loop 6	Loop 7	Loop 8
HMI continuum	30, 41	27	24, 31	22, 35	27, 35	22, 30	19, 27	24, 30
HMI Dopplergram	27, 41	40	19, 23	24, 35	17, 26	20, 30	27, 35	24, 30

are umbral dots as the diameter of these dots varies from 0.2" to 0.8" (Jess et al., 2012a; Yadav and Mathew, 2018).

We also obtained the area of the oscillating region at various atmospheric heights using the contour levels. We surmise that these areas translate to cross-sectional areas of fan loops at different heights (see Figure 3.3). However, caution must be taken while selecting contour levels, which vary among different loops. Here, area of oscillating region decreased from $\approx 2.43 \pm 1.17$ arcsec^2 (8.24 ± 2.14 arcsec^2) in the corona to $\approx 0.18 \pm 1.77$ arcsec^2 (2.06 ± 1.07 arcsec^2) at the photosphere for 95% (80%) contour level. Expansion of the oscillating region, which may be associated with expansion of the flux tube with height, is expected in the solar atmosphere because pressure inside and outside of the flux tube changes differently with height (see details in Aschwanden, 2004). Such expansion of flux tube area from the photosphere to the chromosphere is well noted in the magnetic bright points by Jess et al. (2009) and in umbral dots from the photosphere to the chromosphere by Jess et al. (2012a) using the power maps of 3-min oscillations. However, here we find clear evidence of such expansion of coherent oscillating regions from the photosphere to corona as described in Section 3.2.1, which were not reported before.

Although wave speeds are estimated in the umbral atmosphere at a few heights (e.g., O'Shea et al., 2002; Reznikova et al., 2012; Kobanov et al., 2013), here we estimated the propagation speed of waves from the photosphere to the corona along the identified fan loop locations. Measured speeds are less than the adiabatic acoustic speed at those heights. This confirmed that these are propagating slow magnetoacoustic waves. Moreover, we also noted that the time lags obtained in Figure 3.6 are averaged over multiple frequencies present in the light curves over the time duration of 4 hours. Further analysis reveals that some of these delays are frequency as well as time-interval dependent. Similar features were also noted by Reznikova et al. (2012). However, here we are utilizing only the averaged time lag to calculate the wave propagation speed. Detailed analysis of time interval and frequency-dependent time lags (phase delays) between the oscillations at different heights will provide information on the dispersive nature of the wave type and medium (flux tube), and will be the topic of further exploration. From Table 3.1, we notice that the time lag between AIA 171 and 193 Å passbands is negative (with equal error) even though AIA 193 Å passband is sensitive to higher temperature and height (e.g., Reznikova et al., 2012). Since AIA passbands are multithermal in nature,

AIA 193 Å passband has some contributions from cooler O V and Fe VII lines, which detect plasma from transition region temperatures (Kiddie et al., 2012). As the temperatures of fan loops are found to be around 0.9 MK (e.g., Ghosh et al., 2017), therefore, oscillations recorded in AIA 193 Å passband could be due to the cooler plasma formed at a lower height and temperature than the AIA 171 Å passband. This can explain the negative time lag obtained between the two passbands. The average time lag between chromospheric and photospheric oscillations is also negative, which may indicate some downward propagation of waves. This may also suggest that at this height, some of the magnetoacoustic waves are reflected back (Khomenko and Collados, 2006). Simulation result of Moreels and Van Doorsselaere (2013) for the flux tube suggests the presence of both fast and slow wave modes superimposed on the same structure. Recent result of Chae et al. (2023) also shows downward propagation of chromospheric oscillations in the sunspot umbra, and thus are in agreement with our findings.

To probe the source region of 3-min waves along the fan loops, and thus the connectivity of the solar atmosphere, we utilized amplitude and frequency modulations of these 3-min waves. Amplitude modulations of 3-min waves are already noted in the chromosphere (e.g., Centeno et al., 2006), transition region (e.g., Marsh and Walsh, 2006), and corona (e.g., Sharma et al., 2020). Krishna Prasad et al. (2015) found almost similar periods of amplitude modulations from the photosphere to the corona, from which they concluded that photospheric p-modes externally drive 3-min slow magnetoacoustic waves observed in the coronal fan loops. However, their conclusion was only based on the similar periodicity of amplitude modulations of the order of 20-27 min across all the observed passbands covering the photosphere to coronal heights. Moreover, they compared the modulation period of 5-min oscillations at the photosphere with the modulation period of 3-min oscillations in the upper atmosphere to establish the source of 3-min waves. However, contrary to this, Centeno et al. (2006) inferred that power in the 3-min oscillations observed at the chromospheric heights is directly related to photospheric 3-min oscillations by means of linear wave propagation, rather than any non-linear interaction of 5-min waves. In this work, we found the presence of 3-min oscillations at the photospheric footpoint of the fan loops. Such 3-min oscillations at the base of fan loops were also observed by Jess et al. (2012a) at the photosphere. Stangalini et al. (2012) also found a clear presence of 3-min waves at the photosphere, which were strictly confined to the umbral region. Moreover, we found several corre-

lated amplitude modulation period ranges for 3-min waves, such as 9-14 min, 20-24 min, and 30-40 min (see Figure 3.8). A strong 27 min modulation period was also noted at some atmospheric heights. We have selected only those dominant modulation period ranges that are present at almost all the atmospheric heights. Therefore, based on our findings of similar modulation periods of 3-min waves at all the atmospheric heights, we conclude that 3-min waves in the upper atmosphere are the direct result of 3-min oscillations observed at the photospheric umbral region.

Moreover, we also noticed a well-known change in the dominant period of oscillations with increasing height above the sunspot umbra, i.e., from 5-min in the photosphere to 3-min in the chromosphere (e.g., Löhner-Böttcher, 2016). There are two popular mechanisms proposed to explain this period shift: chromospheric acoustic resonator (Zhugzhda et al., 1983), and linear propagation of waves with frequencies above the acoustic cutoff from the base of the photosphere (Fleck and Schmitz, 1991; Centeno et al., 2006). Recently, Jess et al. (2020) demonstrated the presence of chromospheric resonance cavity above the sunspot; however, see also Felipe (2021). Fleck and Schmitz (1991) in their model surmised that 3-min oscillations are excited already at the base of the photosphere by 5-min oscillations. Recent numerical simulation of Felipe (2019) concluded that both mechanisms require excitation of 3-min waves at the lower heights. Recent models of Wójcik et al. (2018) and Kraśkiewicz et al. (2019) reported that 5-min driving acoustic waves can excite oscillations of shorter periods due to wave reflection. In this work, we have found the presence of 3-min oscillations along with dominant 5-min oscillations at the photosphere. Based on these findings and the above-reported results, we can expect that some of the observed properties of 3-min oscillations at the photosphere, chromosphere, and above will be similar to those of 5-min oscillations at the photosphere due to their common origin. This explains some similarities found between the modulation periods of 3-min oscillations and 5-min oscillations in our analysis. Henceforth, these findings in the lower atmosphere are in accordance with the results of Fleck and Schmitz (1991) and Centeno et al. (2006).

On the basis of a similar modulation period of 5-min and 3-min oscillations, Krishna Prasad et al. (2015) concluded photospheric p-modes as the driver of 3-min waves in coronal fan loops. However, Chae et al. (2017) concluded that 3-min and 5-min oscillations are not connected and occur independently. Furthermore, simulations of Cho and Chae (2020) suggest that 3-min and 5-min oscillations are coupled and originate

from the same source, which lies 1000-2000 km below the photosphere. Whereas Sych and Nakariakov (2008) and Sych and Altyntsev (2023) found that 3-min oscillations are localised in the umbra, while 5-min oscillations are present at the umbra-penumbra boundary. In this work, we also explored the coupling between 3-min and 5-min oscillations at the photosphere using HMI continuum and Dopplergram data. We found a reasonable correlation between modulations of 3-min and 5-min oscillations with huge time lags, as shown in Figure 3.12. We also examined the modulation periods of both the oscillations and found the $\approx$ 20 and 25 min periods to be common in amplitude and frequency modulations of 3-min and 5-min oscillations, respectively. However, the 12 min modulation period observed in 3-min oscillations is not present in the modulation of 5-min oscillations. Furthermore, the simulation result of Cho and Chae (2020) assumes a non-dispersive medium, and thus can not explain the huge time lag obtained between 3-min and 5-min oscillations in this observation. Therefore, any connection between 3-min and 5-min oscillations at the photosphere is still unclear and demands a dedicated study to explore their connection in detail.

Source region of coronal 3-min waves at the photosphere showed enhancement of power of 3-min oscillations in the umbral dots where footpoints of coronal fan loops were anchored (Jess et al., 2012a). Similarly, Kobanov et al. (2013) also found concentration of high frequency ($\approx 2 - min$) oscillations at the temperature minimum and chromospheric levels, and in small regions inside the umbra at the photospheric level, which they speculated to be the location of umbral dots. Furthermore, results of Chae et al. (2017) also suggest that the 3-min chromospheric oscillations in the sunspots are generated by 3-min oscillations occurring in the light bridges and umbral dots due to magneto-convection. However, as noted before, due to the limited spatial resolution of the current dataset (HMI continuum), we could not verify whether identified fan loop footpoints are anchored in the umbral dots.

We also examined the correlations in modulations at different heights (see Figure 3.9), and found that the solar atmosphere is coupled. However, we also noticed that correlation becomes poor between some height pairs (HMI continuum & AIA 1700 Å, and AIA 304 & AIA 171 Å), i.e., at heights where a sharp transition in density or temperature occurs. One possible reason for this decrease could be the amplitude steepening of the waves due to a drastic change in density, which leads to shock formation, especially in the chromosphere and transition region (Bogdan, 2000). The period of

these shocks is also found to be around 3-min.

Furthermore, it should also be noted that finding the connectivity in the solar atmosphere through wave propagation is a very complex task due to drastic changes in the dynamics of the photosphere, chromosphere, and corona. Umbral photosphere is a complex region due to the presence of plasma-$\beta = 1$ layer close to the formation height of the radiation, which affects the wave modes (e.g, Przybylski et al., 2015; Felipe et al., 2020). Propagation and visibility of waves in the photosphere and chromosphere are also affected by opacity effects (e.g., Bellot Rubio et al., 2000; Khomenko et al., 2003; Felipe et al., 2014). Therefore, for a better understanding of propagation of waves in the solar atmosphere, detailed MHD simulations with non-local thermodynamic equilibrium (NLTE) forward modelling will be required in order to interpret the observations of different wave modes and other dynamical processes at various atmospheric heights (e.g., Carlsson and Stein, 1992; Felipe and Socas-Navarro, 2023).

In summary, we probed the magnetic coupling of the solar atmosphere using amplitude and frequency modulations of 3-min waves observed from the photosphere to the corona. The source region of propagating 3-min slow magnetoacoustic waves observed in the coronal fan loops was traced down into the umbral region of the photosphere. These 3-min waves showed periodic modulations in amplitude with periods in the range of about 9-14 min, 20-24 min, and 30-40 min, and are correlated at different atmospheric heights. These 3-min waves also exhibited periodic modulations in their frequency with periods of about 14-20 min and 24-35 min at all the atmospheric heights. Results reveal that 3-min waves observed in the coronal fan loops are driven by 3-min oscillations observed at the photospheric footpoints of these fan loops within the umbra, which may be the sites of umbral dots. The result provides clear evidence of wave propagation from the photosphere to the corona through the chromosphere and the transition region. These results can provide helpful insights into the modelling of wave propagation in the solar atmosphere. Furthermore, we found a reasonable correlation between the 3-min and 5-min oscillations at the photospheric footpoints in the umbra. However, to conclude anything convincingly between both oscillations, dedicated long-duration high-resolution observations are needed so as to resolve the umbral dots to perform a detailed analysis. This may shed some light on whether the 3-min oscillations are driven independently by magneto-convection or are driven by the 5-min p-modes.

Chapter 4

Effect of area divergence and frequency on damping of slow waves

Chromospheric and coronal energy losses in the solar active regions are approximately 2×10^7 and 10^7 erg cm^{-2} s^{-1}, respectively (Withbroe and Noyes, 1977). To maintain the hot atmosphere of the Sun, magnetohydrodynamic (MHD) waves is one of the proposed mechanisms to transfer energy into the upper solar atmosphere (see recent review by Van Doorsselaere et al., 2020). These waves are excited by the interaction of magnetic field lines and convection motions at the photosphere. The available energy flux provided by the photosphere is about 1.2×10^9 erg cm^{-2} s^{-1} for a mean field strength of 500 G (Parnell and De Moortel, 2012). The transfer and conversion of this mechanical energy flux into heat in the upper atmosphere (e.g., Cranmer et al., 2007; van Ballegooijen et al., 2011) is still not completely understood and is commonly called the coronal heating problem. Henceforth, the photosphere can provide sufficient energy to replenish the atmospheric losses, and waves propagating upward may carry these energy fluxes with them into the upper solar atmosphere. Nature of waves, i.e., either longitudinal or transverse, frequency, magnetic topology, wave amplitude, propagation speed, and other parameters such as plasma density, field strength, etc., may decide upon the amount of energy fluxes carried by them.

One of the outward propagating waves is slow magnetoacoustic waves, which are easily detected in the imaging observations due to their compressive nature (e.g., De Moortel et al., 2002b). Banerjee et al. (2011, 2021) provide comprehensive reviews on the propagation of slow magnetoacoustic waves along open structures. The propaga-

tion of these waves from the photosphere to the corona along fan loops is studied in detail by Rawat and Gupta (2023, 2024b), which highlights that 3-min slow magnetoacoustic waves propagating along coronal fan loops owe their origin to broadband 2-3.74 min (3-min) photospheric driver, see details in Chapter 3. Slow magnetoacoustic waves are subjected to damping while propagating in the solar corona (e.g., Gupta, 2014; Krishna Prasad et al., 2014). Propagating waves develop into shocks due to amplitude steepening at heights where a sharp change in density or temperature occurs (such as chromosphere and transition region), which can be observed as saw-tooth patterns in the velocity oscillations (Bogdan, 2000). Ofman et al. (2000) found that slow magnetoacoustic waves steepen non-linearly while propagating into the corona, leading to wave-enhanced dissipation. However, slow wave shock dissipation within the sunspot umbra does not contribute to the umbral atmospheric heating (e.g., Mein and Schmieder, 1981; Felipe et al., 2011). More details can be found in Section 1.4.3.1. Although damping of slow magnetoacoustic waves in the solar atmosphere is very well studied theoretically, calculating the damping flux along the solar atmosphere observationally through wave propagation is very complex. This is due to the fact that the dynamics of the photosphere, chromosphere, and corona are very different. Furthermore, in the lower atmosphere, effects due to opacity and area divergence are difficult to evaluate (Kanoh et al., 2016).

Slow magnetoacoustic waves are subjected to heavy damping while propagating from photosphere to corona and in the corona (e.g., Gupta, 2014; Krishna Prasad et al., 2014, 2017; Meadowcroft et al., 2024). Ideal/apparent damping mechanisms like area divergence and gravitational stratification play an important role in the damping of slow magnetoacoustic waves (De Moortel and Hood, 2004; Wang et al., 2021). However, they do not contribute to real damping and, therefore, should be incorporated to study the actual damping of slow magnetoacoustic waves. These effects are explained in detail in Section 1.5. Damping of these waves is studied in various atmospheric structures, including magnetic pores (e.g., Gilchrist-Millar et al., 2021), umbra (e.g., Kanoh et al., 2016; Krishna Prasad et al., 2017), coronal holes (e.g., Gupta, 2014), coronal loops (e.g., De Moortel and Hood, 2003), etc. These waves are also important for seismological studies and provide estimates on important plasma parameters that are otherwise difficult to calculate in the solar atmosphere such as adiabatic index, compressive viscosity, thermal conductivity, etc. (e.g., Van Doorsselaere et al., 2011; Wang et al., 2015; Krishna

Prasad et al., 2018).

The obtained damping lengths of slow waves propagating along the coronal loops were less than the expected values from thermal conduction, compressive viscosity, optical thin radiation, etc. (e.g., Wang et al., 2021; Ofman et al., 2000; De Moortel and Hood, 2003). Previously, compressive viscosity and thermal conduction have been considered the dominant damping mechanisms (Wang et al., 2015; Mandal et al., 2016). However, later, it was found that the observed damping length is less than that expected from the theory of conduction (Gupta, 2014; Keys et al., 2018). This suggests that the various expected damping mechanisms are insufficient to explain these damping lengths given the observed parameters of the coronal loop temperature, density, and wave period. The relation between damping time and period of waves $\tau_D \approx P^a$, where the value of a is determined by the dominant damping mechanism, which depends on various parameters like loop length, density, temperature, etc., is provided in Wang et al. (2021) and references within.

In this chapter, we investigate the role of area divergence and frequencies on the damping of slow magnetoacoustic waves propagating from the photosphere to the corona (in part A) and in the corona (in part B) along several fan loops rooted in the sunspot umbra. The content presented in Part A of this chapter is already published in Rawat and Gupta (2024a).

4.1 Observations

To investigate the damping of slow magnetoacoustic waves in the solar atmosphere, we are again utilizing multi-wavelength observations of fan loops within the active region NOAA AR 12553 observed on June 16, 2016 by Atmospheric Imaging Assembly (AIA; Lemen et al., 2012), Helioseismic and Magnetic Imager (HMI; Scherrer et al., 2012) both onboard Solar Dynamics Observatory (SDO; Pesnell et al., 2012), and Interface Region Imaging Spectrograph (IRIS; De Pontieu et al., 2014). Details of observation and data reduction for imaging data are provided in Section 3.1. Figure 4.1 shows the images of the sunspot and fan loops as obtained from AIA, IRIS, and HMI passbands, as labelled.

The selected sunspot is slightly off the disc centre (heliocentric coordinates X $\approx$ -25 arcsec, Y $\approx$ -125 arcsec), the angle between local vertical and line-of-sight (LOS) is

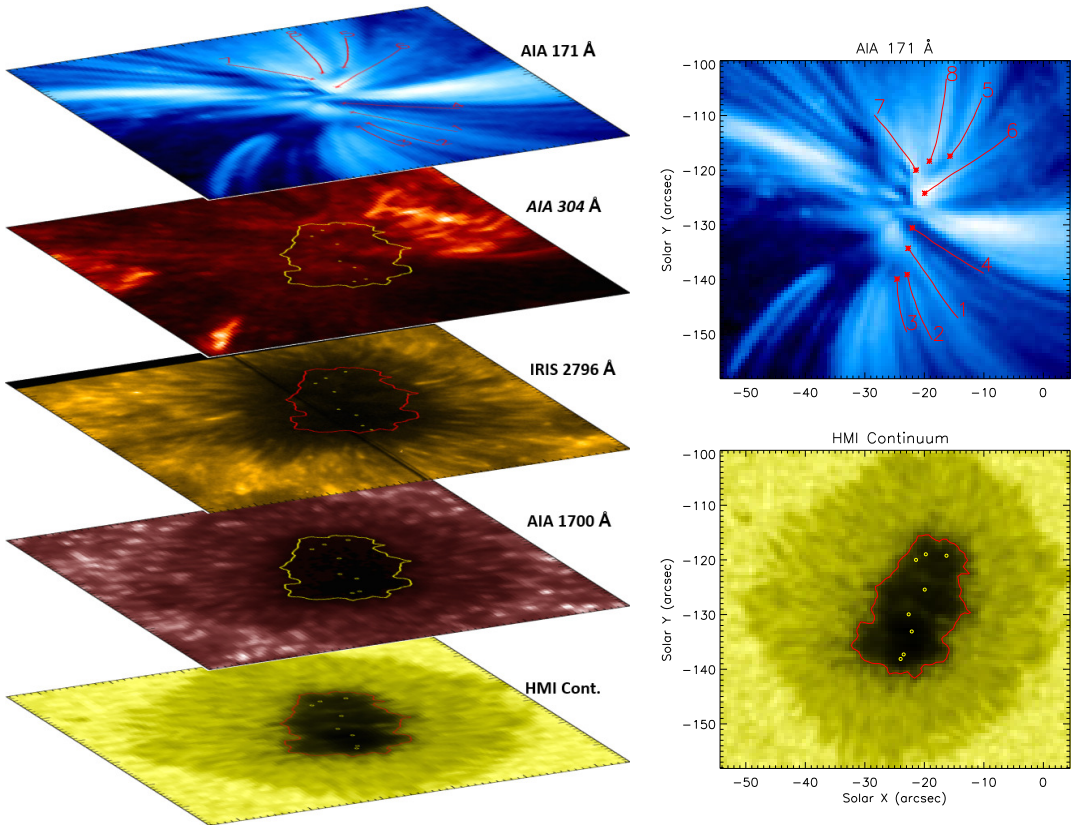

Figure 4.1: Images of sunspot and fan loops obtained at 7:19 UT on June 16, 2016 by various passbands as labelled. Asterisk (*) represents coronal footpoints of all the loops as identified from AIA 171 Å image. Small circles (o) represent the location of all the identified loops at their respective atmospheric heights (see details in Rawat and Gupta, 2023). Contours indicate the umbra-penumbra boundary as obtained from the HMI continuum image.

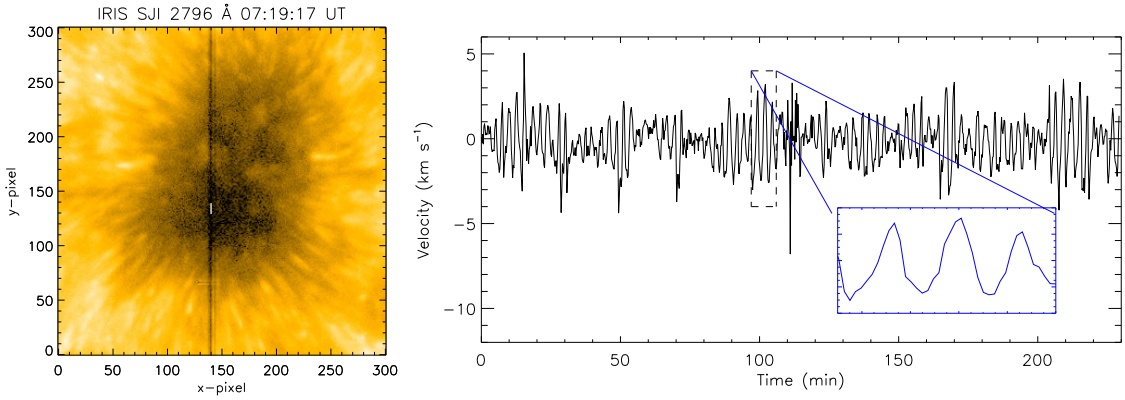

Figure 4.2: Left: IRIS slit-jaw image in Mg II 2796 Å passband. The black line is the position of the IRIS slit. Pixels along a small white line on the slit are averaged over to determine the amplitude of velocity oscillations in the chromosphere above the sunspot umbra. Right: Temporal evolution of Doppler velocity derived from Mg II 2796 Å line formed at the chromosphere above sunspot umbra. Red shifts and blueshifts of chromospheric oscillations are visible and shown by positive and negative values of velocities, respectively. The blue box shows the enlarged view of the dashed box.

$\approx 7.7^{\circ}$, which leads to $\mu = \cos\theta \approx 0.99$. Therefore, any projection effect with respect to the disc centre will be negligible.

4.1.1 IRIS spectroscopic observations

IRIS also observed in spectroscopic mode and recorded the time series spectra in a 2-step raster mode. Both slit width and pixel size along the slit direction are 0.166" pixel^{-1}. Each raster step has an exposure time of 2 s and a slit length of 399 pixels. We have extracted the near-ultraviolet spectra of Mg II at 2796 Å (formation temperature of 10,000 K) from one slit location of the raster to generate the time series. We averaged over the spectra for a region marked with a white line (11-pixels) in Figure 4.2 and further binned over two time-frames to improve upon the signal. The extracted region is representative of the quiet umbral atmosphere. After all binning, the effective cadence becomes 13.76 s. We then fitted average spectral profiles with a single Gaussian function and constant background and further extracted the Doppler shifts and peak intensity of the profiles with time (for more details, see Section B.1). The final Doppler velocity oscillations are plotted in the right panel of Figure 4.2 with the blue box showing an enlarged view of the oscillatory saw-tooth pattern with time.

4.2 Part A: Damping in the lower atmosphere (Photosphere to corona)

The power spectra of intensity and velocity oscillations in the umbral atmosphere reveal the presence of enhanced powers in various period bands (e.g., Krishna Prasad et al., 2017). In sunspots at the photosphere, the power of 5-min oscillations dominates over 3-min oscillations (Bogdan, 2000). At heights above the photosphere, 3-min oscillations dominate due to the acoustic cut-off of 5-min oscillations (e.g., Fleck and Schmitz, 1991; Löhner-Böttcher, 2016). The presence of 3-min oscillations at specific locations in the umbral photosphere was reported by Jess et al. (2012a), and their propagation from photosphere to corona along fan loops was studied in detail by Rawat and Gupta (2023, 2024b), see details in Chapter 3. Moreover, low period oscillations ($\approx$ 1-min) at some atmospheric heights in the umbra are also reported (e.g., Krishna Prasad et al., 2017; Sharma et al., 2020). Wang et al. (2018) reported low period oscillations ($\approx$ 1.5 min) at all the heights above the umbra from imaging observations. Yuan and Walsh (2016) reported low-period oscillations in the corona at the location of light-bridge in sunspot. While propagating, these waves show evidence of damping. Damping of slow magnetoacoustic waves of various periods along the integrated umbral atmosphere from photosphere to transition region was studied by Krishna Prasad et al. (2017), and along open structures in corona were studied by Gupta (2014); Krishna Prasad et al. (2014), etc. All these results indicate some frequency-dependent damping of slow magnetoacoustic waves. Moreover, recently Meadowcroft et al. (2024) reported different damping lengths for 3-min slow waves propagating along the same fan loop observed from different instruments with non-parallel lines of sight.

To balance the total horizontal pressure, the cross-sectional area of the magnetic flux tube increases with height in the solar atmosphere. This leads to the damping of slow magnetoacoustic waves due to area divergence and is related to the conservation of wave energy within the flux tube. Area divergence causes the wave amplitude to decay as $1/\sqrt{(A(s))}$, where A(s) is the cross-sectional area of the coronal loop with height (De Moortel and Hood, 2004). Area divergence does not contribute to heating as the wave energy redistributes itself to conserve wave energy within the flux tube, which is purely a geometric effect. These expanding fields also enhance the transmission of waves to the corona by decreasing the reflection from the chromosphere and transition region (Soler

et al., 2017). Therefore, it is important to take into account the effect of area divergence for an accurate estimate of wave damping.

Till now, most of the work on slow magnetoacoustic wave energy propagation in the umbral atmosphere is carried out either over the whole integrated umbra or at some unidentified location within the umbra (e.g., Kanoh et al., 2016; Chae et al., 2017; Krishna Prasad et al., 2017). Here, we are exploring the effect of area divergence and frequency on the damping of these waves while propagating from the photosphere to the corona along the already identified fan loops rooted in the sunspot umbra, see Chapter 3 and also Rawat and Gupta (2023).

4.2.1 Data Analysis and Results

Figure 4.1 shows the analysed fan loop structures in AIA 171 Å passband. Overplotted contour represents the umbral boundary of a sunspot at 9000 DN, as obtained from the HMI continuum image. We have identified eight fan loops emanating from the sunspot umbra for our study purposes, which are labelled accordingly. In AIA 171 Å image, asterisks (*) represent the coronal footpoints of fan loops from where the loops are visible in the corona. Locations of all the loops at different atmospheric heights from the transition region to the photosphere are already identified (see details in Chapter 3) and marked with small circles (o) in Figure 4.1. We estimate the inclination angle of the traced loops from the photosphere to corona to be $\approx 10^o - 30^o$ as calculated from the spatial offsets between the loop locations identified at the photosphere (HMI continuum) and at the corona (AIA 171 Å). Here, we are presenting results from Loop 6 as a representative example and present results from all the loops in Section 4.2.1.3.

We carried out the analysis for three different cases. Firstly, analysis is carried out for the loop locations identified at different atmospheric heights denoted by small circles (o) and asterisks (*) in Figure 4.1. These are the locations where the correlation value obtained between light curves from two atmospheric heights is maximum and represents the centre of the loop. Secondly, we also carried out the analysis over all the pixels that fall within the contour area where the correlation value between two atmospheric heights becomes ≈95% of the maximum correlation value. This area can be considered as the upper limit on the size of the loop i.e., loop cross-section. The area within this correlation threshold decreases as we move into the lower atmosphere (see Section B.2 for details). This is as per the expectations from the theory of flux tube expansion with

height. Thirdly, analysis is also carried out over the whole integrated umbra as marked by the overplotted contours in Figure 4.1 for comparison with previous results (e.g., Krishna Prasad et al., 2017; Kanoh et al., 2016).

4.2.1.1 Fourier powers and oscillation amplitudes

In Figure 4.3, we show fast Fourier transform (FFT) power spectrum obtained from the background subtracted light curves of loop location 6 from different passbands as labelled (for details see Rawat and Gupta, 2023). Background light curves are obtained by taking 16-min running average of the original light curves at those atmospheric heights. The FFT power spectrum and confidence levels are obtained using the standard IDL routine $fft\_powerspectrum$. Plots clearly show a wide distribution of power peaks in different period ranges. 1–2 min (16.67–8.33 mHz), 2.3–3.6 min (7.25–4.63 mHz), and 4.2–6.0 min (3.97–2.78 mHz) ranges show enhanced powers at different atmospheric heights. Here, we term these three dominant period ranges as 1.5-min, 3-min, and 5-min period bands, respectively. It should also be noted that these period bands have different period (frequency) widths. These period bands are shaded with green, blue, and red colours, respectively. We will be following the same colour code to represent different period bands further in the paper. We finally sum over the FFT powers within their respective bands. Fourier power in the 3-min period band is present in all the passbands, which suggests the propagation of 3-min waves from the photosphere to corona along the fan loops as reported in Chapter 3, see also Rawat and Gupta (2023). Enhanced FFT powers in the 1.5-min period band are present in AIA 1700, IRIS 2796, AIA 304, and AIA 171 Å passbands. The lack of Fourier powers in this band at photospheric heights (HMI continuum and Dopplergram) could be either due to their real absence at these heights or due to the poor cadence of HMI observations, which is 45 s. Enhanced Fourier powers in the 5-min band are present only at the photospheric heights (HMI continuum and Dopplergram) and are absent at higher atmospheric heights, which could be due to atmospheric cutoff.

Since we have found enhanced powers in the 1.5-min and 3-min period bands in almost all the passbands, and thus at all the atmospheric heights, we will be utilizing these period bands for further analysis of wave damping. We apply bandpass filters over these three period ranges on the original light curves (with 3×3 pixel binning for SDO and 5×5 pixel binning for IRIS). Since the absolute wave amplitudes of filtered

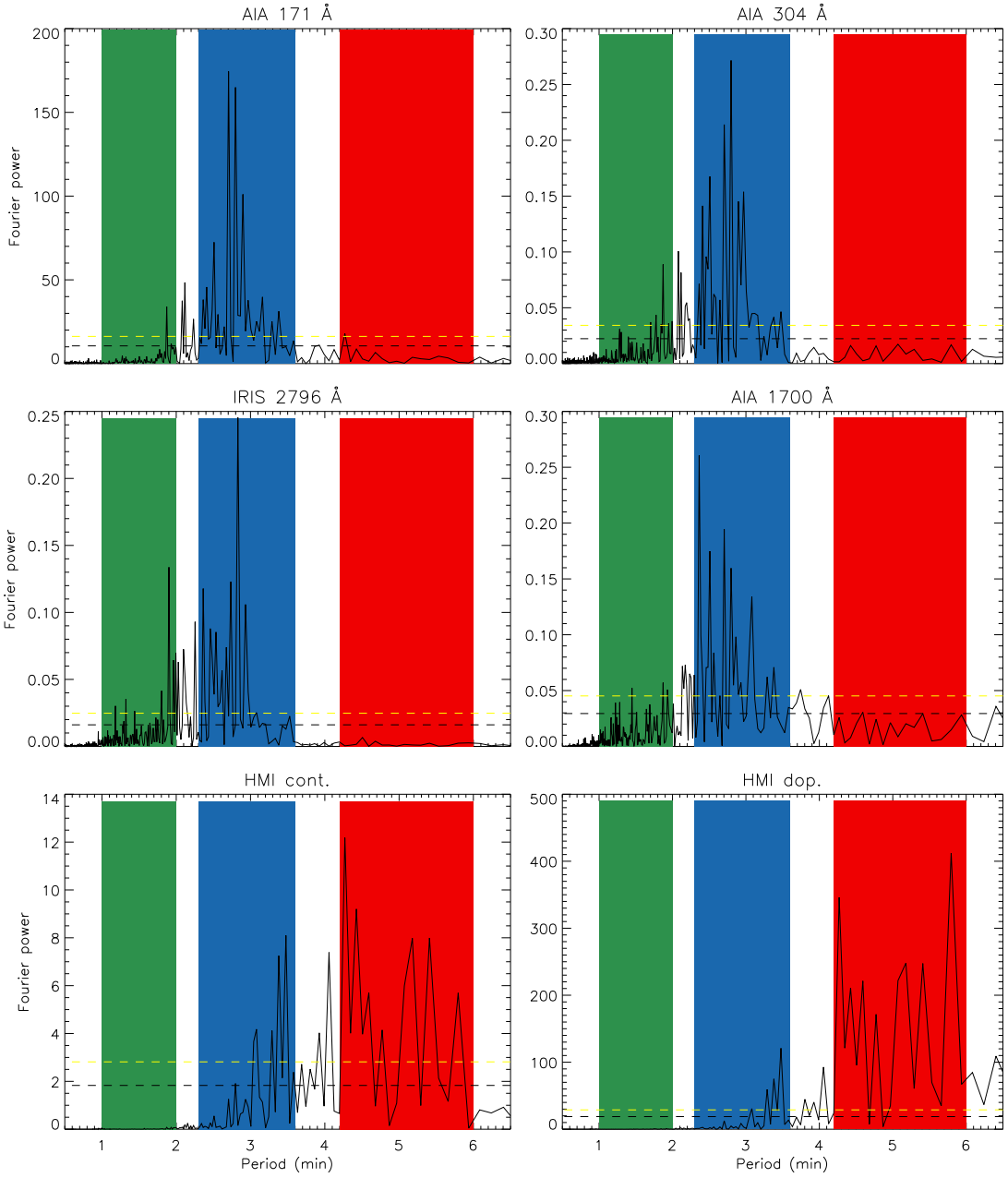

Figure 4.3: Fourier power spectra obtained from background subtracted light curves of Loop 6 locations identified in Figure 4.1 from different passbands as labelled. Shaded regions in green, blue, and red colours denote 1.5-min, 3-min, and 5-min period bands identified for our analysis. Horizontal dashed lines in black and yellow colours represent 95% and 99% confidence levels.

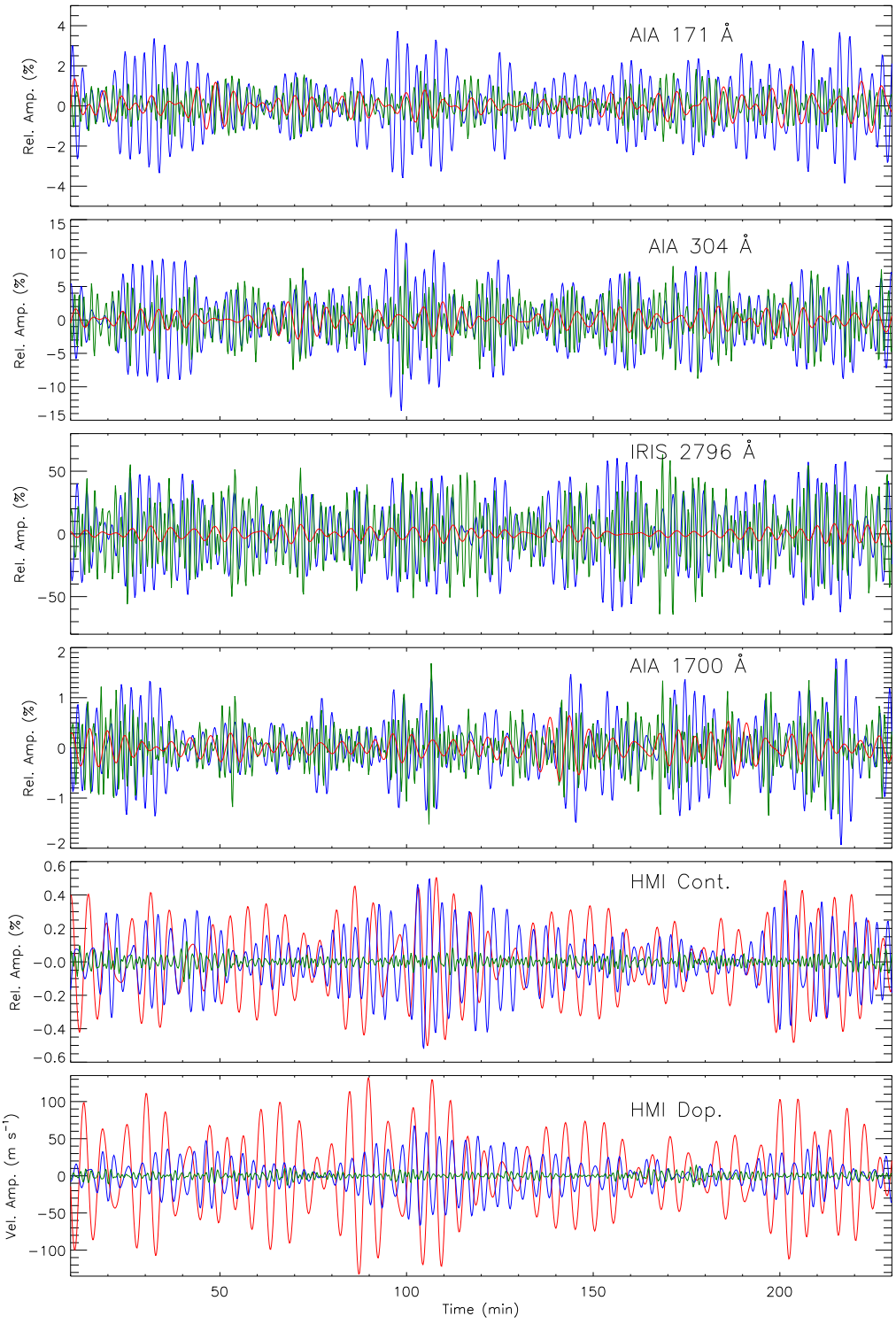

Figure 4.4: Relative intensity and velocity amplitudes for oscillations of 1.5-min, 3-min, and 5-min periods obtained at loop locations from different passbands as labelled. Here, green, blue, and red colours show 1.5-min, 3-min, and 5-min period oscillations, respectively.

light curves in the given period ranges can not be compared directly, these filtered light curves are normalized by background light curves present at that atmospheric height. These normalized filtered light curves represent relative wave amplitudes with time and are shown in Figure 4.4 for 1.5-min, 3-min, and 5-min period bands at all atmospheric heights. These curves show clean intensity oscillations in all three period bands. However, due to the presence of several nearby power peaks in the different period bands, we notice oscillations in the form of unclean wave packets. The bottom panel of Figure 4.4 shows the filtered velocity oscillations obtained from the HMI Dopplergram, which provides the velocity amplitude variations of 1.5-min, 3-min, and 5-min period bands with time. From the plots in Figure 4.3 and Figure 4.4, we notice that 5-min oscillation dominates at the photosphere and 3-min oscillation dominates over 1.5-min oscillation at the higher heights where 5-min oscillation is absent. The root mean square (RMS) relative amplitudes are obtained using the formula $\sqrt{\frac{1}{n}\sum(\frac{I'}{I_o})^2}$ for each period band, where I_o is background light curves and I' is filtered light curves obtained in the ranges shown by shaded region in Figure 4.3. The standard errors in the RMS values are obtained using the formula $\frac{\sigma}{\sqrt{N}}$, where σ is the standard deviation and N is the number of data points (Bevington, 1969). The obtained RMS amplitudes and standard errors at each height are multiplied by $\sqrt{2}$ to determine the relative intensity amplitudes and associated error-bars. In the left panel of Figure 4.5, we plot the relative amplitude of intensity oscillations for different period bands present at various atmospheric heights. Furthermore, we determine the relative intensity amplitude at all the pixels within the loop contours and then average them to determine the relative amplitudes of these waves within the loop cross-sections along the loop.

Relative intensity amplitude variations with height are determined using different methods as mentioned earlier and are plotted in the left panel of Figure 4.5 and Figure 4.6 for single maximum correlated pixel and loop cross-sectional area, respectively. Variations in amplitudes with height are similar for both methods. Relative intensity amplitude variation with height initially shows amplitude steepening due to rapid fall of density. The relative intensity amplitude is maximum at chromospheric height (IRIS 2796 Å), which makes the waves non-linear. This can also be seen in the saw-tooth pattern of velocity oscillations obtained at chromospheric height using Mg II 2796 Å line as shown in the right panel of Figure 4.2, which eventually develops into shocks (Centeno et al., 2006). High-period (5-min) shows atmospheric cutoff as the amplitude of these

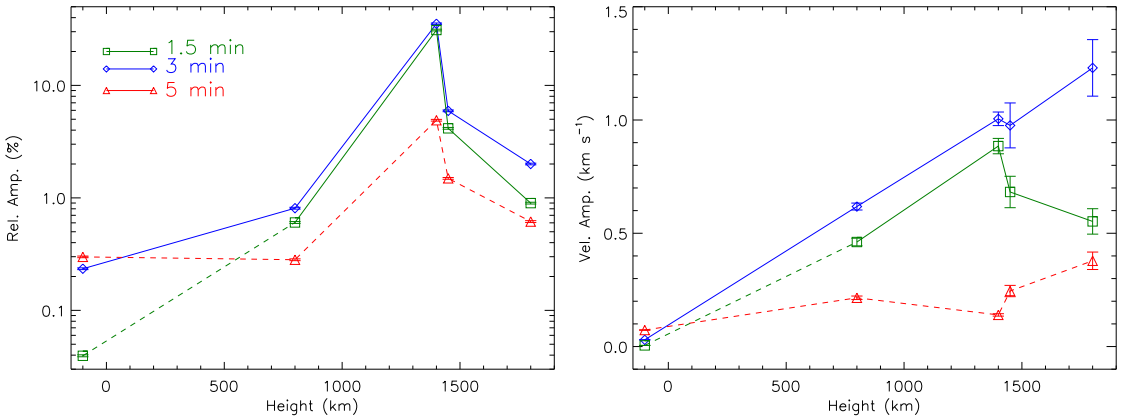

Figure 4.5: Variation of relative intensity amplitudes (left panel) and velocity amplitudes (right panel) of oscillations obtained at loop locations with atmospheric heights.

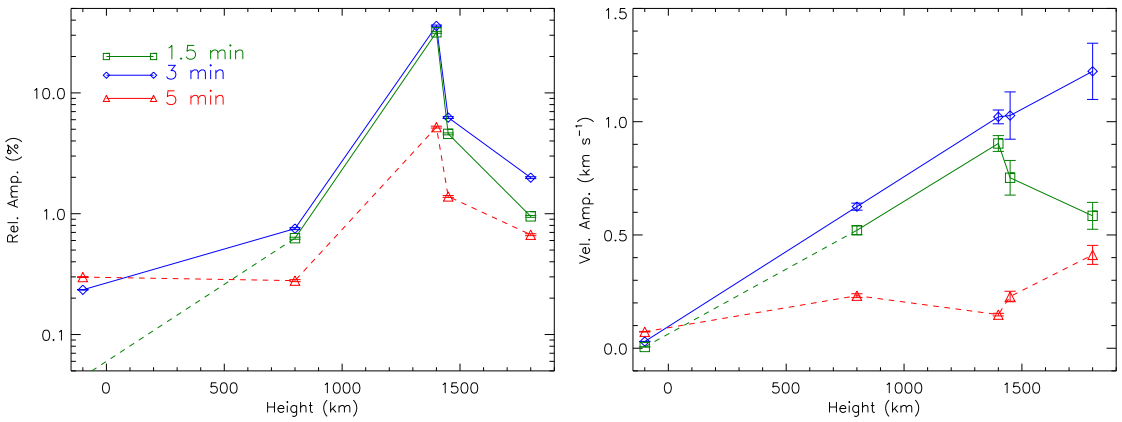

Figure 4.6: Variation of average relative intensity amplitudes (left panel) and velocity amplitudes (right panel) of oscillations obtained within the loop cross-sectional areas with atmospheric heights.

waves decreases as they move from photospheric height to chromospheric height. As seen in the FFT power spectrum, enhanced power in the 1.5-min period band is absent only at the photosphere, whereas enhanced power in the 5-min period band is present only at the photosphere. Therefore, the relative intensity amplitudes of the 5-min period at heights above the photosphere and the 1.5-min period at the photosphere are unreliable. Henceforth, all these unreliable data points are connected using dashed lines in Figure 4.5, and further for representation purposes only.

Velocity amplitudes of 1.5-min, 3-min, and 5-min oscillations are determined assuming linear approximation in the transition region (AIA 304 Å) and corona (AIA 171 Å) using the formula $\frac{I'}{2I_o} = \frac{v'}{v_s}$, where v' is the velocity amplitude and v_s is the speed of sound (Wang et al., 2009). We determined the amplitude of velocity oscillations at the photosphere using HMI Dopplergram data for 3-min and 5-min to be ≈ 33 m s^{-1} and 73 m s^{-1}, respectively, as shown in Figure 4.4. For chromospheric height, velocity amplitude of 1 km s^{-1} was found for 3-min oscillations from Mg II 2796 Å line (see details in Section B.1). Using the velocity amplitudes of photospheric and chromospheric oscillations, we linearly interpolated and extracted the velocity amplitude of 3-min oscillations for the temperature minimum region.

These derived velocity amplitudes of 3-min oscillations will be utilized to calculate wave energy flux. Since we have relative intensity amplitudes of 1.5-min, 3-min, and 5-min intensity oscillations, to calculate velocity amplitudes of 1.5-min and 5-min oscillations for temperature minimum and chromospheric heights, we scaled their relative intensity amplitudes with relative intensity and velocity amplitudes of 3-min oscillations at respective atmospheric heights. Finally, the obtained velocity amplitude variations with height are shown in the right panel of Figure 4.5 and Figure 4.6 for maximum correlated pixel and loop cross-sectional area, respectively. Moreover, inclination of loop from photosphere to corona will change the velocity perturbations by inverse factor of $\cos(10^\circ - 30^\circ) \approx 0.98$-$0.87$ (see Section 4.2.1). This will lead to changes of only about 2-15% and are within the estimated error bars of velocity amplitude.

4.2.1.2 Energy flux of waves

We calculate the total wave energy flux (F) using the formula (e.g., Bruner, 1978; Fossum and Carlsson, 2005), $F = \rho \delta v^2 v_p$ where $\rho, \delta v, v_p$, are mass density, velocity amplitude, and slow wave propagation speed, respectively, and assumes WKB approximation (e.g.,

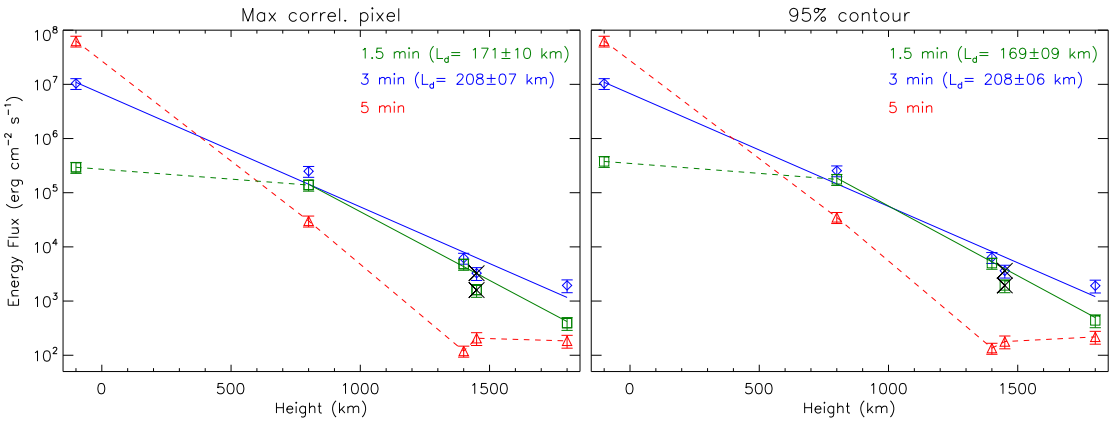

Figure 4.7: Variation of wave energy fluxes at loop locations (left panel) and average wave energy fluxes within the loop cross-sectional areas (right panel) with atmospheric heights.

Bender, 1999). However, under a typical coronal condition of low-beta plasma, sound speed (v_s) is a good approximation to the phase speed of slow magnetoacoustic waves (Wang et al., 2009). Since $\mu \approx 0.99$ for our analysed sunspot, we can assume v_p equals v_s and also any projection effect on velocity perturbations will also be negligible and within the error bars. Sound speed is calculated using the formula $v_s = \sqrt{\frac{\gamma RT}{\mu}}$, where $\gamma = \frac{5}{3}$ is the polytropic index, R =8.314 $\times 10^7$ erg K^{-1} mol^{-1} is the gas constant, μ is the mean molecular weight, and T is the temperature (Aschwanden, 2004). Further, we are utilizing density and temperature from the sunspot atmospheric model of Fontenla et al. (1999) and assume 20% errors in density and temperature, see details in Section B.3.

The estimated wave energy fluxes are decreasing from $\approx 10^7$ erg cm^{-2} s^{-1} at the photosphere to $\approx 2 \times 10^3$ erg cm^{-2} s^{-1} at the low corona for 3-min waves. For 1.5 min waves, energy flux is $\approx 3 \times 10^5$ erg cm^{-2} s^{-1} at the temperature minimum which decreases to ≈ 400 erg cm^{-2} s^{-1} at the low corona. Wave energy flux of 1.5-min waves at the photosphere may be unreliable due to the poor cadence of the HMI continuum. For 5-min waves, energy flux at photosphere is $\approx 6 \times 10^7$ erg cm^{-2} s^{-1} which decays rapidly in the atmosphere. These variations in wave energy fluxes are plotted in Figure 4.7 for loop centre locations at different heights and also for average wave energy fluxes within the loop cross-sectional areas at 95% contour level. Plots show a consistent decrease in wave energy fluxes with height, even though the oscillation amplitudes are increasing with height in the lower atmosphere due to a rapid fall in density. A decrease in wave energy fluxes with height indicates the damping of slow magnetoacoustic waves across these atmospheric layers.

For comparison purposes, we also provide the amplitude of oscillations and average wave energy fluxes over the whole integrated umbra with height in Section B.4. In this case, also obtained amplitudes and wave energy fluxes at different atmospheric heights are of a similar order of magnitude as those obtained for previous cases.

4.2.1.3 Dependence of wave damping on frequency and area divergence

The wave energy flux at different heights in the solar atmosphere are estimated for different cases as mentioned in Section 4.2.1.2 and plotted in Figure 4.7. To determine the dependence of frequency and area divergence on the damping of these waves, we fitted the obtained energy fluxes using an exponential decay function. In Figure 4.7, solid lines represent the best fits with the data following a function $F = F_0 e^{-\frac{h}{L_d}}$, where F is the wave energy flux with height h (see Section B.3), L_d is the damping length, and F_0 is appropriate constant. Fits are performed using $mpfitfun$ routine (Markwardt, 2009). The exponential decay function appears to be consistent with the data. To improve the chi-square of fit, points in black colour cross as shown in Figure 4.7 are excluded from the fit. Damping lengths (L_d) obtained from the maximum correlated pixel are $\approx 171 \pm 10$ km and 208 ± 07 km whereas those from loop cross-sectional area are 169 ± 09 km and 208 ± 06 km for 1.5-min and 3-min period waves respectively. Damping lengths are also printed in Figure 4.7. The damping length of 1.5-min period wave is less than 3-min period wave. This indicates some frequency-dependent damping of slow waves where high-frequency waves are damped faster than low-frequency waves. Also, the damping lengths obtained from maximum correlated pixels and loop areas are similar. This may indicate that wave energy fluxes are uniformly distributed across the loop cross-sections.

Since loops are expanding with the height as reported in Chapter 3 (see also Rawat and Gupta, 2023), the wave energy is redistributed over the whole loop cross-section to conserve the wave energy within the flux tube. This effect will lead to the decay of wave energy flux with height, which is purely a geometric effect without any actual physical damping of waves. To take this geometric effect into account so as to estimate the actual damping of slow magnetoacoustic waves, we multiplied the wave energy flux by the cross-sectional area of the loop at that respective height. The cross-sectional area of the loop at ≈ 95 % contour level is provided in Section B.2. The obtained variation of total wave energy content at different atmospheric heights for different periods are shown in Figure 4.8. The plot clearly demonstrates the actual decay of total wave energy content

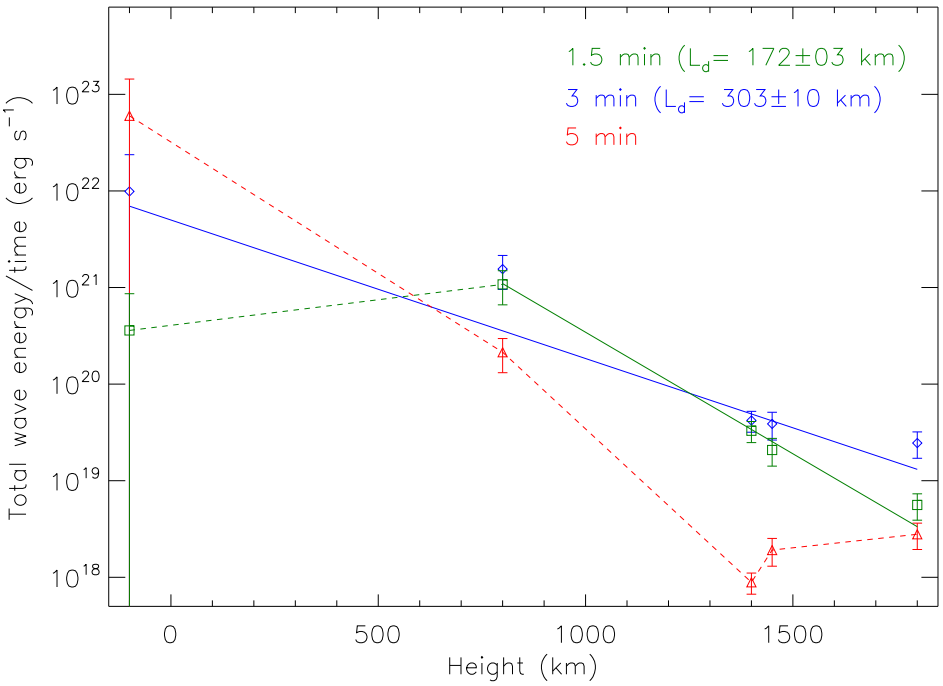

Figure 4.8: Variation of total wave energy content within the loop cross-sectional areas with atmospheric heights.

carried by slow magnetoacoustic waves propagating from the photosphere to the corona along the fan loop. We again fitted the total wave energy curves with exponential decay functions to obtain the actual damping lengths. Obtained actual damping lengths (L_d) in this case are $\approx$ 172$\pm$03 km and 303$\pm$10 km for 1.5-min and 3-min period waves respectively. These damping lengths are for actual damping of total wave energy content with height, which are larger than the damping lengths obtained from the wave energy fluxes with height. Findings indicate that area divergence does play a role in the damping of slow magnetoacoustic waves.

We performed the same analysis on the other seven loops identified in Figure 4.1. Here also all the loops show the presence of 1.5-min, 3-min and 5-min period waves. Similar variations of relative intensity and velocity amplitudes along the solar atmosphere are noted. Damping lengths of wave energy fluxes for 1.5-min period are less than the damping lengths of 3-min period for all the loops. Damping lengths obtained from identified loop locations and loop cross-sectional areas are listed in Table 4.1. Findings confirm almost uniform distribution of wave energy fluxes across the loop cross-sections. However, the longer damping length of the total wave energy content propagating along the different loops is due to the area expansion of the loops, and thus indicates area-dependent damping of waves. Table 4.1 also shows different damping

Table 4.1: Damping lengths (km) for slow magnetoacoustic wave energy flux (erg cm^{-2} s^{-1}) and total wave energy content (erg s^{-1}) propagating along different fan loops identified in Figure 4.1. Damping lengths (km) are presented for loop locations and within loop cross-sectional areas obtained at 95% contour level.

Loop no.	Damping length (km) for flux at max correl. pixel		Damping length (km) for average flux for pixels within 95% contour		Damping length (km) for total wave energy content within 95% contour	
	for 1.5-min	for 3-min	for 1.5-min	for 3-min	for 1.5-min	for 3-min
1	131±07	190±05	139±06	188±05	168±04	231±06
2	161±14	307±18	165±14	259±13	160±04	250±11
3	169±15	243±11	160±13	241±11	129±03	225±10
4	170±10	220±08	175±10	226±06	186±04	300±04
5	231±24	220±13	222±21	216±09	250±04	341±11
6	171±10	208±07	169±09	208±06	172±03	303±10
7	155±11	220±08	166±12	221±08	167±04	264±09
8	199±18	249±12	195±16	246±11	203±04	306±10

lengths for 1.5-min and 3-min period bands as found above. Results provide a clear dependence of frequency and loop area divergence on the damping of slow waves.

4.2.2 Discussion and Summary

In this work, we utilized the FFT power spectra of fan loops rooted in the sunspot umbra and found waves with different periods. We noticed enhanced powers in three period bands such as 1—2 min (16.67–8.33 mHz), 2.3—3.6 min (7.25–4.63 mHz) and 4.2–6.0 min (3.97–2.78 mHz) at different atmospheric heights. 1–2 min period band is present above the photosphere, 2.3–3.6 min period band is present at all the atmospheric heights, whereas 4.2–6 min period band is present only at the photosphere. The 1.5-min period band is also reported by Wang et al. (2018) at different atmospheric heights within the umbra. The absence of 1.5-min period at the photosphere could be either due to poor cadence of HMI data or due to their real absence in our observations. However, it should be noted that Krishna Prasad et al. (2017) also did not find any enhancement in 1.5-min period band at the photospheric height despite having better cadence data. Yuan and Walsh (2016) detected short period (≈1-min) oscillations at light-bridge locations within sunspot umbra. Additionally, we could not find any significant power enhancement in the 3-min period band in the power spectrum of the integrated umbra at the photosphere, though significant enhancements were observed at heights above the photosphere (see Section B.4). This is similar to the previous reports (e.g., Krishna Prasad et al., 2017). This could be due to the fact that 3-min enhancements are found only at the specific locations in the umbral photosphere, potentially at the sites of umbral dots (Jess et al., 2012a) and also at the footpoints of fan loops (Rawat and Gupta, 2023).

We estimated wave energy fluxes for 3-min and 5-min period bands at the photosphere which are $\approx 10^7$ and $\approx 6 \times 10^7$ erg cm^{-2} s^{-1} respectively whereas that for 1.5-min period at temperature minimum region is $\approx 5 \times 10^5$ erg cm^{-2} s^{-1} which are similar to the previous reports. Kanoh et al. (2016) estimated the slow magnetoacoustic waves energy fluxes for 6-10 mHz (1.7-2.7 min) band at the photosphere as 2×10^7 erg cm^{-2} s^{-1} and Krishna Prasad et al. (2017) reported energy fluxes to be $\approx 10^7$ erg cm^{-2} s^{-1} for 3-min period waves. For 5-min period band, Gilchrist-Millar et al. (2021) reported slow wave energy flux to be $\approx 3 \times 10^7$ erg cm^{-2} s^{-1} at an atmospheric height of 100 km inside the pore. As waves propagate upward, these energy fluxes decay with height and provide evidence of wave damping as demonstrated in Figure 4.7. The sharp drop in energy fluxes from photosphere to chromosphere can be due to leaky wave characteristics (Cally, 1986), strong shock dissipation, and radiative cooling (Felipe et al., 2011). These waves propagating along loops can also get damped due to various non-ideal MHD effects depending on the different physical conditions of the loop (Wang et al., 2021). There are several damping mechanisms proposed for slow magnetoacoustic waves, such as compressive viscosity (e.g, Ofman et al., 2000), thermal conduction (e.g, De Moortel and Hood, 2003), area divergence (e.g, De Moortel and Hood, 2004), mode coupling (e.g, De Moortel and Hood, 2004), shocks (e.g, Verwichte et al., 2008), etc.

In this work, we obtained the damping length of ≈208 km for 3-min slow wave energy flux propagating along fan loops from photosphere to corona and ≈ 170 km for 1.5-min period waves propagating from the temperature minimum region to corona. Krishna Prasad et al. (2017) reported damping lengths of ≈ 149 km and 119 km from decay of relative intensity amplitude of slow wave propagation in integrated umbra from chromosphere to transition region for periods ≈ 2.5-min and 1.3-min, respectively. Both results indicate some frequency-dependent damping of slow magnetoacoustic waves in the lower atmosphere. Frequency-dependent damping lengths are also reported in the corona along open structures (e.g., Gupta, 2014; Krishna Prasad et al., 2014). We also noted that wave energy flux at the centre of the loop and average wave energy flux obtained within the loop cross-sections (at ≈ 95% contour level) are of similar order (see Figure 4.7). Fluxes are similar because the velocity amplitudes at all the pixels within the loop cross-sections are almost similar. This may indicate that wave energy fluxes are uniformly distributed across the fan loop cross-sections, and also that a similar damping mechanism is operating throughout the umbra. Therefore, damping

of slow magnetoacoustic waves propagating in different regions of the solar atmosphere shows some kind of frequency-dependent damping, even though different damping mechanisms might be operating at different heights.

One of the dominant damping mechanisms of slow magnetoacoustic waves is area divergence, which is very well studied in the solar corona (De Moortel and Hood, 2004). However, its influence in the lower atmosphere is still unexplored. In this work, we utilized the cross-sectional area of the fan loops obtained at different heights in the lower atmosphere (Rawat and Gupta, 2023). We explored the effect of area expansion on wave damping by multiplying the loop cross-sectional area by the energy flux of slow waves at that atmospheric height. The obtained total slow wave energy propagating along the fan loop in unit time at different heights is plotted in Figure 4.8 and represents the actual damping of slow waves. Here, the damping lengths are 172 ± 03 km and 303 ± 10 km for 1.5-min and 3-min periods, respectively. After incorporating the effect of area divergence, the actual damping lengths obtained are larger than those found from the damping of wave energy fluxes. This indicates that the waves are losing energy faster (i.e., the damping length is short) when the area divergence effects are not considered. This is due to the fact that wave energy is redistributed across the loop cross-sections due to area divergence. This clearly explains the importance of area divergence in the damping of waves.

Moreover, it should be noted that calculating the actual damping of wave energy flux along the solar atmosphere is a very complex problem, as the dynamics of the photosphere, chromosphere, and corona are very different. Furthermore, the umbral photosphere itself is a complex region due to the presence of plasma-$\beta = 1$ layer which affects the propagation of wave modes (e.g., Przybylski et al., 2015). Additionally, while calculating the energy fluxes, we are assuming waves to be linear. Calculated energy fluxes for 3-min waves at photosphere, chromosphere, and corona are $\approx 10^7$, $\approx 10^4$, and $\approx 10^3$ erg cm^{-2} s^{-1}. However, how much of this wave energy flux is damped, how much is getting reflected, and how much is propagating upwards still needs detailed investigation (e.g., Soler et al., 2017). Detailed MHD simulations with non-local thermodynamic equilibrium modeling will be required to understand the wave dynamical processes at various atmospheric heights (e.g., Felipe and Socas-Navarro, 2023).

In summary, we studied the damping of slow magnetoacoustic waves propagating along fan loops in the umbral atmosphere and showed oscillations in the period bands

1.5-min, 3-min, and 5-min. We estimated slow magnetoacoustic wave energy fluxes propagating along the fan loops at different heights and provided evidence of wave damping with damping lengths of $\approx$ 170 km and $\approx$ 208 km for 1.5-min and 3-min periods, respectively, for Loop 6. We showed the decay of total wave energy content within the loop cross-section with height and provided evidence of actual damping of slow magnetoacoustic waves from the photosphere to corona with damping lengths of $\approx$ 172 km and $\approx$ 303 km for 1.5-min and 3-min periods, respectively, for the same loop. We note that the damping lengths of 1.5 min waves before and after incorporating the area divergence effect are almost similar. This is due to the fact that low-period waves damp much faster, much before the effect of area divergence becomes significant. Results showed some frequency-dependent damping of slow magnetoacoustic wave energy flux with height, where high-frequency waves are damped faster than low-frequency waves. We have also demonstrated the importance of the role of area divergence in the damping of slow magnetoacoustic waves.

4.3 Part B: Damping in the corona

All the damping mechanisms mentioned for slow waves in Section 1.5 were unable to explain the rapid damping of slow waves, indicating that other damping mechanisms are also involved. Zavershinskii et al. (2019); Kolotkov et al. (2019, 2021) suggested an additional damping mechanism in which magnetoacoustic waves perturb the coronal thermal equilibrium, leading to wave-induced thermal misbalance (TM), which alters the heating/cooling processes operating in the plasma. This wave-induced misbalance between plasma cooling and heating processes causes the amplification or attenuation, and also dispersion, of slow magnetoacoustic waves known as the thermal misbalance (Belov et al., 2021). This is considered a natural mechanism to exchange energy between waves and plasma. This imbalance is responsible for the phase shifts between the perturbations of various plasma parameters, e.g., density, temperature, etc. Thermal misbalance plays an important role for slow waves propagating along high-density, low temperature, and strong magnetic coronal loops (Belov et al., 2021; Duckenfield et al., 2021). Duckenfield et al. (2021) found that after including the effect of thermal misbalance, the obtained damping times coincide with observed damping times of the

order of 10-100 minutes. Authors also found a strong dependence of this imbalance on the magnetic field strength of the loop. Although the propagation and damping of slow magnetoacoustic waves in the solar atmosphere is very well studied theoretically, calculating the parameters involved in the damping of these waves along the loops observationally through wave propagation is very complex (e.g., Wang et al., 2021).

Theoretically, it is found that slow waves are weakly dispersive (Roberts, 2019). However, recently, Zhao et al. (2025) noted the frequency-dependent phase speed of slow waves in the Fourier domain and thus the dispersive nature of slow waves propagating along coronal loops. The authors suggested that this dispersive nature can be the influence of thermal misbalance or geometric dispersion in the coronal loop. This can further explain the frequency-dependent damping of slow waves noted by Gupta (2014); Krishna Prasad et al. (2014).

In this chapter, we present for the first time a direct observation of the frequency-dependent phase speed of slow waves and provide direct evidence of the dispersive nature of slow waves propagating along coronal fan loops rooted in the sunspot umbra.

4.3.1 Data Analysis and Results

Figure 4.9 shows the analysed fan loop structures belonging to AR 12553 in AIA 171, 193, 131, and 211 Å passbands. We have identified quiescent fan loops emanating from the sunspot umbra for our study purposes and labelled them accordingly. We carried out our analysis on manually traced loops in the corona, see Figure 4.9. The lines along the loops represent the location of loops for our analysis. Here, we present the results from Loop 3 as a representative example, and provide the summary of results from all the loops in Section 4.3.1.3.

4.3.1.1 Time-distance and Frequency-distance maps

We plot the intensity evolution along the different locations of Loop 3 in Figure 4.10. Light curves were obtained by averaging over three pixels across the slit to improve the signal-to-noise ratio. We utilize these averaged light curves further in our analysis. In the left panel of Figure 4.10, we show the original light curves obtained at different locations along the loop. The overplotted blue line is the background light curves (I_o) obtained by taking 18-min running average of the original light curves at those loop locations. We further obtained the normalized filtered light curves obtained from the

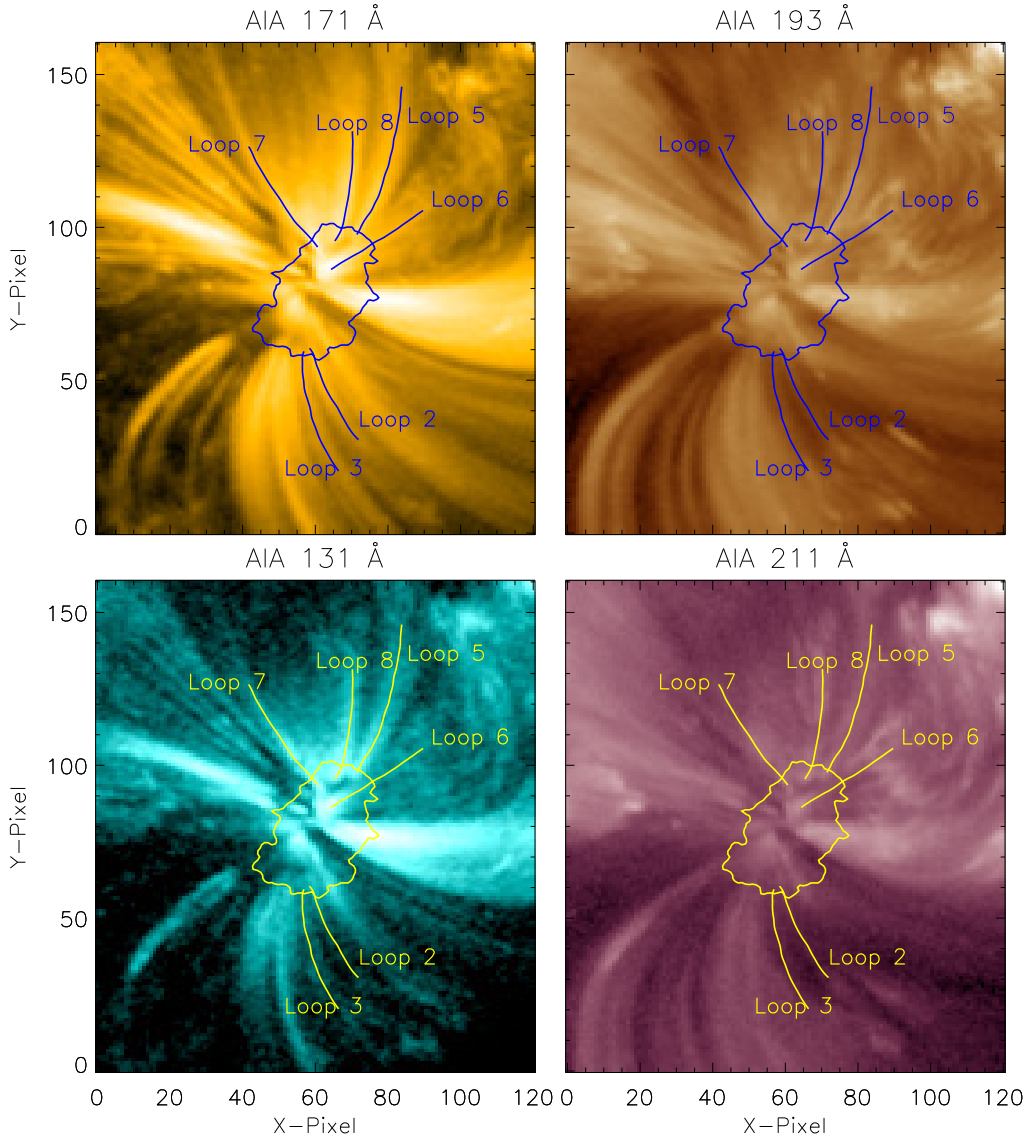

Figure 4.9: Image of fan loop system belonging to AR 12553 obtained by various pass-bands as labelled. The solid lines on the images represent the manual tracing of coronal fan loops. The contour indicates the umbra-penumbra boundary as obtained from the HMI continuum image.

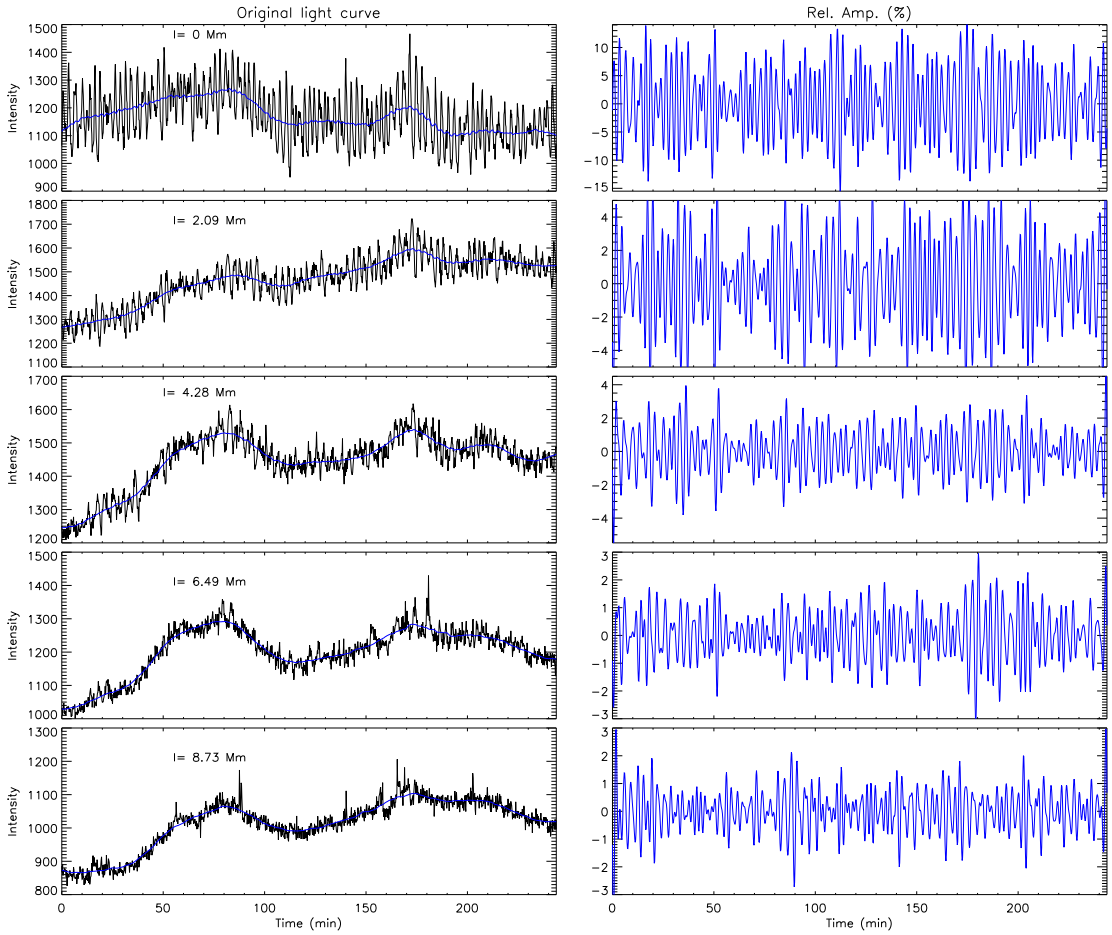

Figure 4.10: Left: Original light curves at different locations along Loop 3 as labelled. The overplotted blue lines show the background trend at each loop location. Right: Relative intensity amplitudes for the 3-min period band obtained at various loop locations.

original light curve as shown in right panel of Figure 4.10. We utilized detrended light curves by subtracting the background light curve from the original light curve to obtain the time-distance intensity map along the fan loop, as shown in Figure 4.11. Here, we are using a 4 h long time series to increase the frequency resolution. Here, diagonal or slanted intensity enhancements provide clear signatures of the propagation of these oscillations. Thus, from such maps, it becomes possible to estimate the periods and phase speed of waves. This time-distance map also shows a fall in the intensity of propagating signals as we move away from the coronal loop footpoint.

In Figure 4.12, we show the frequency-distance map along the loop obtained from the Fourier transform of the time-distance map shown in Figure 4.11. The FFT power map is obtained using the standard IDL routine $fft\_powerspectrum$. Plots clearly show a wide distribution of oscillatory power around a 3-min period band (1.8-4 min or 4-8.1 mHz).

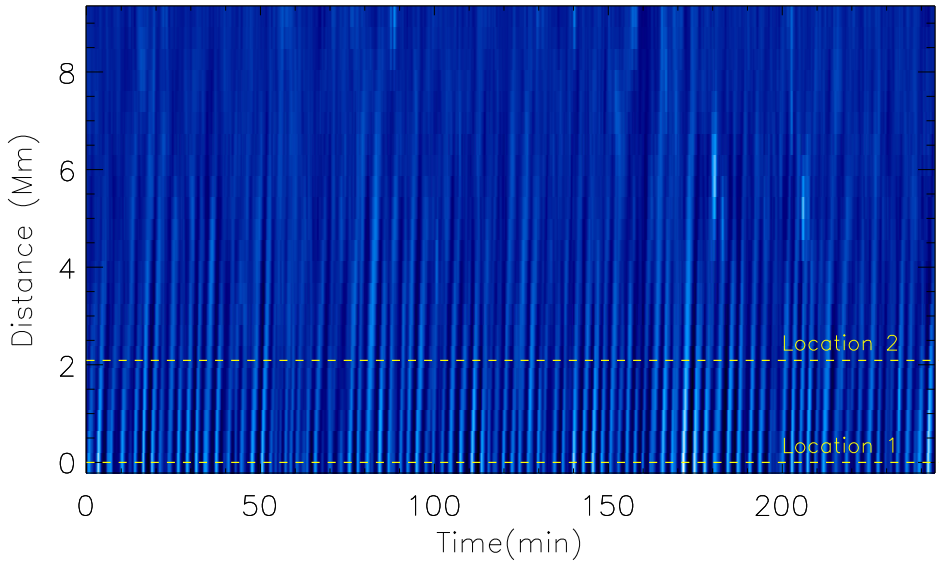

Figure 4.11: Time-distance map obtained from AIA 171 Å along coronal fan Loop 3. The yellow dashed lines show the location of the loop used to determine the time lag.

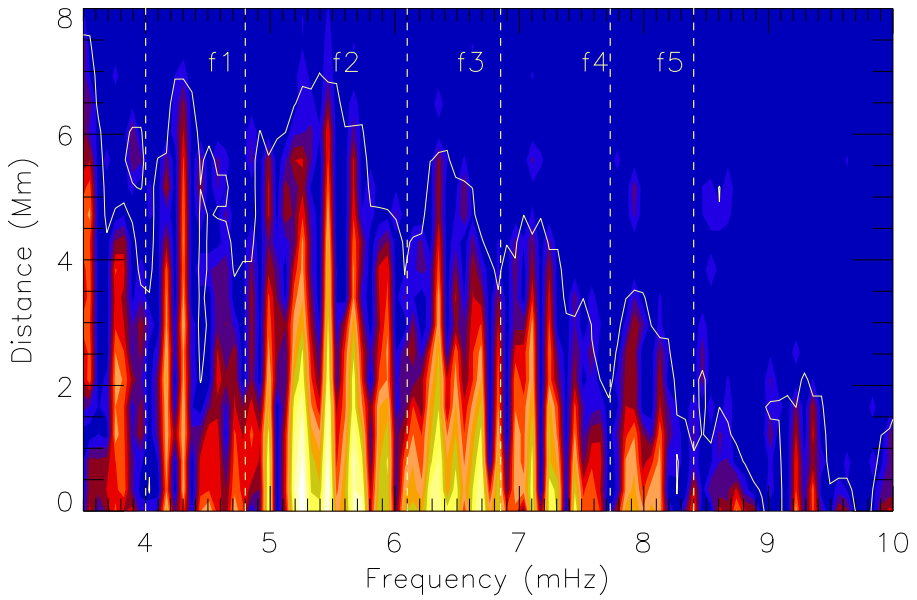

Figure 4.12: Frequency-distance Fourier power map (power in logarithmic scale) obtained from time-distance map shown in Figure 4.11.

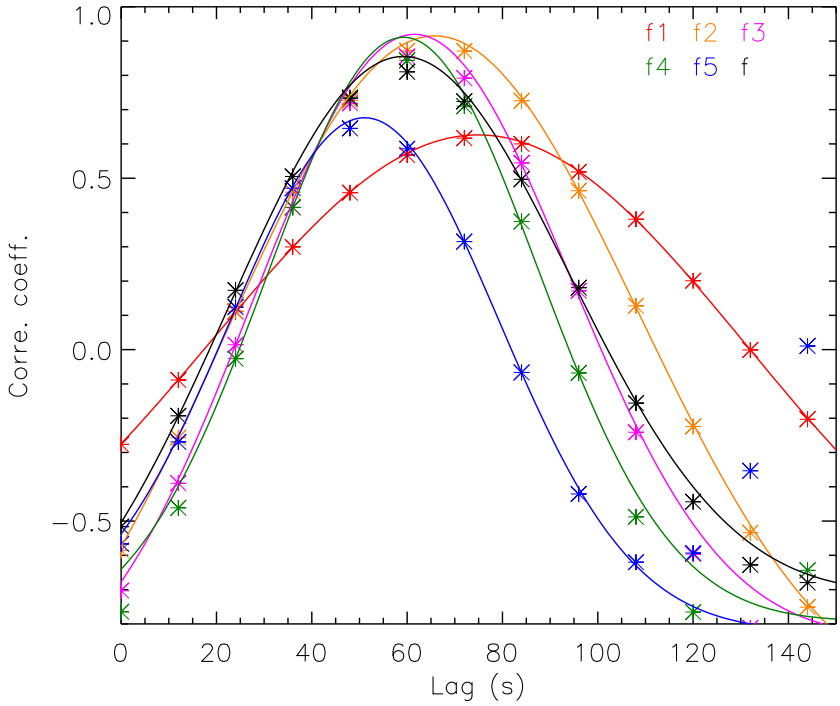

Figure 4.13: Variation of cross-correlation coefficients with respect to time lag obtained between filtered light curves in different frequency bands as labelled.

This band is shown by starting and ending dashed lines in Figure 4.12, and denoted as f. We divide this frequency band f in various frequency sub-bands f_1, f_2, f_3, f_4 and f_5, representing 4-4.8, 4.8-6.1, 6.1-6.85, 6.85-7.73 and 7.73-8.1 mHz frequency bands and denoted by red, orange, purple, green and blue colours, respectively. These bands are identified to study properties of propagating waves within these sub-bands and any variations within. We will be using the same colour code for these bands further in the Chapter. These frequency bands are selected visually based on the power enhancements in the frequency-distance map shown in Figure 4.12. We applied bandpass filters over the whole period (or frequency) range on the original light curves, and obtained the filtered light curves (I') in the given period range. These curves show clean intensity oscillations in this period range. However, due to the presence of several nearby power peaks in the whole 3-min period band, we notice oscillations in the form of unclean wave packets as shown in Figure 4.10 (see also e.g. Rawat and Gupta, 2023).

4.3.1.2 Dispersive nature of slow waves

We determine the phase speed in the 3-min period band by cross-correlating the two light curves at different heights of the same loop. For this purpose, we have used

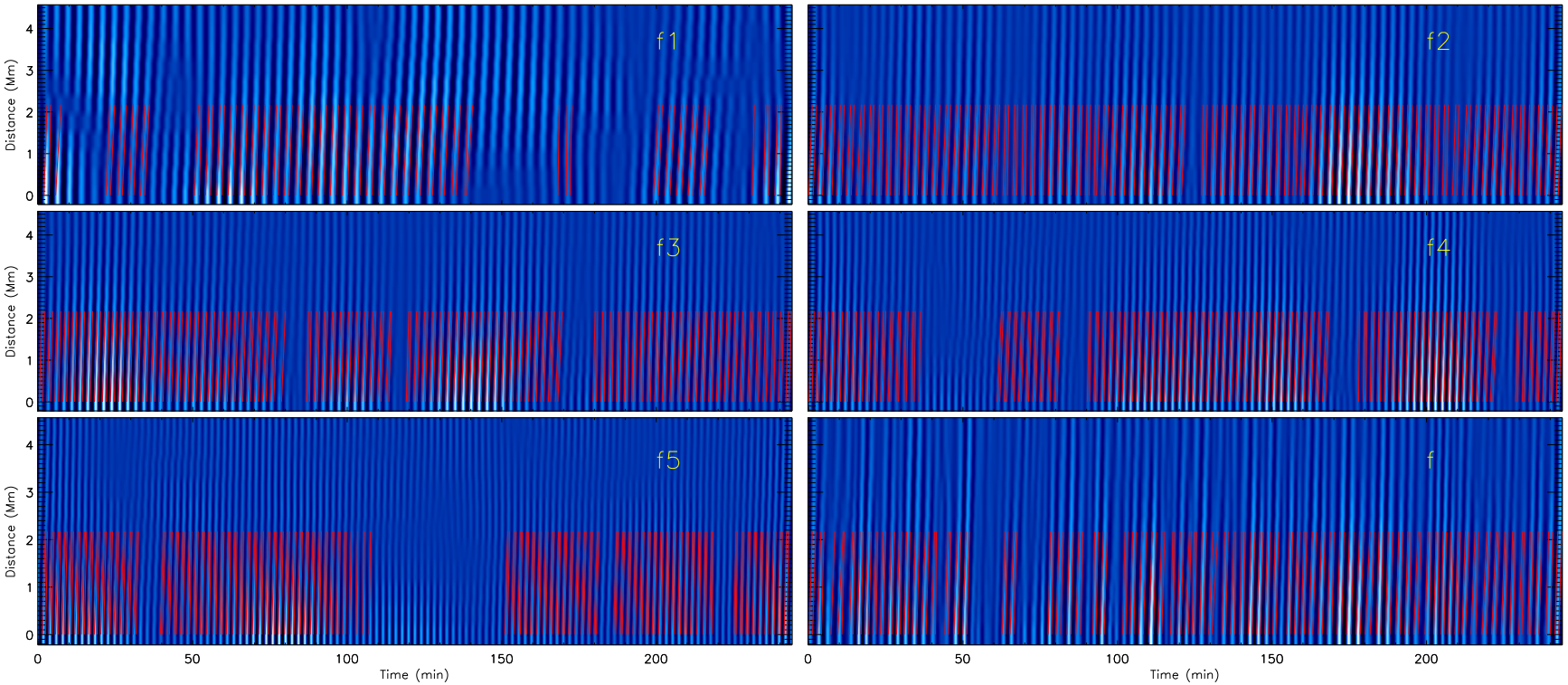

Figure 4.14: Time-distance maps obtained in different frequency bands as labelled along the Loop 3. Red slits are used to determine the phase speed of propagating waves in the different frequency bands.

filtered light curves at two locations, 1 (0 Mm) and 2 (2.09 Mm), shown by dashed lines in Figure 4.11. The same distance has been used for determining the time lag from the time-distance map. Using IDL routine *c_correlate*, we cross-correlated the two light curves. We fitted the correlation curves with a Gaussian and linear function and determined the time lag at which the correlation peaks, as shown in Figure 4.13. The time lag and the distance between the two locations (km) were used to obtain the phase speed. For the error estimate, we have assumed the error in time as the fitting error, and take pixel resolution of the AIA passbands as error in distance, which is 435 km (0.6" pixel^{-1}). These are plane projected phase speeds that provide lower limits on the wave speeds.

We also determine the phase speed of propagating intensity disturbances by using filtered time-distance maps in the selected period bands as labelled in Figure 4.14. On the maps, we plot red slits over the boundaries of the cleanest bright ridges. These slits are plotted using the IDL routine *contour*. Slits are selected only for those lines that have a positive slope and can propagate up to 2.09 Mm, so that we can plot the maximum number of slits. For each slit, we determined the starting and ending times and subtracted them to determine the time lag. We then obtained the average time lag for each frequency band. For the error in time lag, we determined the standard deviation of all the time lags. These slits provide the phase speed of these waves and show an increase in the slopes of the ridges with frequency.

The time lags and phase speeds in the different frequency bands, along with their error from both methods, are provided in Table 4.2. These estimates clearly show different phase speeds in different frequency bands. These phase speeds increase with frequency, highlighting the dispersive nature of these waves or the medium. We also noted the different phase speeds in different AIA passbands along the coronal fan loop, showing some temperature dependence.

4.3.1.3 Apparent damping of waves

To determine the relative amplitude of wave propagation in the various frequency bands, we utilized the filtered light curves and normalized them with the background light curves present at that location. These normalized filtered light curves represent relative wave amplitudes with time, as shown in the right panel of Figure 4.10. The root mean square (RMS) relative amplitudes and its standard error are obtained using

the formula $\sqrt{\frac{1}{n}\sum(\frac{I'}{I_o})^2}$ and $\frac{\sigma}{\sqrt{n}}$ respectively for each period band (Bevington, 1969) as explained in Section 4.2.1.1. The obtained RMS amplitudes and standard errors at each height are multiplied by $\sqrt{2}$ to determine the relative intensity amplitudes and associated error bars. In Figure 4.15, we plot the relative amplitude of intensity oscillations for the selected period bands along the loop. Plots show a consistent decrease in relative amplitude along the loop, which indicates the damping of slow magnetoacoustic waves along the loop.

We further fit these amplitudes with an exponential decay function and a constant

$$A(h) = A_0 e^{-(\frac{h}{\lambda_A})} + A_1, \tag{4.1}$$

where $A(h)$ is the wave amplitude along loop length h, λ_A is the damping length, A_0 and A_1 are appropriate constant. Here, $1/\lambda_A \approx \alpha$, which is the damping factor as described in Kinsler et al. (1999). These fittings are performed using the $mpfitfun$ routine (Markwardt, 2009), which utilizes least-squares minimization to fit the damping function to the observed data. The damping lengths decrease with an increase in frequency, demonstrating the frequency-dependent damping. The damping lengths in various frequency bands and AIA passbands are provided in Table 4.2. Damping lengths obtained in various AIA coronal passbands are also different, which indicates some temperature dependence.

We performed a similar analysis over the five other loops identified in Figure 4.9. All the loops show the dispersive nature of the slow magnetoacoustic waves as the phase speed increases with frequency. However, the number of frequency bands in different loops are different. In Figure 4.16, we plot the phase speed of slow waves in different frequency bands normalized by the phase speed obtained over the whole frequency range in all the loops. Phase speed normalization is carried out to avoid the effect of different inclinations of different loops, so as to compare them all together. We find the normalized phase speed to increase with frequency, showing the dispersive nature of the slow magnetoacoustic waves. Phase speeds are different for loops observed in different AIA passbands, showing some temperature dependence. Additionally, all the loops show decay in relative intensity amplitudes along the loops. We determined the damping lengths in the range of 0.4-4.6 Mm for all the loops in different frequency bands in all four AIA passbands.

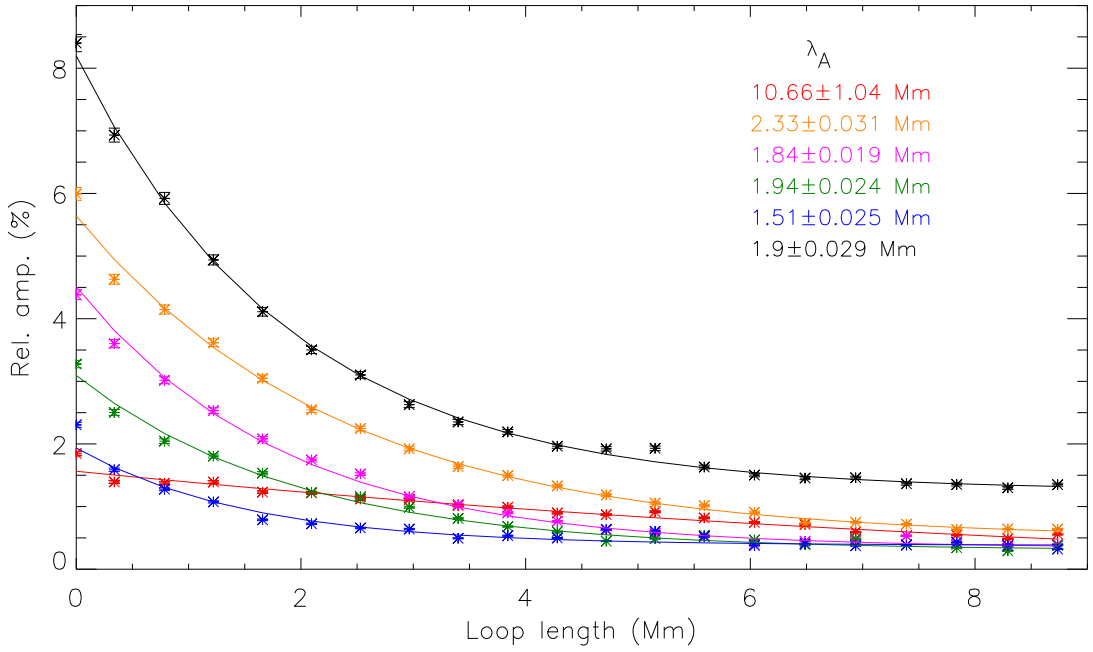

Figure 4.15: Variation of relative amplitudes along the loop length in the selected period bands along the Loop 3.

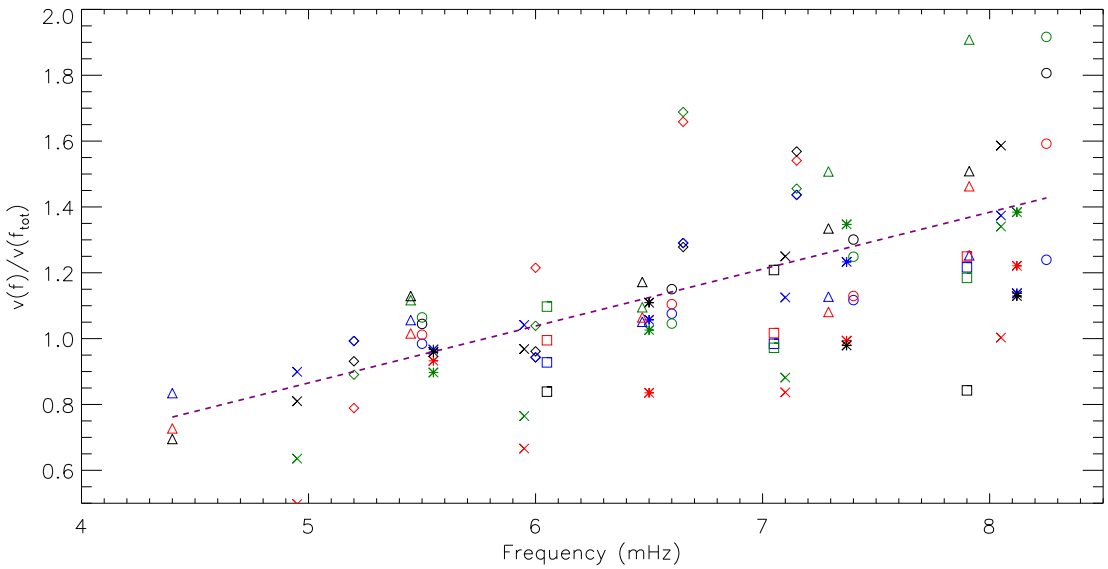

Figure 4.16: Variation of phase speed of slow waves at different frequencies for all the loops observed in AIA 171, 193, 131, and 211 Å passbands shown in blue, red, green, and black, respectively. Phase speeds in different frequency bands are normalized by the phase speeds obtained over the whole frequency range (f). The symbols asterisk, triangle, diamond, square, cross, and circle represent Loop 2, Loop 3, Loop 5, Loop 6, Loop 7, and Loop 8, respectively.

Table 4.2: Time lag (s) and projected phase speed $v(\omega)$ (km s^{-1}) of slow magnetoacoustic waves propagating along fan Loop 3 for different frequency bands, obtained from two different methods. The frequency bands f_1, f_2, f_3, f_4, f_5, and f represent the frequency range of 4–4.8 mHz, 4.8–6.1 mHz, 6.1–6.85 mHz, 6.85–7.73 mHz, 7.73–8.1 mHz, and the full band 4–8.1 mHz, respectively. Damping lengths λ_A (Mm) of relative amplitude of slow magnetoacoustic waves in each frequency band are also provided.

Passbands	Correlation		Time-distance		Damp. length
freq. (mHz)	lag (s)	speed (km s^{-1})	lag (s)	speed (km s^{-1})	λ_A (Mm)
131 Å					
f_1 (4.4)	115.28±4.02	18.16±3.59	46.71±14.68	44.74±16.54	–
f_2 (5.45)	92.14±1.25	22.73±4.43	64.96±21.54	32.17±12.37	1.08 ± 0.03
f_3 (6.47)	83.53±0.64	25.07±4.88	66.24±13.64	31.55±8.94	1.45 ±0.04
f_4 (7.29)	77.73±0.62	26.94±5.25	48.12±13.77	43.43±15.03	1.01 ±0.05
f_5 (7.91)	45.71±0.79	45.81±8.95	38.02±18.77	54.97±29.17	0.54±0.05
f	77.79±0.09	26.92±5.23	72.55±21.02	28.81±10.06	1.41 ±0.09
171 Å					
f_1 (4.4)	75.23±1.52	27.84±5.45	66.65±20.52	31.36±11.42	10.66±1.03
f_2 (5.45)	65.10±1.00	32.39±6.28	52.65±13.85	39.70±12.99	2.38±0.03
f_3 (6.47)	60.86±0.64	34.78±6.71	52.90±11.48	39.50±11.51	1.89±0.02
f_4 (7.29)	59.09±0.44	35.43±6.90	49.32±11.55	42.37±12.90	1.87±0.02
f_5 (7.91)	51.05±0.83	41.01±8.01	42.89±9.37	42.89±14.58	1.56±0.03
f	58.10±0.03	36.04±7.01	59.54±14.49	37.58±12.18	1.9±0.03
193 Å					
f_1 (4.4)	44.84±1.83	46.70±9.53	64.23±31.22	32.54±17.04	–
f_2 (5.45)	54.19±1.10	38.64±7.77	45.99±14.10	45.44±16.50	4.59±0.20
f_3 (6.47)	38.96±1.15	53.74±10.86	43.89±7.39	47.62±12.26	3.28±0.1
f_4 (7.29)	51.75±0.45	40.46±8.10	43.21±10.44	48.36±15.01	2.61±0.09
f_5 (7.91)	53.68±0.65	39.01±7.82	31.93±15.11	65.44±33.49	1.92±0.14
f	42.79±0.17	48.94±8.55	46.71±14.68	44.74±16.54	3.54±0.17
211 Å					
f_1 (4.4)	84.04±0.99	24.92±4.85	87.79±38.55	23.81±10.45	–
f_2 (5.45)	62.43±1.06	33.54±6.55	54.03±20.05	38.68±14.35	1.58±0.04
f_3 (6.47)	59.03±0.64	35.47±6.91	52.06±12.06	40.14±9.30	1.59±0.04
f_4 (7.29)	47.47±0.63	49.75±8.60	45.71±16.92	45.71±16.92	1.27±0.04
f_5 (7.91)	29.71±0.71	70.49±13.82	40.45±19.52	51.67±24.94	1.34±0.14
f	51.59±0.08	40.59±7.9	61.02±21.40	34.25±12.01	1.47±0.08

4.3.2 Discussion and Summary

In this work, we utilized intensity oscillations along the fan loops rooted in the sunspot umbra to explore the reason for the observed frequency-dependent damping of slow waves. Slow magnetoacoustic waves in the corona damp faster than any proposed damping mechanisms (Wang et al., 2021). This short length scale is ideal for studying the frequency-dependent damping and exploring the cause behind it. We noticed enhanced oscillatory power in the 1.8-4 min period band up to a certain loop length as shown in Figure 4.12. This is similar to the previous reports (e.g., De Moortel et al., 2002b; Sharma et al., 2020). Krishna Prasad et al. (2014) found the damping length of amplitude of the 3-min slow wave propagating along the coronal loops to be ≈2 Mm. These waves propagating along coronal loops get damped due to various ideal, non-ideal MHD effects and thermal misbalances depending on the different physical conditions of the loop (Wang et al., 2021; Belov et al., 2021).

In the solar corona, the damping lengths within 3-min period bands vary between ≈0.4-4.6 Mm and show some frequency dependence. Here, the damping lengths decrease with increasing frequency, see Table 4.2. Such frequency dependence is already noted for coronal fan loops and plumes (Krishna Prasad et al., 2014; Gupta, 2014). Waves also showed evidence of dispersion where higher frequency waves are propagating with higher speeds, see Table 4.2. Loops do not expand much in the first few Mm due to very large density stratification ≈50 Mm (see details in Rawat et al., 2025). These scale heights are very large compared to the observed damping length of the 3-min slow waves. Therefore, for the selected frequency range in corona, the effect of gravitational stratification and area divergence is negligible on the damping and dispersion of these waves. This makes the selected loop region and frequency range ideal to study the dispersive nature of the waves, which purely depends on the properties of the waves and their medium.

In summary, in this work, we report for the first time the direct observations of the dispersive nature of slow magnetoacoustic waves within the 3-min period band propagating along the different coronal fan loops. These waves also showed a well-known temperature-dependent propagation speed. We also studied the frequency-dependent damping of slow magnetoacoustic waves within the 3-min period band propagating along coronal fan loops and estimated their damping lengths. We find that slow wave phase speeds increase with frequency, whereas their corresponding damping length

decreases with frequency. We suggest that one of the possible reasons for frequency-dependent damping could be the dispersive nature of these waves. We also suggest some inverse relation between the damping lengths of waves and their frequency of propagation as provided in Kinsler et al. (1999) where $\lambda_A \propto \frac{1}{f^2}$.

Chapter 5

Magnetic field and plasma-β along fan loops

Sunspots on the surface of the Sun are intense collections of magnetic field lines or flux tubes, with near-vertical field strengths of $\approx$ 2000 G at the photosphere (Borrero and Ichimoto, 2011). The signatures of these magnetic field lines extending upward into the corona are visible as loops in coronal images. Various structures and loops within the sunspots show evidence of propagating 3-min slow waves (Khomenko and Collados, 2015). Magnetic field strength decreases rapidly along the solar atmosphere and is difficult to measure at higher heights. However, oscillations in coronal loops have been used to estimate the magnetic field strength in the corona (e.g., Nakariakov and Ofman, 2001; Van Doorsselaere et al., 2008b; Erdélyi and Taroyan, 2008; Taroyan and Erdélyi, 2009; Jess et al., 2016). Using MHD wave theory, Wang et al. (2007) determined magnetic field and plasma-β in the range 21-51 G and 0.15-0.91, respectively for hot loops showing standing slow waves. Recently, Yang et al. (2020) measured the plane-of-sky component of the global coronal magnetic field to be 1-4 G at 1.05 to 1.35 $R_{\odot}$.

Si et al. (2020) determined the average coronal magnetic field of 270$\pm$5 G using the spectroscopic data from Hinode. Similarly, Brooks et al. (2021) measured the coronal loop magnetic field strength and plasma-β in the range 60-150 G and 0.0005-0.001, respectively. Coronal magnetic field strengths are also measured using magnetic field extrapolation techniques (e.g., De Rosa et al., 2009). Li et al. (2020) determined the magnetic field and plasma-β around 10 G and 0.02-0.1, respectively, along a thin coronal loop emanating from a non-sunspot region using the PFSS extrapolation technique.

Plasma-β along the loops decides the potentiality of magnetic fields (Gary, 2001) and characteristics of different waves present in the loops (Jess et al., 2015). Gary (2001) developed a model for plasma-β variation above the active region from the photosphere to the corona by combining various models and observational data. Mathew et al. (2004) utilized spectropolarimetric measurements and determined plasma-β in the range of 0.5-1 inside the photospheric umbra. Jess et al. (2013) obtained the plasma-β=1 contour at the photospheric outer boundary of the sunspot penumbra using temperature and density from the sunspot model of Maltby et al. (1986) and the magnetic field from HMI magnetogram. Bourdin (2017) used a 3D magnetohydrodynamic model of the solar corona over an active region to determine the plasma-β from the photosphere to the corona. Cho et al. (2017) solved analytical functions of the cut-off frequency and estimated the average plasma-β value $\approx$0.83-0.86 within the umbra.

Till now, all these results have been reported either in the global corona or only at certain loop segments. Variations of these parameters along the whole loops are still unexplored due to their non-traceability in the lower atmosphere and thus remain unclear.

In the Chapter 3, we demonstrated the unique technique using 3-min slow waves to trace loops from the corona to the photosphere via the transition region and chromosphere in the umbral atmosphere, along with their cross-sectional areas. Using these tracings, we studied the propagation and damping properties of slow waves along the loops for the first time from the photosphere to corona in detail in Chapter 3 and Chapter 4, see also Rawat and Gupta (2023, 2024a,b). These findings can now also be utilized to estimate magnetic field strength and plasma-β along loops from the photosphere to the corona, which were not possible before due to their non-traceability. The content of this chapter is published in the Rawat et al. (2025).

5.1 Observations

To determine the variations of magnetic field and plasma-β along the fan loops rooted within the sunspot umbra, we need to trace the fan loops in the lower atmosphere (photosphere to low corona), where loops are not visible. These loops can be traced in the lower atmosphere using 3-min slow waves (details of the technique are provided in Chapter 3 and also in Rawat and Gupta, 2023). For this purpose, we have identified an

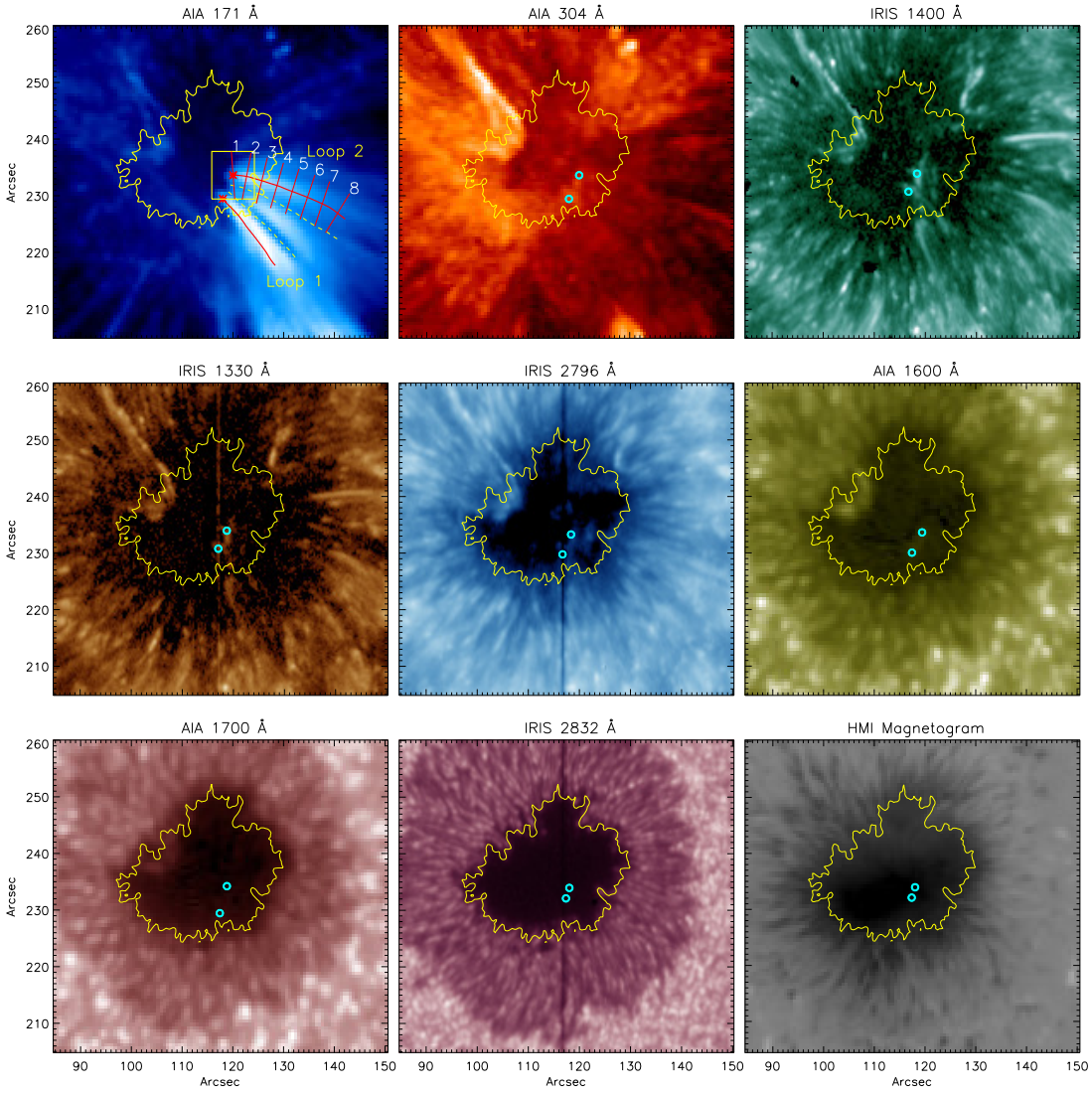

Figure 5.1: Images of sunspot and fan loops belonging to AR 12470 obtained from different AIA, IRIS, and HMI passbands as labelled. The red lines on the AIA 171 Å image represent the manual tracing of coronal fan Loops 1 and 2, and asterisk symbols (*) represent their coronal footpoints. The yellow dashed lines represent the background regions for those loops. The sample slits across the coronal Loop 2 are marked with solid red lines and numbered. The box enclosing the coronal footpoint of Loop 2 indicates the region chosen to identify loop locations at the lower atmospheric heights. Small circles (o) over different panels represent the loop locations identified at that atmospheric height (see details in Section 5.2.1). Contours over different panels indicate the umbra–penumbra boundary as obtained from the IRIS 2832 Å image.

appropriate dataset observed by the Atmospheric Imaging Assembly (AIA; Lemen et al., 2012), the Helioseismic and Magnetic Imager (HMI; Scherrer et al., 2012) both onboard the Solar Dynamics Observatory (SDO; Pesnell et al., 2012), and the Interface Region Imaging Spectrograph (IRIS; De Pontieu et al., 2014). To obtain good coverage over the lower atmosphere, we have identified an active region that was observed by all four IRIS slit jaw images (SJIs). This makes the tracing of the loops in the lower atmosphere more robust. The sunspot studied here belongs to the Active Region (AR) 12470, observed on 2015 December 19. We obtained 55 min of simultaneous data starting from 13:26:22 UT, as shown in Figure 5.1. We also utilize data from the sunspot belonging to AR 12553 observed on 2016 June 16, in which several fan loops were already traced and analysed in Rawat and Gupta (2023, 2024a,b), see also Chapter 3 and Chapter 4. Here also, we selected a few quiescent loops for our analysis as presented in Figure 3.2.

Images obtained from the IRIS-SJI passbands have an exposure time of 2 s with an effective cadence of 12.75 s, 0.332″ pixel^{-1} resolution, and 169″×182″ field of view. The analysed sunspot is slightly off the disc centre (heliocentric coordinates X ≈ 115″, Y ≈ 235″), the angle between the local vertical and the line-of-sight is ≈ 25^{o}, which leads to μ = cos θ ≈ 0.90. Therefore, we have ignored any projection effects on intensity oscillations and other parameters.

We co-aligned the AIA, IRIS, and HMI datasets using the IRIS-SJI 2796 Å and AIA 1700 Å image pair and the IRIS-SJI 2832 Å and HMI continuum image pair by utilizing the cross-correlation method. AIA, IRIS, and HMI images are derotated with respect to the starting time of IRIS using SSW routines. The identified dataset provides a unique opportunity to study atmospheric seismology through wave propagation along the whole solar atmosphere.

Norton et al. (2006) estimated the formation height of the HMI from Fe I 6173 Å line. They derived the HMI continuum formation height from line continuum to be ≈21 km, and HMI Doppler and magnetogram formation height from the line core to be ≈ 269 km above the optical depth of unity (τ_{5000}=1). These formation heights correspond to temperatures around 4200 K and 3700 K, respectively (Fontenla et al., 1999). AIA 171, 304, 1600, and 1700 Å passbands correspond to a coronal temperature ≈ 0.8 MK, transition region temperature ≈0.05 MK, chromospheric temperature ≈5700 K and lower chromospheric temperature ≈ 4500 K, respectively.

IRIS-SJI-1330 and 1400 Å passbands correspond to transition region temperatures ≈

20,000 K and 63,000 K, derived from C II and Si IV spectral lines, respectively. IRIS-SJI-2796 Å corresponds to a chromospheric temperature ≈ 10,000 K derived from the Mg II, and IRIS-SJI-2832 Å corresponds to a photospheric temperature ≈ 4200 K derived from the photospheric continuum (De Pontieu et al., 2014).

5.2 Data Analysis and Results

Figure 5.1 shows the analysed fan loop system rooted in the sunspot umbra in AR 12470 in AIA 171 Å image. The overplotted contour represents the umbral boundary identified from the IRIS-SJI-2832 Å passband. Fan loops are manually traced on the AIA 171 Å image, and asterisk (*) symbols represent the loop footpoints in the corona. We analyse several clean loops from AR 12470 and 12553. However, here we present results from Loop 2 from AR 12470 as a representative example, due to its 40% longer length and lower background signal, which allows estimation of loop cross-sections up to longer distances as compared to Loop 1. Section 5.2.4 summarizes the results from all the selected loops emanating from the sunspot umbra in AR 12470 and 12553.

5.2.1 Loop locations and cross-section areas at different heights

5.2.1.1 Upper atmosphere (corona)

To determine the diameter and cross-sectional area along the coronal fan loops in the AIA 171 Å image, we obtained the intensity profile along several slits across the loop. We fitted the intensity profiles with the Gaussian function and a linear background (e.g., Gupta et al., 2019). We then extracted the full width at half maximum (FWHM) of the fitted Gaussian as the diameter of the loop. Obtained diameter at coronal footpoint is ≈ 3.28±0.28 pixel. Sample intensity profiles and fittings at a few slit locations, marked in Figure 5.1, are presented in Figure 5.2.

5.2.1.2 Lower atmosphere (photosphere to corona)

For the lower atmospheric heights, where the loops are not visible, we devised a technique to trace back the footpoints and cross-section areas of coronal loops on the photosphere through the transition region and chromosphere in Chapter 3, see also Rawat and Gupta (2023). There we studied fan loops emanating from sunspot umbra belonging to AR 12533 (7° S, 8° N) observed simultaneously by IRIS and SDO on 2016 June 16.

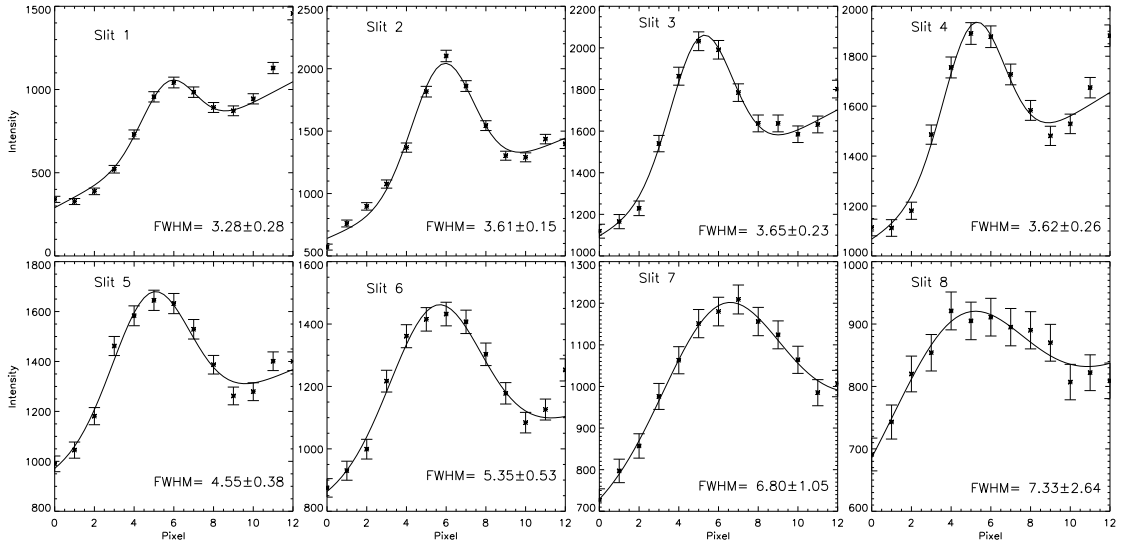

Figure 5.2: Intensity profiles along several slits across the coronal Loop 2 marked in Figure 5.1 as observed in the AIA 171 Å passband. All intensity profiles are fitted with the Gaussian function with a linear background. The obtained FWHM of the Gaussian function represents the diameter of the coronal loop along its length.

Due to a poor signal, data from the 1400 Å passband were not utilized. Therefore, we had very limited coverage over the whole solar atmosphere. In this study, along with AR 12553, we utilize a new dataset belonging to the sunspot of AR 12470, which was observed in all four passbands of IRIS SJIs, along with SDO. Together, these passbands provide better coverage over the whole solar atmosphere (details in Section 5.1). This makes the tracing of loops more robust in the lower atmosphere. Sunspots host waves and oscillations of a 3-min period in the umbral atmosphere, and both 3-min and 5-min oscillations at the umbral photosphere (for details see, Khomenko and Collados, 2015). In Chapter 3, we utilized the presence of 3-min oscillations over the whole umbral atmosphere observed by the IRIS and SDO passbands to trace and identify the photospheric footpoints of coronal loops in the lower atmosphere through the transition region and chromosphere. There, we also measured the propagation speed of 3-min waves and found them to be less than the acoustic speed at all the atmospheric heights, which confirmed that these are slow magnetoacoustic waves propagating along the traced loops. Here, we utilize the same technique to trace and identify the photospheric footpoints using a dataset with a larger number of passbands. This provides robust tracing of loops over the whole solar atmosphere through multiple coverages in the transition region and chromosphere. This also enabled us to deduce a better estimate of the loop

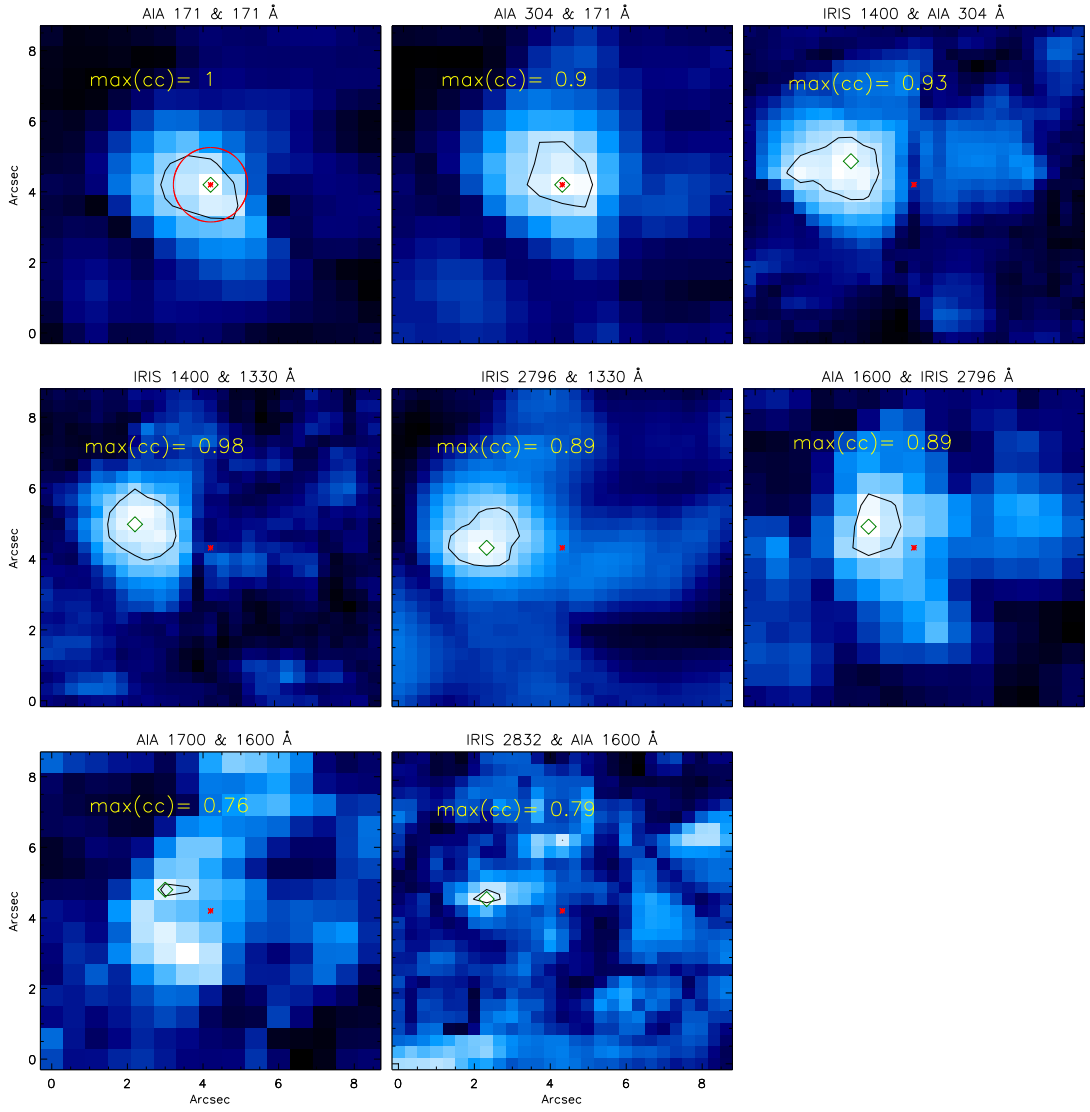

Figure 5.3: Correlation images obtained between various atmospheric heights as labelled. In each panel, the asterisk symbol (*) in the centre refers to the coronal footpoint of Loop 2, and the red circle represents the cross-section of the loop obtained from the AIA 171 Å image using the FWHM method. Overplotted black contours are obtained at $\approx 94 \pm 2\%$ of maximum correlation values. The green diamond ($\diamond$) symbols represent the locations of the maximum correlated pixel and the loop location at that height.

cross-sectional areas at different heights in the umbral atmosphere.

As per the method described in Chapter 3 and Rawat and Gupta (2023), we identified several fan loops in the AIA 171 Å image. We performed a correlation analysis to determine the loop locations and cross-sectional areas at different atmospheric heights in the lower atmosphere. We choose a box of size 9"×9" shown by the yellow box in the AIA 171 Å image in Figure 5.1 by positioning the coronal footpoint of Loop 2 in the centre of the box. We utilized 3-min (2-3.7 min period band) filtered light curves to perform the correlation analysis, which makes correlations depend only on 3-min oscillations. For correlating light curves between different passbands having different cadences, we first interpolated the light curves with longer cadences to light curves with smaller cadences using the IDL routine *interpol*. We have first interpolated the IRIS 1400 Å light curves to 12 s cadence to match the cadence of the 304 Å passband and also interpolated the AIA 1600 Å light curves to 12.75 s cadence to match the cadence of the IRIS 2796 and 2832 Å passbands. We correlated the light curve at the coronal loop footpoint in AIA 171 Å with light curves at each pixel in 9"×9" box. The correlation image is then created by noting the maximum correlation coefficients at each pixel in the box. The pixel with the maximum correlation coefficient in the correlation image depicts the location of the loop at that atmospheric height. This location was further utilized to identify the loop location and cross-sectional area at the lower heights in the solar atmosphere by cross-correlating the light curves again with the 9"×9" size box from the nearest temperature passband, as described above. In this way, we are able to trace the loop locations at different atmospheric heights till we locate their footpoint at the photosphere. The identified loop locations are marked with green diamonds (⋄) in Figure 5.3 and are also marked by small circles in Figure 5.1. In Figure 5.4, we show the fast Fourier transform (FFT) power spectrum obtained from the original light curves of the loop locations at various atmospheric heights, as labelled. The FFT power spectrum is yielded using the standard IDL routine $fft\_powerspectrum$. The associated plots show the distribution of power peaks in the period range of approximately 2–3.7 min at all the atmospheric heights, shaded with blue colour. We applied a bandpass filter over the period range of 2–3.7 min (blue shaded region in Figure 5.4) on the original signals. The filtered signals are shown in Figure 5.5. Filtration provides a clean intensity oscillation in the 2–3.7 min period range. Due to several nearby power peaks in this period band, we see oscillations in the form of unclean wave packets with modulations in oscillation

amplitude.

A contour level of about 92% of the maximum correlation coefficient value on the correlation image for the loop footpoint in the corona matches fairly well to the loop cross-section obtained from the FWHM. At various other heights in the lower atmosphere, closed contours are obtained within 94 ± 2 % of the maximum correlation values. The pixels with the maximum correlation coefficients in the correlation images depict the location of the loop at that atmospheric height. These locations are marked as small circles in Figure 5.1.

Further, we take the sum of the area of all the pixels falling within the contour of $\approx 94 \pm 2\%$ of the maximum correlation value of the correlation image between two atmospheric heights. This area can be considered as the representative size of the loop, i.e., the loop cross-section. The area within this correlation threshold decreases as we move into the lower atmosphere. This indicates loop expansion with increasing height in the lower atmosphere and suggests the geometric spreading of 3-min slow waves along the expanding loop. Furthermore, we determine the area scale height in the lower atmosphere by fitting the obtained cross-sectional area with an exponentially rising function

$$A(h) = A_o e^{\frac{h}{\lambda_A}}. \tag{5.1}$$

Here, $A(h)$ is the cross-sectional area at loop length h, λ_A is the area scale height, and A_o is an appropriate constant. The obtained area scale height for the lower atmosphere is $\lambda_{Al} \approx 518 \pm 46$ km.

To obtain the cross-sectional area along the loop in the corona, we calculated $\pi(\frac{FWHM}{2})^2$. The cross-sectional area along the loop is increasing, as shown in Figure 5.6. This expansion can also be visualized in the AIA 171 Å image in Figure 5.1. The obtained area of the loop footpoint in the corona is 3.04 ± 0.26 arcsec^2 from the FWHM method and 3.24 ± 0.18 arcsec^2 from the correlation analysis. Both values are well within the error bar. We fitted the area expansion along the coronal fan loop using an exponentially rising function with a constant background and obtained scale height $\lambda_{Ac} \approx 18.89 \pm 5.77$ Mm.

The cross-sectional area shown in Figure 5.6 is as per the expectations from the theory of flux tube expansion with height, where expansion in the lower atmosphere is faster (smaller λ_A) than expansion along the corona (larger λ_A). This is because the

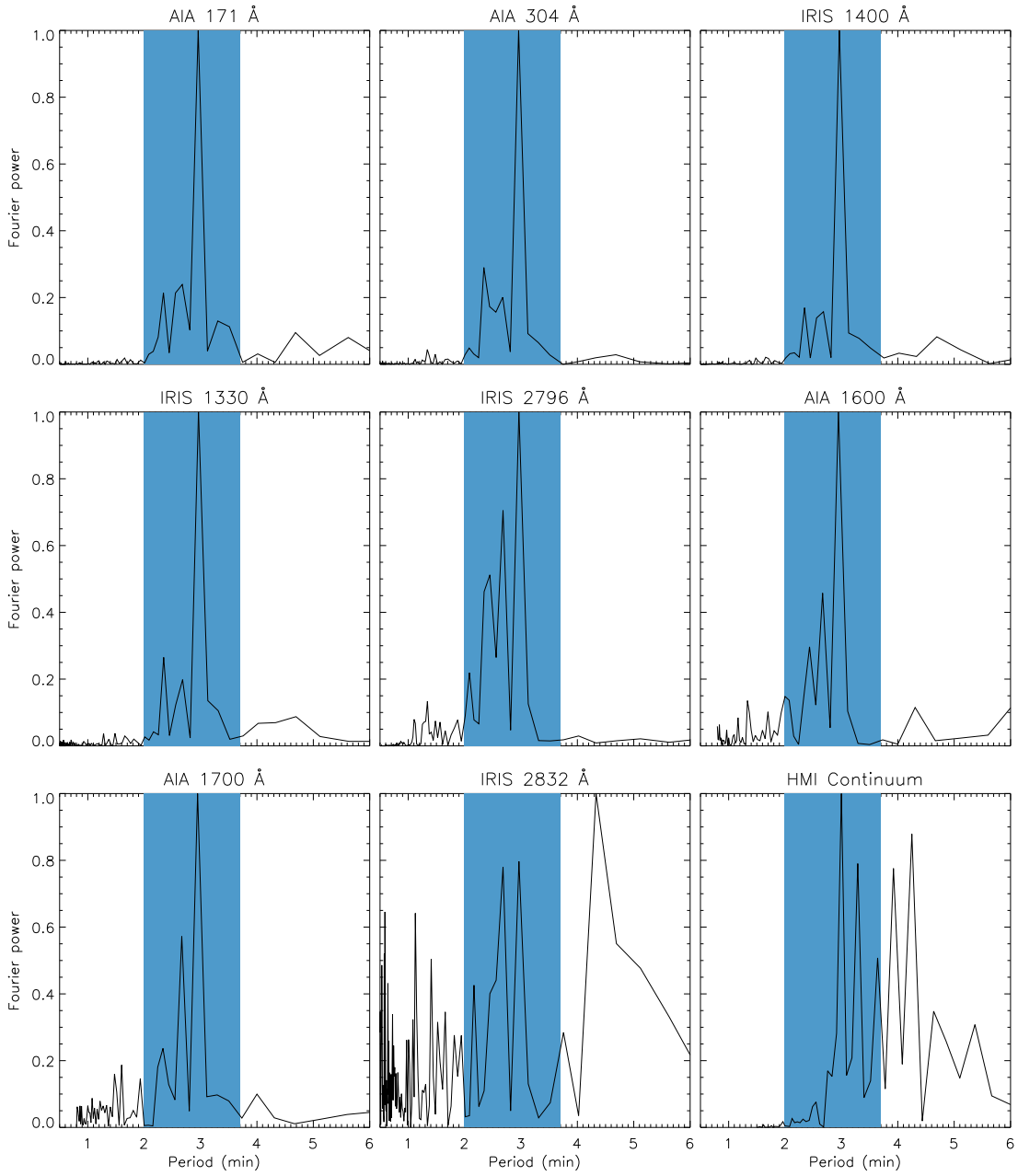

Figure 5.4: FFT power spectrum of original light curves obtained at each location of Loop 2 in the solar atmosphere as shown in Figure 5.1. Shaded regions in light blue colour denote the 3-min period band used to produce the filtered light curves shown in Figure 5.5.

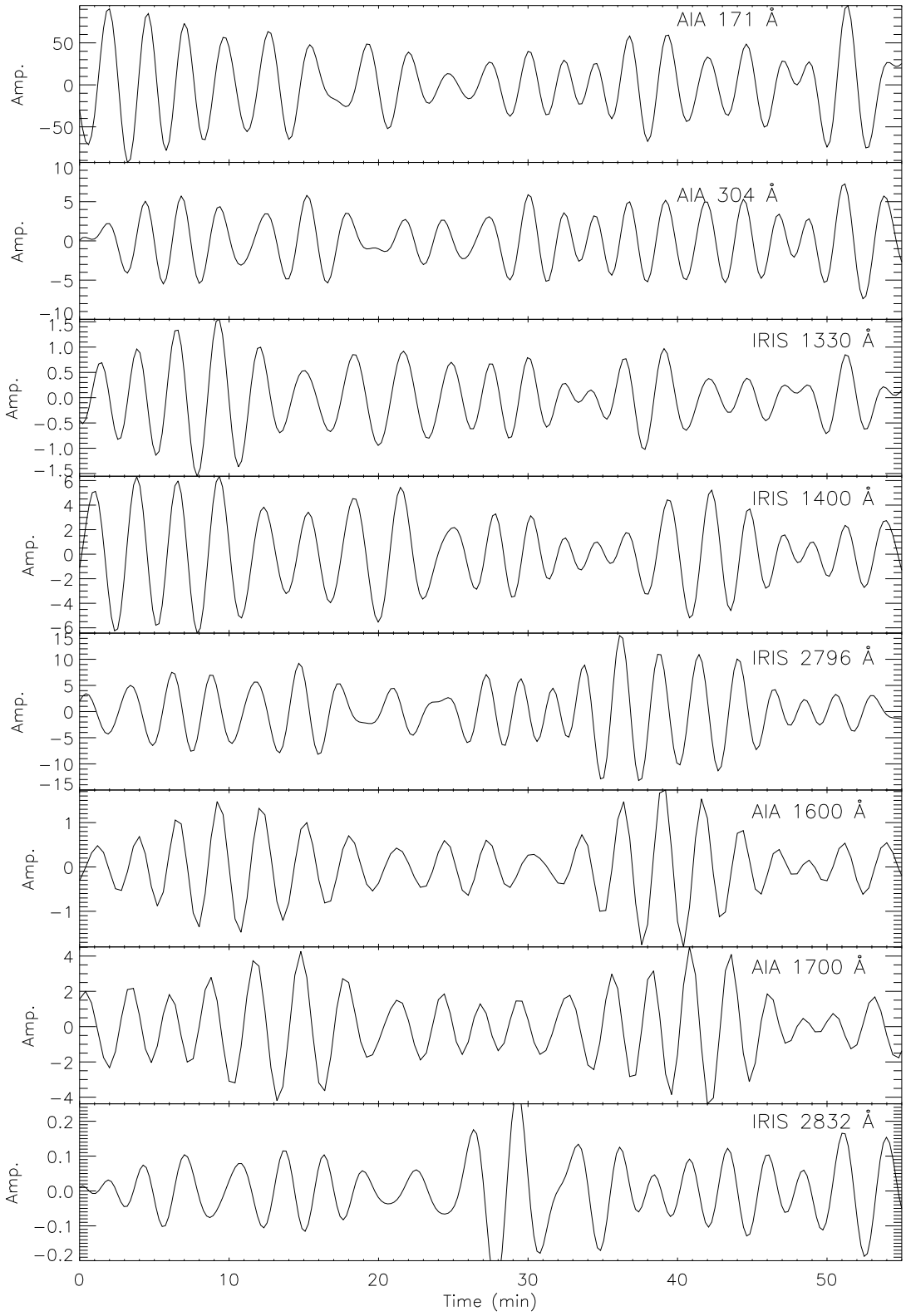

Figure 5.5: 3-min filtered light curves obtained from original light curves.

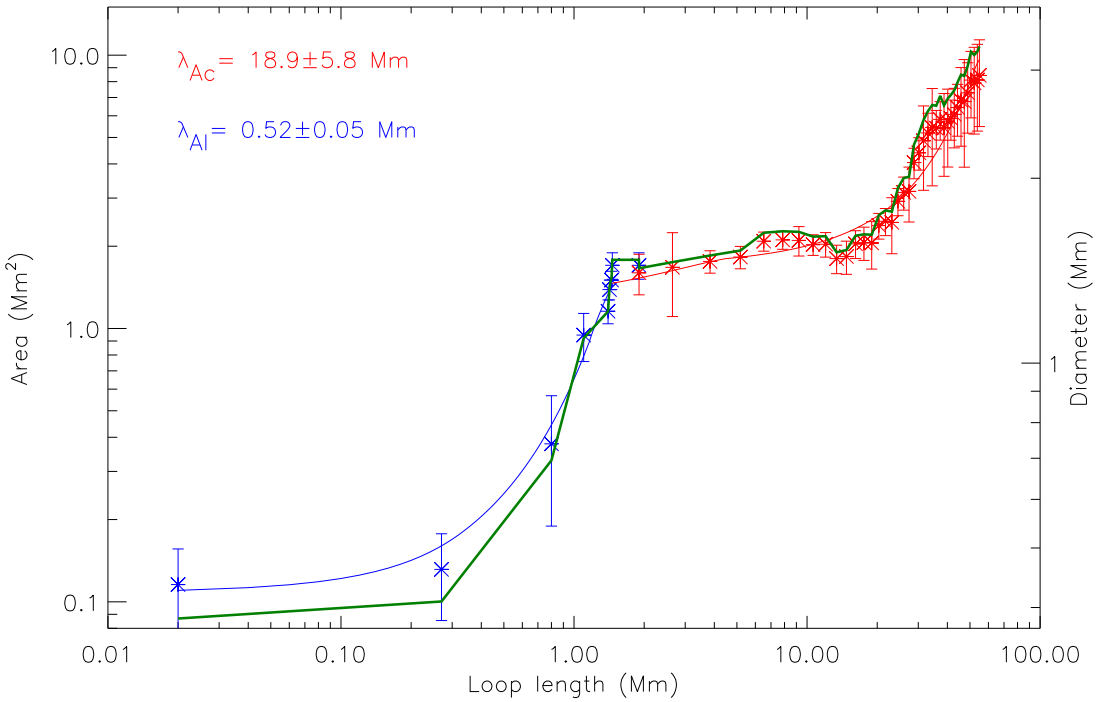

Figure 5.6: Cross-sectional area of the loop along its length. The area of the loop in the lower solar atmosphere is fitted with an exponentially rising function, shown in a blue solid line. The area along the coronal loop is also fitted with an exponentially rising function with a constant background, shown in the red solid line. Obtained area scale heights (λ_A) are printed in their respective colour code at the top left corner. The green line represents the equivalent diameter (w) of the loop along its length (right axis).

pressure scale height in the lower atmosphere is much smaller than that in the corona due to the steep change in atmospheric temperature. We also provide the diameter (w) of the loop in Figure 5.6, derived from the loop cross-sectional area upon assuming equivalent cylindrical loop geometry ($w = 2\sqrt{\frac{A(h)}{\pi}}$).

5.2.2 Temperature and density along the loop

In the corona, plasma emits across the entire electromagnetic spectrum. The emission processes and their dependence on density and temperature are well understood (e.g., Phillips et al., 2008; Del Zanna and Mason, 2018). Differential emission measure (DEM) represents the amount of plasma present at different temperatures along the line-of-sight (LOS). Intensity (I_i) from all six coronal EUV passbands of AIA/SDO can be modeled as $\int R_i(T)DEM(T)dT$ where R_i represents the temperature response function of each passband that is determined from the CHIANTI package (Dere et al., 1997; Dufresne et al., 2024). We also identified a quiet region near the loop, as shown by the dashed line in Figure 5.1 for background/foreground subtraction. We obtained the background-subtracted intensity along the loop by subtracting the background intensity from the loop intensity. The respective background-subtracted intensities along the loop from all six coronal passbands were then subjected to the regularized inversion code developed by Hannah and Kontar (2012) to obtain the DEM along the loop structure. The DEMs are 2 min averaged to enhance signal-to-noise ratios. The sensitivity of each AIA passband has degraded over time, using $AIA\_GET\_RESPONSE$ procedure, we have applied appropriate correction factors to the intensity and corrected the temperature response of each passband.

The DEM profile shown in Figure 5.7 is obtained at the coronal footpoint location marked with the red circle (o) in the top panel of Figure 5.1. This DEM profile is a double-peaked function. To identify loop and foreground/background emissions, we properly isolate the two peaks and integrate them over the given temperature ranges. The loops are clearly visible when the first peak is integrated, which indicates that the loops are emitting in this temperature range. The double-peaked behaviour is visible all along the loop. However, at the end of the loop, the two peaks merge in the background. We fitted the first peak by a Gaussian function and a polynomial of degree one. The blue line in Figure 5.7 shows the fitted DEM curve. Note that the vertical axis in Figure 5.7 shows the DEM, and the horizontal axis displays the temperature on a logarithmic scale.

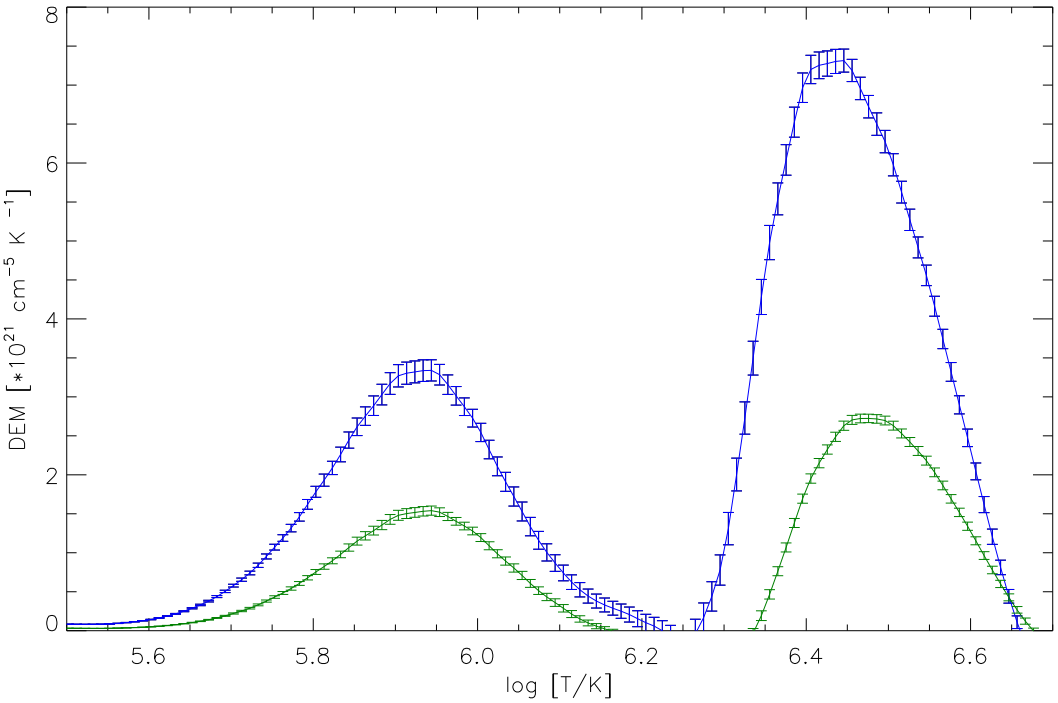

Figure 5.7: DEM profiles at the coronal footpoint of the Loop 2 shown by the asterisk in Figure 5.1. The green and blue curves are obtained with and without background-subtracted intensities, respectively.

The temperature at which the first Gaussian peak is considered as a measure of the loop temperature, whereas the area under this Gaussian curve provides the total emission measure (EM). The emission measure and electron number density (N_e) of the loop are related as $N_e = \sqrt{\frac{EM}{w}}$, where w is the width of the loop. We obtained the width of the loop as the FWHM of the intensity profile across the loop, as shown in Figure 5.2. Temperature and density variations along the loop in the corona are shown by red colour symbols in Figure 5.8.

The temperature along the loop slightly increases, although this increase is well within the error bars. The average temperature along the loop is 0.86 MK. Since the density obtained from the DEM method (5×10^9 cm^{-3}) at the coronal footpoint is slightly different from the density obtained from the sunspot model (10^{10} cm^{-3}, Fontenla et al., 1999), we scaled the density of the sunspot model by dividing it with 2 in Figure 5.8 to match the density at the coronal footpoint. Furthermore, we have assumed a 15% error in density and temperature in all our calculations (e.g., Gupta et al., 2019). The blue and red colours represent variations in the lower atmosphere and corona, respectively, and the same colour code will be used throughout.

For the lower atmosphere, since the temperature sensitivity of each IRIS and SDO

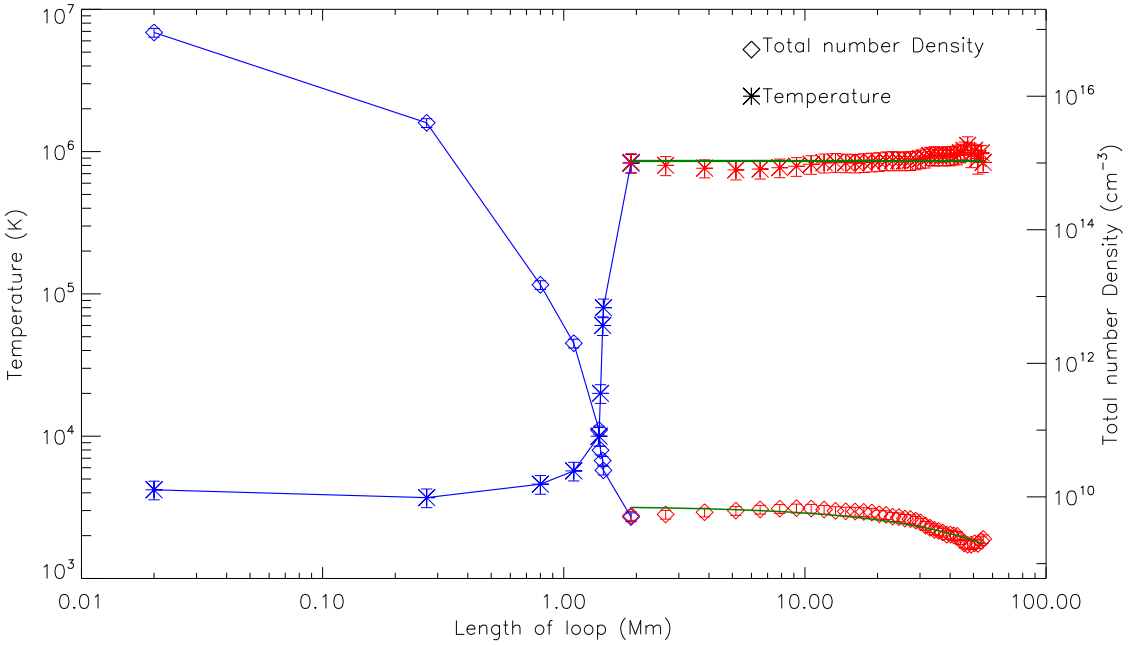

Figure 5.8: Temperature (left y-axis) and total number density (right y-axis) as a function of loop length shown by asterisks (*) and diamonds ($\diamond$), respectively. Temperature and density from the photosphere to the corona are obtained from the sunspot model of Fontenla et al. (1999) and shown in blue lines, whereas those in the corona are obtained using DEM analysis and shown in red symbols. The green lines overplotted over coronal temperature and density represent average loop temperature and a fitted exponentially decaying function, respectively.

passband is well known (see Section 5.1), we deduce the formation height and thus total number density ($N = N_e + N_h$; plasmas in the lower atmosphere are partially ionized) by utilizing the sunspot model of Fontenla et al. (1999), and plotted in Figure 5.8. In this model, the 0 km height represents the $\tau = 1$ layer at 5000 Å in the sunspot umbra.

5.2.3 Loop inclination

We fitted the total number density variation along the loop in the corona with an exponential decay function shown with the green line in the right panel of Figure 5.8. The fit provides observed density scale height $\lambda_{d\_obs} \approx 12.9 \pm 0.73$ Mm along the coronal loop. This is a plane-of-sky projected scale height due to the inclination of the loop. All the fits are performed using the MPFITFUN routine (Markwardt, 2009). We compare this λ_{d_obs} with the expected density scale height (λ_{d_exp}) from hydrostatic equilibrium in corona, i.e., $\lambda(T) = \frac{k_b T}{\mu m_p g} \approx 46[\frac{T}{1MK}]$ Mm, where μ is mean molecular weight, m_p is the mass of the proton, and g is the acceleration due to gravity at the solar surface (see e.g., Aschwanden et al., 1999b; Gupta et al., 2015). Since the average temperature of the

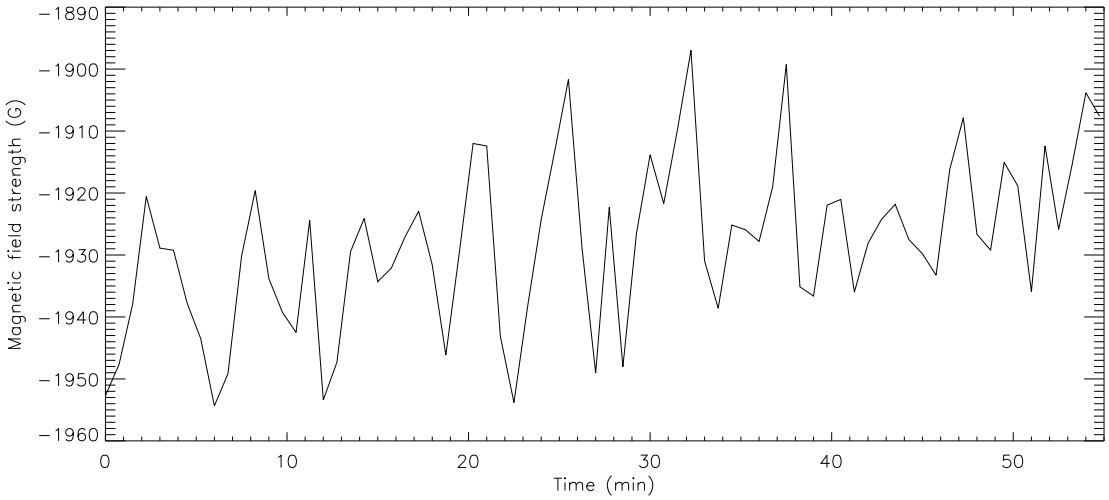

Figure 5.9: The line of sight magnetic field oscillations at the photospheric footpoint of the loop.

loop is 0.86±0.13 MK, $\lambda_{d\_exp} \approx 39.56 \pm 5.98$ Mm. This difference in both scale heights provides the inclination angle (ϕ) of the loop,

$$\cos(\phi) = \frac{\lambda_{d\_obs}}{\lambda_{d\_exp}} \tag{5.2}$$

(e.g., Aschwanden et al., 1999b). The loop is $\phi = 71^\circ$ inclined with respect to the plane-of-sky. Therefore, we have corrected the coronal loop length by multiplying it by a factor of 3.07.

5.2.4 Magnetic field strength and plasma-β along the fan loop

Loops are a manifestation of magnetic flux tubes in which the total magnetic flux remains constant along their length. We have already obtained the cross-sectional area of the loop at the photosphere ($A_p \approx 0.22$ arcsec^2) and its variation along the loop length ($A(h)$) as shown in Figure 5.6. From the loop tracing, we have identified the loop footpoint at the photosphere and obtained the magnetic field using the HMI magnetogram data (at atmospheric height 269 km). The magnetic field variation at the photospheric footpoint of the loop is shown in Figure 5.9. We determined the root mean square (RMS) magnetic field strength (B_p) with one sigma error at the photosphere as 1928 ± 13 G during the 55-min time sequence. The magnetic field strength along the loop length is calculated using

$$B(h) = \frac{B_p A_p}{A(h)}. \tag{5.3}$$

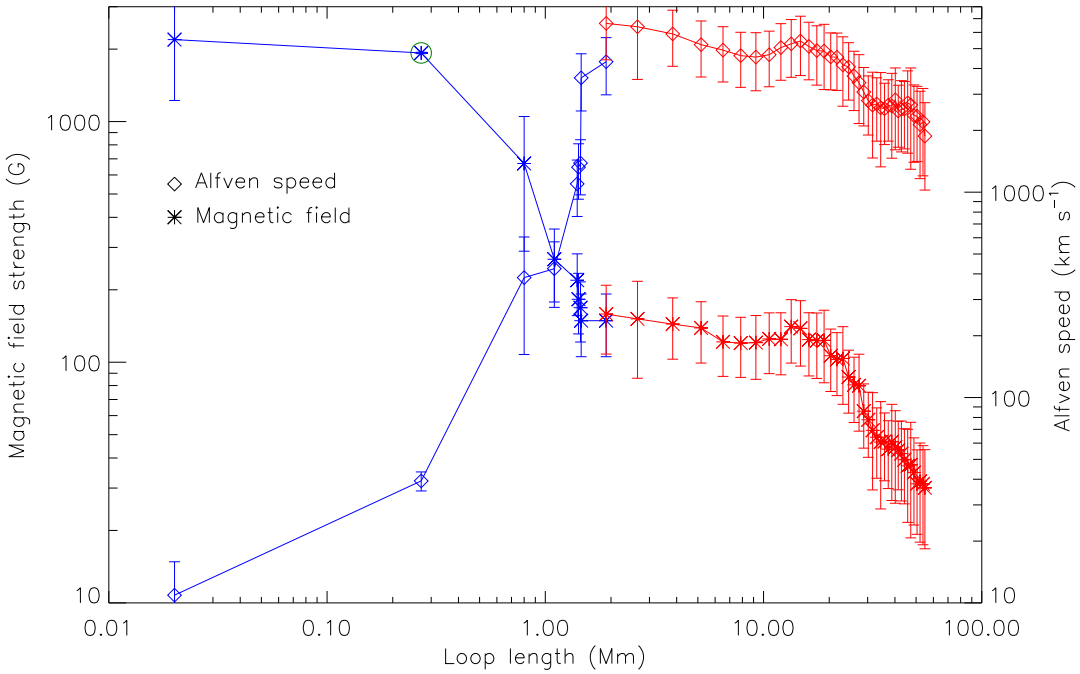

Figure 5.10: Variation of magnetic field strength (left axis) and Alfvén wave speed (right axis) along the loop. The green circle (O) represents the RMS magnetic field strength obtained from the HMI magnetogram.

The error in $B(h)$ is calculated from errors in the cross-sectional area and photospheric magnetic field strength. The obtained magnetic field variation with the error bars along the loop length is plotted in Figure 5.10. We obtained the magnetic field strength at the coronal footpoint $\approx$ 158$\pm$50 G. Furthermore, we also determined the Alfvén speed variation along the loop length using,

$$V_A(h) = \frac{B(h)}{\sqrt{4\pi\rho(h)}} \tag{5.4}$$

where $\rho(h) = N_e(h)m_e + N_h(h)m_h$ is the total mass density and plotted in Figure 5.8. Alfvén speed increases in the lower atmosphere, peaks at the coronal footpoint, and then decreases further in the corona. Such speed variation are also noted before (e.g., Aschwanden et al., 1999b; Cranmer and van Ballegooijen, 2012).

The obtained density, temperature, and magnetic field strength are further utilized to estimate the plasma-β along the loop using Equation 1.18. The results are presented in Figure 5.11. The dark blue shaded region in the left panel represents the variation of plasma-β along Loop 2. In the bottom left panel, we fitted a straight line between the temperature minimum region and photospheric plasma-β values. We extended it fur-

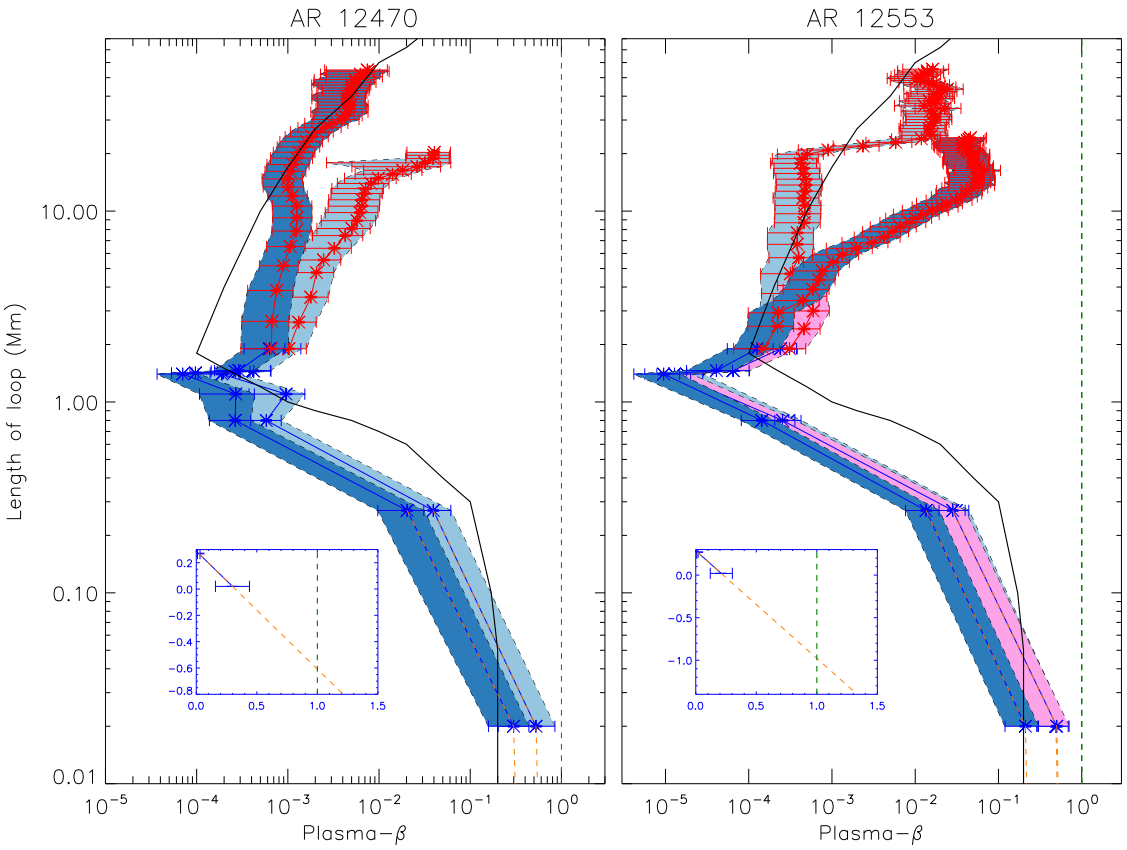

Figure 5.11: Left: Variation of plasma-β along the fan loops belonging to AR 12470, where light and dark blue shaded regions are for loops 1 and 2, respectively. Right: Variation of plasma-β along the fan loops belonging to AR 12553, where the light blue, dark blue, and pink shaded regions are for loops 3, 5, and 6, respectively. The black solid lines represent data points extracted from Gary (2001) for the umbral region. The vertical green dashed lines indicate the plasma-$\beta = 1$ layer. The orange dashed lines are the linear extrapolation of data points to determine the plasma-$\beta = 1$ layer. The small boxes in the lower left corners show the height at which loops 2 and 5 cross the plasma-$\beta \approx 1$ layer as representative examples.

Table 5.1: Various parameters derived along fan loops identified in AR 12470 and 12553. λ_{Al} and λ_{Ac} are the area scale heights of loops from the photosphere to the transition region and in the corona, respectively. B_p and B_c are magnetic fields at photospheric and coronal footpoints of fan loops, respectively. $< T >$ and N_{cf} are the average coronal loop temperature and total number density at the coronal footpoint, respectively. V_{Ac} is the Alfvén speed at coronal footpoints. β_p and β_c are the plasma-β values at photospheric and coronal footpoints, respectively. The plasma-$\beta \approx 1$ heights along fan loops are measured with respect to the optical depth of unity ($\tau_{5000} = 1$).

Loop no.	λ_{Al} (km)	λ_{Ac} (Mm)	B_p (G)	B_c (G)	$< T >$ (MK)	N_{cf} cm^{-3}	V_{Ac} (km s^{-1})	β_p	β_c	$\beta \approx 1$ height (km)
AR 12470										
1	521±44	5.85±1.85	1828±12	164±59	0.85	7.8×10^9	5173	0.52	0.001	-227
2	518±46	18.89±5.77	1928±13	158±50	0.86	5.0×10^9	6637	0.30	0.0006	-617
AR 12553										
3	884±152	4.08±0.55	1596±15	236±86	0.86	5.2×10^9	10004	0.49	0.0002	-264
5	769±114	4.22±1.1	1907±120	224±82	0.82	3.0×10^9	12209	0.21	0.0001	-980
6	900±168	–	2269±06	227±83	0.89	5.1×10^9	9146	0.50	0.0003	-244

ther to find the plasma-$\beta = 1$ layer at ≈ -617 km height, as shown in the orange dashed line. The negative height signifies that the plasma-$\beta = 1$ layer is below the photosphere ($\tau_{5000} = 1$). The plasma-β at the photospheric and coronal footpoints are 0.3 ± 0.14 and 0.0006 ± 0.0003, respectively. Additionally, as we move along the loop in the corona, the loop merges with the background corona, making it difficult to measure any loop parameters beyond 60-70 Mm. Moreover, density estimation from DEM analysis may change depending upon background subtraction location; accordingly, plasma-β estimates in the corona will also change. However, such changes will be well within the estimated error bars of about 50%.

We performed a similar analysis on the other fan loops identified in AR 12470 (see Figure 5.1) and also in AR 12553 (see Figure 3.2), where loops were already traced in Chapter 3. All the loop footpoints at the photosphere are directed toward the umbral centre, and their cross-sectional areas are smaller than their coronal counterparts, as found for Loop 2. The results suggest more or less similar statistics for all the loops in the lower atmosphere and corona with similar plasma-β variations. The summary of all the analysed loops is provided in Table 5.1.

5.3 Summary

In this work, we traced several umbral fan loops in the corona and from the corona to the photosphere, where loops are not visible. We obtained their cross-sectional area at different heights in the solar atmosphere and located their photospheric footpoints.

The area of Loop 2 decreased from 3.24±0.36 arcsec^2 (1.70±0.19 Mm^2) in the corona to 0.22±0.11 arcsec^2 (0.11±0.05 Mm^2) at the photosphere. The scale height of area expansion for Loop 2 from the photosphere to the corona is ≈ 0.52 Mm, whereas that in the corona is ≈ 19 Mm. Such expansions are expected in the solar atmosphere (see Section 1.5). Similar loop expansion from photosphere to corona is also noted by Bailey et al. (2025, and references therein).

We estimated the magnetic field strength of 158 ± 50 G at the coronal loop footpoint that decreases slowly along the coronal loop. Our estimates match very well with the magnetic field values reported by Brooks et al. (2021) using the recently developed spectroscopic diagnostic technique and also with the measurement of Gupta and Nayak (2022) of about 143 G along the transient loop using the magnetic field extrapolation method. These coronal magnetic field measurements along the loops are much larger than the usually quoted average global coronal magnetic field strength of 1-4 G (Lin et al., 2004; Yang et al., 2020), and also the average coronal loop magnetic field of 4-30 G obtained from kink oscillations (Nakariakov and Ofman, 2001; Aschwanden and Schrijver, 2011). Such large estimates of the magnetic fields along the loops will lead to larger Alfvén wave energy flux than those quoted in literature (e.g., Banerjee et al., 2009; McIntosh et al., 2011; Gupta et al., 2019) as needed in Alfvén wave heating models (e.g. Grant et al., 2018; Karampelas et al., 2024).

Plasma-β variations reported by Gary (2001) for the umbral regions are similar to those obtained for fan loops with slightly different values (see Figure 5.11). Interestingly, plasma-β values at chromospheric heights are consistently smaller than those provided in Gary (2001). At longer loop lengths, fan loops merge with the active region background, and our plasma-β values also merge with Gary (2001). The differences in the values could be due to the fact that we are tracing single isolated loops, whereas the values extracted from Gary (2001) are for integrated sunspot umbra. The overall similarity with the variation pattern of Gary (2001) indicates that our loop tracing method works well in the lower atmosphere. The value of plasma-β<1 along the whole loop length from the photosphere to the corona indicates that the umbral loops are potential in nature (e.g., Borrero and Ichimoto, 2011). We also noted that the plasma-β=1 layer exists at sub-photospheric heights (e.g., Cally et al., 1994). This layer is important for helioseismological studies (e.g., Khomenko and Collados, 2015) and demands a detailed investigation.

In summary, we obtained variations of cross-sectional area expansion, magnetic field strength, and plasma-β along the individual loops from the photosphere to the corona. Estimated parameters will provide useful ingredients for the MHD modeling of loops emanating from the sunspot regions and wave dynamics in the density-stratified and expanding waveguides (e.g. Taroyan and Erdélyi, 2009; Luna-Cardozo et al., 2012). It will also be important to carry out detailed statistical investigations of the estimates on magnetic field and plasma-β along loops emanating from different regions on the Sun and their comparison with different techniques.

Chapter 6

Spectroscopic diagnostics of coronal fan loops

The high temperature of the solar corona is an 80-year-long-standing problem in solar physics. Loops, which are considered the building blocks of the solar atmosphere, act as a waveguide and carry waves that may heat the solar atmosphere (Reale, 2014). These loops are classified into three categories depending on their characteristic temperatures: cool loops ($\leq$ 1 MK), warm loops ($\approx$ around 1 MK), and hot loops (3-5 MK). Loops are distinguishable in corona as their intensity is about 20%–30% stronger than foreground/background diffuse emission (Del Zanna and Mason, 2003; Viall and Klimchuk, 2012). To calculate various plasma parameters along the loops, various spectroscopic and imaging data techniques are developed to provide us with density, temperature, etc., see details in the Section 2.2.

The ubiquitous presence of outward propagating Alfvén wave, and slow waves along coronal loops are reported in the solar corona(e.g., Tomczyk et al., 2007; Krishna Prasad et al., 2012). Evidence of damping of propagating Alfvén waves and slow waves along coronal loops have also been reported (e.g., Gupta, 2017; Meadowcroft et al., 2024). However, the signature of dissipation of these mechanical/non-thermal wave energies into heat energy is still not observed (e.g., van Ballegooijen et al., 2011). Alfvén waves are incompressible and transverse in nature, which generally makes them difficult to observe through imaging instruments.

Alfvén waves are considered as a potential candidate to heat the solar corona as they can carry a large energy flux generated at the photosphere without much damping

along magnetic field lines (Hollweg, 1978; van Ballegooijen et al., 2014). However, their incompressible nature makes it difficult to explain how they can be a major supplier of heat to coronal plasma (e.g., Hollweg, 1997). Therefore, Alfvén waves need an efficient dissipation mechanism to explain their role in the heating of plasma, such as phase mixing, mode conversion, resonant absorption, or turbulence. The proposed Alfvén wave heating models are discussed in the recent review of Van Doorsselaere et al. (2020) and references therein. These models propose that these incompressible waves transfer their energy to compressible waves, which can easily damp in the solar atmosphere. Some more details on Alfvén waves are provided in Section 1.4.3.2.

Previously, on assuming average coronal magnetic field strength of ≈ 10 G in coronal active regions (e.g., Lin et al., 2000; Van Doorsselaere et al., 2008b), the reported Alfvén wave energy fluxes were of the order $\approx 10^6$ erg cm^{-2} s^{-1} (e.g., Tomczyk et al., 2007; Gupta et al., 2019). These wave energy fluxes are less than the energy flux required to maintain the active region corona, i.e., $\approx 10^7$ erg cm^{-2} s^{-1}(Withbroe and Noyes, 1977). Therefore, it was considered that though Alfvén waves can heat the quiet Sun corona, but can not heat the hot and dense active region corona (e.g., Tomczyk et al., 2007; McIntosh et al., 2011). However, in the recent work, Brooks et al. (2021) and Rawat et al. (2025) reported significantly higher magnetic field strength and Alfvén wave speeds along the coronal loops. These new estimates can significantly increase the previously underestimated Alfvén wave energy flux.

Here, we present a comparison of plasma parameters obtained from imaging and spectroscopic instruments to explore plasma and wave properties along the coronal fan loop structures anchored within a sunspot. Fan loop structures provide an excellent site to study the propagation of waves in the corona, see Chapter 3. In this chapter, we focus on estimating the temperature, density, and non-thermal velocity along these loops using simultaneous imaging and spectroscopic data. We will further determine the Alfvén wave energy flux along these fan loops in the corona.

6.1 Observations

The analysed fan loop system belongs to active region NOAA AR 11101 was observed simultaneously by Extreme Ultraviolet Imaging spectrometer (EIS; Culhane et al., 2007)

Table 6.1: List of EIS emission lines selected for our analysis. Lines are emitted by different ions at different wavelengths, formed at their peak formation temperature.

Ion	λ_{obs} Å	Temp. MK
Mg V	276.16	0.32
Fe VIII	185.21	0.54
Fe IX	197.86	0.86
Fe X	184.54	1.06
Fe XI	192.82	1.28
Fe XII	192.39	1.50
Fe XII	195.12	1.50
Fe XII	186.88	1.50
Fe XIII	201.12	1.72
Fe XIV	270.53	1.94

onboard (Hinode; Kosugi et al., 2007) and (AIA; Lemen et al., 2012) onboard Solar Dynamics Observatory (SDO; Pesnell et al., 2012) on 2010 August 30. We obtained 2 h of data starting from 11:13:30 UT, as shown in Figure 6.3. AIA extreme ultraviolet (EUV) images provide good coverage over the transition region and the corona at a resolution of 0.6" pixel^{-1} and a cadence of 12 s.

The EIS performed a raster scan with a 1" slit and an exposure time of 60 s and moved with a step size of 2". The raster scan started at 11:13:34 UT and covered a field of view of 240"$\times$512". Observations were performed over the wavelength range of 180-204 Å and 248-284 Å. We followed the standard procedures for preparing the EIS data using IDL routine EIS_PREP, available in the solar software (SSW; Freeland and Handy, 1998), which calibrates and corrects for the slit tilt and orbital drift. The spatial offset in the solar Y-direction at different wavelengths was corrected by co-aligning the images with EIS Fe XII 195.12 Å. We extracted regions with EIS FOV from the full disc images of AIA/SDO.

For an optically thin corona, the emission line intensity (I) can be given as

$$I(\lambda_{i,j}) = \int C(T_e, N_e) N_e^2 dh, \tag{6.1}$$

Here, the abundance is assumed to be constant over the source volume (Feldman, 1992), N_e is the electron number density, h is the column depth of emitting plasma along the line-of-sight (See Section 2.2).

For our analysis purpose, we have identified several isolated and unblended spectral

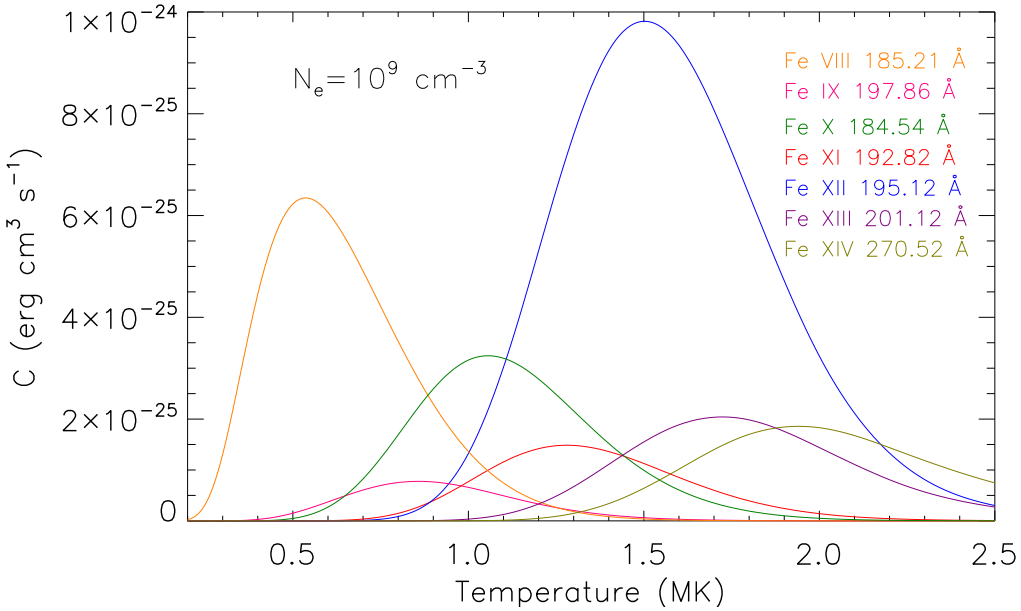

Figure 6.1: Contribution functions of various spectral lines used in this study.

lines having good signal strength, which are tabulated in Table 6.1. In Figure 6.1, we plot contribution functions of the selected EIS spectral lines obtained at a constant electron number density $N_e = 10^9$ cm^{-3} using the CHIANTI database (Del Zanna et al., 2021). All the selected spectral line profiles are then fitted with a Gaussian function. In Figure 6.2, we show sample spectral line profiles along with their fitted Gaussian profiles.

Imaging data allows us to co-align data from different instruments, and thus allows us to simultaneously utilize data from different instruments operating at different wavelengths. All AIA images are derotated with respect to the EIS starting observation time. We fitted all the EIS spectral line profiles with a Gaussian function using EIS_AUTO_FIT. This routine provides 1σ error on the fitted parameters. Since EIS sensitivity is deteriorating, we have further recalibrated the obtained intensity and error bars using (Del Zanna, 2013). We co-aligned EIS and AIA observations using EIS 195 Å and AIA 193 Å images using the cross-correlation method. In Figure 6.3, we plot monochromatic intensity maps of the fan loop system obtained from various EIS spectral lines (top panels). We also plot AIA images of the fan loop system from the different passbands sensitive to the same ions as in the top panels.

The identified data set provides a unique opportunity to study the spatial, temporal, and spectral evolution of waves in intensity and Doppler broadening along the plane-of-sky and line-of-sight, respectively, in the corona. Additionally, this is among the few rare observations where the fan loops emanating from the unipolar sunspot are rastered

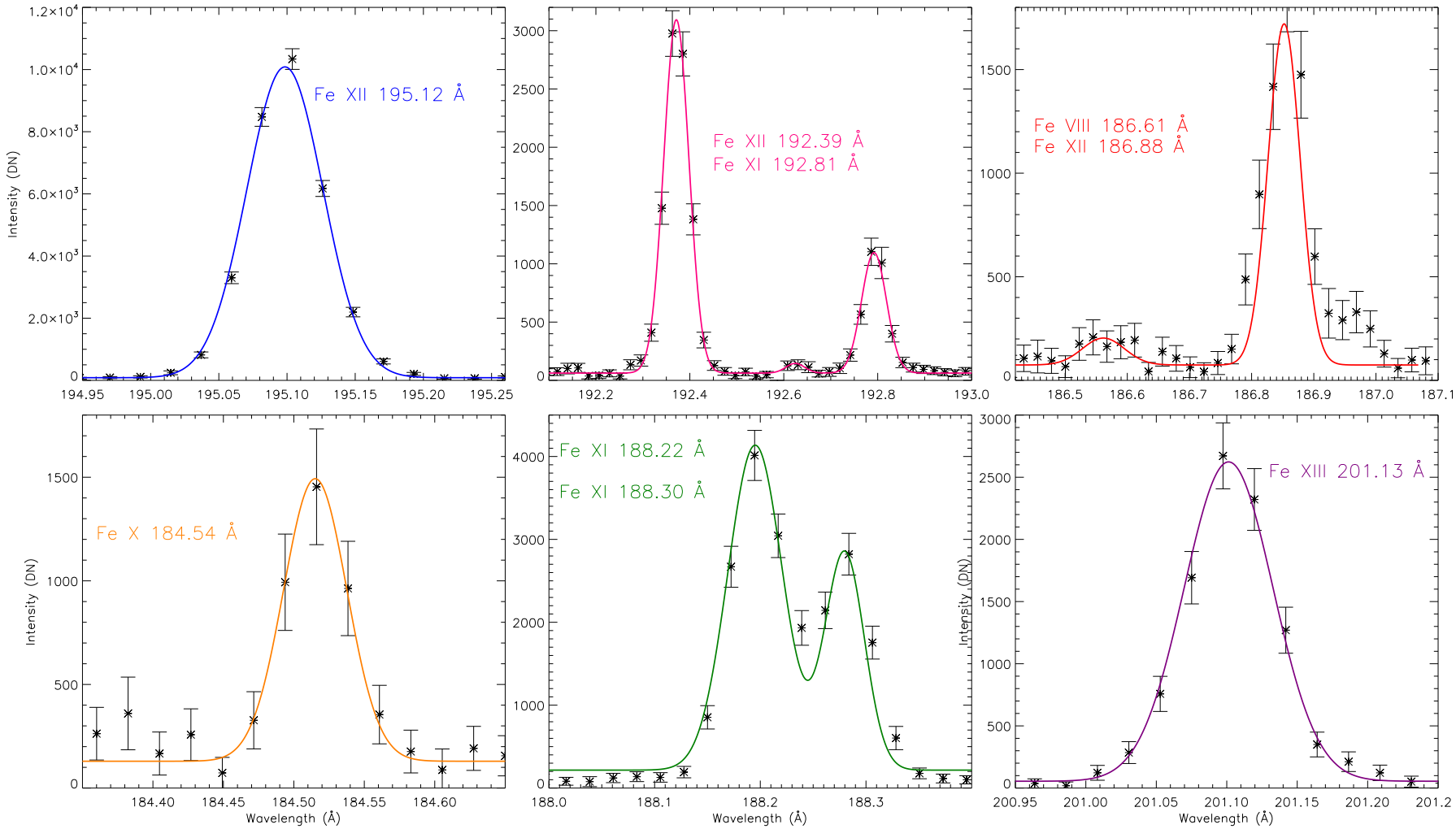

Figure 6.2: Sample spectral line profiles obtained at the coronal loop footpoint along with their fitted Gaussian functions.

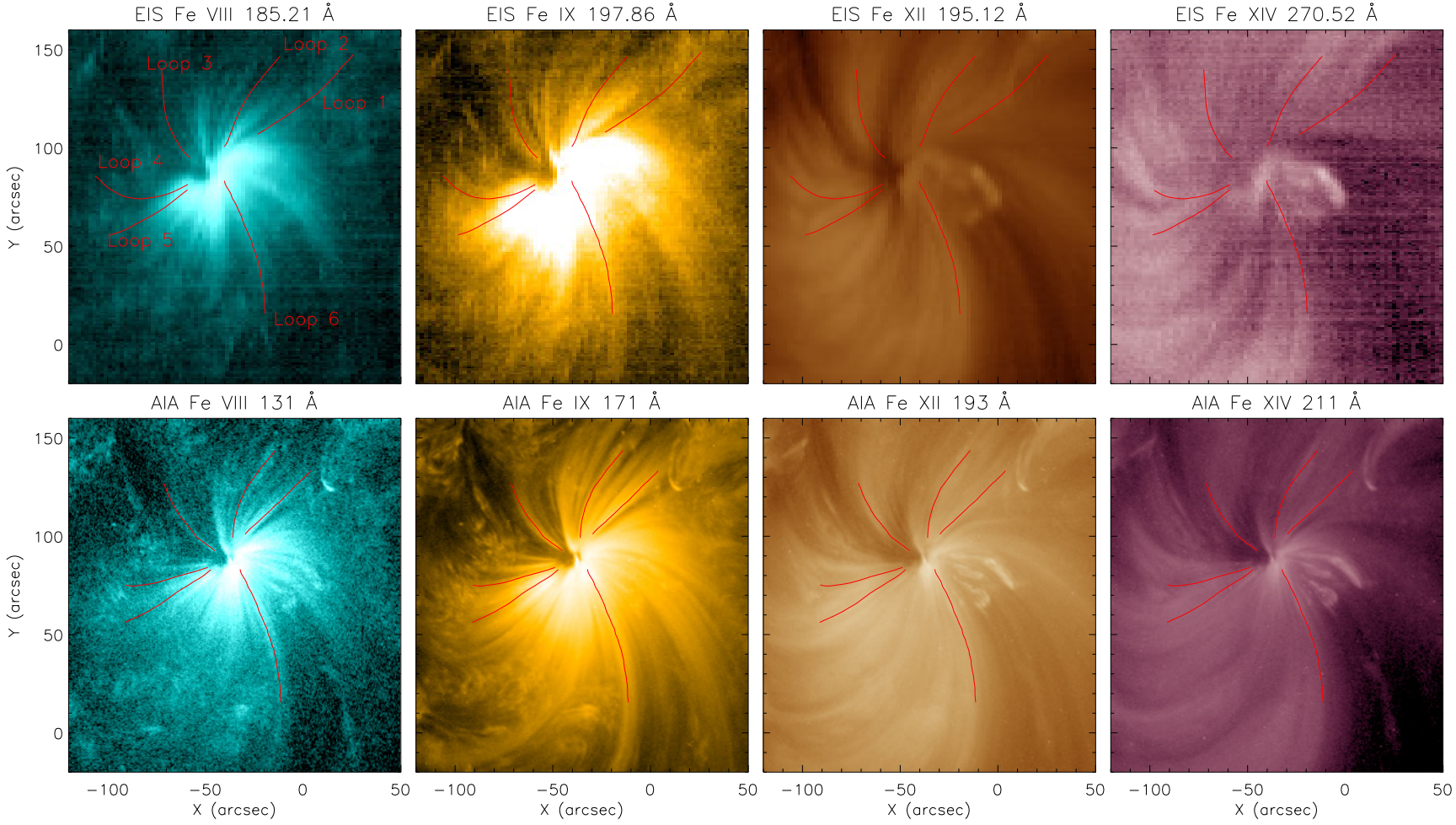

Figure 6.3: Top panels: Monochromatic intensity map of fan loop system obtained from various EIS spectral lines as labelled. Bottom panels: Images of the fan loop system from the different AIA passbands sensitive to the same ions as in the top panels.

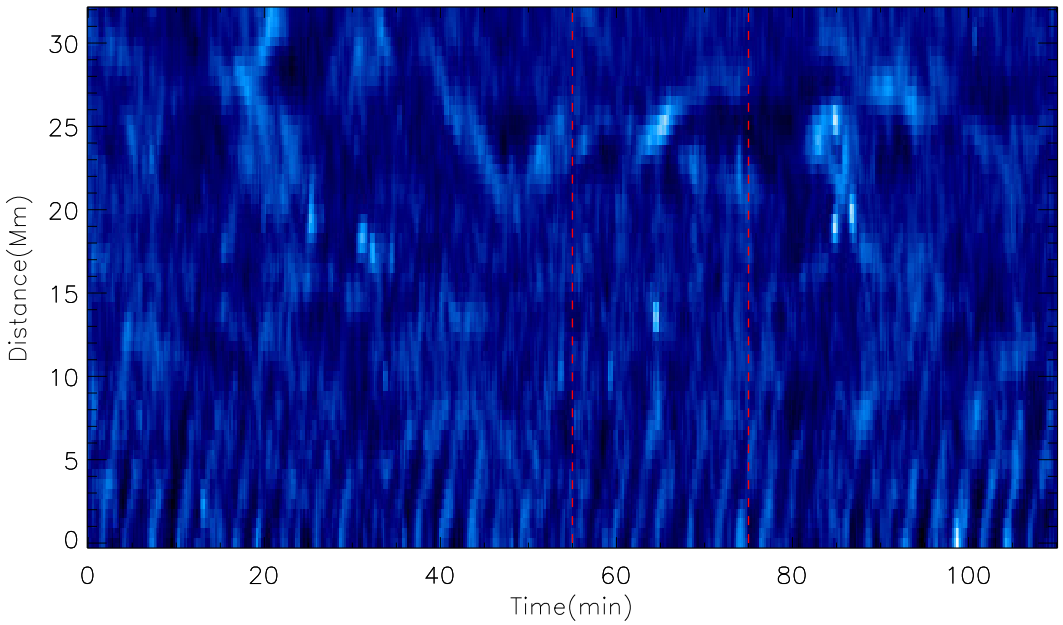

Figure 6.4: Time–distance maps produced from detrended light curves along the Loop 1 identified in Figure 6.3 for AIA 171 Å passband. The 3-min period slow waves propagating along the loop are visible as alternate bright and dark ridges at the bottom of the plots. The red dashed box shows the time duration at which the loop was traced by EIS.

with the EIS 1" slit.

6.2 Analysis and Results

Figure 6.3 shows the analysed fan loops in the solar corona observed by AIA and EIS as labelled. We have identified six fan loops, which are clearly visible in the hot and cool AIA passbands and several EIS spectral lines. These loops can be traced in the AIA and EIS images. The overplotted lines represent the manual tracing of the loops. Since loops are traced separately in the AIA and EIS images, there might be slight offsets along the loop locations from the AIA and EIS. Here, we present results for Loop 1 as a representative example.

6.2.1 Loop evolution/Stability

To determine the stability of the loop with time during the EIS raster, we obtained the detrended light curves from AIA 171 Å by subtracting the background light curves (18-min running average of the original light curves) from the original light curves at those loop locations. These detrended light curves are further utilized to plot the time-distance

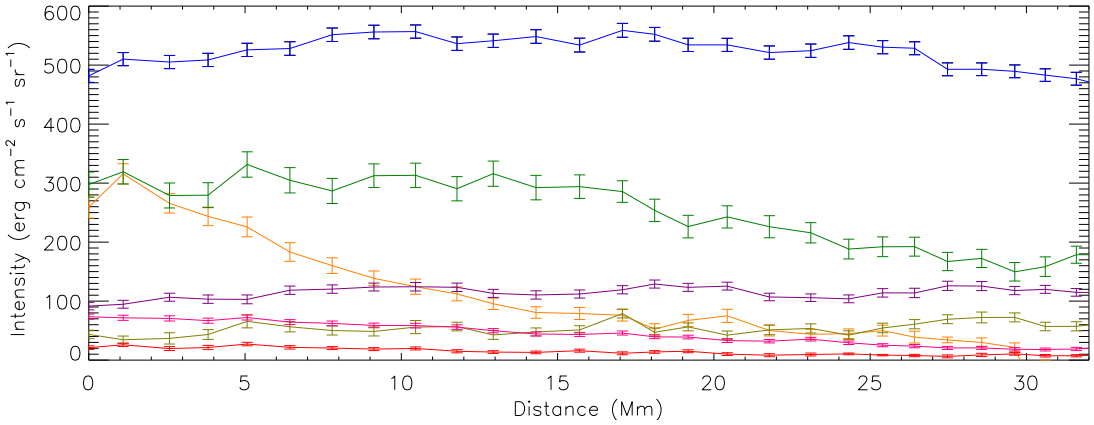

Figure 6.5: Intensities in different spectral lines plotted in different colours along the coronal Loop 1. The colour code for different ions is the same as in Figure 6.1, i.e., Fe VIII (orange), Fe IX (pink), Fe X (green), Fe XI (red), Fe XII (blue), Fe XIII (purple), and Fe XIV (olive).

intensity map along the fan loop, as shown in Figure 6.4. The time-distance image shows intensity evolution with time along the fan loop in the form of alternate bright and dark regions, indicating the presence of well-known 3-min slow magnetoacoustic waves, see Chapter 4. Here, we are plotting a 120 min long time series during which EIS was observing the fan loop system. The red box shows the time duration during which the loop was rastered by EIS. We note that up to a few Mm from the coronal loop footpoint, there are no strong brightenings, and the loop is not evolving when the EIS slit was rastering the loop. These indicate that the loops under study are quiescent loops.

6.2.2 Plasma diagnostics

In Figure 6.5, we plot the intensity variation along the loop for selected spectral lines. 1-σ error bar associated with the intensity is also overplotted on the data points. All plasma diagnostics are performed over these intensities. While calculating density along loops, background subtraction plays an important role (e.g., Del Zanna and Mason, 2003). Therefore, we tried to determine the background in the vicinity of the loop. We noticed a change in the structure of the active region for high and low temperatures. This makes the uniform tracing of loops and their corresponding backgrounds for both temperatures very difficult. Therefore, we have selected only those loops that are visible in both high and low temperature images. Additionally, due to non-uniformity in the background, we perform plasma diagnostics using original intensities only. This can have some line-of-sight integration effects.

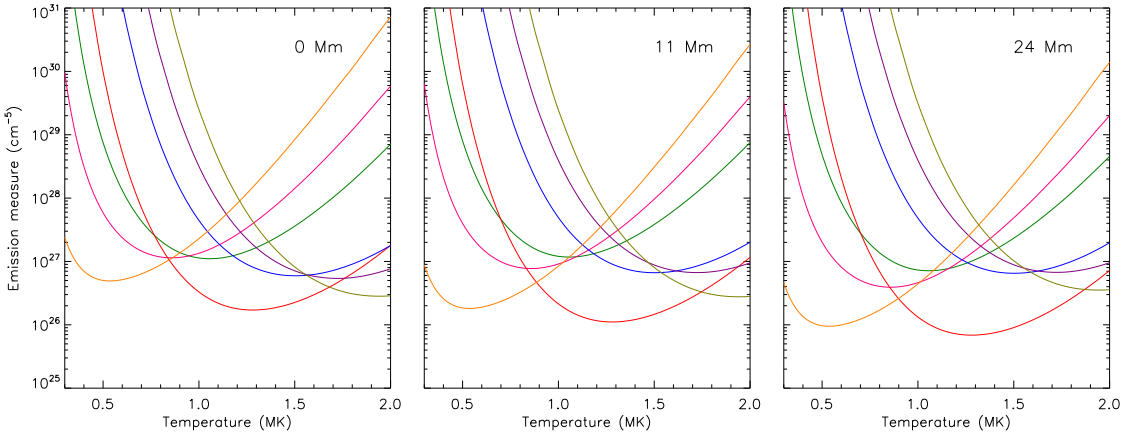

Figure 6.6: EM loci curves obtained from spectral lines provided in Figure 6.1 at different loop lengths as labelled.

6.2.2.1 Temperature

The plasma electron temperature (T_e) can be determined using various emission lines from ions with different ionization stages. The contribution functions of spectral lines depend on temperatures, as shown in Figure 6.1. These observed intensities along Loop 1, as shown in Figure 6.5, are used to determine the temperature using the EM loci method. This is an effective technique to estimate the electron temperature (e.g., Del Zanna et al., 2002). In this method, we plot the emission measures (EM) calculated using Equation 2.20, which are ratios of observed intensities with the corresponding contribution functions for different spectral lines as a function of temperature.

To determine temperature, we utilize density-insensitive emission lines Fe VIII 185.21 Å, Fe IX 197.86 Å, Fe X 184.53 Å, Fe XI 192.82 Å, Fe XII 192.39 Å, Fe XIII 201.12 Å and Fe XIV 270.53 Å to obtain the EM loci curves. We obtained EM loci curves along the whole loop. In Figure 6.6, we plot sample EM loci curves along three locations along Loop 1 as labelled. The EM loci curves obtained from these spectral lines intersect at different temperatures, indicating that the loop is multi-thermal in nature. This can be due to the presence of multiple unresolved strands or thin loops within the traced loop (e.g., Klimchuk, 2015).

To determine the temperature where the maximum number of EM curves intersect, we plot a histogram of the EM loci curves with respect to temperature along Loop 1. In Figure 6.7, temperature is on the x-axis, and the frequency of cuts at that particular temperature is on the y-axis. The histogram shows two prominent peaks, one below 1 MK and another above 1 MK. The distribution shows the dual temperature component

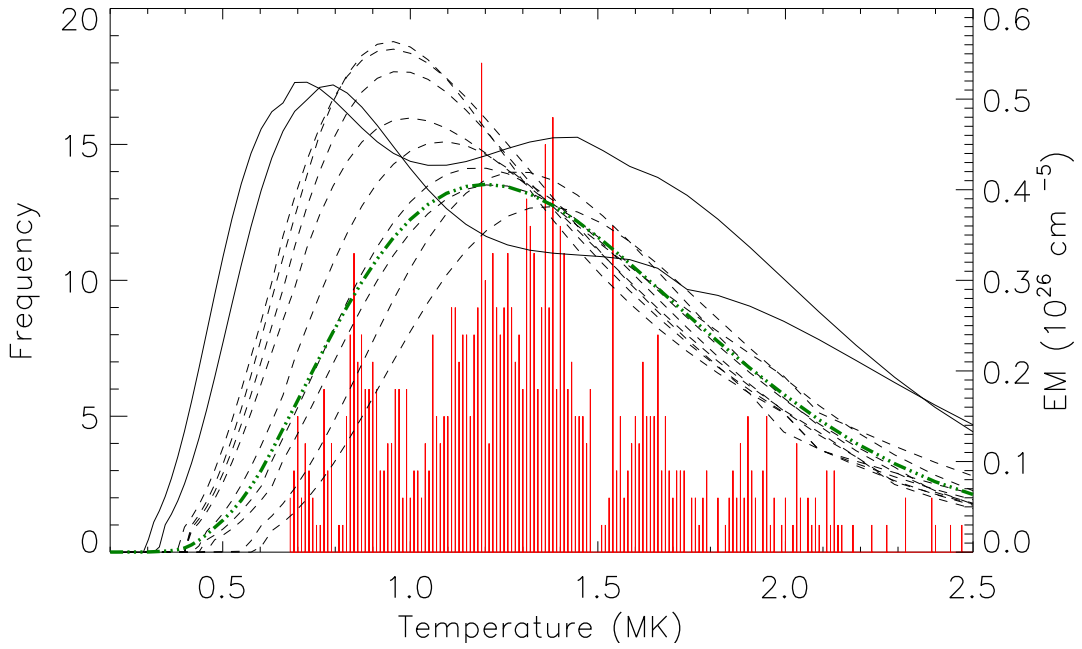

Figure 6.7: The histogram of all the EM loci intersections. Frequency (left y-axis) and emission measure (right y-axis) as a function of temperature. The overplotted solid black lines show the EM curves obtained from DEM analysis near the loop footpoint, 5 pixels apart. The dashed black lines show EM curves away from the footpoint, 5 pixels apart along Loop 1. The green dash-dot line represents the averaged EM profile obtained along the whole Loop 1.

nature of the loop (cool and warm). To further verify this, we determined the average of the intersection points for spectral line combinations from Fe VIII to Fe XI (low temperature), Fe XI to Fe XIV (high temperature), and Fe VIII to Fe XIV (average temperature). Fe XI is common in both high and low temperatures as its contribution function falls in the middle of the temperature range, as shown in Figure 6.1. The temperature along the loop is obtained from lower temperature ions (red colour) and higher temperature ions (blue colour), as shown in Figure 6.8. The error bars on temperature are the standard deviation of these intersecting points at that location. Figure 6.8 suggests that the loop has two temperature components, and both components are nearly isothermal along the loop.

To compare the estimated temperature from the EIS spectroscopic data with the AIA imaging data, we employ the differential emission measure (DEM) tool developed by Cheung et al. (2015). This utilizes six EUV coronal passbands of AIA 94, 131, 171, 193, 211, and 335 Å. The overplotted solid black lines on Figure 6.7 represent the EM curves obtained from DEM analysis along the loop, near the footpoint (5 pixels apart). These EM curves resolve the dual temperature component. The dashed black lines show only

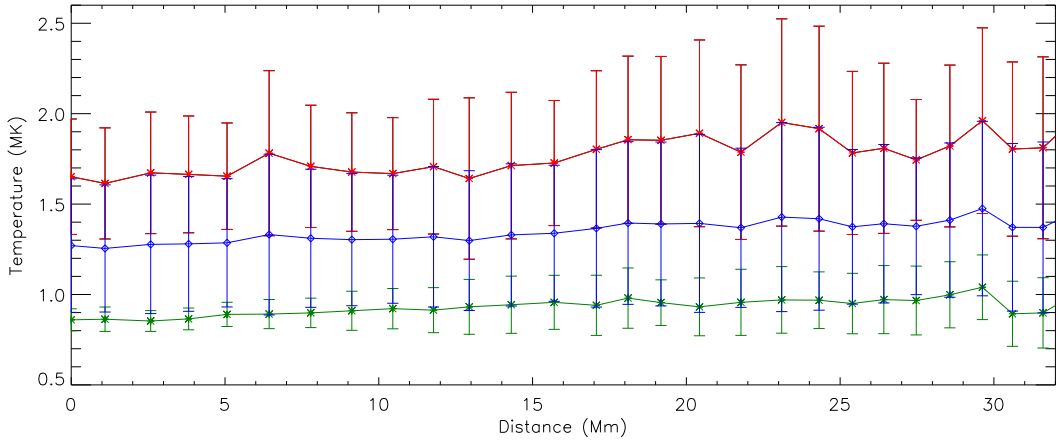

Figure 6.8: Temperature variation along the coronal Loop 1 from the EM-loci curves using EIS spectral lines. The red, blue, and green colours represent temperature variations of high, average, and low components along the loop.

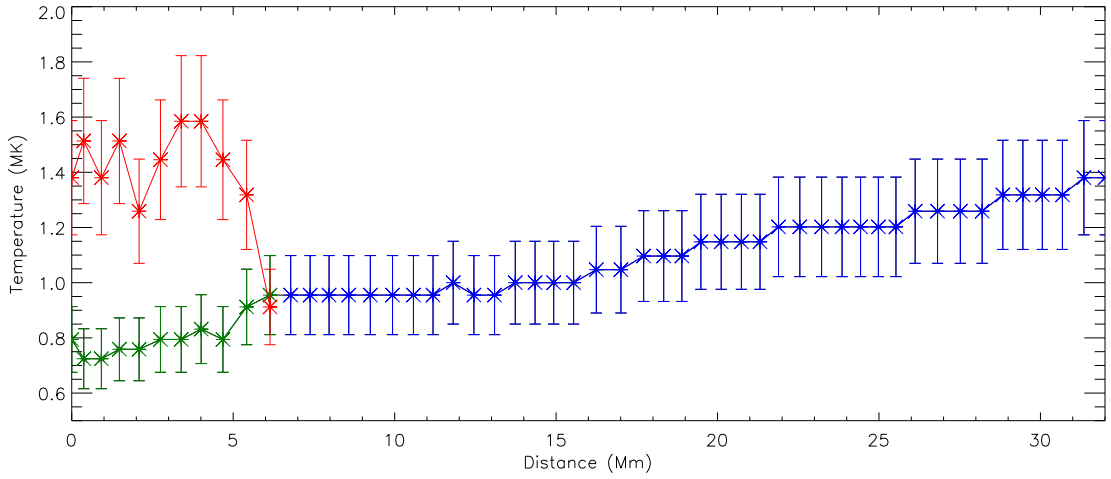

Figure 6.9: Temperature variation along the loop obtained from DEM analysis. Red and green colour represents the temperature obtained from high and low temperature DEM peaks. Blue colour represents the temperature obtained from the single DEM peak.

a single temperature component away from the footpoint (5 pixels apart) in Figure 6.7, although the loop is clearly visible in both hot and cool AIA passbands (see Figure 6.3). The green dash-dot line shows the EM curve averaged over the whole loop. This curve very nicely overlays the EM loci histogram obtained from the EIS spectral lines, even though it has a single peak, and the EIS histogram has two peaks in temperature.

The DEM peaks around 0.85 MK and 1.4 MK near the coronal footpoint represent the emission from the fan loops. However, due to the limitations in the temperature resolution of DEM, the double peaks are not resolved further along the loop, and we find only a single peak at the mean temperature. Due to this, the temperature profile obtained along the loop from AIA imaging data shows a slight increase in temperature as shown in Figure 6.9.

6.2.2.2 Emission measure

We also obtained the average EM variation along the loop from EIS spectral lines using Equation 2.20. The EM variations for high, low, and average temperatures are shown in red, blue, and green colours, respectively, in Figure 6.10. The variations in EM of these temperature components are similar to the intensity variations of the spectral lines belonging to that temperature range along Loop 1, as shown in Figure 6.5.

We have also estimated EM along the loop from DEM curves shown in Figure 6.7. The emission measure from the first peak (low temperature) and second peak (high temperature) is shown in green and red colour, respectively. The blue coloured data points are from a single temperature peak as shown in Figure 6.9. EM curves near the loop footpoint clearly show the appearance of dual temperature plasma components.

The emission measure of the low temperature (green colour) component is higher than that of the high temperature (red colour) component obtained from both imaging and spectroscopic techniques, showing dominance of the low temperature plasma component near the loop footpoint. The increase in emission measure for higher temperature can be due to the presence of some brightening at the loop or along the line-of-sight at around 20-25 Mm, as shown in Figure 6.4.

To further explore EM distribution at different temperatures, we show EM images of the fan loop system obtained in different temperature ranges, 0.5-0.9 MK, 1.1-1.4 MK, and 1.6-3 MK in Figure 6.12. EM images are obtained at a time around 12:10 UT and averaged over 1 min. This is the time when EIS was rastering over Loop 1

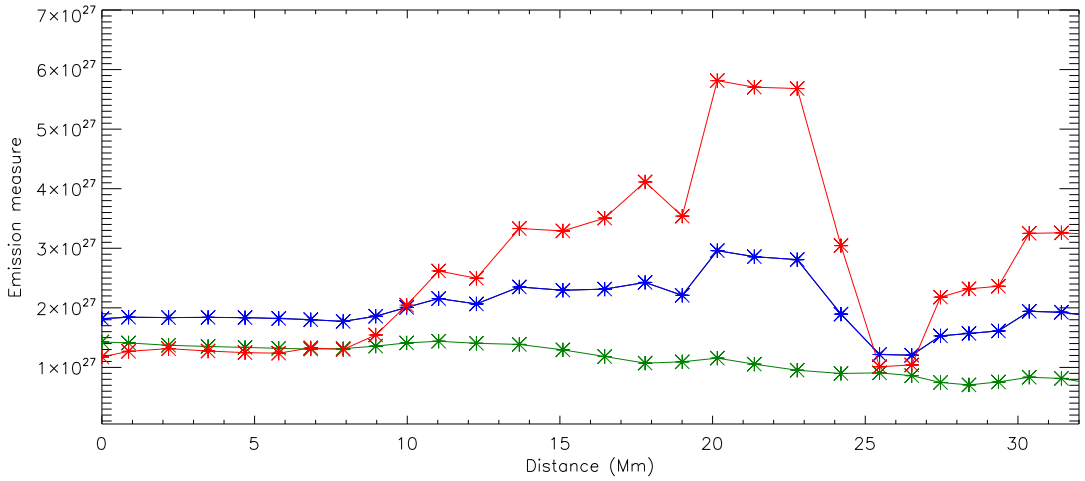

Figure 6.10: Average EM variation along the coronal Loop 1 as obtained from the EM loci curves for three temperature components shown in Figure 6.8.

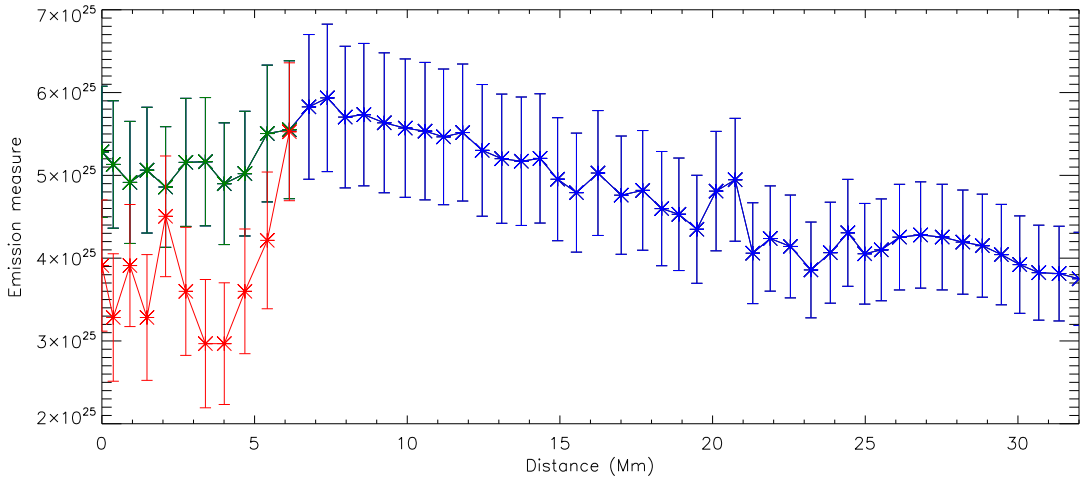

Figure 6.11: Average EM variation along the coronal Loop 1 as obtained from the DEM analysis for three temperature components shown in Figure 6.9

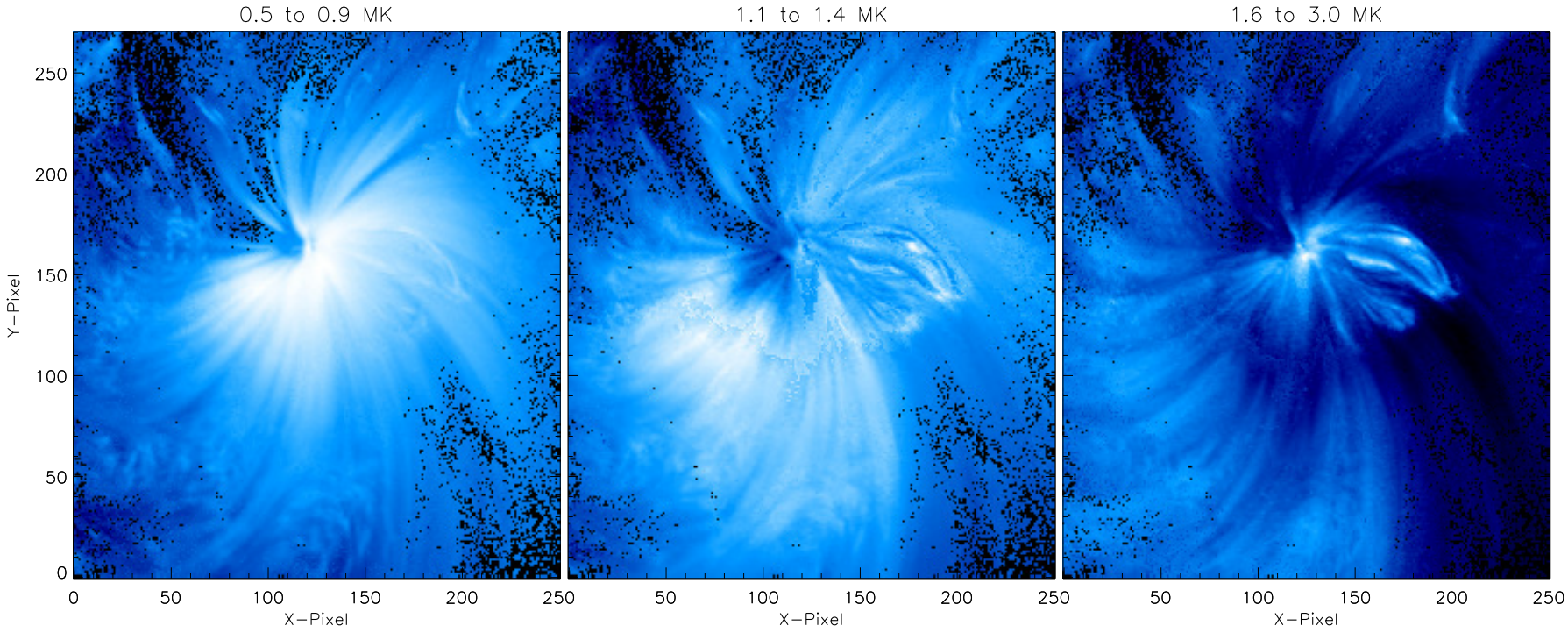

Figure 6.12: EM images obtained from DEM analysis in different temperature bins as labelled. Images highlight the temperature variations along the loops.

as shown in Figure 6.4. Loops are visible over the entire temperature range; however, we notice a change in the intensity of the loops as we move higher in temperature. In the left panel of Figure 6.12, i.e., in the low temperature range, the footpoint region of the loops shows strong emission. The footpoint temperature can be even lower, as the loop footpoints are also visible in the Mg V spectral line, which probes the transition region temperature of about 0.3 MK, as shown in Section C.1. In the middle panel of Figure 6.12, i.e., average temperature range, the footpoint region of the loops shows slightly weak emission. In the right panel of Figure 6.12, i.e., in the high temperature range, the middle portion of the loops shows weak emission, and the footpoint region of the loops shows strong emission, which could be either due to footpoint brightening or some hot background/foreground along the line-of-sight. In summary, EM images do highlight the multi-thermal temperature variation along the loops.

6.2.2.3 Density

Electron number density (N_e) is derived by using the intensity ratio of two emission lines of the same ion with different electron density dependence. This method provides the mean electron number density along the line-of-sight, which depends purely on atomic processes within the ion (see details in Section 2.2.2.2). The variation of intensity ratio of the two spectral lines, with one sensitive and the other insensitive with respect to the electron density, is obtained from CHIANTI v.10.1 (Del Zanna et al., 2021). We use the ratio obtained from density-sensitive line pairs of Fe XII 186.88/195.12, as shown in Figure 6.13. Using this ratio, we determine the electron number densities along the loop length as shown in Figure 6.14. The density plot shows a slow decrease in density along the loop, highlighting the large density scale height, and thus the overdense nature of these loops.

We further obtained electron densities along the loop using DEM analysis. Using the EM values at peak temperatures as shown in Figure 6.11 and upon assuming the plasma filling factor to be 1, we estimated the electron number density (n_e) along the loop using Equation 2.13, where h is the diameter of the loop.

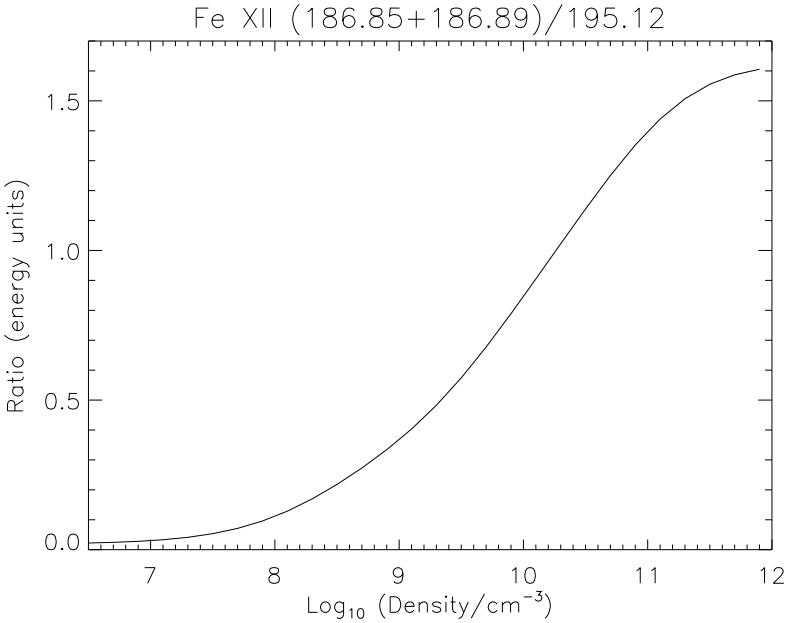

Figure 6.13: Variation of intensity ratio Fe XII (186.85+186.89)/195.12 with electron number density obtained from CHIANTI database.

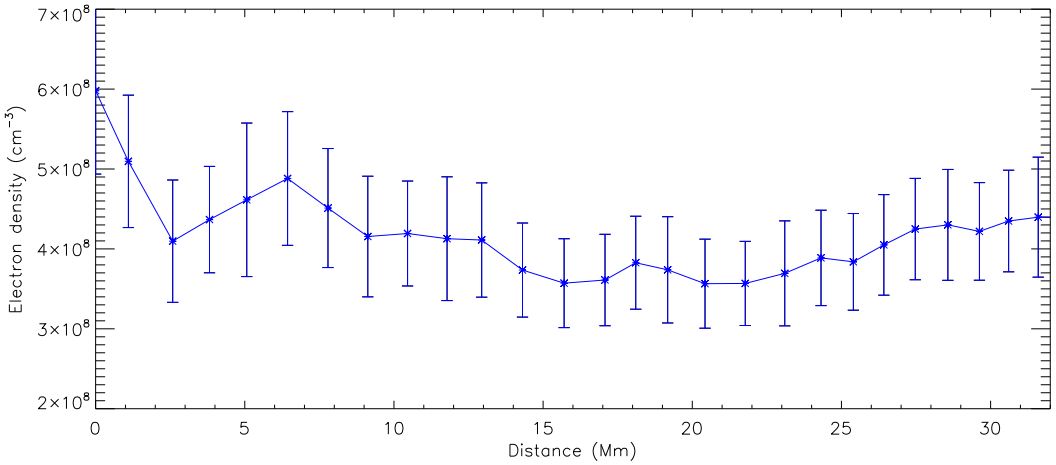

Figure 6.14: Variation of electron number density along Loop 1 obtained from the EIS Fe XII line ratio method.

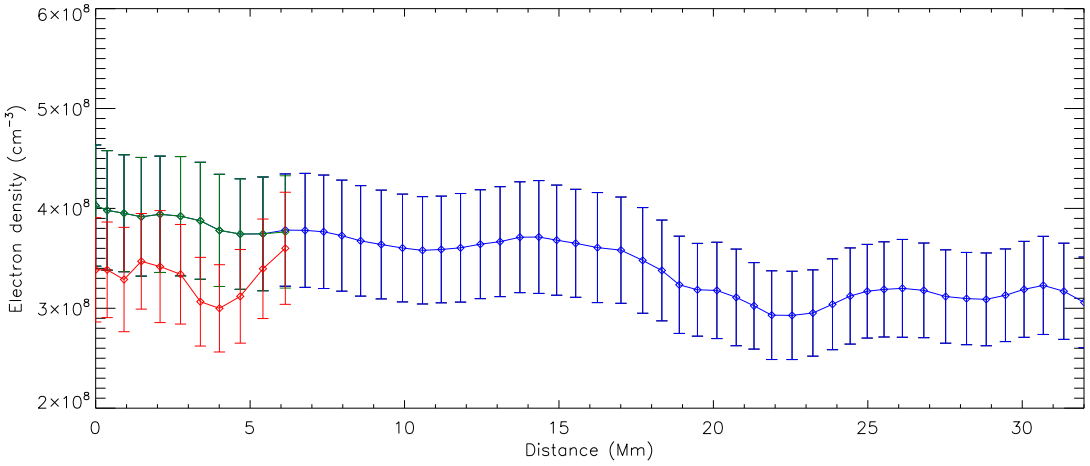

Figure 6.15: Variation of electron number density along Loop 1 obtained from the DEM technique using the AIA imaging data.

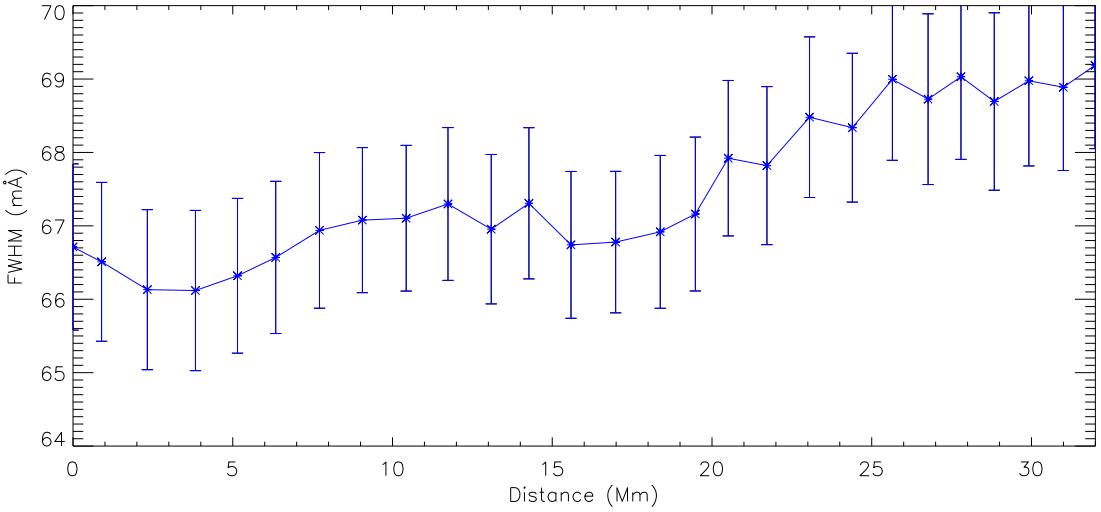

Figure 6.16: Variation of FWHM obtained from spectral line fitting as shown in Figure 6.2 obtained along the loop from 195.12 Å spectral lines as labelled.

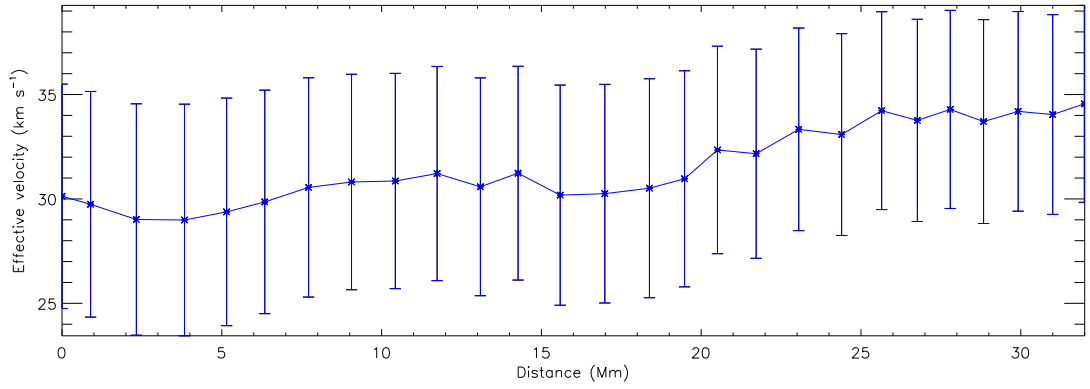

Figure 6.17: Variation of effective velocity (thermal and non-thermal combined) obtained along the loop from 195.12 Å spectral lines as labelled.

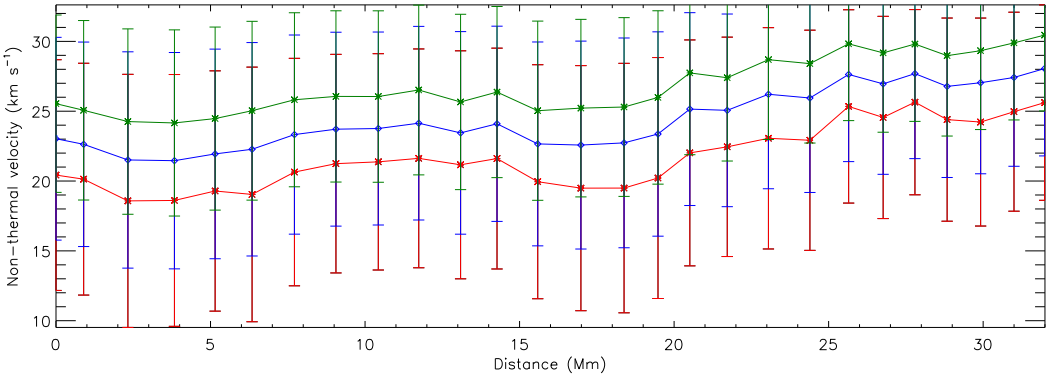

Figure 6.18: Variation of non-thermal velocity along the loop from 195.12 Å spectral lines as labelled.

6.2.2.4 Alfvén wave velocity amplitude

We obtained the FWHM of the Fe XII 195.12 Å spectral line by fitting a Gaussian profile over the observed intensity profiles along Loop 1. This FWHM can be expressed as

$$FWHM = \sqrt{[4ln2(\frac{\lambda}{c})^2(\frac{2k_bT_i}{M_i} + v_{nth}^2) + W_{inst}^2]}, \tag{6.2}$$

where k_b is Boltzmann constant, λ is wavelength of spectral line, c is speed of light, T_i is ion temperature, M_i is ion mass, v_{nth} is non-thermal velocity, and W_{inst} is the instrumental width. The EIS instrumental width for the 1" slit varies between 56 and 59 mÅ for a central 512 pixels. This can be calculated using IDL routine EIS_SLIT_WIDTH [1].

After subtracting instrumental width and converting FWHM into velocity units using Equation 2.17, we determined the effective velocity v_{eff} as

$$v_{eff} = \sqrt{(\frac{2k_bT_i}{M_i} + v_{nth}^2)}. \tag{6.3}$$

The effective velocity obtained from Fe XII 195.12 Å is plotted in Figure 6.17. The error bars on effective velocities are calculated using errors in the fitting parameters and instrumental width error of ≈2 mÅ.

We further calculated non-thermal velocity (v_{nth}), which can be considered as the Alfvén wave velocity amplitude. This is an important component in calculating Alfvén wave energy flux. The non-thermal velocity is calculated after subtracting the thermal

[1] https://sohoftp.nascom.nasa.gov/solarsoft/hinode/eis/doc/eis_notes/07_LINE_WIDTH/eis_swnote_07.pdf

Table 6.2: Plasma and wave parameters derived at coronal loop footpoints using EIS spectroscopic data. Loop footpoints are at three different temperatures as presented in Figure 6.8.

Loop	Temperature MK			Density cm^{-3}	Velocity amplitude km s^{-1}			Alfvén wave energy flux erg $cm^{-2}s^{-1}$		
1	0.86	1.65	1.27	5.98×10^{8}	25.54	20.43	23.03	1.29×10^{7}	0.82×10^{7}	1.05×10^{7}
2	0.87	1.75	1.31	3.94×10^{8}	26.73	21.23	24.13	1.15×10^{7}	0.72×10^{7}	0.93×10^{7}
3	0.93	1.69	1.33	5.44×10^{8}	29.41	24.52	27.07	1.63×10^{7}	1.13×10^{7}	1.38×10^{7}
4	0.87	1.61	1.26	5.20×10^{8}	29.05	25.01	26.99	1.56×10^{7}	1.15×10^{7}	1.34×10^{7}
5	0.84	1.60	1.24	6.57×10^{8}	28.19	23.86	25.96	1.64×10^{7}	1.18×10^{7}	1.40×10^{7}
6	0.77	1.77	1.30	8.14×10^{8}	25.79	22.55	19.22	1.53×10^{7}	1.17×10^{7}	0.85×10^{7}

velocity component from the effective velocity. The thermal component is calculated assuming plasma is in thermal equilibrium; therefore, we have approximated $T_e = T_i$. The obtained non-thermal velocity amplitude is shown in Figure 6.18 for the dual temperature component and the average temperature component in their respective colours. The error bar on non-thermal velocities was calculated using the error in effective velocities and the error in temperature. The non-thermal velocity, i.e., Alfvén wave velocity amplitude of these waves, is almost constant along the loop length within the error range.

6.2.3 Alfvén wave energy flux

We further calculate Alfvén wave energy flux using

$$E_A = \rho v_{nth}^2 v_A = \sqrt{\frac{\rho}{4\pi}} v_{nth}^2 B, \tag{6.4}$$

where ρ is mass density ($\rho = \mu m_p N_e$, m_p is proton mass, μ is 1.27), $v_A = \frac{B}{\sqrt{4\pi\rho}}$ is Alfvén speed and B is magnetic field. Here, we are assuming a magnetic field strength of 197 G at the coronal loop footpoint (Rawat et al., 2025), see Chapter 5. Alfvén wave energy flux at the loop footpoint is about $\approx 10^7$ erg cm^{-2} s^{-1}. This wave energy flux can easily account for the active region radiative losses, see Table 2.2.

We performed a similar analysis on the other five loops identified in Figure 6.3. We found that in most of the loops, the densities fall very slowly, which suggests an overdense nature of the loops. Here also, Alfvén energy flux at coronal loop footpoint is of the order of $\approx 10^7$ erg cm^{-2} s^{-1} as found for Loop 1. The estimated plasma and Alfvén wave parameters at all the loop footpoints are tabulated in Table 6.2.

6.3 Discussion and conclusion

In this work, we selected a few coronal loops that are visible in images of both AIA/SDO and EIS/Hinode hot and cool temperatures. Using the spectroscopic data of EIS and imaging data of AIA, we estimated various plasma parameters along coronal loops using various techniques and compared them. Spectroscopic diagnostics were used to measure electron density, temperature, non-thermal velocity, and thus Alfvén wave energy flux at the loop footpoints. The loops were clearly visible in various spectral lines covering the peak formation temperature of 0.5–2 MK. We determined the electron number density and temperature along the coronal loops using the line ratio and EM loci method, respectively. We further compared the density and temperature obtained from the spectroscopic method with the density and temperature obtained using the DEM analysis, utilizing imaging data.

Results obtained from the EM-loci technique clearly show that plasma in the line-of-sight and along the loop is of a dual nature, as all the EM curves cut at a single point for the combination of high and low temperature spectral lines. The result also indicates that the temperature along the loop is also constant (within the obtained error bars), and highlights its isothermal nature within the high and low temperature ranges. Gupta et al. (2019) also studied the long coronal loop, and found the loop to be nearly isothermal along and across the loop length.

We determined the temperature along the loop using the spectroscopic EIS method and plotted a histogram, which shows a dual temperature structure along the loop. One plasma component was below 1 MK, and another was above 1 MK along the whole traced loop. We further compared these temperatures along the loop with a combination of spectral lines sensitive to lower (Fe VIII-XI) and higher (Fe XI-XIV) temperatures, and found two similar temperature distributions along the loop. This highlights the existence of two temperature plasma components along the loops, ranging from 0.8-1.05 MK and 1.6-1.8 MK. We also obtained the average temperature along the loops. We further compared these temperature profiles with temperatures derived from DEM analysis carried out using AIA data from tools provided by Cheung et al. (2015). Our findings again highlight the dual temperature component of these loops, where the lower temperature plasma dominates the emission near the loop footpoints, and as we move further away, the high temperature plasma emission dominates. The lower temperature obtained at

the loop footpoint can be even smaller, as the footpoint regions look bright in Mg V 2796.16 Å spectral line probing 0.32 MK, as shown in Section C.1 (Young et al., 2007). However, this needs further detailed investigation.

DEM analysis revealed the dual temperature nature of the loops only up to a few pixel lengths (4-5 Mm), after that, two DEM peaks merge and provide an average temperature along the loop. Analysis demonstrates the superiority of spectroscopic data over imaging data in resolving the multiple temperature components along the loops.

From DEM analysis, we again found that the emission measure along the loop is high for the low temperature component and low for the high temperature component, only up to a few pixels along the loop length (4-5 Mm), then the two components merge. Then, after a few pixel lengths, the emission measure from the higher temperature component is stronger than the low temperature component. Results from both techniques highlight that at the loop footpoints, low-temperature plasma emission dominates.

We obtained the electron density along the loop using the density-sensitive EIS spectral line pair Fe XII λ 186.88/λ 195.12. Obtained number densities from spectroscopic data is around $\approx 6\times10^{8}$ cm^{-3} near the footpoint, which falls to $\approx 4\times10^{8}$ cm^{-3} at farther along the loop. This indicates the overdense nature of these fan loops.

From the FWHM of the spectral line obtained by fitting a Gaussian function over the observed intensity profiles along the loops, we estimated the effective and non-thermal velocities (Alfvén wave velocity amplitude) along the coronal loop lengths. The strongest line Fe XII 195.12 Å shows an almost constant effective and non-thermal velocity along the loop. The non-thermal velocity obtained from Fe XII 195.12 Å line is $\approx$20 and 25 km s^{-1} with a slight increase with height, though within the error bar. Such almost constant non-thermal velocity along the loop length has also been noted in Gupta et al. (2019).

Upon combining all these parameters with the latest magnetic field estimate of $\approx$ 200 G at the coronal footpoint of these loop as quoted in Chapter 5 and Rawat et al. (2025), we obtained Alfvén wave energy flux to be $\approx 10^{7}$ erg cm^{-2} s^{-1}, which is sufficient to maintain the hot active region corona. Henceforth, Alfvén waves can be considered as playing an important role in the heating of active region corona.

Chapter 7

Conclusions and future prospects

This thesis work deals with the MHD waves dynamics along umbral fan loops. These waves play an important role in the heating of the solar corona. For this purpose, we have utilized several multi-wavelength imaging and spectroscopic observations of sunspots taken from the AIA, HMI, IRIS, and EIS instruments.

Most of the observations were taken in EUV and UV emission lines originating from chromospheric, transition region, and coronal temperatures. Some coverage of photospheric emissions was also obtained. We focused on unipolar sunspots near the disc centre for our analysis. These sunspots host several coronal fan loops originating from their umbral regions and show clear signatures of 3-min propagating waves. In this chapter, we summarize the results obtained in this thesis work along with the conclusions drawn. We further mention the future plans that are useful to advance our understanding of wave dynamics using recent and upcoming solar missions.

7.1 Summary of results

7.1.1 Source region of 3-min slow waves

All the fan loops rooted in the sunspot umbra constantly show a 3-min period propagating slow magnetoacoustic waves in the corona. However, their origin in the lower atmosphere were unclear.

- Loop tracing

  We employed the correlation technique to trace the fan loops in the lower atmosphere, which are otherwise only visible in the corona. We traced the footpoints

of several fan loops at different atmospheric heights from the corona to the photosphere using the 3-min waves and also obtained their cross-sectional areas. We measured their phase speeds and found them to be less than the speed of sound, which confirms that these are 3-min slow-magnetoacoustic waves.

- Amplitude and frequency modulations

  We traced the origin of these waves by utilizing their amplitude and frequency modulation characteristics with time while propagating along the traced waveguides. These modulation periods are in the range of 20–35 min present at all heights. Based on our findings, we interpret that 3-min slow magnetoacoustic waves propagating in the coronal fan loops are driven by 3-min oscillations observed at the photospheric footpoints of these fan loops in the umbral region.

- Relation between 3-min and 5-min (p-modes) waves

  We also explored any connection between 3-min and 5-min (p-modes) oscillations observed at the photospheric footpoints of these loops and found them to be weakly coupled.

7.1.2 Damping of waves

- Photosphere to corona (Lower atmosphere)

  Using the traced loops and their cross-sectional areas as described above for the lower atmosphere, we investigated the role of area divergence and frequencies on the damping of slow magnetoacoustic waves propagating from the photosphere to the corona along several fan loops rooted in the sunspot umbra. To investigate frequency dependence, we utilized 1–2, 2.3–3.6, and 4.2–6 min period bands. We estimated the energy flux of propagating 3-min slow magnetoacoustic waves along the fan loops and obtained a damping length of 208 ± 7 km. We further investigated the role of the area expansion of these loops in the damping of these slow magnetoacoustic waves. We deduced the decay of total wave energy content within the loop cross-sectional area with height, and estimated the damping length in this case to be 303 ± 10 km. Finding reveals that the area expansion of loops with height plays an important role in the damping of these waves from the photosphere to the corona. Results also show some frequency-dependent damping

of slow magnetoacoustic wave energy fluxes with height, where high-frequency waves are damped faster than low-frequency waves.

- Along the coronal fan loops (Upper atmosphere)

  3-min period band slow magnetoacoustic waves, upon reaching the corona, show a clear dispersive nature. We selected 5 frequency bands within the 3-min (1.8-4 min) band and determined the phase speed in these frequency bands, $v(\omega)$. The phase speed increases with frequency, which highlights the dispersive nature of slow magnetoacoustic waves in the corona. The Fourier power maps of waves along fan loops show frequency-dependent damping within the 3-min period band. The result highlights the relation between the dispersive nature of the waves and their frequency-dependent damping.

7.1.3 Seismological applications

- Refinement of the loop tracing method

  To obtain a better coverage over different atmospheric heights, we identified a unipolar sunspot near the disc centre observed in all four IRIS passbands. We then refined the loop tracing by utilizing more passbands in the lower atmosphere. We have also traced the loops visible in the corona and obtained their cross-sections using the FWHM method. We determined the area expansion scale heights of the loops.

- Total number density and temperature along the loops

  We determined the total number density and temperature along the loop. For heights below the corona, we utilized the sunspot umbra model of Fontenla et al. (1999). In corona, we utilized the differential emission measure (DEM) analysis tool developed by Hannah and Kontar (2012) using the AIA data.

- Magnetic field and plasma-β along the loops

  We calculated the magnetic field and plasma-β variations along magnetically structured loops from the photosphere to the corona. We find the RMS magnetic field strengths in the range 1596-2269 G at the photospheric footpoints of the fan loops, which decrease rapidly to 158-236 G at the coronal footpoints. We estimated the plasma-β at the photospheric and coronal footpoints in the range 0.2-0.5 and

0.0001-0.001, respectively. We found plasma-β <1 along the whole loop, whereas the plasma-β ≈1 layer is found to be at sub-photospheric heights.

7.1.4 Spectroscopic diagnostics

- Density and temperature along coronal loops

  We determined the electron number density and temperature along the coronal loops using the line ratio and EM loci methods, respectively, using the spectroscopic data obtained from EIS. These methods provide precise values of density and temperature as we are using spectrally resolved lines. We found that in most of the loops, the densities fall very slowly and are found to be overdense. We also found the existence of two temperature plasma components along the loops, ranging from 0.8-1.05 MK and 1.6-1.8 MK. We also obtained the average temperature along the loops, varying between 1.2-1.4 MK. We further compared these temperature profiles with temperatures derived from DEM analysis carried out using AIA data from tools provided by Cheung et al. (2015). Our results highlight the dual temperature component of these loops, where the low temperature dominates near the loop footpoints and further away, high temperature dominates.

- Alfvén wave velocity amplitude and energy flux

  From the FWHM of the spectral line obtained by fitting a Gaussian function over the observed intensity profiles, we determined the non-thermal velocity (Alfvén wave velocity amplitude) along the coronal loops. We found that the non-thermal velocity remains almost constant along the loop length for the Fe XII 195.12 Å spectral line. Upon combining all these plasma parameters with the magnetic field strength along fan loops, we determined the Alfvén wave energy flux to be $\approx 2\times10^7$ erg cm^{-2} s^{-1}, which is sufficient to heat the active region corona.

These results are achieved using multi-wavelength imaging and spectroscopic observations.

7.2 Conclusions

Finally, we provide the final conclusions drawn in this thesis based on the results presented above.

- We devised a novel analysis technique that can identify the loop location and the cross-section area of fan loops in the lower solar atmosphere (photosphere to corona) where they are otherwise invisible.

- We found that 3-min slow magnetoacoustic waves propagating along coronal fan loops are driven by 3-min oscillations observed at the photospheric foot-points of these fan loops in the sunspot umbral region.

- We found that the area divergence plays an important role in the damping of waves in the lower solar atmosphere and should be taken into account while studying wave damping.

- In the corona, these waves show a clear dispersive nature, which can possibly explain the frequency-dependent damping characteristic of slow waves.

- Our loop tracing technique demonstrates the seismological potential of 3-min slow waves omnipresent in the umbral sunspot atmosphere to probe and map isolated loops and determine magnetic field and plasma-β along these loops. We found that the magnetic field strength in these loops at the coronal footpoint is higher than previously reported.

- We further utilized spectroscopic data to estimate Alfvén energy flux at coronal loop footpoints and found that Alfvén waves carry enough energy flux to heat the active region corona.

- Finally, our results provide clear evidence of magnetic coupling of the solar atmosphere through propagation of 3-min waves along fan loops at different atmospheric heights.

- Though our results are obtained mainly from slow wave propagation, identification of wave guide in the umbral atmosphere and the effect of area divergence will be applicable to other types of waves as well.

7.3 Future prospects

We now discuss the future directions in continuation of the current projects and as follow-ups to these projects.

- Determine the mechanism/source region of different MHD wave modes and periods present in the umbral atmosphere.
- Identify the presence of a resonant cavity in these waveguides.
- Decouple the different wave modes propagating along the waveguides and assess their contribution to solar atmospheric heating.
- Explore the variation of power-law distribution and indices along highly resolved coronal loops.
- To determine the actual frequency-dependent damping of slow magneto-acoustic waves after incorporating the area divergence effect along coronal loops.
- Statistics of plasma-β variation for different loops originating from different solar structures.
- Impact of small episodic brightenings and large transients happening at the loop footpoint, along the loop, and near the loop on wave propagation and other mode generation.
- Comparing the actual damping lengths with the various proposed damping mechanisms and determining the parametric dependence of various plasma parameters involved in the heating of the solar atmosphere.

The future of solar physics is bright, as various space-based and ground-based observatories have become operational in the past few years. DKIST (first-light, January 2020), Solar Orbiter (SolO; launched, February 2020), and Aditya-L1 (launched, September 2023) observations are aimed at mapping the physical conditions in the solar atmosphere. Coordinated observations using instruments from DKIST, IRIS, SDO, SUIT, SolO, Hinode, etc., can be utilized to observe the solar atmosphere and inner heliosphere, addressing the long-standing problems in the area of solar and space physics (e.g., Martinez Pillet et al., 2023). These observations will further enhance our understanding of waves and transients in the solar atmosphere.

Appendix A

A.1 Cross-section of coronal fan loop in AIA 171 Å image

To determine the cross-sectional area of the coronal foot-point in AIA 171 Å image, we obtained the intensity across the coronal loop foot-point and fitted it with a Gaussian with a linear function over that intensity distribution as shown in Figure A.1. The Full-Width Half Maximum (FWHM) of the fitted Gaussian function provides the diameter of the loop at that location in the corona (e.g., Gupta et al., 2019). The obtained diameter is $\approx 1.76 \pm 0.18$ arcsec (1.27 ± 0.13 Mm) for loop 6.

A.2 Correlation image in corona

Correlation images obtained between AIA 171 Å image and filtered light curves obtained at coronal loop foot-points in AIA 193 Å (left panel) and 171 Å (right panel) are presented in Figure A.2. For details on the method, see Section 3.2.1.

A.3 Artefact due to solar rotation

In Section A.3, we show average Fourier power spectra of sunspot umbra obtained by averaging individual Fourier powers at each pixel within the umbra. The Fourier power follows a power-law with a strong peak at 3.9 min. This peak is an artefact due to pixel crossing time, which occurs due to differential rotation of sunspots as described in Norton et al. (2021). We calculated the theoretical value of this artefact for our dataset. The analysed sunspot is located at $\approx 7^{\circ}$ south latitude. Using the sswidl routine *diff_rot* (based on Howard et al., 1990), we determined the differential rotation rate of this sunspot as 1.88 km s^{-1}. Since 1-pixel (0.6arcsec) here represents 435 km,

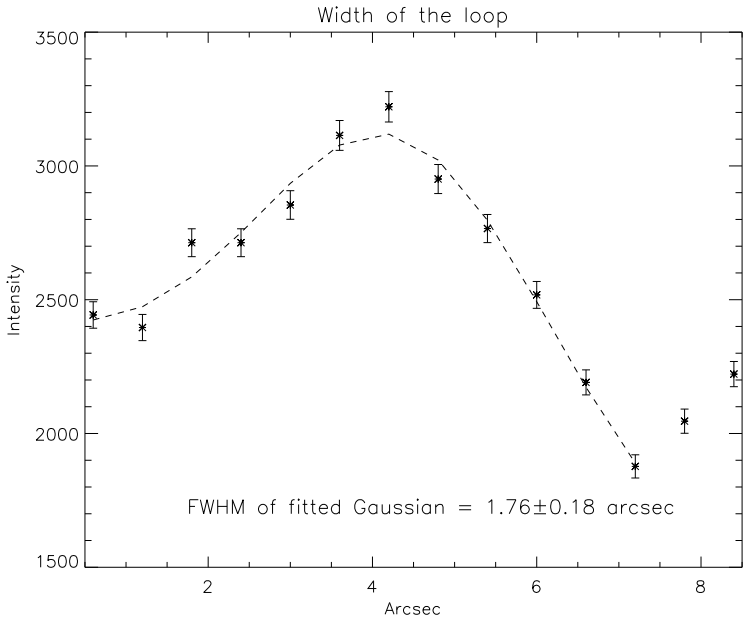

Figure A.1: Gaussian with linear function fitted over the intensity distribution across the coronal foot-points of loop 6 as observed in AIA 171 Å passband.

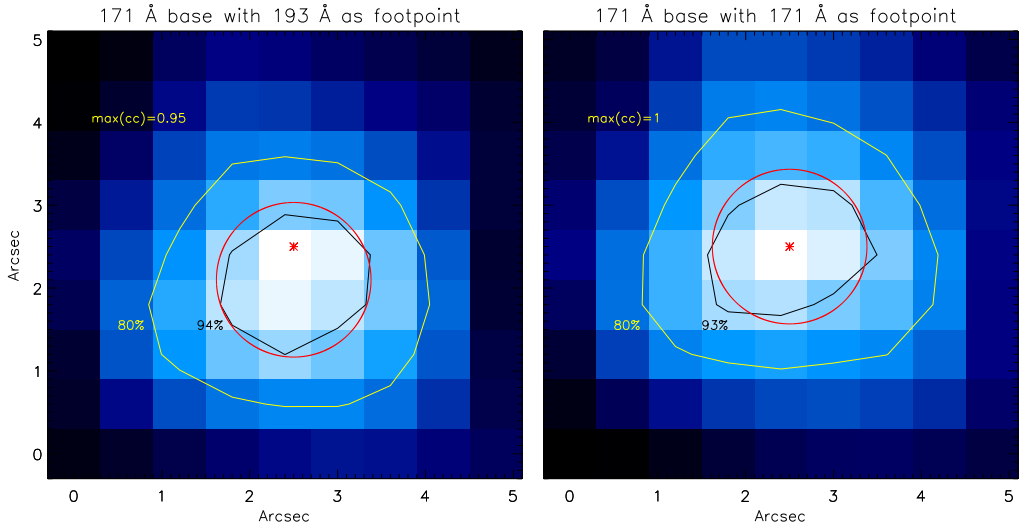

Figure A.2: Correlation images obtained in corona as labelled. In each panel, the asterisk sign (*) in the centre refers to the coronal foot-point of loop 6 as obtained from AIA 171 Å image. The red circle represents a cross-section of the loop obtained from FWHM as described in Appendix A.1. Overplotted yellow colour contours are obtained at 80% of the maximum correlation value. Overplotted black contours, as labelled, are obtained from the maximum correlation value to fit the red circle.

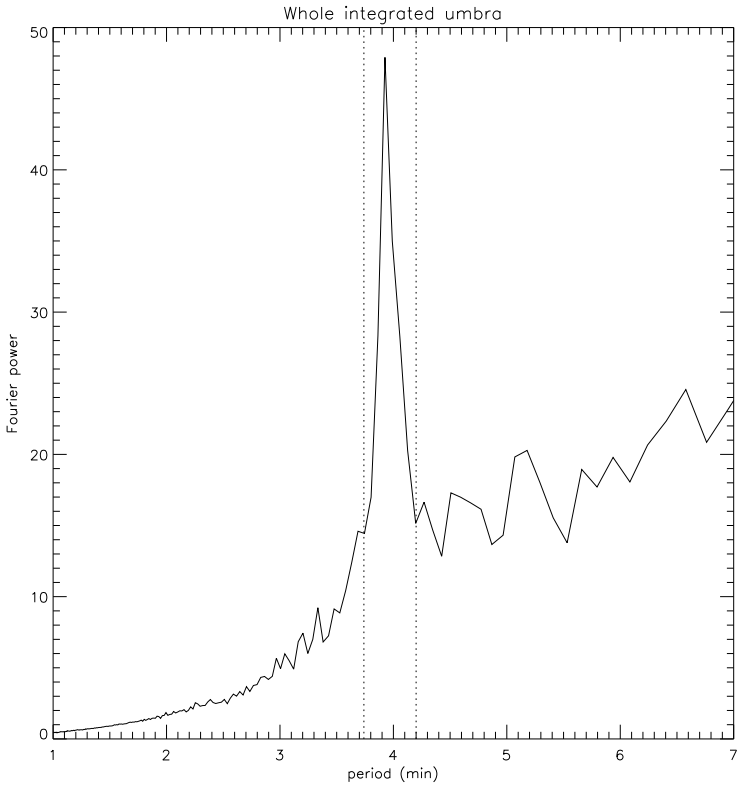

Figure A.3: Average Fourier power spectrum of full umbra. The peak at 3.9 min is an artefact corresponding to the 'pixel-crossing' time. Two vertical dashed lines at 3.74 and 4.2 min show the period window excluded from our analysis.

which leads to the pixel crossing time to be around 3.86 min. This value is the same as the peak found in the Fourier power spectra. Also, there will be a slight shift in the latitude for each loop foot-point or locations within the umbra, which can shift this artefact by a few seconds. Therefore, we are taking the 3.74-4.2 min period window as the spread of this artefact. This artefact is more noticeable when two nearby pixels have significant intensity gradients.

A.4 Temperature profile for umbra

Formation heights in the sunspot umbra for a particular passband sensitive to one temperature are shown in Figure A.4. For the purpose, we have utilised the umbral model of de Oliveira e Silva et al. (2022), which they claimed is close to the atmospheric models of Fontenla et al. (1999, 2009) and others. Here, atmospheric model of de Oliveira e Silva et al. (2022) is preferred over models of Maltby et al. (1986) and Avrett et al. (2015) due to the higher upper boundary of de Oliveira e Silva et al. (2022), which includes an

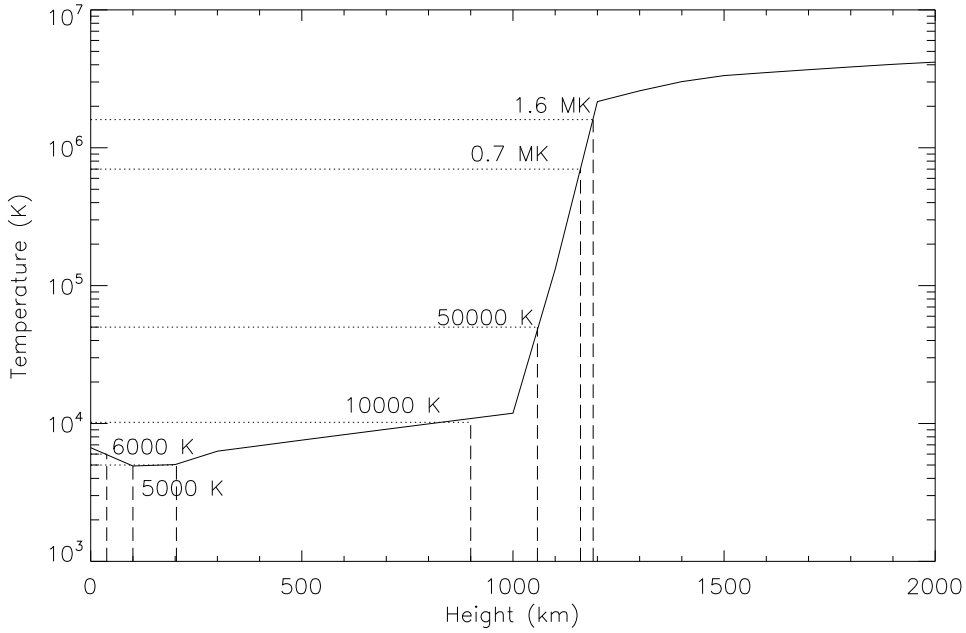

Figure A.4: Height-temperature profile for sunspot umbra extracted from de Oliveira e Silva et al. (2022). Formation heights (denoted by vertical dashed lines) for passbands sensitive to a particular temperature (denoted by horizontal dotted lines) are also provided.

extended corona.

A.5 Randomization bootstrap analysis

To check the reliability of correlation coefficient values, we are performing a randomization bootstrap analysis. In this method, it is assumed that in non-periodic time series data, the order in which the data is taken is not important. For example, suppose there is no periodicity in the time series. In that case, the order of intensity (or any variable) with respect to time can be changed from x_1, x_2,... x_n to a randomly arranged $x_{r(1)}$, $x_{r(2)}$,... $x_{r(n)}$, where n is the number of data points and $r(1)$, $r(2)$,... $r(n)$ is a random permutation of the data points (e.g., O'Shea et al., 2001; Sharma et al., 2017). Here we are randomizing the amplitude modulation curves obtained earlier from different heights.

In Figure 3.9, pink colour lines are obtained by correlating randomized amplitude modulation curves obtained from the wavelet spectrum of upper height with the randomized amplitude modulation curves obtained from the lower height, as labelled using the method described above. Similarly, purple lines are obtained from amplitude modulation curves resulting from the extrema method. We have performed this randomiza-

tion test 300 times using all 1200 data points of the time sequence. All 300 randomized correlation curves are plotted with the same colour lines. All these lines together provide a band for correlation values, and any value beyond this band can be considered a reliable correlation coefficient value. Here we can see that the band ranges approximately between -0.1 to 0.1, which means that if the correlation coefficient value between the two curves is above 0.1 or below -0.1, then the correlation values can be considered reliable.

Appendix B

B.1 Average umbral Mg II 2796 Å line profile

We have extracted the average near-ultraviolet spectra of Mg II 2796 Å in the umbral region marked with a white line (11-pixels) in Figure 4.2. We then fitted average spectral profiles with the Gaussian function and constant background as shown in Figure B.1. The fitted parameters were used to extract Doppler shifts and thus Doppler velocity oscillations as shown in the right panel of Figure 4.2.

The fitted parameters were also used to extract peak intensity with time, and thus, the relative intensity amplitude is obtained from spectroscopic data. We then determined the relative intensity amplitude near the slit from imaging data (assuming similar intensity and velocity oscillations) and found that the intensity amplitude obtained from spectroscopic data is 1.25 times larger than the intensity amplitude obtained from imaging data. Therefore, to obtain velocity amplitudes from imaging data (IV_{amp}), we are using formula $\frac{SI_{amp}}{SV_{amp}} = \frac{II_{amp} \times 1.25}{IV_{amp}}$, where II_{amp} and SI_{amp} are relative intensity amplitude obtained from imaging and spectroscopic data, respectively, and SV_{amp} is velocity amplitude obtained from spectroscopic data for 3-min oscillations.

B.2 Area of loop cross-sections

Variation of cross-sectional areas of loop 6 at different atmospheric heights (at ≈95% of the maximum correlation values) is shown in Figure B.2. Here, we see flux tube expansion with height. Details on the technique and methodology for deriving loop cross-sections are described in the Chapter 3, see also Rawat and Gupta (2023). Since we are tracing the same loop, we can assume the filling factor to be one from the photosphere to the corona. However, at the photosphere, the loop cross-section is limited

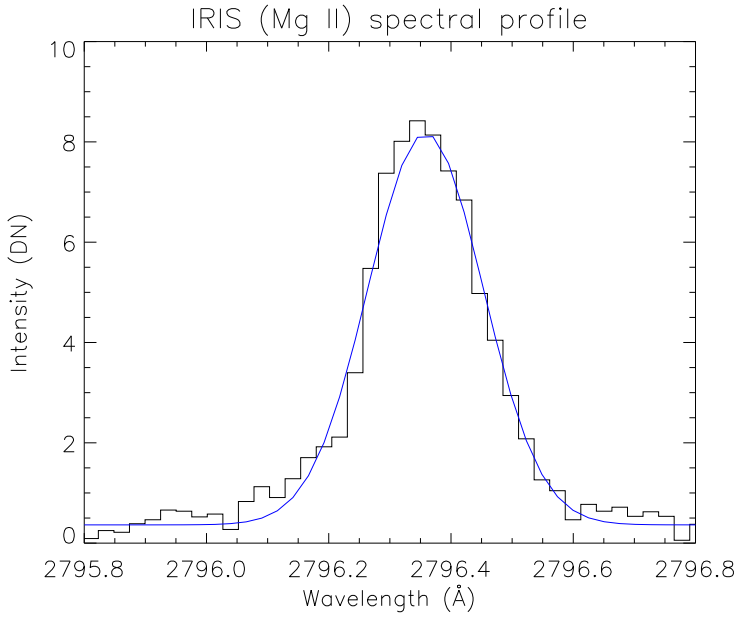

Figure B.1: Average line profile of Mg II 2796 Å over 11-pixels along the slit and binned over two time frames at 7:20 UT. The profile is fitted with a Gaussian function in blue colour.

to 1-pixel due to limitations on resolution. We have assumed 1- and 2-pixel errors in the width of the loops calculated using SDO and IRIS passband, respectively. 1-pixel of SDO and 2-pixel of IRIS passbands correspond to 435 km and 241 km on the Sun, respectively.

B.3 Temperature and density of loop from photosphere to corona

To determine the formation heights for AIA, IRIS, and HMI passbands in the sunspot umbra, we utilize the sunspot model of Fontenla et al. (1999). Temperature and density variations with respect to the formation height are shown in Figure B.3. We associate the temperature at the peak of response functions as the passband temperature and obtain the corresponding formation heights. However, all these passbands will also have some cooler and hotter temperature contributions as well (e.g., O'Dwyer et al., 2010). Simultaneously at those formation heights, we determine electron (N_e) and hydrogen (N_h) number density separately. The mass density is given by $\rho = (N_e + N_h)m_p$, where m_p is the proton mass ($m_p = 1.67 \times 10^{-24}$ g) (Aschwanden, 2004). The left axis shows the temperature, and the right axis shows the total mass density (ρ). Furthermore, we have assumed 20% error in density and temperature in all our calculations (e.g., Gupta

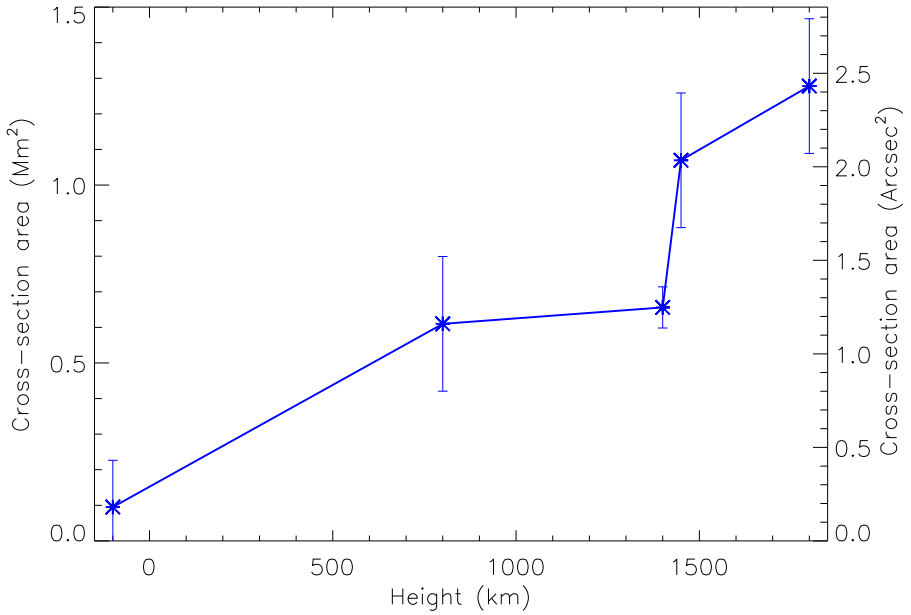

Figure B.2: Variation of cross-sectional area of loop 6 for 95% contour level with height. The vertical bars represent errors in the cross-sectional area.

et al., 2019). These values play a key role in determining the wave energy fluxes with height.

B.4 Results from integrated umbra

Previously, Kanoh et al. (2016) and Krishna Prasad et al. (2017) calculated the wave amplitudes and energy fluxes in the umbral atmosphere over the entire integrated umbra. For comparison with previous results, we also carried out a similar analysis on the integrated umbra (see HMI continuum image of Figure 4.1). We determined the average FFT power spectra of the whole umbra at all the atmospheric heights, and obtained the presence of various periods as shown in Figure B.4. We performed a similar analysis as described earlier to derive relative intensity amplitude, velocity amplitude, and wave energy flux in the umbra for three period bands and plot them in Figure B.5. Due to a lack of significant enhancement in the FFT power of the 3-min period band at the photosphere, we are considering it as an unreliable data point. The damping lengths of wave energy flux for 1.5-min and 3-min period bands obtained from temperature minimum to corona are printed at the top right corner of Figure B.5.

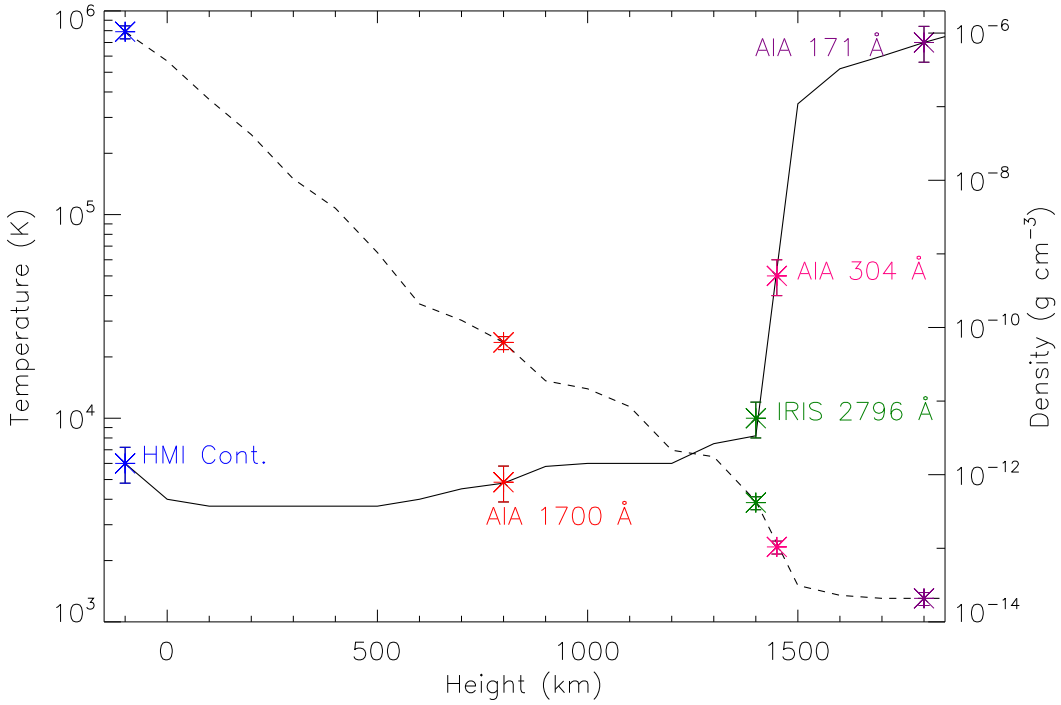

Figure B.3: Temperature and total mass density as a function of height shown by solid and dashed lines, respectively, for the sunspot model extracted from Fontenla et al. (1999). The axis on the left shows the temperature, and the right shows the mass density. Different coloured asterisk symbols (*) are used to represent different passbands as labelled.

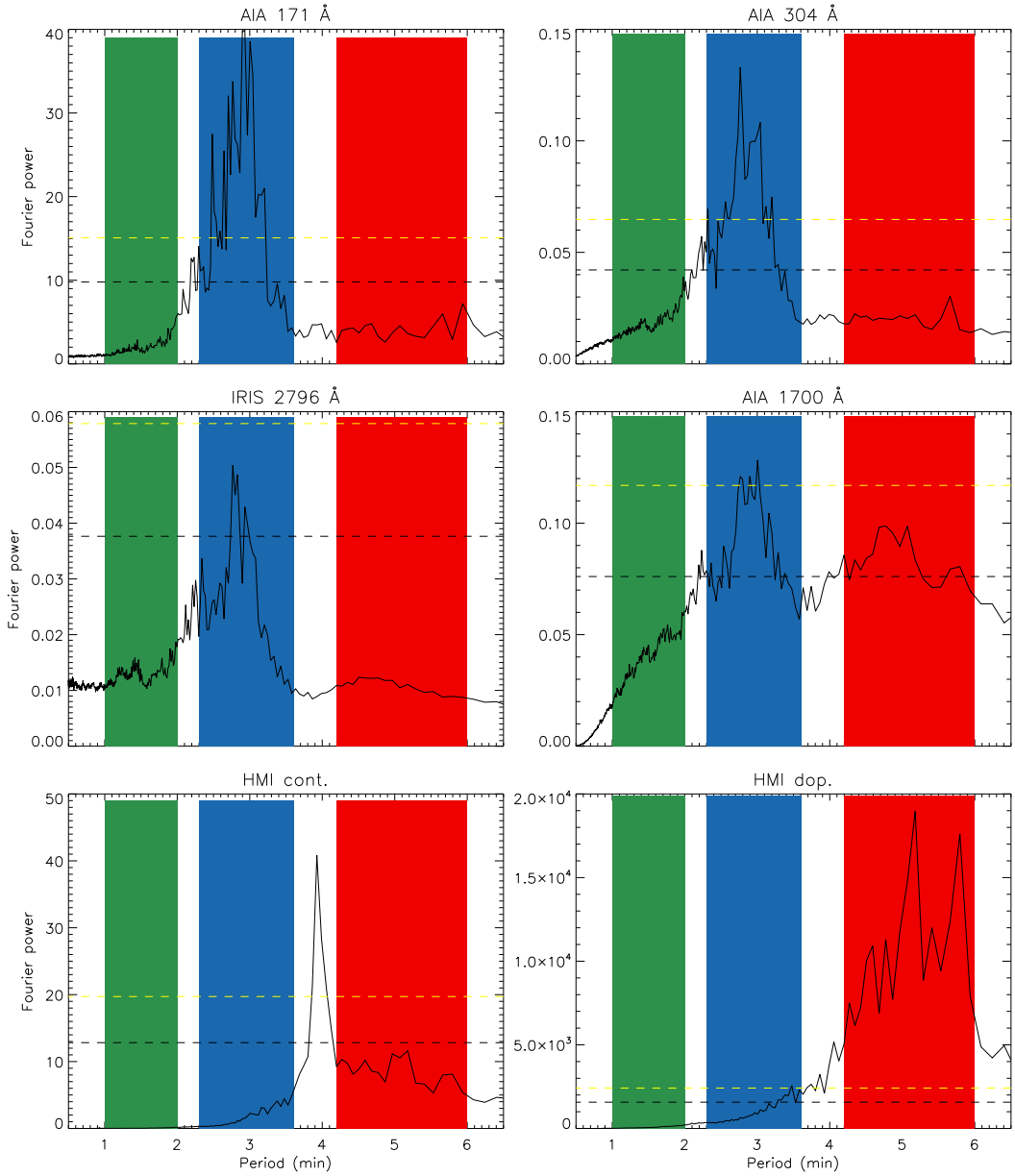

Figure B.4: Average Fourier power spectra obtained from background-subtracted light curves at different heights, as labelled, for the integrated umbra shown by the contour above the HMI continuum image in Figure 4.1. Shaded regions in green, blue, and red colours denote 1.5-min, 3-min, and 5-min period bands, respectively, identified for our analysis. Horizontal dashed lines in black and yellow colours represent 95% and 99% average confidence levels.

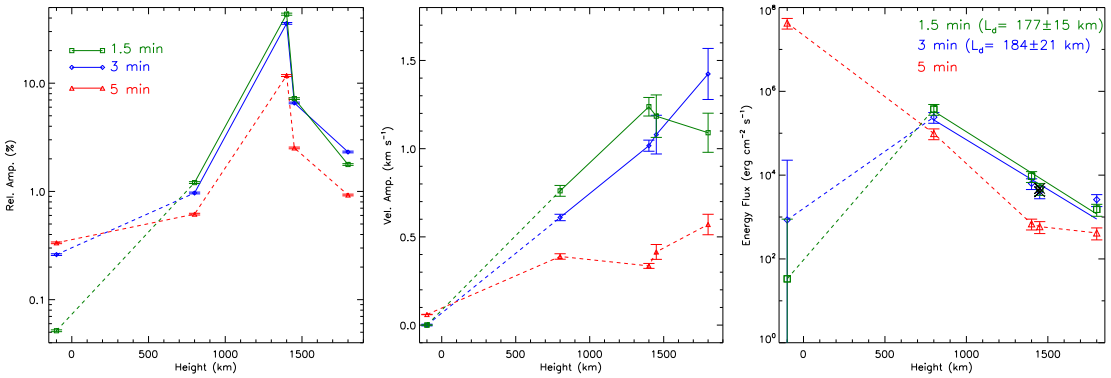

Figure B.5: Variation of average relative intensity amplitudes (left panel), velocity amplitudes (middle panel), and average wave energy fluxes (right panel) with atmospheric heights derived for the whole integrated umbra.

Appendix C

C.1 Loop footpoint temperature

According to Young et al. (2007), Mg V 2796.16 Å is very weak in most circumstances. However, the line is significantly enhanced at loop footpoints and provides valuable temperature information as shown in the left panel of Figure C.1. This further highlights the low temperature at the coronal footpoint and can be a topic of future exploration. The red and yellow contours obtained from EIS Mg V and AIA 171 Å image are overplotted on the EIS Fe VIII image. Images and contours highlight the accuracy of alignment of EIS images among themselves, and also with AIA passbands.

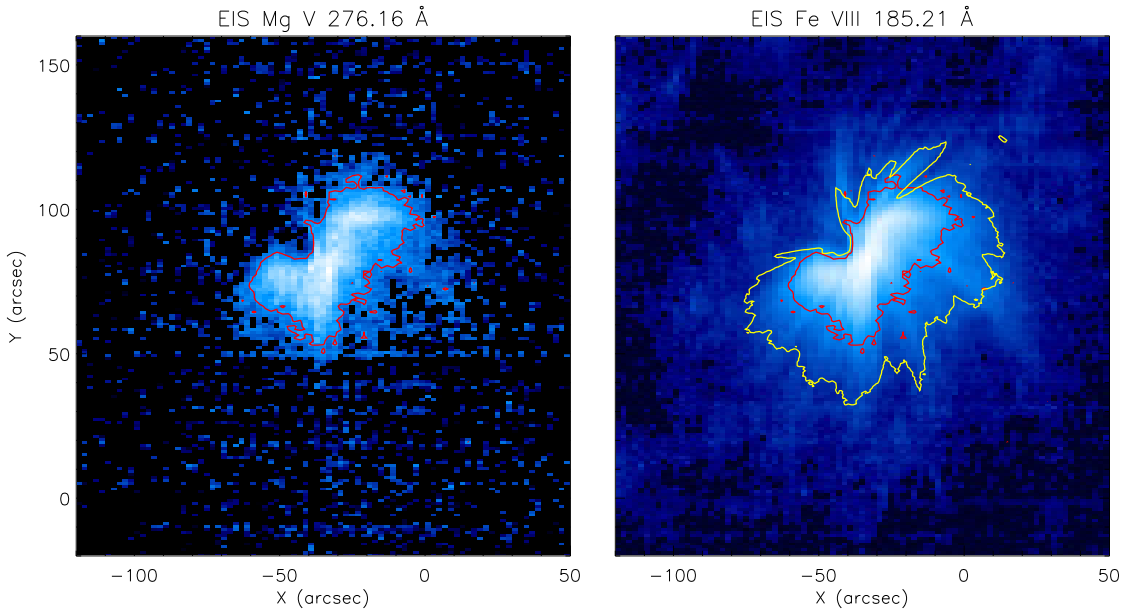

Figure C.1: Monochromatic intensity map of fan loop system obtained from low temperature spectral lines as labelled.

Bibliography

Alfvén, H. (1947). Magneto hydrodynamic waves, and the heating of the solar corona. , 107:211.

Anfinogentov, S. A., Antolin, P., Inglis, A. R., Kolotkov, D., Kupriyanova, E. G., McLaughlin, J. A., Nisticò, G., Pascoe, D. J., Krishna Prasad, S., and Yuan, D. (2022). Novel Data Analysis Techniques in Coronal Seismology. , 218(3):9.

Arlt, R. and Vaquero, J. M. (2020). Historical sunspot records. *Living Reviews in Solar Physics*, 17(1):1.

Arregui, I. (2015). Wave heating of the solar atmosphere. *Philosophical Transactions of the Royal Society of London Series A*, 373(2042):20140261–20140261.

Aschwanden, M. J. (2004). *Physics of the Solar Corona. An Introduction*.

Aschwanden, M. J., Fletcher, L., Schrijver, C. J., and Alexander, D. (1999a). Coronal Loop Oscillations Observed with the Transition Region and Coronal Explorer. , 520(2):880–894.

Aschwanden, M. J., Newmark, J. S., Delaboudinière, J.-P., Neupert, W. M., Klimchuk, J. A., Gary, G. A., Portier-Fozzani, F., and Zucker, A. (1999b). Three-dimensional Stereoscopic Analysis of Solar Active Region Loops. I. SOHO/EIT Observations at Temperatures of (1.0-1.5) $\times$ 10^6 K. , 515(2):842–867.

Aschwanden, M. J. and Schrijver, C. J. (2011). Coronal Loop Oscillations Observed with Atmospheric Imaging Assembly—Kink Mode with Cross-sectional and Density Oscillations. , 736(2):102.

Avrett, E., Tian, H., Landi, E., Curdt, W., and Wülser, J. P. (2015). Modeling the Chromosphere of a Sunspot and the Quiet Sun. , 811(2):87.

Bailey, Z., Bandyopadhyay, R., Habbal, S., and Druckmüller, M. (2025). Measurement of Turbulence Injection Scale Down to the Chromosphere. , 980(2):L20.

Banerjee, D., Gupta, G. R., and Teriaca, L. (2011). Propagating MHD Waves in Coronal Holes. , 158:267–288.

Banerjee, D., Krishna Prasad, S., Pant, V., McLaughlin, J. A., Antolin, P., Magyar, N., Ofman, L., Tian, H., Van Doorsselaere, T., De Moortel, I., and Wang, T. J. (2021). Magnetohydrodynamic Waves in Open Coronal Structures. , 217(7):76.

Banerjee, D., O'Shea, E., Goossens, M., Doyle, J. G., and Poedts, S. (2002). On the theory of MAG waves and a comparison with sunspot observations from CDS/SoHO. , 395:263–277.

Banerjee, D., Pérez-Suárez, D., and Doyle, J. G. (2009). Signatures of Alfvén waves in the polar coronal holes as seen by EIS/Hinode. , 501(3):L15–L18.

Beckers, J. M. and Tallant, P. E. (1969). Chromospheric Inhomogeneities in Sunspot Umbrae. , 7:351–365.

Bel, N. and Leroy, B. (1977). Analytical Study of Magnetoacoustic Gravity Waves. , 55:239.

Bellot Rubio, L. R., Collados, M., Ruiz Cobo, B., and Rodríguez Hidalgo, I. (2000). Oscillations in the Photosphere of a Sunspot Umbra from the Inversion of Infrared Stokes Profiles. , 534(2):989–996.

Belov, S. A., Molevich, N. E., and Zavershinskii, D. I. (2021). Dispersion of Slow Magnetoacoustic Waves in the Active Region Fan Loops Introduced by Thermal Misbalance. , 296(8):122.

Bender, Orszag, S. A. C. M. (1999). *Advanced mathematical methods for scientists and engineers I: asymptotic methods and perturbation theory.*

Bevington, P. R. (1969). *Data reduction and error analysis for the physical sciences*.

Bhatnagar, A. and Livingston, W. (2005). *Fundamentals of Solar Astronomy*, volume 6.

Boerner, P., Edwards, C., Lemen, J., Rausch, A., Schrijver, C., Shine, R., Shing, L., Stern, R., Tarbell, T., Title, A., Wolfson, C. J., Soufli, R., Spiller, E., Gullikson, E., McKenzie, D., Windt, D., Golub, L., Podgorski, W., Testa, P., and Weber, M. (2012). Initial Calibration of the Atmospheric Imaging Assembly (AIA) on the Solar Dynamics Observatory (SDO). , 275(1-2):41–66.

Bogdan, T. J. (2000). Sunspot Oscillations: A Review - (Invited Review). , 192:373–394.

Bogdan, T. J. and Judge, P. G. (2006). Observational aspects of sunspot oscillations. *Philosophical Transactions of the Royal Society of London Series A*, 364(1839):313–331.

Borrero, J. M. and Ichimoto, K. (2011). Magnetic Structure of Sunspots. *Living Reviews in Solar Physics*, 8(1):4.

Bourdin, P. A. (2017). Plasma Beta Stratification in the Solar Atmosphere: A Possible Explanation for the Penumbra Formation. , 850(2):L29.

Brooks, D. H. and Warren, H. P. (2016). Measurements of Non-thermal Line Widths in Solar Active Regions. , 820(1):63.

Brooks, D. H., Warren, H. P., and Landi, E. (2021). Measurements of Coronal Magnetic Field Strengths in Solar Active Region Loops. , 915(1):L24.

Bruner, Jr., E. C. (1978). Dynamics of the solar transition zone. , 226:1140–1146.

Cally, P. S. (1986). Leaky and Non-Leaky Oscillations in Magnetic Flux Tubes. , 103(2):277–298.

Cally, P. S., Bogdan, T. J., and Zweibel, E. G. (1994). Umbral Oscillations in Sunspots: Absorption of p-Modes and Active Region Heating by Mode Conversion. , 437:505.

Cargill, P. J., Warren, H. P., and Bradshaw, S. J. (2015). Modelling nanoflares in active regions and implications for coronal heating mechanisms. *Philosophical Transactions of the Royal Society of London Series A*, 373(2042):20140260–20140260.

Carlsson, M. and Stein, R. F. (1992). Non-LTE Radiating Acoustic Shocks and CA II K2V Bright Points. , 397:L59.

Centeno, R., Collados, M., and Trujillo Bueno, J. (2006). Spectropolarimetric Investigation of the Propagation of Magnetoacoustic Waves and Shock Formation in Sunspot Atmospheres. , 640:1153–1162.

Chae, J., Cho, K., Lim, E.-K., and Kang, J. (2022). Propagating Alfvénic Waves Observed in the Chromosphere around a Small Sunspot: Tales of 3-minute Waves and 10-minute Waves. , 933(1):108.

Chae, J., Lee, J., Cho, K., Song, D., Cho, K., and Yurchyshyn, V. (2017). Photospheric Origin of Three-minute Oscillations in a Sunspot. , 836(1):18.

Chae, J., Lim, E.-K., Lee, K., Kwak, H., Lee, K.-S., Kang, J., and Kang, S. (2023). Why Do Chromospheric Oscillations in Sunspot Umbrae Appear to Propagate Downward? , 944(2):L52.

Cheung, M. C. M., Boerner, P., Schrijver, C. J., Testa, P., Chen, F., Peter, H., and Malanushenko, A. (2015). Thermal Diagnostics with the Atmospheric Imaging Assembly on board the Solar Dynamics Observatory: A Validated Method for Differential Emission Measure Inversions. , 807(2):143.

Chitta, L. P., Peter, H., Parenti, S., Berghmans, D., Auchère, F., Solanki, S. K., Aznar Cuadrado, R., Schühle, U., Teriaca, L., Mandal, S., Barczynski, K., Buchlin, É., Harra, L., Kraaikamp, E., Long, D. M., Rodriguez, L., Schwanitz, C., Smith, P. J., Verbeeck, C., Zhukov, A. N., Liu, W., and Cheung, M. C. M. (2022). Solar coronal heating from small-scale magnetic braids. , 667:A166.

Cho, I. H., Cho, K. S., Bong, S. C., Moon, Y. J., Nakariakov, V. M., Park, J., Baek, J. H., Choi, S., Kim, Y. H., and Lee, J. (2017). Determination of the Alfvén Speed and Plasma-beta Using the Seismology of Sunspot Umbra. , 837(1):L11.

Cho, K. and Chae, J. (2020). Source Depth of Three-minute Umbral Oscillations. , 892(2):L31.

Cooley, J. W., Lewis, P. A. W., and Welch, P. D. (1969). The Fast Fourier Transform and Its Applications. *IEEE Transactions on Education*, 12(1):27–34.

Cranmer, S. R. and van Ballegooijen, A. A. (2012). Proton, Electron, and Ion Heating in the Fast Solar Wind from Nonlinear Coupling between Alfvénic and Fast-mode Turbulence. , 754(2):92.

Cranmer, S. R., van Ballegooijen, A. A., and Edgar, R. J. (2007). Self-consistent Coronal Heating and Solar Wind Acceleration from Anisotropic Magnetohydrodynamic Turbulence. , 171(2):520–551.

Şahin, S., Yurchyshyn, V., Kumar, P., Kilcik, A., Ahn, K., and Yang, X. (2019). Magnetic Field Dynamics and Varying Plasma Emission in Large-scale Coronal Loops. , 873(1):75.

Culhane, J. L., Harra, L. K., James, A. M., Al-Janabi, K., Bradley, L. J., Chaudry, R. A., Rees, K., Tandy, J. A., Thomas, P., Whillock, M. C. R., Winter, B., Doschek, G. A., Korendyke, C. M., Brown, C. M., Myers, S., Mariska, J., Seely, J., Lang, J., Kent, B. J., Shaughnessy, B. M., Young, P. R., Simnett, G. M., Castelli, C. M., Mahmoud, S., Mapson-Menard, H., Probyn, B. J., Thomas, R. J., Davila, J., Dere, K., Windt, D., Shea, J., Hagood, R., Moye, R., Hara, H., Watanabe, T., Matsuzaki, K., Kosugi, T., Hansteen, V., and Wikstol, Ø. (2007). The EUV Imaging Spectrometer for Hinode. , 243(1):19–61.

de la Cruz Rodríguez, J., De Pontieu, B., Carlsson, M., and Rouppe van der Voort, L. H. M. (2013). Heating of the Magnetic Chromosphere: Observational Constraints from Ca II λ8542 Spectra. , 764(1):L11.

de Moortel, I. (2009). Longitudinal Waves in Coronal Loops. , 149(1-4):65–81.

De Moortel, I. and Browning, P. (2015). Recent advances in coronal heating. *Philosophical Transactions of the Royal Society of London Series A*, 373(2042):20140269–20140269.

De Moortel, I. and Hood, A. W. (2003). The damping of slow MHD waves in solar coronal magnetic fields. , 408:755–765.

De Moortel, I. and Hood, A. W. (2004). The damping of slow MHD waves in solar coronal magnetic fields. II. The effect of gravitational stratification and field line divergence. , 415:705–715.

De Moortel, I., Ireland, J., Hood, A. W., and Walsh, R. W. (2002a). The detection of 3 5 min period oscillations in coronal loops. , 387:L13–L16.

De Moortel, I., Ireland, J., and Walsh, R. W. (2000). Observation of oscillations in coronal loops. , 355:L23–L26.

De Moortel, I., Ireland, J., Walsh, R. W., and Hood, A. W. (2002b). Longitudinal intensity oscillations in coronal loops observed with TRACE I. Overview of Measured Parameters. , 209(1):61–88.

De Moortel, I., Munday, S. A., and Hood, A. W. (2004). Wavelet Analysis: the effect of varying basic wavelet parameters. , 222(2):203–228.

De Moortel, I. and Nakariakov, V. M. (2012). Magnetohydrodynamic waves and coronal seismology: an overview of recent results. *Royal Society of London Philosophical Transactions Series A*, 370:3193–3216.

de Oliveira e Silva, A. J., Selhorst, C. L., Costa, J. E. R., Simões, P. J. A., Giménez de Castro, C. G., Wedemeyer, S., White, S. M., Brajša, R., and Valio, A. (2022). A Genetic Algorithm to Model Solar Radio Active Regions From 3D Magnetic Field Extrapolations. *Frontiers in Astronomy and Space Sciences*, 9:911118.

De Pontieu, B., McIntosh, S. W., Carlsson, M., Hansteen, V. H., Tarbell, T. D., Schrijver, C. J., Title, A. M., Shine, R. A., Tsuneta, S., Katsukawa, Y., Ichimoto, K., Suematsu, Y., Shimizu, T., and Nagata, S. (2007). Chromospheric Alfvénic Waves Strong Enough to Power the Solar Wind. *Science*, 318(5856):1574.

De Pontieu, B., Testa, P., Martínez-Sykora, J., Antolin, P., Karampelas, K., Hansteen, V., Rempel, M., Cheung, M. C. M., Reale, F., Danilovic, S., Pagano, P., Polito, V., De Moortel, I., Nóbrega-Siverio, D., Van Doorsselaere, T., Petralia, A., Asgari-Targhi,

M., Boerner, P., Carlsson, M., Chintzoglou, G., Daw, A., DeLuca, E., Golub, L., Matsumoto, T., Ugarte-Urra, I., McIntosh, S. W., and the MUSE Team (2022). Probing the Physics of the Solar Atmosphere with the Multi-slit Solar Explorer (MUSE). I. Coronal Heating. , 926(1):52.

De Pontieu, B., Title, A. M., Lemen, J. R., Kushner, G. D., Akin, D. J., Allard, B., Berger, T., Boerner, P., Cheung, M., Chou, C., Drake, J. F., Duncan, D. W., Freeland, S., Heyman, G. F., Hoffman, C., Hurlburt, N. E., Lindgren, R. W., Mathur, D., Rehse, R., Sabolish, D., Seguin, R., Schrijver, C. J., Tarbell, T. D., Wülser, J. P., Wolfson, C. J., Yanari, C., Mudge, J., Nguyen-Phuc, N., Timmons, R., van Bezooijen, R., Weingrod, I., Brookner, R., Butcher, G., Dougherty, B., Eder, J., Knagenhjelm, V., Larsen, S., Mansir, D., Phan, L., Boyle, P., Cheimets, P. N., DeLuca, E. E., Golub, L., Gates, R., Hertz, E., McKillop, S., Park, S., Perry, T., Podgorski, W. A., Reeves, K., Saar, S., Testa, P., Tian, H., Weber, M., Dunn, C., Eccles, S., Jaeggli, S. A., Kankelborg, C. C., Mashburn, K., Pust, N., Springer, L., Carvalho, R., Kleint, L., Marmie, J., Mazmanian, E., Pereira, T. M. D., Sawyer, S., Strong, J., Worden, S. P., Carlsson, M., Hansteen, V. H., Leenaarts, J., Wiesmann, M., Aloise, J., Chu, K. C., Bush, R. I., Scherrer, P. H., Brekke, P., Martinez-Sykora, J., Lites, B. W., McIntosh, S. W., Uitenbroek, H., Okamoto, T. J., Gummin, M. A., Auker, G., Jerram, P., Pool, P., and Waltham, N. (2014). The Interface Region Imaging Spectrograph (IRIS). , 289(7):2733–2779.

De Rosa, M. L., Schrijver, C. J., Barnes, G., Leka, K. D., Lites, B. W., Aschwanden, M. J., Amari, T., Canou, A., McTiernan, J. M., Régnier, S., Thalmann, J. K., Valori, G., Wheatland, M. S., Wiegelmann, T., Cheung, M. C. M., Conlon, P. A., Fuhrmann, M., Inhester, B., and Tadesse, T. (2009). A Critical Assessment of Nonlinear Force-Free Field Modeling of the Solar Corona for Active Region 10953. , 696(2):1780–1791.

DeForest, C. E. and Gurman, J. B. (1998). Observation of Quasi-periodic Compressive Waves in Solar Polar Plumes. , 501:L217.

Del Zanna, G. (2013). A revised radiometric calibration for the Hinode/EIS instrument. , 555:A47.

Del Zanna, G., Dere, K. P., Young, P. R., and Landi, E. (2021). CHIANTI—An Atomic Database for Emission Lines. XVI. Version 10, Further Extensions. , 909(1):38.

Del Zanna, G., Landini, M., and Mason, H. E. (2002). Spectroscopic diagnostics of stellar transition regions and coronae in the XUV: AU Mic in quiescence. , 385:968–985.

Del Zanna, G. and Mason, H. E. (2003). Solar active regions: SOHO/CDS and TRACE observations of quiescent coronal loops. , 406:1089–1103.

Del Zanna, G. and Mason, H. E. (2018). Solar UV and X-ray spectral diagnostics. *Living Reviews in Solar Physics*, 15(1):5.

Dere, K. P., Landi, E., Mason, H. E., Monsignori Fossi, B. C., and Young, P. R. (1997). CHIANTI - an atomic database for emission lines. , 125:149–173.

Duckenfield, T. J., Kolotkov, D. Y., and Nakariakov, V. M. (2021). The effect of the magnetic field on the damping of slow waves in the solar corona. , 646:A155.

Dufresne, R. P., Del Zanna, G., Young, P. R., Dere, K. P., Deliporanidou, E., Barnes, W. T., and Landi, E. (2024). CHIANTI—An Atomic Database for Emission Lines—Paper.

XVIII. Version 11, Advanced Ionization Equilibrium Models: Density and Charge Transfer Effects. , 974(1):71.

Edlén, B. (1943). Die Deutung der Emissionslinien im Spektrum der Sonnenkorona. Mit 6 Abbildungen. , 22:30.

Edmonds, M. and Bond, P. (2022). Book review: Solar Surveyors: Observing the Sun from Space (Bond). *Journal of the British Astronomical Association*, 132:387.

Erdélyi, R. and Taroyan, Y. (2008). Hinode EUV spectroscopic observations of coronal oscillations. , 489(3):L49–L52.

Feldman, U. (1992). REVIEW: Elemental abundances in the upper solar atmosphere. , 46(3):202–220.

Felipe, T. (2019). Origin of the chromospheric three-minute oscillations in sunspot umbrae. , 627:A169.

Felipe, T. (2021). Signatures of sunspot oscillations and the case for chromospheric resonances. *Nature Astronomy*, 5:2–4.

Felipe, T., Khomenko, E., and Collados, M. (2010). Magneto-acoustic Waves in Sunspots: First Results From a New Three-dimensional Nonlinear Magnetohydrodynamic Code. , 719(1):357–377.

Felipe, T., Khomenko, E., and Collados, M. (2011). Magnetoacoustic Wave Energy from Numerical Simulations of an Observed Sunspot Umbra. , 735(1):65.

Felipe, T., Kuckein, C., González Manrique, S. J., Milic, I., and Sangeetha, C. R. (2020). Chromospheric Resonances above Sunspots and Potential Seismological Applications. , 900(2):L29.

Felipe, T. and Socas-Navarro, H. (2023). Impact of opacity effects on chromospheric oscillations inferred from NLTE inversions. , 670:A133.

Felipe, T., Socas-Navarro, H., and Khomenko, E. (2014). Synthetic Observations of Wave Propagation in a Sunspot Umbra. , 795(1):9.

Fleck, B. and Schmitz, F. (1991). The 3-min oscillations of the solar chromosphere - A basic physical effect? , 250(1):235–244.

Fontenla, J., White, O. R., Fox, P. A., Avrett, E. H., and Kurucz, R. L. (1999). Calculation of Solar Irradiances. I. Synthesis of the Solar Spectrum. , 518(1):480–499.

Fontenla, J. M., Curdt, W., Haberreiter, M., Harder, J., and Tian, H. (2009). Semiempirical Models of the Solar Atmosphere. III. Set of Non-LTE Models for Far-Ultraviolet/Extreme-Ultraviolet Irradiance Computation. , 707(1):482–502.

Fossum, A. and Carlsson, M. (2005). High-frequency acoustic waves are not sufficient to heat the solar chromosphere. , 435(7044):919–921.

Foukal, P. V. (2004). *Solar Astrophysics, 2nd, Revised Edition*.

Freeland, S. L. and Handy, B. N. (1998). Data Analysis with the SolarSoft System. , 182(2):497–500.

Gary, G. A. (2001). Plasma Beta above a Solar Active Region: Rethinking the Paradigm. , 203(1):71–86.

Ghosh, A., Tripathi, D., Gupta, G. R., Polito, V., Mason, H. E., and Solanki, S. K. (2017). Fan Loops Observed by IRIS, EIS, and AIA. , 835(2):244.

Gilchrist-Millar, C. A., Jess, D. B., Grant, S. D. T., Keys, P. H., Beck, C., Jafarzadeh, S., Riedl, J. M., Van Doorsselaere, T., and Ruiz Cobo, B. (2021). Magnetoacoustic wave energy dissipation in the atmosphere of solar pores. *Philosophical Transactions of the Royal Society of London Series A*, 379(2190):20200172.

Giordano, S., Berrilli, F., Del Moro, D., and Penza, V. (2008). The photospheric structure of a solar pore with light bridge. , 489(2):747–754.

Giovanelli, R. G. (1984). *Secrets of the sun*.

Goossens, M. (1994). Alfvén wave heating. , 68(1-4):51–62.

Goossens, M. (2003). *An introduction to plasma astrophysics and magnetohydrodynamics*, volume 294.

Goossens, M., Andries, J., and Arregui, I. (2006). Damping of magnetohydrodynamic waves by resonant absorption in the solar atmosphere. *Philosophical Transactions of the Royal Society of London Series A*, 364(1839):433–446.

Goossens, M., Erdélyi, R., and Ruderman, M. S. (2011). Resonant MHD Waves in the Solar Atmosphere. , 158(2-4):289–338.

Grant, S. D. T., Jess, D. B., Stangalini, M., Jafarzadeh, S., Fedun, V., Verth, G., Keys, P. H., Rajaguru, S. P., Uitenbroek, H., MacBride, C. D., Bate, W., and Gilchrist-Millar, C. A. (2022). The Propagation of Coherent Waves Across Multiple Solar Magnetic Pores. , 938(2):143.

Grant, S. D. T., Jess, D. B., Zaqarashvili, T. V., Beck, C., Socas-Navarro, H., Aschwanden, M. J., Keys, P. H., Christian, D. J., Houston, S. J., and Hewitt, R. L. (2018). Alfvén wave dissipation in the solar chromosphere. *Nature Physics*, 14(5):480–483.

Grotrian, W. (1939). Zur Frage der Deutung der Linien im Spektrum der Sonnenkorona. *Naturwissenschaften*, 27(13):214–214.

Gupta, G. R. (2014). Observations of dissipation of slow magneto-acoustic waves in a polar coronal hole. , 568:A96.

Gupta, G. R. (2017). Spectroscopic Evidence of Alfvén Wave Damping in the Off-limb Solar Corona. , 836(1):4.

Gupta, G. R., Banerjee, D., Teriaca, L., Imada, S., and Solanki, S. (2010). Accelerating Waves in Polar Coronal Holes as Seen by EIS and SUMER. , 718:11–22.

Gupta, G. R., Del Zanna, G., and Mason, H. E. (2019). Exploring the damping of Alfvén waves along a long off-limb coronal loop, up to 1.4 $R_{\odot}$. , 627:A62.

Gupta, G. R. and Nayak, S. S. (2022). Spectroscopic and imaging observations of transient hot and cool loops by IRIS and SDO. , 512(3):3149–3162.

Gupta, G. R., Teriaca, L., Marsch, E., Solanki, S. K., and Banerjee, D. (2012). Spectroscopic observations of propagating disturbances in a polar coronal hole: evidence of slow magneto-acoustic waves. , 546:A93.

Gupta, G. R., Tripathi, D., and Mason, H. E. (2015). Spectroscopic Observations of a Coronal Loop: Basic Physical Plasma Parameters Along the Full Loop Length. , 800:140.

Gurman, J. B., Leibacher, J. W., Shine, R. A., Woodgate, B. E., and Henze, W. (1982). Transition region oscillations in sunspots. , 253:939–948.

Hannah, I. G. and Kontar, E. P. (2012). Differential emission measures from the regularized inversion of Hinode and SDO data. , 539:A146.

Hasan, S. S. and Rutten, R. J., editors (2010). *Magnetic Coupling between the Interior and Atmosphere of the Sun*, volume 19 of *Astrophysics and Space Science Proceedings*.

Heyvaerts, J. and Priest, E. R. (1983). Coronal heating by phase-mixed shear Alfven waves. , 117:220–234.

Hollweg, J. V. (1978). Alfvén waves in the solar atmosphere. , 56(2):305–333.

Hollweg, J. V. (1997). Comment on "Gravitational Damping of Alfvén Waves in Stellar Atmospheres and Winds". , 488(2):895–897.

Howard, R. F., Harvey, J. W., and Forgach, S. (1990). Solar Surface Velocity Fields Determined from Small Magnetic Features. , 130(1-2):295–311.

Huang, Z., Li, B., and Xia, L. (2019). Observations of small-scale energetic events in the solar transition region: explosive events, UV bursts, and network jets. *Solar-Terrestrial Physics*, 5(2):58–68.

Hudson, H. S. (1991). Solar flares, microflares, nanoflares, and coronal heating. , 133(2):357–369.

Infeld, E. (1998). Introduction to Plasma Physics, by R. J. Goldston and P. H. Rutherford, Institute of Physics Press, Bristol, 1995, xvii+491 pages. ISBN 0750 3032 5 5 hc; 0750 3018 3 X pb. Â£98.00 hc; Â£29.50 pb. *Journal of Plasma Physics*, 59(2):387–389.

Ionson, J. A. (1978). Resonant absorption of Alfvénic surface waves and the heating of solar coronal loops. , 226:650–673.

Jess, D. B., De Moortel, I., Mathioudakis, M., Christian, D. J., Reardon, K. P., Keys, P. H., and Keenan, F. P. (2012a). The Source of 3 Minute Magnetoacoustic Oscillations in Coronal Fans. , 757(2):160.

Jess, D. B., Jafarzadeh, S., Keys, P. H., Stangalini, M., Verth, G., and Grant, S. D. T. (2023). Waves in the lower solar atmosphere: the dawn of next-generation solar telescopes. *Living Reviews in Solar Physics*, 20(1):1.

Jess, D. B., Mathioudakis, M., Erdélyi, R., Crockett, P. J., Keenan, F. P., and Christian, D. J. (2009). Alfvén Waves in the Lower Solar Atmosphere. *Science*, 323(5921):1582.

Jess, D. B., Morton, R. J., Verth, G., Fedun, V., Grant, S. D. T., and Giagkiozis, I. (2015). Multiwavelength Studies of MHD Waves in the Solar Chromosphere. An Overview of Recent Results. , 190(1-4):103–161.

Jess, D. B., Pascoe, D. J., Christian, D. J., Mathioudakis, M., Keys, P. H., and Keenan, F. P. (2012b). The Origin of Type I Spicule Oscillations. , 744(1):L5.

Jess, D. B., Reznikova, V. E., Ryans, R. S. I., Christian, D. J., Keys, P. H., Mathioudakis, M., Mackay, D. H., Krishna Prasad, S., Banerjee, D., Grant, S. D. T., Yau, S., and Diamond, C. (2016). Solar coronal magnetic fields derived using seismology techniques applied to omnipresent sunspot waves. *Nature Physics*, 12(2):179–185.

Jess, D. B., Reznikova, V. E., Van Doorsselaere, T., Keys, P. H., and Mackay, D. H. (2013). The Influence of the Magnetic Field on Running Penumbral Waves in the Solar Chromosphere. , 779(2):168.

Jess, D. B., Snow, B., Houston, S. J., Botha, G. J. J., Fleck, B., Krishna Prasad, S., Asensio Ramos, A., Morton, R. J., Keys, P. H., Jafarzadeh, S., Stangalini, M., Grant, S. D. T., and Christian, D. J. (2020). A chromospheric resonance cavity in a sunspot mapped with seismology. *Nature Astronomy*, 4:220–227.

Judge, P. G. (2020). *The Sun: A Very Short Introduction*.

Kamio, S., Hara, H., Watanabe, T., Fredvik, T., and Hansteen, V. H. (2010). Modeling of EIS Spectrum Drift from Instrumental Temperatures. , 266(1):209–223.

Kanoh, R., Shimizu, T., and Imada, S. (2016). Hinode and IRIS Observations of the Magnetohydrodynamic Waves Propagating from the Photosphere to the Chromosphere in a Sunspot. , 831(1):24.

Karampelas, K., Van Doorsselaere, T., Guo, M., Duckenfield, T., and Pelouze, G. (2024). Kelvin-Helmholtz instability and heating in oscillating loops perturbed by power-law transverse wave drivers. , 688:A80.

Kentischer, T. J. and Mattig, W. (1995). Oscillations above sunspot umbrae. , 300:539.

Keys, P. H., Morton, R. J., Jess, D. B., Verth, G., Grant, S. D. T., Mathioudakis, M., Mackay, D. H., Doyle, J. G., Christian, D. J., Keenan, F. P., and Erdélyi, R. (2018). Photospheric Observations of Surface and Body Modes in Solar Magnetic Pores. , 857(1):28.

Khomenko, E. and Cally, P. S. (2012). Numerical Simulations of Conversion to Alfvén Waves in Sunspots. , 746(1):68.

Khomenko, E. and Collados, M. (2006). Numerical Modeling of Magnetohydrodynamic Wave Propagation and Refraction in Sunspots. , 653(1):739–755.

Khomenko, E. and Collados, M. (2015). Oscillations and Waves in Sunspots. *Living Reviews in Solar Physics*, 12.

Khomenko, E. V., Collados, M., and Bellot Rubio, L. R. (2003). Magnetoacoustic Waves in Sunspots. , 588(1):606–619.

Kiddie, G., De Moortel, I., Del Zanna, G., McIntosh, S. W., and Whittaker, I. (2012). Propagating Disturbances in Coronal Loops: A Detailed Analysis of Propagation Speeds. , 279:427–452.

Kinsler, L. E., Frey, A. R., Coppens, A. B., and Sanders, J. V. (1999). *Fundamentals of Acoustics, 4th Edition*.

Klimchuk, J. A. (2006). On Solving the Coronal Heating Problem. , 234(1):41–77.

Klimchuk, J. A. (2015). Key aspects of coronal heating. *Philosophical Transactions of the Royal Society of London Series A*, 373(2042):20140256–20140256.

Kobanov, N. I., Chelpanov, A. A., and Kolobov, D. Y. (2013). Oscillations above sunspots from the temperature minimum to the corona. , 554:A146.

Kolotkov, D. Y., Nakariakov, V. M., and Zavershinskii, D. I. (2019). Damping of slow magnetoacoustic oscillations by the misbalance between heating and cooling processes in the solar corona. , 628:A133.

Kolotkov, D. Y., Zavershinskii, D. I., and Nakariakov, V. M. (2021). The solar corona as an active medium for magnetoacoustic waves. *Plasma Physics and Controlled Fusion*, 63(12):124008.

Kosovichev, A. G. and Sekii, T. (2007). Initial Observations of Sunspot Oscillations Excited by Solar Flare. , 670(2):L147–L149.

Kosugi, T., Matsuzaki, K., Sakao, T., Shimizu, T., Sone, Y., Tachikawa, S., Hashimoto, T., Minesugi, K., Ohnishi, A., Yamada, T., Tsuneta, S., Hara, H., Ichimoto, K., Suematsu, Y., Shimojo, M., Watanabe, T., Shimada, S., Davis, J. M., Hill, L. D., Owens, J. K., Title, A. M., Culhane, J. L., Harra, L. K., Doschek, G. A., and Golub, L. (2007). The Hinode (Solar-B) Mission: An Overview. , 243(1):3–17.

Kraśkiewicz, J., Murawski, K., and Musielak, Z. E. (2019). Cutoff periods of magnetoacoustic waves in the solar atmosphere. , 623:A62.

Krishna Prasad, S., Banerjee, D., and Van Doorsselaere, T. (2014). Frequency-dependent Damping in Propagating Slow Magneto-acoustic Waves. , 789(2):118.

Krishna Prasad, S., Banerjee, D., Van Doorsselaere, T., and Singh, J. (2012). Omnipresent long-period intensity oscillations in open coronal structures. , 546:A50.

Krishna Prasad, S., Jess, D. B., and Khomenko, E. (2015). On the Source of Propagating Slow Magnetoacoustic Waves in Sunspots. , 812(1):L15.

Krishna Prasad, S., Jess, D. B., Van Doorsselaere, T., Verth, G., Morton, R. J., Fedun, V., Erdélyi, R., and Christian, D. J. (2017). The Frequency-dependent Damping of Slow Magnetoacoustic Waves in a Sunspot Umbral Atmosphere. , 847(1):5.

Krishna Prasad, S., Raes, J. O., Van Doorsselaere, T., Magyar, N., and Jess, D. B. (2018). The Polytropic Index of Solar Coronal Plasma in Sunspot Fan Loops and Its Temperature Dependence. , 868(2):149.

Lemen, J. R., Title, A. M., Akin, D. J., Boerner, P. F., Chou, C., Drake, J. F., Duncan, D. W., Edwards, C. G., Friedlaender, F. M., Heyman, G. F., Hurlburt, N. E., Katz, N. L., Kushner, G. D., Levay, M., Lindgren, R. W., Mathur, D. P., McFeaters, E. L., Mitchell, S., Rehse, R. A., Schrijver, C. J., Springer, L. A., Stern, R. A., Tarbell, T. D., Wuelser, J.-P., Wolfson, C. J., Yanari, C., Bookbinder, J. A., Cheimets, P. N., Caldwell, D., Deluca, E. E., Gates, R., Golub, L., Park, S., Podgorski, W. A., Bush, R. I., Scherrer, P. H., Gummin, M. A., Smith, P., Auker, G., Jerram, P., Pool, P., Soufli, R., Windt, D. L., Beardsley, S., Clapp, M., Lang, J., and Waltham, N. (2012). The Atmospheric Imaging Assembly (AIA) on the Solar Dynamics Observatory (SDO). , 275(1-2):17–40.

Li, D., Yuan, D., Goossens, M., Van Doorsselaere, T., Su, W., Wang, Y., Su, Y., and Ning, Z. (2020). Ultra-long and quite thin coronal loop without significant expansion. , 639:A114.

Lin, H., Kuhn, J. R., and Coulter, R. (2004). Coronal Magnetic Field Measurements. , 613(2):L177–L180.

Lin, H., Penn, M. J., and Tomczyk, S. (2000). A New Precise Measurement of the Coronal Magnetic Field Strength. , 541(2):L83–L86.

Lin, R. P., Schwartz, R. A., Kane, S. R., Pelling, R. M., and Hurley, K. C. (1984). Solar hard X-ray microflares. , 283:421–425.

Lites, B. W. (1984). Photoelectric observations of chromospheric sunspot oscillations. II - Propagation characteristics. , 277:874–888.

Lites, B. W. (1986). Photoelectric Observations of Chromospheric Sunspot Oscillations. III. Spatial Distribution of Power and Frequency in Umbrae. , 301:992.

Lites, B. W., Thomas, J. H., Bogdan, T. J., and Cally, P. S. (1998). Velocity and Magnetic Field Fluctuations in the Photosphere of a Sunspot. , 497(1):464–482.

Liu, W. and Ofman, L. (2014). Advances in Observing Various Coronal EUV Waves in the SDO Era and Their Seismological Applications (Invited Review). , 289(9):3233–3277.

Löhner-Böttcher, J. (2016). *Wave phenomena in sunspots*. PhD thesis, Albert Ludwigs University of Freiburg, Germany.

Louis, R. E., Bayanna, A. R., Mathew, S. K., and Venkatakrishnan, P. (2008). Dynamics of Sunspot Light Bridges as Revealed by High-Resolution Images from Hinode. , 252(1):43.

Luna-Cardozo, M., Verth, G., and Erdélyi, R. (2012). Longitudinal Oscillations in Density Stratified and Expanding Solar Waveguides. , 748(2):110.

Maltby, P., Avrett, E. H., Carlsson, M., Kjeldseth-Moe, O., Kurucz, R. L., and Loeser, R. (1986). A New Sunspot Umbral Model and Its Variation with the Solar Cycle. , 306:284.

Mandal, S., Magyar, N., Yuan, D., Van Doorsselaere, T., and Banerjee, D. (2016). Forward Modeling of Propagating Slow Waves in Coronal Loops and Their Frequency-dependent Damping. , 820(1):13.

Markwardt, C. B. (2009). Non-linear Least-squares Fitting in IDL with MPFIT. In Bohlender, D. A., Durand, D., and Dowler, P., editors, *Astronomical Data Analysis Software and Systems XVIII*, volume 411 of *Astronomical Society of the Pacific Conference Series*, page 251.

Marsh, M. S., De Moortel, I., and Walsh, R. W. (2011). Observed Damping of the Slow Magnetoacoustic Mode. , 734(2):81.

Marsh, M. S. and Walsh, R. W. (2006). p-Mode Propagation through the Transition Region into the Solar Corona. I. Observations. , 643(1):540–548.

Martinez Pillet, V., Cauzzi, G., Tritschler, A., Harra, L., Andretta, V., Vourlidas, A., Raouafi, N., Alterman, B. L., Bellot Rubio, L., Cranmer, S. R., Gibson, S., De Groof, A., Ko, Y. K., Lepri, S. T., Linker, J., Malaspina, D. M., Matthews, S., Müller, D., Parenti, S., Petrie, G., Spadaro, D., Ugarte-Urra, I., Warren, H., and Zouganelis, I. (2023). Solar Physics in the 2020s: DKIST, Parker Solar Probe, and Solar Orbiter as a Multi-Messenger Constellation. In Cauzzi, G. and Tritschler, A., editors, *The Era of Multi-Messenger Solar Physics*, volume 372 of *IAU Symposium*, pages 3–16.

Martínez-Sykora, J., Hansteen, V., and Carlsson, M. (2009). Twisted Flux Tube Emergence from the Convection Zone to the Corona. II. Later States. , 702(1):129–140.

Mason, J. P., Werth, A., West, C. G., Youngblood, A., Woodraska, D. L., Peck, C. L., Aradhya, A. J., Cai, Y., Chaparro, D., Erikson, J. W., Ganesan, K., Geerdts, T. R., Hoang, T. D., Horning, T. M., Jin, Y., Liu, H., Lordi, N., Luo, Z., Menon, T. S., Meyer, J. C., Nelson, E. E., Oliver, K. A., Ramirez Ortiz, J. L., Osborne, A., Patterson, A., Pellatz, N., Pitten, J., Shitara, N., Steckhahn, D., Visal, A., Wang, H., Wang, C., Wickenden, E., Wilson, J., Wu, M., Yegovtsev, N., Zimmermann, I. H., Aaron, J. H., Abdullah, J. T., Abrams, J. M., Abrashoff, R., Acevedo, A. B., Acha, I., Meza Acosta, D. M., Adam, M. M., Adams, D. Q., Adams, K. N., Adams, E. R., Akbar, Z. A., Akruwala, U. H., Al-Ghazwi, A., Alabbas, B. H., Alawadhi, A. A., Alharbi, Y. A., Alahmed, M. S., Albakr, M. A., Albalushi, Y. J., Albaum, J., Aldhamen, A., Ales, N., Alesmail, M., Alhabeeb, A., Alhamli, D., Alhuseini, I., Alkaabi, S., Alkhezzi, T., Alkubaisi, M., Allanqawi, N., Allsbrook, M., Almohsen, Y. A., Almquist, J. T., Alnaji, T., Alnasrallah, Y. A., Alonzi, N., Alosaimi, M., Alqabani, E., Alrubaie, M., Alsinan, R. A., Altenbern, A. L., Altokhais, A., Alyami, S. A., Ameijenda, F., Amer, H., Amos, M., Anderson, H. J., Andrew, C., Andringa, J. C., Angwin, A., Van Anne, G., Aramians, A., Arango, C. V., Archibald, J. W., Arias-Robles, B. A., Aryan, M., Ash, K., Astalos, J., Atchley-Rivers, N. S., Augenstein, D. N., Austin, B. W., Avula, A., Aycock, M. C., Baflah, A. A., Balaji, S., Balajonda, B., Balcer, L. M., Baldwin, J. O., Banda, D. J., Bard, T., Barmore, A., Barnes, G. M., Barnhart, L. D. W., Barone, K. M., Bartman, J. L., Bassel, C., Bastias, C. S., Bat-Ulzii, B., Batra, J., Battist, L., Bay, J., Beach, S., Beard, S., Beato, Q. I., Beattie, R., Beatty, T., De La Beaujardiere, T., Beauprez, J. N., Beck, M. G., Beck, L., Becker, S. E., Behr, B., Behrer, T. A., Beijer, J., Belei, B. J., Belknap, A. L., Bell, A., Bence, C., Benke, E., Berhanu, N., Berriman-Rozen, Z. D., Bertuccio, C., Berv, O. A., Biediger, B. B., Biehle, S. J., Billig, B., Billingsley, J., Billman, J. A., Biron, C. J., Bisacca, G. E., Blake, C. A., Blandon, G., Blevins, O., Blouin, E., Bodzianowski, M., Boeyink, T. A., Bondar, M., Bone, L., De Los Monteros Bonilla, A. E., Borelli, W. T., Borgerding, L. R., Bowen, T., Boyer, C., Boyer, A., Boyle, A. P., Boyne, T., Branch, D., Brecl, A. E., Brennan, D. J., Brimhall, A. J., Brockman, J. L., Brookins, S., Brown, G. T., Brown, C. L., Brown, R., Brownlow, J., Brumage-Heller, G., Brumley, P. J., Bryan, S., Brzostowicz, A., Buhamad, M., Bullard-Connor, G., Ramirez Bunsow, J. R., Burns, A. C., Burritt, J. J., Burton, N. D., Burton, T., Busch, C., Butler, D. R., Buxton, B. W., C. Toups, M., Cabbage, C. C., Cage, B., Cahn, J. R., Campbell, A. J., Canales, B. P., Cancio, A. R., Carey, L., Carillion, E. L., Carpender, M. A., Carpenter, E., and Chadda, S. (2023). Coronal Heating as Determined by the Solar Flare Frequency Distribution Obtained by Aggregating Case Studies. , 948(2):71.

Mathew, S. K., Solanki, S. K., Lagg, A., Collados, M., Borrero, J. M., and Berdyugina, S. (2004). Thermal-magnetic relation in a sunspot and a map of its Wilson depression. , 422:693–701.

Mathioudakis, M., Jess, D. B., and Erdélyi, R. (2013). Alfvén Waves in the Solar Atmosphere. From Theory to Observations. , 175(1-4):1–27.

McIntosh, S. W., de Pontieu, B., Carlsson, M., Hansteen, V., Boerner, P., and Goossens, M. (2011). Alfvénic waves with sufficient energy to power the quiet solar corona and fast solar wind. , 475(7357):477–480.

Meadowcroft, R. L., Zhong, S., Kolotkov, D. Y., and Nakariakov, V. M. (2024). Observation of a propagating slow magnetoacoustic wave in a coronal plasma fan with SDO/AIA and SolO/EUI. , 527(3):5302–5310.

Mein, N. and Schmieder, B. (1981). Mechanical flux in the solar chromosphere. III - Variation of the mechanical flux. , 97(2):310–316.

Moreels, M. G. and Van Doorsselaere, T. (2013). Phase relations for seismology of photospheric flux tubes. , 551:A137.

Morton, R. J., Sharma, R., Tajfirouze, E., and Miriyala, H. (2023). Alfvénic waves in the inhomogeneous solar atmosphere. *Reviews of Modern Plasma Physics*, 7(1):17.

Morton, R. J., Tomczyk, S., and Pinto, R. (2015). Investigating Alfvénic wave propagation in coronal open-field regions. *Nature Communications*, 6:7813.

Morton, R. J., Verth, G., Jess, D. B., Kuridze, D., Ruderman, M. S., Mathioudakis, M., and Erdélyi, R. (2012). Observations of ubiquitous compressive waves in the Sun's chromosphere. *Nature Communications*, 3:1315.

Nakariakov, V. M. and Kolotkov, D. Y. (2020). Magnetohydrodynamic Waves in the Solar Corona. , 58:441–481.

Nakariakov, V. M. and Ofman, L. (2001). Determination of the coronal magnetic field by coronal loop oscillations. , 372:L53–L56.

Nakariakov, V. M., Ofman, L., Deluca, E. E., Roberts, B., and Davila, J. M. (1999). TRACE observation of damped coronal loop oscillations: Implications for coronal heating. *Science*, 285:862–864.

Nakariakov, V. M., Verwichte, E., Berghmans, D., and Robbrecht, E. (2000). Slow magnetoacoustic waves in coronal loops. , 362:1151–1157.

Nakariakov, V. M., Zhong, S., Kolotkov, D. Y., Meadowcroft, R. L., Zhong, Y., and Yuan, D. (2024). Diagnostics of the solar coronal plasmas by magnetohydrodynamic waves: magnetohydrodynamic seismology. *Reviews of Modern Plasma Physics*, 8(1):19.

Narayanan, A. (2013). *An Introduction to Waves and Oscillations in the Sun*.

Norton, A. A., Graham, J. P., Ulrich, R. K., Schou, J., Tomczyk, S., Liu, Y., Lites, B. W., Ariste, A. L., Bush, R. I., Socas-Navarro, H., and Scherrer, P. H. (2006). Spectral Line Selection for HMI: A Comparison of Fe I 6173 Å and Ni I 6768 Å. , 239(1-2):69–91.

Norton, A. A., Stutz, R. B., and Welsch, B. T. (2021). Oscillations observed in umbra, plage, quiet-Sun and the polarity inversion line of active region 11158 using Helioseismic Magnetic Imager/Solar Dynamics Observatory data. *Philosophical Transactions of the Royal Society of London Series A*, 379(2190):20200175.

Nye, A. H. and Hollweg, J. V. (1980). Alfvén waves in sunspots. , 68(2):279–295.

O'Dwyer, B., Del Zanna, G., Mason, H. E., Weber, M. A., and Tripathi, D. (2010). SDO/AIA response to coronal hole, quiet Sun, active region, and flare plasma. , 521:A21.

Ofman, L., Nakariakov, V. M., and Sehgal, N. (2000). Dissipation of Slow Magnetosonic Waves in Coronal Plumes. , 533(2):1071–1083.

O'Shea, E., Banerjee, D., Doyle, J. G., Fleck, B., and Murtagh, F. (2001). Active region oscillations. , 368:1095–1107.

O'Shea, E., Muglach, K., and Fleck, B. (2002). Oscillations above sunspots: Evidence for propagating waves? , 387:642–664.

Parchevsky, K. and Kosovichev, A. (2006). Suppression of amplitude of 5-min oscillations in sunspots due to the lack of acoustic sources. In Fletcher, K. and Thompson, M., editors, *Proceedings of SOHO 18/GONG 2006/HELAS I, Beyond the spherical Sun*, volume 624 of *ESA Special Publication*, page 39.

Parker, E. N. (1988). Nanoflares and the Solar X-Ray Corona. , 330:474.

Parnell, C. E. and De Moortel, I. (2012). A contemporary view of coronal heating. *Philosophical Transactions of the Royal Society of London Series A*, 370(1970):3217–3240.

Pence, W. D., Chiappetti, L., Page, C. G., Shaw, R. A., and Stobie, E. (2010). Definition of the Flexible Image Transport System (FITS), version 3.0. , 524:A42.

Pesnell, W. D., Thompson, B. J., and Chamberlin, P. C. (2012). The Solar Dynamics Observatory (SDO). , 275(1-2):3–15.

Peter, H., Gudiksen, B. V., and Nordlund, A. (2005). Coronal Heating Through Braiding of Magnetic Field Lines Synthesized Coronal EUV Emission and Magnetic Structure. In Innes, D. E., Lagg, A., and Solanki, S. A., editors, *Chromospheric and Coronal Magnetic Fields*, volume 596 of *ESA Special Publication*, page 14.1.

Phillips, K. J. H., Feldman, U., and Landi, E. (2008). *Ultraviolet and X-ray Spectroscopy of the Solar Atmosphere*.

Press, W. H., Flannery, B. P., and Teukolsky, S. A. (1986). *Numerical recipes. The art of scientific computing*.

Priest, E. (2014). *Magnetohydrodynamics of the Sun*.

Przybylski, D., Shelyag, S., and Cally, P. S. (2015). Spectropolarimetrically Accurate Magnetohydrostatic Sunspot Model for Forward Modeling in Helioseismology. , 807(1):20.

Rawat, A. and Gupta, G. (2023). Exploring source region of 3-min slow magnetoacoustic waves observed in coronal fan loops rooted in sunspot umbra. , 525(4):4815–4831.

Rawat, A. and Gupta, G. (2024a). Effect of area divergence and frequency on damping of slow magnetoacoustic waves propagating along umbral fan loops. , 533(1):1166–1177.

Rawat, A. and Gupta, G. (2024b). Exploring Magnetic Coupling of Solar Atmosphere Through Frequency Modulations of 3-min Slow Magnetoacoustic Waves. *Bulletin de la Societe Royale des Sciences de Liege*, 93(2):948–961.

Rawat, A. and Gupta, G. (2025). Spectroscopic diagnostics of fan loops using AIA and EIS. *In Prep.*

Rawat, A., Gupta, G., Van Doorsselaere, T., Prasad, S. K., and Erdélyi, R. (2025). Understanding the Magnetic Field and Plasma-β along Umbral Fan Loops Traced Using 3 Minute Slow Waves. , 988(1):L26.

Reale, F. (2014). Coronal Loops: Observations and Modeling of Confined Plasma. *Living Reviews in Solar Physics*, 11(1):4.

Reznikova, V. E., Shibasaki, K., Sych, R. A., and Nakariakov, V. M. (2012). Three-minute Oscillations above Sunspot Umbra Observed with the Solar Dynamics Observatory/Atmospheric Imaging Assembly and Nobeyama Radioheliograph. , 746(2):119.

Riethmüller, T. L., Solanki, S. K., van Noort, M., and Tiwari, S. K. (2013). Vertical flows and mass flux balance of sunspot umbral dots. , 554:A53.

Roberts, B. (2019). *MHD waves in the solar atmosphere*.

Sakurai, T. (2017). Heating mechanisms of the solar corona. *Proceedings of the Japan Academy, Series B*, 93:87–97.

Scherrer, P. H., Schou, J., Bush, R. I., Kosovichev, A. G., Bogart, R. S., Hoeksema, J. T., Liu, Y., Duvall, T. L., Zhao, J., Title, A. M., Schrijver, C. J., Tarbell, T. D., and Tomczyk, S. (2012). The Helioseismic and Magnetic Imager (HMI) Investigation for the Solar Dynamics Observatory (SDO). , 275(1-2):207–227.

Schmassmann, M., Rempel, M., Bello González, N., Schlichenmaier, R., and Jurčák, J. (2021). Characterization of magneto-convection in sunspots. The Gough-Tayler stability criterion in MURaM sunspot simulations. , 656:A92.

Schou, J., Scherrer, P. H., Bush, R. I., Wachter, R., Couvidat, S., Rabello-Soares, M. C., Bogart, R. S., Hoeksema, J. T., Liu, Y., Duvall, T. L., Akin, D. J., Allard, B. A., Miles, J. W., Rairden, R., Shine, R. A., Tarbell, T. D., Title, A. M., Wolfson, C. J., Elmore, D. F., Norton, A. A., and Tomczyk, S. (2012). Design and Ground Calibration of the Helioseismic and Magnetic Imager (HMI) Instrument on the Solar Dynamics Observatory (SDO). , 275(1-2):229–259.

Sharma, A., Gupta, G. R., Tripathi, D., Kashyap, V., and Pathak, A. (2017). Direct Observations of Different Sunspot Waves Influenced by Umbral Flashes. , 850(2):206.

Sharma, A., Tripathi, D., Erdélyi, R., Gupta, G. R., and Ahmed, G. A. (2020). Wave amplitude modulation in fan loops as observed by AIA/SDO. , 638:A6.

Si, R., Brage, T., Li, W., Grumer, J., Li, M., and Hutton, R. (2020). A First Spectroscopic Measurement of the Magnetic-field Strength for an Active Region of the Solar Corona. , 898(2):L34.

Soler, R., Terradas, J., Oliver, R., and Ballester, J. L. (2017). Propagation of Torsional Alfvén Waves from the Photosphere to the Corona: Reflection, Transmission, and Heating in Expanding Flux Tubes. , 840(1):20.

Spruit, H. C. (2013). Essential Magnetohydrodynamics for Astrophysics. *arXiv e-prints*, page arXiv:1301.5572.

Srivastava, A. K., Ballester, J. L., Cally, P. S., Carlsson, M., Goossens, M., Jess, D. B., Khomenko, E., Mathioudakis, M., Murawski, K., and Zaqarashvili, T. V. (2021). Chromospheric Heating by Magnetohydrodynamic Waves and Instabilities. *Journal of Geophysical Research (Space Physics)*, 126(6):e029097.

Stangalini, M., Giannattasio, F., Del Moro, D., and Berrilli, F. (2012). Three-minute wave enhancement in the solar photosphere. , 539:L4.

Stein, R. F. (2012). Solar Surface Magneto-Convection. *Living Reviews in Solar Physics*, 9(1):4.

Sych, R. (2016). MHD Wave in Sunspots. *Geophysical Monograph Series*, 216:467–487.

Sych, R. and Altyntsev, A. (2023). Siberian Radioheliograph: sunspot oscillations in 3-6 GHz band. , 519(3):4397–4407.

Sych, R., Zaqarashvili, T. V., Nakariakov, V. M., Anfinogentov, S. A., Shibasaki, K., and Yan, Y. (2012). Frequency drifts of 3-min oscillations in microwave and EUV emission above sunspots. , 539:A23.

Sych, R. A. and Nakariakov, V. M. (2008). The Pixelised Wavelet Filtering Method to Study Waves and Oscillations in Time Sequences of Solar Atmospheric Images. , 248(2):395–408.

Taroyan, Y. and Erdélyi, R. (2009). Heating Diagnostics with MHD Waves. , 149(1-4):229–254.

Tian, H., Kleint, L., Peter, H., Weber, M., Testa, P., DeLuca, E., Golub, L., and Schanche, N. (2014). Observations of Subarcsecond Bright Dots in the Transition Region above Sunspots with the Interface Region Imaging Spectrograph. , 790(2):L29.

Tomczyk, S., McIntosh, S. W., Keil, S. L., Judge, P. G., Schad, T., Seeley, D. H., and Edmondson, J. (2007). Alfvén Waves in the Solar Corona. *Science*, 317(5842):1192–1196.

Torrence, C. and Compo, G. P. (1998). A Practical Guide to Wavelet Analysis. *Bulletin of the American Meteorological Society*, 79(1):61–78.

Upendran, V. and Tripathi, D. (2021). On the Impulsive Heating of Quiet Solar Corona. , 916(1):59.

Vadawale, S. V., Mithun, N. P. S., Mondal, B., Sarkar, A., Janardhan, P., Joshi, B., Bhardwaj, A., Shanmugam, M., Patel, A. R., Adalja, H. K. L., Goyal, S. K., Ladiya, T., Tiwari, N. K., Singh, N., and Kumar, S. (2021). Observations of the Quiet Sun during the Deepest Solar Minimum of the Past Century with Chandrayaan-2 XSM: Sub-A-class Microflares outside Active Regions. , 912(1):L13.

van Ballegooijen, A. A., Asgari-Targhi, M., and Berger, M. A. (2014). On the Relationship Between Photospheric Footpoint Motions and Coronal Heating in Solar Active Regions. , 787(1):87.

van Ballegooijen, A. A., Asgari-Targhi, M., Cranmer, S. R., and DeLuca, E. E. (2011). Heating of the Solar Chromosphere and Corona by Alfvén Wave Turbulence. , 736(1):3.

Van Doorsselaere, T., Nakariakov, V. M., and Verwichte, E. (2008a). Detection of Waves in the Solar Corona: Kink or Alfvén? , 676(1):L73.

Van Doorsselaere, T., Nakariakov, V. M., Young, P. R., and Verwichte, E. (2008b). Coronal magnetic field measurement using loop oscillations observed by Hinode/EIS. , 487(2):L17–L20.

Van Doorsselaere, T., Srivastava, A. K., Antolin, P., Magyar, N., Vasheghani Farahani, S., Tian, H., Kolotkov, D., Ofman, L., Guo, M., Arregui, I., De Moortel, I., and Pascoe, D. (2020). Coronal Heating by MHD Waves. , 216(8):140.

Van Doorsselaere, T., Wardle, N., Del Zanna, G., Jansari, K., Verwichte, E., and Nakariakov, V. M. (2011). The First Measurement of the Adiabatic Index in the Solar Corona Using Time-dependent Spectroscopy of Hinode/EIS Observations. , 727(2):L32.

Verdini, A., Grappin, R., and Velli, M. (2012). Coronal heating in coupled photosphere-chromosphere-coronal systems: turbulence and leakage. , 538:A70.

Vernazza, J. E., Avrett, E. H., and Loeser, R. (1981). Structure of the solar chromosphere. III. Models of the EUV brightness components of the quiet sun. , 45:635–725.

Verwichte, E., Haynes, M., Arber, T. D., and Brady, C. S. (2008). Damping of Slow MHD Coronal Loop Oscillations by Shocks. , 685(2):1286–1290.

Viall, N. M., De Moortel, I., Downs, C., Klimchuk, J. A., Parenti, S., and Reale, F. (2021). The Heating of the Solar Corona. In Raouafi, N. E. and Vourlidas, A., editors, *Solar Physics and Solar Wind*, volume 1, page 35.

Viall, N. M. and Klimchuk, J. A. (2012). Evidence for Widespread Cooling in an Active Region Observed with the SDO Atmospheric Imaging Assembly. , 753(1):35.

von Rekowski, B. and Hood, A. W. (2008). Photospheric cancelling magnetic features and associated phenomena in a stratified solar atmosphere. , 385(4):1792–1812.

Wang, F., Deng, H., Li, B., Feng, S., Bai, X., Deng, L., Yang, Y., Xue, Z., and Wang, R. (2018). High-frequency Oscillations in the Atmosphere above a Sunspot Umbra. , 856(1):L16.

Wang, T., Innes, D. E., and Qiu, J. (2007). Determination of the Coronal Magnetic Field from Hot-Loop Oscillations Observed by SUMER and SXT. , 656(1):598–609.

Wang, T., Ofman, L., Sun, X., Provornikova, E., and Davila, J. M. (2015). Evidence of Thermal Conduction Suppression in a Solar Flaring Loop by Coronal Seismology of Slow-mode Waves. , 811(1):L13.

Wang, T., Ofman, L., Yuan, D., Reale, F., Kolotkov, D. Y., and Srivastava, A. K. (2021). Slow-Mode Magnetoacoustic Waves in Coronal Loops. , 217(2):34.

Wang, T. J., Ofman, L., Davila, J. M., and Mariska, J. T. (2009). Hinode/EIS observations of propagating low-frequency slow magnetoacoustic waves in fan-like coronal loops. , 503(3):L25–L28.

Watanabe, H., Kitai, R., Ichimoto, K., and Katsukawa, Y. (2009). Magnetic Structure of Umbral Dots Observed with the Hinode Solar Optical Telescope. , 61:193.

Wilson, A. and Maskelyne, N. (1774). Observations on the Solar Spots. By Alexander Wilson, M. D. Professor of Practical Astronomy in the University of Glasgow. Communicated by the Rev. Nevil Maskelyne, Astronomer Royal. *Philosophical Transactions of the Royal Society of London Series I*, 64:1–30.

Wilson, P. R. (1969). On the Properties of Umbral Dots. , 10(2):404–415.

Withbroe, G. L. and Noyes, R. W. (1977). Mass and energy flow in the solar chromosphere and corona. , 15:363–387.

Wójcik, D., Murawski, K., and Musielak, Z. E. (2018). Acoustic waves in two-fluid solar atmosphere model: cut-off periods, chromospheric cavity, and wave tunnelling. , 481(1):262–267.

Wülser, J. P., Jaeggli, S., De Pontieu, B., Tarbell, T., Boerner, P., Freeland, S., Liu, W., Timmons, R., Brannon, S., Kankelborg, C., Madsen, C., McKillop, S., Prchlik, J., Saar, S., Schanche, N., Testa, P., Bryans, P., and Wiesmann, M. (2018). Instrument Calibration of the Interface Region Imaging Spectrograph (IRIS) Mission. , 293(11):149.

Yadav, R. and Mathew, S. K. (2018). Physical Properties of Umbral Dots Observed in Sunspots: A Hinode Observation. , 293(4):54.

Yang, Z., Bethge, C., Tian, H., Tomczyk, S., Morton, R., Del Zanna, G., McIntosh, S. W., Karak, B. B., Gibson, S., Samanta, T., He, J., Chen, Y., and Wang, L. (2020). Global maps of the magnetic field in the solar corona. *Science*, 369(6504):694–697.

Young, P. R., Del Zanna, G., Mason, H. E., Dere, K. P., Landi, E., Landini, M., Doschek, G. A., Brown, C. M., Culhane, L., Harra, L. K., Watanabe, T., and Hara, H. (2007). EUV Emission Lines and Diagnostics Observed with Hinode/EIS. , 59:S857.

Young, P. R., Doschek, G. A., Warren, H. P., and Hara, H. (2013). Properties of a Solar Flare Kernel Observed by Hinode and SDO. , 766(2):127.

Young, P. R., Tian, H., Peter, H., Rutten, R. J., Nelson, C. J., Huang, Z., Schmieder, B., Vissers, G. J. M., Toriumi, S., Rouppe van der Voort, L. H. M., Madjarska, M. S., Danilovic, S., Berlicki, A., Chitta, L. P., Cheung, M. C. M., Madsen, C., Reardon, K. P., Katsukawa, Y., and Heinzel, P. (2018). Solar Ultraviolet Bursts. , 214(8):120.

Yuan, D., Sych, R., Reznikova, V. E., and Nakariakov, V. M. (2014). Multi-height observations of magnetoacoustic cut-off frequency in a sunspot atmosphere. , 561:A19.

Yuan, D. and Walsh, R. W. (2016). Abnormal oscillation modes in a waning light bridge. , 594:A101.

Zavershinskii, D. I., Kolotkov, D. Y., Nakariakov, V. M., Molevich, N. E., and Ryashchikov, D. S. (2019). Formation of quasi-periodic slow magnetoacoustic wave trains by the heating/cooling misbalance. *Physics of Plasmas*, 26(8):082113.

Zhao, J., Felipe, T., Chen, R., and Khomenko, E. (2016). Tracing p-mode Waves from the Photosphere to the Corona in Active Regions. , 830(1):L17.

Zhao, J., Wang, T., and Chen, R. (2025). Observed dispersive properties of the slow magnetoacoustic waves propagating in coronal fan loops above sunspots. , 538(2):797–808.

Zhugzhda, I. D., Locans, V., and Staude, J. (1983). Seismology of Sunspot Atmospheres. , 82(1-2):369–378.

Zhukov, V. I. (2005). Oscillations on the Sun in regions with a vertical magnetic field. II. On the calculation of the sunspot umbral oscillations. , 433(3):1127–1132.